Freie Universität Berlin

FACHBEREICH PHYSIK, 14195 BERLIN, GERMANY

A Path to Monochiral Ensembles of Carbon Nanotubes and their Properties

im Fachbereich Physik der Freien Universität Berlin eingereichte Dissertation

Heiko DUMLICH

May 16, 2013

erste Version: 7. Januar 2013

Abgabe der Dissertation: 10. Januar 2013

1. Gutachterin: Prof. Stephanie REICH

2. Gutachter: Prof. Daniel SEBASTIANI

Datum der Disputation: 25. Februar 2013

Vorsitzender: Prof. Joachim HEBERLE

1. Beisitzende Professorin: Prof. Stephanie REICH

2. Beisitzender Professor: Prof. Daniel SEBASTIANI

Beisitzender wissenschaftlicher Mitarbeiter: Dr. Ivan VERZHBITSKIY

Studentische Beisitzerin: Silke KERRUTH

A Path to Monochiral Ensembles of Carbon Nanotubes and their Properties

Heiko Dumlich

Fachbereich Physik

Freie Universität Berlin

Arnimallee 14

14195 Berlin

Germany

e-mail: heiko.dumlich@fu-berlin.de
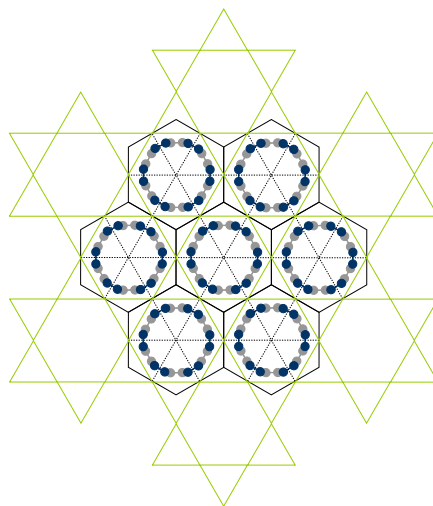
Summary

This thesis studies the synthesis of carbon nanotubes and properties of monochiral carbon nanotube bundles. The synthesis is studied with a focus on chiral selectivity for which a simplistic growth model based on geometric arguments is developed, which is based on preliminary work performed in the diploma thesis of the author, see Reference [1]. We performed density functional theory calculations of carbon nanotube cap structures on nickel, iron and nickel-iron alloy catalyst clusters to obtain input parameters for our growth model. The adhesion and excess energies between nanotube caps and catalyst particles vary in a wide range between different chiralities and catalyst compositions; In contrast to earlier calculations on flat surfaces we do not find evidence for a preference of certain chiralities. However, a higher charge transfer to armchair caps than to zigzag caps and increasing charge transfer with higher iron content in the catalyst particle is observed, which induces an electric dipole moment. This points to a higher reactivity of armchair edges and a faster growth rate on iron compared to nickel. Our growth model leads to chirality dependent growth rates during the growth phase/elongation process of the nanotubes that depends on the catalyst composition, which has recently been experimentally confirmed. [2, 3] The number of carbon edge atoms decreases from armchair to zigzag edges, which serves as a simple geometric argument for a lower growth rate of low chiral angle (zigzag) tubes, as the number of carbon atoms that can add at the edge is reduced compared to higher chiral angle (*e.g.* armchair) tubes. The study on the nanotube bundles focuses on the bundling and debundling process of carbon nanotubes and the electronic properties of the bundles, especially the dependence on the intertube orientation is considered. We find that nanotubes that share symmetry operations (*e.g.* a S_6 screw-rotation axis) of the bundle show a dependence of the electronic structure, the binding energy and the intertube distance on the orientation of the tubes inside of the bundle. The orientation dependence allows to adjust the properties of the tubes and leads to a rich electronic behavior, *e.g.* switching between semi-metallic and metallic character. Tubes that do not share symmetry elements do not show a dependence of their properties on the intertube orientation. In conclusion we were able to show, that carbon nanotubes have a chirality dependent growth rate, which together with post processing methods allows to produce monochiral bundles with fascinating properties.

Zusammenfassung

Diese Doktorarbeit beschäftigt sich mit der Herstellung von Kohlenstoffnanoröhren und den Eigenschaften von monochiralen Bündeln. Der Fokus bei der Untersuchung des Wachstumprozesses liegt auf der Produktion von chiral-selektierten Kohlenstoffnanoröhren, wobei ein einfaches geometrisches Wachstumsmodell basierend auf den Vorarbeiten in der Diplomarbeit des Autors, siehe Referenz [1], entwickelt wird. Systeme aus Kohlenstoffkappen und katalytischen Partikeln aus Metallen wurden mit Hilfe der Dichte-Funktional-Theorie berechnet, um Parameter für das Wachstumsmodell zu bestimmen. Die Adhäsions- und Überschussenergien zwischen Kappen und Partikeln zeigen eine große Varianz in Abhängigkeit der Chiralität der Kappen und Komposition der Partikel. Im Gegensatz zu früheren Studien auf flachen Oberflächen, finden wir keinen Hinweis auf die Bevorzugung bestimmter Chiralitäten. Stattdessen finden wir einen höheren Ladungstransfer zu Armchair-Kappen als zu Zigzag-Kappen, der auch mit höherem Eisenanteil im Partikel ansteigt und dadurch ein elektrisches Dipolmoment induziert. Dies weist auf eine höhere Reaktivität der Armchair-Enden und eine schnellere Wachstumsrate auf Eisen im Vergleich zu Nickel hin. Unser Wachstumsmodell liefert eine chiralitäts- und katalysatorzusammensetzungsabhängige Wachstumsrate, welche kürzlich experimentell beobachtet wurde. [2, 3] Die Anzahl an Kohlenstoffatomen am Ende der Röhre sinkt von hohen chiralen Winkeln (armchair) zu tiefen chiralen Winkeln (zigzag). Dies liefert ein geometrisches Argument für eine schnellere Wachstumsrate an Röhren mit hohen chiralen Winkeln, da für diese mehr Atome pro Zeit hinzugefügt werden können. Der Fokus bei der Untersuchung der Bündel liegt auf dem Bündelungs- und Entbündelungsprozess sowie auf den elektronischen Eigenschaften der Bündel. Speziell wurden die Eigenschaften in Abhängigkeit der Orientierung der Röhren im Bündel zueinander untersucht. Nanoröhren, die Symmetrieoperationen mit dem Bündel teilen, zeigen eine Orientierungsabhängigkeit der Bindungsenergie, des Röhrenabstandes sowie der elektronischen Struktur. Eine Änderung der Orientierung der Röhren erlaubt es z.B. zwischen metallischem und semi-metallischem Charakter zu wechseln. Röhren, die keine Symmetrieoperationen mit dem Bündel teilen, zeigen keine Orientierungsabhängigkeit der Eigenschaften.

List of Publications

1. <u>Heiko Dumlich</u> Growth of Carbon Nanotubes on Catalytic Metal Particles, Diploma Thesis (FU Berlin, Berlin, 2009) (**unveröffentlicht**)

2. <u>Heiko Dumlich</u> and Stephanie Reich, Phys. Rev. B **82**, 085421 (2010)

3. <u>Heiko Dumlich</u> and Stephanie Reich, Phys. Status Solidi B **247**, 2722 (2010)

4. Carolin Blum, Ninette Stürzl, Frank Hennrich, Sergei Lebedkin, Sebastian Heeg, <u>Heiko Dumlich</u>, Stephanie Reich, and Manfred M. Kappes, ACS Nano **5**, 2847 (2011)

5. <u>Heiko Dumlich</u> and Stephanie Reich, Phys. Rev. B **84**, 064121 (2011), Phys. Rev. B **86**, 179905(E) (2012)

6. <u>Heiko Dumlich</u>, Michael Gegg, Frank Hennrich, and Stephanie Reich, Phys. Status Solidi B **248**, 2589 (2011)

7. <u>Heiko Dumlich</u>, John Robertson, and Stephanie Reich arXiv.org/abs/1305.0145 (2013)

Contents

Stillstand

Ernest und sein Zwillingsbruder William konnten sich nicht leiden. Ihren qwirligen Freund Hermann Ludwig Ferdinand jedoch versuchten sie immer um sich zu haben. Einerseits versuchten die Zwillingsbrüder so weit voneinander entfernt zu bleiben, wie sie konnten. Andererseits wollten sie dennoch möglichst nah bei Hermann Ludwig Ferdinand sein. Man konnte gar von einer Anziehung zwischen Hermann Ludwig Ferdinand und ihnen sprechen. Zwischen den Zwillingen hingegen konnte man guten Gewissens von einer Abstoßung sprechen. Zum Glück war William momentan nicht zu sehen und Ernest konnte sich ganz allein mit Hermann Ludwig Ferdinand austauschen. Im Gegensatz zu Ernest, der wie ein Berg in der Landschaft stand und sich durch fast nichts in Bewegung setzen ließ, war Hermann wie ein Bach, ständig in Bewegung. Hermann Ludwig Ferdinand drehte einmal mehr in seinem leicht vertrakten Muster seine Runden, während Ernest sich nur dann bewegte, wenn er gezwungen wurde, da er viel schwermütiger als Hermann Ludwig Ferdinand war. Man hätte es eigentlich nicht erwartet, aber Ernest war dennoch viel dünner als Hermann. Es passierte nichts, Ernest langweilte sich fast ein wenig, als er William in der Ferne erspähte.

1 Introduction

This dissertation studies the growth and separation of carbon nanotubes to enrich nanotubes of certain properties. Carbon nanotubes are a synthetic carbon material which has been recently discovered considering the timescale of human technological development. [4] While other natural carbon allotropes, like graphite and diamond were known and used for thousands of years, [5, 6] multi-walled carbon nanotubes have been first observed as late as 1991, [4] even though claims of a first production reach back to the 1950s. [7] The technology to produce fullerenes, another carbon allotrope, was discovered a few years earlier (1985) [8] and served as an unexpected starting point to manufacture nanotubes. [4] Both fullerenes and nanotubes were later found to occur in nature. [9–15] Fullerenes naturally occur in certain carbon-rich rocks and outer space. [9–12] Nanotubes were found to be accidently produced in flames of, *e.g.*, natural gas or methane, [13–15] and could already be verified in 10,000 year old ice cores. [14]

This study focuses on single-walled carbon nanotubes, which were first produced in 1993, [16, 17] only two years after the discovery of multi-walled carbon nanotubes. [4] Single-walled carbon nanotubes are hollow cylindrical tubes with carbon atoms on their surface. [4, 18] Their diameter to length ratios of down to 10^{-8} make them quasi one dimensional. [1, 18] The one dimensionality and the variety of carbon atom arrangements on the surface of the tubes, called chirality, generate individualised material properties that are interesting for fundamental studies in physics. [18–21] At the same time these properties render them interesting for applications and fueled initial hopes that carbon nanotubes might be used as a superior material, superseding common materials in almost every imaginable field. [22, 23] After more then twenty years of research the hopes for carbon nanotubes are still high, but even though many possible applications had been proposed, the majority of them could not be turned into commercial applications yet. [22–30] One of the prob-

lems in carbon nanotube production is that many carbon allotropes are produced in similar processes, [31, 32] which made technological advancement necessary to allow for production of high purity single-walled carbon nanotube ensembles. [33] Even though the technology in the production of selected single-walled carbon nanotubes made significant progress, [2, 3, 34–41] the major unresolved problem nowaday still remains to produce nanotubes in a way to use them in devices, with properties optimised for their use. [23] Therefore nanotubes need to be produced with a specific chirality, as even high-purity single-walled carbon nanotube growth processes tend to grow nanotubes of various chiralities. [42] This dissertation focuses on a theoretical understanding of methods to produce nanotubes with a specific chirality, either directly by growth, see Chapter 2 and References [43–45] or through the methodic selection of carbon nanotubes after the growth process by exploitation of their properties, see Chapter 3 and References [46–48] It also offers a future perspective on monochiral bundles and their properties, which might lead to new applications. [46, 47]

The introduction of this dissertation presents the basic knowledge about carbon nanotubes and the methods - based on electronic strucure theory - applied to understand them, their properties, their growth process, and their separation process. To understand the properties of carbon nanotubes it is instrumental to understand the properties of the basic units they are made of. [18, 49] The smallest unit is a single carbon atom which forms hexagonal units on the tube wall. [4, 18] In a two-dimensional arrangement the hexagonal carbon units form a sheet called graphene. [50] As a tube can be regarded as a rolled up graphene sheet, most of the properties derived for graphene can be used as a starting point to derive the properties of carbon nanotubes (graphene sheet model). [18–20, 49]

1.1 Carbon Nanotubes

The first chapter of the introduction is focused on carbon nanotubes and their properties. In the first section [1] the basic properties of carbon and carbon nanotubes are presented. The second section focuses on the structure of carbon nanotubes derived from the graphene sheet model and introduces the chirality of carbon nanotubes. In the third section carbon nanotube bundles and their properties are discussed. The last section of the carbon nanotubes chapter finishes with an introduction of the growth process of nanotubes with a focus on chemical vapor deposition and a review on ideas for chirality selective growth.

1.1.1 Basics

Carbon nanotubes are made of carbon atoms arranged in a cylindrical tube, see Figure 1.1 a). [18] Elementary carbon is a non-metal with six electrons, six protons and the most common isotope $^{12}_{6}$C has six neutrons. [51] It tends to form chains with other carbon atoms, [51] assembling into mats of carbon, *e.g.*, graphene [50] or under the correct conditions [4] and with the help of template particles it can even assemble into carbon nanotubes. [52, 53] The ground state electron configuration of carbon is $1s^2$ $2s^2$ $2p^2$, with 4 valence electrons. [51] Carbon is the material which forms the highest variety of structures. [51] To illustrate the ability of carbon to produce various structures of significantly different properties, we present the properties of the natural allotropes graphite and diamond in detail. [51] Diamond is one of the hardest known materials as the atoms in diamond form sp^3-hybridized bonds ($[\uparrow]_s[\uparrow \mid \uparrow \mid \uparrow]_p \rightarrow [\uparrow \mid \uparrow \mid \uparrow \mid \uparrow]_{sp^3}$), leading to a structure where every carbon atom is surrounded by four other carbon atoms, the diamond structure. [51] The carbon-carbon distance in diamond is $d = 1.54$ Å, [51] it is insulating with a bandgap of 5.47 eV and therefore transparent for light. [54] The properties of graphite are completely different compared to the properties of diamond. [51] Graphite is used as a lubricant, while diamond is used to cut other materials. [51] The lubricity of graphite results from its layered structure, especially structural lubricity/superlubricity occurs for incommensurate graphite layers. [51, 55, 56] The individual carbon layers

---

[1]The section is partly based on Section 4.7 of the book "Anorganische Chemie" of Riedel, see Reference [51] pages 505 ff. and Section I.1.1 of the diploma thesis of the author, see Reference [1].
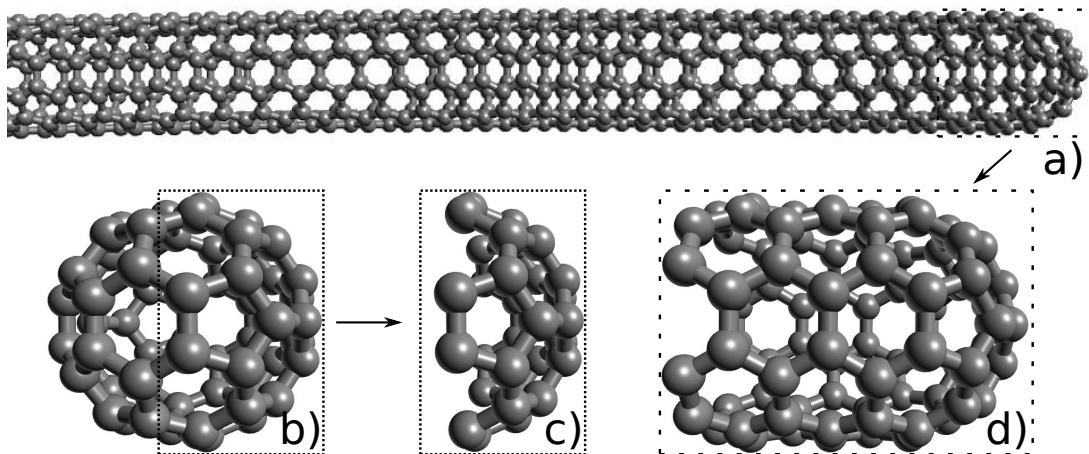
Figure 1.1: Ball and stick models of carbon nanotube and fullerene structures generated with *Avogadro*. [57] a) A carbon nanotube ending in a cap. b) A Buckminsterfullerene/fullerene composed of 60 carbon atoms with a soccer ball like structure. [8] c) One of many possible carbon nanotube caps derived from the C_{60} fullerene. d) A closer view on the end of the nanotube, showing that it ends in the cap derived from the C_{60} fullerene.

of graphite bind through van der Waals interaction. [51] The in-plane σ bonds are covalently formed by sp^2 hybridisation ($[\uparrow]_s[\uparrow \mid \uparrow \mid \uparrow]_p \rightarrow [\uparrow \mid \uparrow \mid \uparrow]_{sp^2}[\uparrow]_p$). [51] The distance between the carbon atoms in a graphite layer is smaller than the distance of carbon atoms in the diamond structure with only $d = 1.42$ Å. [51] The interplane distance between the graphite layers is $d = 3.35$ Å and results from the π-orbitals of the bonds perpendicular to the planes and their van der Waals interaction with bonds of the neighbor planes. [51] The π-orbitals of neighboring C-atoms in one plane can overlap and allow electrons to delocalise. [51] This makes graphite conducting parallel to the carbon planes. [51] The large distance between the layers makes graphite a much worse conductor perpendicular to the layers. [51] Carbon has, as we have shown, interesting properties already in its natural occuring allotropes. If it comes to more recent carbon structures, we can speak of a real zoo of new allotropes.

We will focus here only on single-walled carbon nanotubes and the carbon allotropes most relevant for this dissertation and neglect other carbon allotropes like, *e.g.*, carbon fibres, [7, 58] carbon onions, [59] and carbon nanohorns. [60] The fullerenes, [8] see Figure 1.1 b), respectively as half fullerenes form the end struc-

tures of carbon nanotubes, called caps, see Figure 1.1 c) and d). [18] Fullerenes can therefore be regarded as ultra short carbon nanotubes, or vice versa nanotubes as fullerene tubules. [52, 61] Fullerenes contain 12 pentagons that induce the curvature to close them. [9] A nanotube cap needs to have 6 pentagons to yield the curvature to grow a nanotube from it. [62, 63] The term *nanotube* is used for a conglomerate of structures, which all have a cylindrical base unit in common. [18] A single-walled carbon nanotube, see Figure 1.1 a), consists of only one wall, however, the way the atoms arrange on the wall, called chirality, determines the properties of the single-walled nanotube. [18–20, 61, 64] Multi-walled nanotubes are composed of concentric single-walled nanotubes, which determine their properties. [4, 18, 24, 32, 65, 66] The carbon allotrope which lately received the largest interest is graphene, the first stable two dimensional atomic crystal. [50, 67, 68] Graphene can be regarded as the building block/unit of fullerenes, nanotubes and also graphite, as it consists of single layers of hexagonal sp^2-hybridized carbon, equivalent to a single layer of graphite. [18] In the next section, Section 1.1.2, we will show how the graphene sheet model can be applied to derive common properties of carbon nanotubes simply by consideration of geometry/symmetry.

In the following we want to have a look at the macroscopic and microscopic properties of single-walled carbon nanotubes. As-grown carbon nanotube samples come with an ensemble of different chiralities. [42] They look like a black powder of fine short wires in macroscopic amounts, which results from the agglomeration of nanotubes of various chiralities. [1] Nanotube solutions are mostly gray to black, depending on its concentration and the surfactant. [34, 37] If the nanotubes are treated by a post processing method to separate the chiralities, phases of various colors turn up, representing an enrichment of nanotubes of a certain chirality. [34, 37, 41, 69] An individual nanotube can neither be seen by the naked eye nor by an optical microscope. [18] The smallest nanotube, which has been recently predicted has an outer diameter of only 0.32 nm, consisting of a double helical carbon chain with alternating bond order. [70] The largest diameter single-walled carbon nanotubes reach up to ≈ 10 nm. [71, 72] The longest single-walled nanotubes were reported to reach up to cm length and were theoretically predicted to be able to reach up to m length. [73–75] Therefore nanotubes can have extreme diameter to length ratios of at least up to $2 \cdot 10^{-8}$. [1] The same ratio applies to the comparison of the diameter

of a soccer ball to the diameter of the earth. [1] This quasi one-dimensionality leads to fascinating properties, *e.g.*, van-Hove singularities, which are singularities in the density of states. [76, 77] Nanotubes have to be isolated, however, before the properties can be studied. [78] Otherwise nanotubes will form bundles due to van der Waals interaction between the nanotube walls, similar to graphite layers. [18, 79, 80] The aggregation of nanotubes into bundles can, *e.g.*, quench the fluorescence by interaction of semiconducting and metallic tubes, which substantially broadens the absorption spectra. [78] Once separated the isolated tubes can be metallic, semi-metallic or semiconducting with various bandgaps only depending on the way the atoms arrange on the tube surface, meaning the chirality, [19, 20] see Section 1.1.2.

In summary we presented the basic properties of carbon, which lead to a whole zoo of allotropes with significantly different properties. [51] The carbon nanotube is one of the most interesting and recent allotropes with properties that depend on the symmetry/geometry of the tube. [18]

1.1.2 Structure and Chirality

In this section [2] we present the structure of carbon nanotubes and the properties, which result, especially, from the chirality of the tubes.

As described in the introduction the single-walled carbon nanotube has a hollow cylinder like structure. [4, 18] It can be imagined to be built of a rolled up sheet of hexagonal-oriented carbon atoms, called graphene. [4, 18, 50] Some mechanical properties of carbon nanotubes can be explained by a continuum model of a hollow cylinder, see Chapter 6 of Reference [18]. Many other properties can be derived from the properties of graphene (graphene sheet model) which serves as the basis for the nanotube structure and allows to derive the properties through boundary conditions/constrictions. [18–20, 49] The electronic band structure, for example, follows from the arrangement of the carbon atoms on the tube wall, called chirality. [18] To define the chirality, we first describe the geometry of the two dimensional graphene model. The graphene basis vectors $\vec{a}_1$, $\vec{a}_2$ form an angle of $60°$ and can be defined

---

[2] This section is based on standard introductions into the topic of carbon nanotube structure and symmetry, which can be found in chapter two and three of the textbook of Reich *et al.*, see Reference [18], in the review article about the fundamental properties of single-walled carbon nanotubes by White and Mintmire, see Reference [49], and the diploma thesis of the author, see Reference [1].
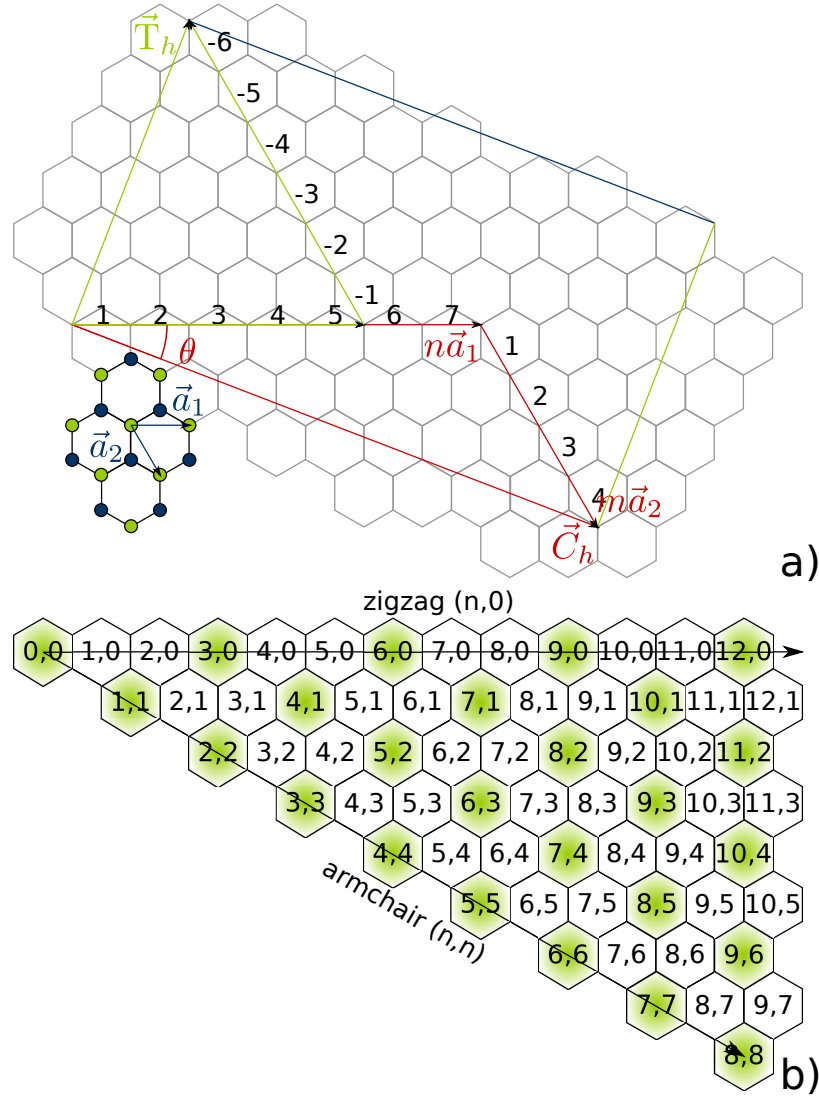
Figure 1.2: Model of a graphene sheet. a) Rolling the graphene sheet around the circumferential vector $\vec{C}_h$ leads to the nanotube of the chirality (n, m), [1, 18, 37, 49] here $(7, 4)$. The graphene basis vectors $\vec{a}_1$ and $\vec{a}_2$ are presented at the left side. The chiral angle θ is the angle between $\vec{a}_1$ and $\vec{C}_h$. [18, 19] The translational vector $\vec{T}_h$ describes the translational symmetry along the tube-axis. [18, 49, 81] b) The chiralities marked by a green hexagon have metallic/semi-metallic character. [18–20, 49] All other chiralities are semiconducting with bandgap size inversely depending on the diameter. [37, 49, 61, 64, 81, 82] The figures are similar to figures in Reference [37] (courtesy of M. S. Arnold's PhD thesis) or Reference [1].

by: [18, 49]

$$\vec{a}_1 = a \cdot \vec{e}_1 = a \cdot (1,0) \,, \tag{1.1}$$

$$\vec{a}_2 = \frac{a}{2} \cdot \vec{e}_1 - \frac{\sqrt{3}a}{2} \cdot \vec{e}_2 = a \cdot \left(\frac{1}{2}, -\frac{\sqrt{3}}{2} \right) \,, \tag{1.2}$$

where $a = \sqrt{3}d_{\text{C-C}} = 2.461$ Å is the graphene lattice constant, $d_{C-C} = 1.421$ Å is the carbon-carbon bond length/distance, and $\vec{e}_1$ and $\vec{e}_2$ are the unit vectors in x and y direction of the cartesian coordinate system, [49] see Figure 1.2 a) at the left side. The graphene basis has two carbon atoms at $0 \cdot (\vec{a}_1 + \vec{a}_2)$ (green) and $\frac{2}{3} \cdot (\vec{a}_1 + \vec{a}_2)$ (blue), see Figure 1.2 a) at the left side. Rolling the graphene sheet around the circumference allows to completely define the geometry of a carbon nanotube by the two chiral indices (n, m) which specify the relative positions of two points on the hexagonal sheet of carbon atoms. [1, 18, 49] The circumference yields the chiral/circumferential/"roll-up" vector:

$$\vec{C}_h = n\vec{a}_1 + m\vec{a}_2, \tag{1.3}$$

which allows to derive many properties, [1, 18, 49] see Figure 1.2 a).

The translational vector, that describes the translational symmetry along the tube axis,

$$\vec{T}_h = (2m + n) \, \vec{a}_1 - (2n + m) \, \vec{a}_2, \tag{1.4}$$

can be constructed perpendicular to the circumferential vector $\vec{C}_h$ lying in the honeycomb lattice, which allows to determine the minimum translational repeat length by $T = \sqrt{3}\frac{|\vec{C}_h|}{L}$ with $L = \gcd(2m + n, 2n + m)$, where gcd stands for the greatest common divisor. [49, 81] This means $L = g$, with $g = \gcd(n, m)$, unless $\frac{(n-m)}{3g}$ is an integer, in that case $L = 3g$. [49, 81] The unit cell of a nanotube is formed by the cylindrical surface with the height T and the diameter d. [18] The number of carbon atoms in the translational unit cell can be large, [49, 81] which results in a high demand of computer power for calculations involving large unit cells. To determine the number of carbon atoms in the unit cell of a carbon nanotube, we first consider the unit cell of graphene, which is a hexagon that contains $2 = 6 \cdot \frac{1}{3}$ carbon atoms. [49] The area of the graphene unit cell can be

calculated with $A_g = |\vec{a}_1 \times \vec{a}_2| = \frac{\sqrt{3}}{2}a^2$. [49] The area of the strip that is rolled up to form the minimum sized translational unit cell of the nanotube is given by $A_T = \sqrt{3}\frac{|\vec{C}_h|}{L} \cdot \left|\vec{C}_h\right| = \sqrt{3}\frac{|\vec{C}_h|^2}{L} = \sqrt{3}a^2\left(n^2 + nm + m^2\right)/L$. [49] The number of carbon atoms in the unit cell n_{C} follows from the number of hexagons contained in the translational unit cell multiplied by 2 (two carbon atoms per hexagon):

$$n_{\mathrm{C}} = 2\frac{A_T}{A_g} = 4\frac{\left(n^2 + nm + m^2\right)}{L}, \tag{1.5}$$

with $n_{\mathrm{C}} = 4g$ for achiral tubes. [49]

Further important indexes are the chiral angle θ and the diameter d of the tube, which can also be used to describe the chirality of a carbon nanotube. [18, 49]

The chiral angle θ is measured clockwise from $\vec{a}_1$ to the circumferential vector $\vec{C}_h$: [49]

$$\theta = \arccos\left(\frac{\vec{a}_1 \cdot \vec{C}_h}{|\vec{a}_1| \cdot |\vec{C}_h|}\right) = \arccos\left(\frac{2n + m}{2\sqrt{n^2 + nm + m^2}}\right) = \arctan\left(\frac{\sqrt{3}m}{2n + m}\right). \tag{1.6}$$

The chiral angle is ordinarily defined for $0° \leq \theta \leq 30°$ with $n \geq m \geq 0$ resulting in a right handed tube. [3] [18, 19] An equivalent tube with left handed helix and $30° \leq \theta \leq 60°$ can be found for $0 \leq n \leq m$. [18] Further angles are only repetitions of the tube structures contained in the first $\theta = 60°$ following from the hexagonal ($60°$) rotational symmetry of graphene. [18] Achiral tubes, meaning $(n,0)$ with $\theta = 0°$ ($\theta = 60°$), called zigzag and (n,n) with $\theta = 30°$, called armchair, see Figure 1.2, obviously do not have a handedness. [18, 19] All chiral tubes $n \neq m \neq 0$ possess a left- or right-handedness, however, the tube properties discussed in this thesis do not depend on the handedness, [49] therefore we will not consider handedness, with the exception of chiral tubes in bundles, see Section 3.3. Tubes of the same chirality can have a different handedness, which can influence how well their surfaces fit to each other if they are put right next to each other in a bundle. [83]

The diameter of a nanotube can be derived from the formula of the circumference of a circle, representing the two dimensional projection along the tube axis of the

---

[3] The handedness of a nanotube is the way the hexagon-spiral of the nanotube rotates, that can be left-handed or right-handed. [18]
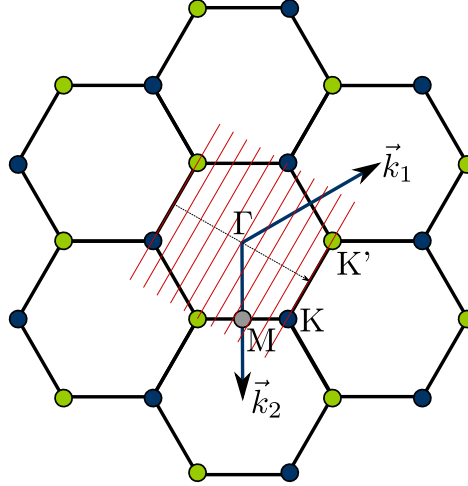
Figure 1.3: Brillouin zone of a graphene sheet with reciprocal lattice vectors and high symmetry points Γ, K, K', and M. The figure is similar to figures in Reference [49] or Reference [1].

cylindrical tube

$$d = \frac{\left|\vec{C}_h\right|}{\pi} = \frac{a}{\pi}\sqrt{n^2 + nm + m^2} = \frac{a}{\pi}\sqrt{N}, \qquad (1.7)$$

with $N = n^2 + nm + m^2$ and $a = 2.461$ Å the graphene lattice constant. [18, 49, 84]

To generate the structure of a nanotube of a certain chirality only two atoms and the symmetry are needed. [49, 81] The two atoms are mapped onto a cylinder and the application of rotations and screw operations allows to generate the positions of the other atoms. [49, 81] We used the program "wrapping.exe" [4] to generate the major part of the tube structures used in this thesis.

The chirality of the tube decides its electronic and mechanical properties. [18] Nanotubes can be metallic as well as semiconducting. [18–20, 61, 64] To derive the electronic properties we can use the graphene sheet model. [18–20, 49] The reciprocal lattice vectors of the graphene sheet can be calculated from the graphene

[4]The program wrapping was used in the version published on 09/14/2004 by Shigeo Maruyama, maruyama@photon.t.u-tokyo.ac.jp, http://reizei.t.u-tokyo.ac.jp/ maruyama/wrapping3/wrapping.zip. A few selected chiralities were generated by symmetry considerations and pen and paper work.

basis vectors $\vec{a}_1$, $\vec{a}_2$ of Equation (1.1) and (1.2): [5]

$$\vec{k}_1 = \frac{2\pi}{a} \cdot \vec{e}_1 + \frac{2\pi}{\sqrt{3}a} \cdot \vec{e}_2 = \frac{2\pi}{a} \cdot \left(1, \frac{1}{\sqrt{3}}\right), \tag{1.8}$$

$$\vec{k}_2 = -\frac{4\pi}{\sqrt{3}a} \cdot \vec{e}_2 = \frac{2\pi}{a} \cdot \left(0, -\frac{2}{\sqrt{3}}\right), \tag{1.9}$$

and $\vec{k}_3 = \frac{2\pi}{a} \cdot \vec{e}_3 = \frac{2\pi}{a} \cdot (0, 0, 1)$. [49] This allows to draw the Brillouin zone of graphene, see Figure 1.3. The high symmetry points can be found at

$$\Gamma = 0 \cdot \left(\vec{k}_1 + \vec{k}_2\right) = (0, 0), \tag{1.10}$$

$$K = \frac{1}{3} \cdot \left(\vec{k}_1 + 2\vec{k}_2\right) = \frac{2\pi}{a} \left(\frac{1}{3}, -\frac{1}{\sqrt{3}}\right), \tag{1.11}$$

$$M = \frac{1}{2} \cdot \vec{k}_2 = \frac{2\pi}{a} \left(0, -\frac{1}{\sqrt{3}}\right). \tag{1.12}$$

The band structure can be restricted to the first Brillouin zone, because of the periodicity of the graphene lattice. [49] The valence band and conduction band touch each other at the K points shown at the corners of the first Brillouin zone. [49] The wavevectors of the K points are given with $\pm \left(2\vec{k}_1 + \vec{k}_2\right)/3$, $\pm \left(\vec{k}_1 + 2\vec{k}_2\right)/3$, and $\pm \left(\vec{k}_1 - \vec{k}_2\right)/3$. [49] This can be used to determine if a certain chirality is metallic or semiconducting by using a one-parameter tight-binding model [6] with periodic boundary conditions for the circumferential vector:

$$\vec{k} \cdot \vec{C}_h = 2\pi j, \tag{1.13}$$

with integer j. [19, 20, 49] The boundary condition restricts the nanotube states to a set of parallel lines (red) in the reciprocal lattice of graphene, [18–20, 49] see Figure 1.3 for the example of the $(5, 5)$ tube. Each parallel line corresponds to

---

[5]The reciprocal lattice vectors are defined by $\vec{k}_1 = 2\pi \frac{\vec{a}_2 \times \vec{a}_3}{\vec{a}_1 \cdot \vec{a}_2 \times \vec{a}_3}$ and cyclic permutations, [85] where $\vec{a}_1$, $\vec{a}_2$ are given by Equation (1.1) and (1.2) which are extended with a zero z-component and $\vec{a}_3 = (0, 0, 1)$ is the unit vector in z-direction.
[6]The tight binding model for graphene is presented in detail in the book of Reich *et al.* for the nearest neighbor and third-nearest neighbors, see Reference [18].

a different j, is perpendicular to $\vec{C}_h$, and has a distance of $2\pi/\left|\vec{C}_h\right| = 2/d$ to its neighboring lines. [18, 49] Inserting the wavevector $\vec{k} = \left(\vec{k}_1 - \vec{k}_2\right)/3$ in Equation (1.13) yields the condition $n - m = 3j$, which means that the K point will only be on an allowed line (metallic), for about $1/3$ of the nanotube chiralities. [49] The other $2/3$ of the chiralities are semiconducting with a band gap depending inversely on the diameter of the tube. [49, 61, 64, 81, 82] Only the armchair tubes, however, are truly metallic as the curvature shifts the lines slightly away from the K points, which leads to a small gap for tubes with bands of the same symmetry (non armchair). [49] More details on the properties of carbon nanotubes can be found in the literature, see , *e.g.*, References [18, 49]. In the following we list some experimental methods to determine the nanotube chirality and discuss the problems that are involved with the derivation of a chirality distribution.

Carbon nanotubes obtained in the experimental growth process generally have a wide chirality distribution. [42] Several methods can be used to determine the chirality of carbon nanotubes. The high resolution transmission electron microscopy (HRTEM) combined with electron diffraction can determine the chirality, however, the method is not feasible for large amounts of nanotubes/nanotube ensembles. [86] Therefore methods that can be applied to the whole nanotube sample are required for a fast analysis. The most commonly used methods to determine the chirality distribution of a nanotube ensemble are photoluminescence spectroscopy [42, 87] and Raman spectroscopy. [42, 88, 89] The photoluminescence (PL) intensity depends on the chirality of the tubes, which makes it necessary to divide the experimental PL intensity by a calculated PL intensity to receive an estimated abundance of the tubes. [87] One problem is that the calculated PL intensity heavily relies on assumptions, *e.g.*, that only one relaxation path from the E_{22}^{S} to E_{11}^{S} energy level of the nanotubes dominates. [87] The abundance of chiralities has consequently been found to quantitatively depend on the method to determine the chiralities. [89] This generates large uncertainties in all nanotube abundance determinations based on photoluminescence. [90] Further many studies do not analyse as-grown tube ensembles, but postprocess the tubes before they are analysed. [78] It has been suggested, that certain chiralities are removed through this process, while others are enriched by this process, *e.g.* zigzag and near-zigzag tubes might be removed through the postprocessing. [91] This is a problem for all theoretical models, as the comparison
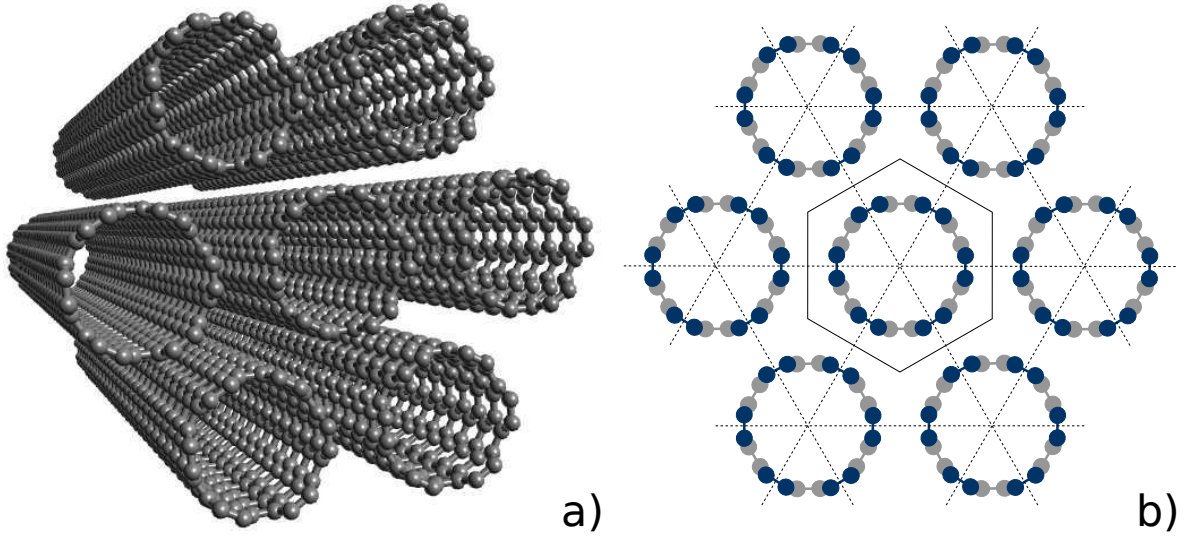
Figure 1.4: a) Ball and stick model of a bundle of seven $(6,6)$ carbon nanotubes in a trigonal configuration. b) Two dimensional projection of the unit cells of the $(6,6)$ tube bundle, blue atoms are in the top row and gray atoms are in the bottom row of the unit cell. The trigonal configuration resembles the close packed structure for two dimensional systems, [92] which for bundles of nanotubes is also the close-packing. [80, 93] The Figure 1.4 b) was inspired by References [46, 48] of the author of this thesis.

between theoretical estimates and experimental results contains some arbitrariness due to the problem of the chirality determination. [89]

This section presented the chirality of carbon nanotubes and the properties that can be derived from it. The nanotubes exhibit fascinating properties based on their geometry, *e.g.* they can be metallic or semiconducting. [18–20, 49] The chirality distribution of a nanotube sample, which corresponds to the different abundances of nanotube chiralities in a sample, is not trivial to determine, which limits the comparability between theoretical predictions of chirality distributions and experimental observations. [42, 89]

1.1.3 Bundles

In this section we present the aggregation of carbon nanotubes and the properties of the aggregates/bundles. We further focus on the difference to individual tubes and how bundles can be separated.

Carbon nanotubes tend to form bundles/ropes/aggregates of tubes induced by van der Waals interaction between individual tubes, see Figure 1.4. [16, 80, 94] Bundles often consist of about 20-100 tubes. [18, 80] To get an impression how incredibly thin nanotubes are we can consider a bundle of 100 nanotubes and compare it to a human hair. The bundle has a diameter of about $d \approx$ 4-50 nm, [7] while the diameter of a human hair is $d \approx$ 17-181 μm, [97] making a bundle about 200-60000 times thinner than a human hair. The formation of a bundle significantly changes the properties of the carbon nanotubes. [18, 65, 80, 83, 95, 98–102] The most important reason for the significant change of the properties is the interaction with neighboring tubes, which mainly occurs through the π-orbitals of nearest neighbor tubes. [103–105] Bundling reduces the symmetry, even for tubes of the same chirality. [18, 100, 102, 106] This is a result of the hexagonal packing of the bundles which yields a D_{6h} point group. [18, 80, 102] The tubes in the bundle in general yield another point group, which allows only for a smaller subgroup to be shared between the bundle structure and the nanotubes of the bundle, *e.g.* D_{2h} for achiral tubes and D_2 for chiral tubes. [18, 102] Changing the intertube orientation of the tubes in the bundle can further reduce the symmetry, [18, 102] *e.g.* to C_{2h}. [18] Therefore the properties of bundles depend on the intertube orientation. [102, 107, 108]

The trigonal structure observed for bundles of nanotubes [80] is not necessarily the only possible nanotube bundle configuration. Therefore studies tested the stability of other possible configurations, *e.g.* a tetragonal configuration was found to be energetically less stable for $(6, 6)$ tubes in a bundle. [93] The trigonal character starts for bundles of seven tubes. However, bundles of less tubes are also possible, which can change the optimal structure of the bundle. Bundles of two tubes generate constrictions for chiral tubes, which can form helices, while achiral tubes can orient optimally to each other in a parallel structure. [103] Three tubes generally form a trigonal structure, however, linear configurations have also been studied theoretically. [104] Bundles of four tubes tend to create a close packed two dimensional

---

[7]We assume a trigonal bundle structure, with one tube in the first shell of the bundle, $6 \cdot \left(0 + 2 \cdot \frac{1}{2}\right) = 6$ tubes in the second shell, ..., and $6 \cdot \left(n - 2 + 2 \cdot \frac{1}{2}\right) = 6 \cdot (n - 1)$ tubes in the nth shell. To approximate the diameter of the bundle we consider a hexagonal form of the bundle with five shells, meaning 91 tubes to find a hexagonal side length of $t = 5 \cdot l_0 + 6 \cdot d$, where $l_0 = 3.4$ Å [95] is the intertube distance and d is the diameter of a nanotube. This leads to a hexagonal side to side distance of $D = \sqrt{3} \cdot t$, [96] which we compare to the human hair diameter.

rhomboedric-like shape, [105] also a tetragonal shape is possible, but less stable as shown for the bulk bundle. [93] Five tube bundles create a square like shape with one tube in the middle of the bundle [104] or a pentagonal-like bundle. Six tubes might create a bundle with a hexagonal-like shape or one tube in the middle enclosed in a five tube shell or an irregular shape. Starting with seven tubes a first shell around the inner tube is created, which still varies in shape, however, the inner tube will mostly be influenced by its six next nearest neighbor tubes, as the interaction becomes weaker with increasing distance. [104, 105] Therefore we considered an inner tube in a trigonal unit cell for the calculations presented in this thesis, which compares to the situation of a nanotube crystal, see Chapter 3.

The nanotubes in bundles were observed to have a circular cross section, corresponding to the cross section of isolated tubes. [80] Bundles of carbon nanotubes with increasing diameters, however, have been found to undergo a structural transition. [109, 110] The tubes in the bundle deform according to the hexagonal structure of the bundle and become hexagonal/rounded-hexagonal instead of circular. [109, 110] This was attributed to the increase in interaction energy between flattened surfaces of neighboring tubes, *e.g.* like for graphene layers in graphite. [110] This only happens for larger diameter tubes ($d \geq 25$Å), [109] as it costs energy to deform the bonds in the intratube binding, which for small diameter tubes with high curvature is energetically less preferable. [110] In our study we consider small diameter tubes with circular cross sections, see Chapter 3. Small diameter tubes are preferable to obtain chirality selected samples, as the number of possible chiralities grows with the diameter [18, 37] and the diameter of the tube can be controlled by the size of the particle, [52, 111–115] which makes the tube diameter a possible criterium to narrow the chirality distribution during the chirality selective growth process, see Section 1.1.4.

Another interesting aspect for the structure of bundles is the possibility to form helices of tubes in the bundle. [103] The tubes in a bundle are not necessarily aligned parallel, they can form a helical structure if the energy gain received from the optimum orientational alignment of the neighboring tubes is larger then the energy costs induced through the coiling stress, however, this was suggested to be less likely if a large number of tubes is in the bundle. [103] But for two chiral tubes of low pitch angle χ the probability to form a double helix like structure is high, as could be shown

with high resolution transmission electron microscopy (HRTEM) recently. [103] Another possibility to deform the structure of the bundle is by the application of a magnetic field. [116] The form of the bundles of nanotubes can be shaped by the magnetic fields, if a magnetic catalyst particle is at the tip of the bundle, whose growth direction is controlled by the external magnetic field. [116]

From the experimental point of view bundles are often not desirable, as they hide the properties of the individual nanotubes in the bundle, *e.g.* by quenching the fluorescence. [78] The electrostatic charging of tubes in the bundle separates the tubes, however, only temporarily, as they discharge through contact with ambient molecules in the air. [117] Therefore the bundles need to be destroyed and the nanotubes have to be separated. [78] Recently a lot of effort has been put into this research field. [34, 36, 37, 41, 118, 119] In the following we will give a short overview on some possible ways to post process the nanotubes and isolate the tubes.

Prior to achieving isolated tubes a first step was to remove certain (metallic) tubes from the bundles. [24] It was shown that single-walled carbon nanotubes in bundles of a mix of metallic and semiconducting tubes can be selectively removed by current-induced electrical breakdown, meaning that a high enough current is applied to the bundle which leads to the selective creation of defects/oxidation at tubes that have higher conductivities (metallic tubes). [24]

The first nanotube post processing procedure to successfully destroy bundles and separate the tubes was performed by ultrasonication, centrifugation and addition of sodium dodecyl sulphate (SDS) surfactants, which form micelles around the individual nanotubes. [78] Other studies following this approach have optimized the procedure to select certain chiralities by the change of surfactants, an overview can be found in the review article of Hersam in Reference [37]. The most approaches follow the same procedure of using a surfactant to select nanotubes in combination with other post processing methods to obtain monochiral samples of nanotubes which include, *e.g.* dielectrophoresis, chromatography [36, 41, 119] and ultracentrifugation [34]. [37] One of the most promising approaches is the single-surfactant multicolumn gel chromatography method of the group of Kataura, which allows a cost efficient and easy separation of carbon nanotubes. [41] An allyl dextran-based size-exclusion gel (Sephacryl S-200, GE Healthcare) fills a column in which single-walled carbon nanotubes solved in an aqueous sodium dodecyl sulphate (SDS)

solution are added on top of the gel. [41] The interaction strength between the gel and the nanotubes depends on the structure (chirality) of the nanotubes. [41] The tubes that have the strongest interaction with the gel have the highest probability to occupy the adsorption sites of the gel. [41] Overloading the column with nanotubes leads to a replacement of weaker interacting chiralities with stronger interacting chiralities at the adsorption sites, which increases the selectivity of the gel. [41] Repeating this procedure in vertically aligned columns allows to effectively separate the nanotube ensembles into selected chiralities. [41] The details of the selective process, however, are not well understood. [41] It is believed that the coverage of SDS on the nanotubes scales the interaction strength between the gel and the tubes, [41] therefore it is of interest to understand the interaction between the nanotubes and the surfactant. Especially the influence of the chirality in the binding strength between the surfactant and the tubes is important. The differing bond curvatures, resulting from the surface π-electron states of different chiralities, were suggested to be a possible reason for the variation of the SDS coverage on the tube surfaces. [41] A recent study of the Kataura group suggested that the metal-semiconducting tube separation can be understood by the Gibbs free energy of adsorption, which is lower for semiconducting tubes than for metallic tubes. [120]

In Chapter 3 we investigate the binding strength between the nanotubes in a bundle. The binding strengths between the tubes to each other have to be compared to the binding strength of a surfactant to the tubes to determine, if tubes will stay in the bundle structure or form a complex with the surfactant and leave the bundle structure. [104, 105] A general dispersion mechanism was suggested by Strano *et al.* that considers the effect of the ultrasonication. [121] The ultrasonication "frays" the bundle ends, which then allow surfactant molecules to adsorb and further broaden the gap in an "unzippering" fashion until the process terminates with the release of an isolated surfactant coated nanotube in solution. [121] In general the nanotube separation of the bundle is a reversible process, which leads to a dynamic equilibrium as a function of carbon nanotube and surfactant concentration. [121] In recent studies the separation of nanotubes with the surfactant sodium dodecyl sulphate (SDS) [105] and the solvation with aniline [104] have been studied.

Duan *et al.* used a molecular mechanics approach with force fields to geometry optimize systems of SDS and nanotubes with the aim of finding their minimal ener-

gies and morphologies. [105] The van der Waals interaction was modeled by a sum of Lennard-Jones potentials. [105] The external tube, that is meant to be separated, can either interact with one, two or three neighboring tubes. [105] The morphology of the surfactants on the nanotube surface depends on the number density of the surfactants; [105] First the SDS molecules wrap around the tube in a circular alignment (maximizing the surface interaction) which transforms to a cylindrical micelle around the nanotubes with increasing number density, however, to disperse the nanotube the SDS molecules first have to get between the tubes. [105] This is possible due to increased intertube distances, which models the effect of ultrasonication. [105] To disperse the nanotubes a sufficient number of SDS surfactants has to adsorb to the nanotube surface, which leads to a higher binding energy between SDS and the tube than the intertube binding energy. [105]

The binding energy between aniline and a tube covered by aniline was found to be smaller than the binding energy of a bundle of seven tubes, therefore aniline is not able to separate/solve nanotubes. [104] Even if the aniline molecule would enter the bundle it would be squeezed out by thermally induced vibrations. [104] This was found to correspond to the experimental observation, that aniline is not a good solvent and it was suggested that larger π systems are needed to provide enough adsorption strength to be able to separate the tubes from the bundle. [104] One caveat of the studies on the dispersion of nanotubes, however, is, that they do not study the effect of the chirality of the tubes on the dispersion. Also the effect of other, especially chiral, surfactants in the dispersion process stays as a future problem. [105]

It is not always desired to destroy the bundles of nanotubes, as monochiral bundles can also yield interesting properties. [122] However, as bundles of nanotubes generally consist of nanotubes with various diameters and chiralities possible properties of monochiral bundles are suppressed. [122] Therefore it is desirable to use post processing techniques to design monochiral bundles. Bundles enriched with zigzag and near zigzag nanotubes have recently been observed, [91] pointing to a possible structure dependence of the binding strength between nanotubes in a bundle, which we investigate in Chapter 3.

In this section we learned that nanotubes hide their fascinating properties through averaging effects induced by the mixed chirality bundles. [18, 122] Therefore separat-

ing the tubes of the bundle to individual tubes is desired, at best the process would also be chirality selective. [37, 41, 78] Beneath the possibility of post processing the nanotubes, there is also another way to produce chirality selected nanotube samples, the chirality selective growth, which we present in the next section (Section 1.1.4) and as a part of our research study in Chapter 2.

1.1.4 Growth

In this section [8] we present the basics on the growth of carbon nanotubes, as well as the advanced topic of chirality selective growth of carbon nanotubes. We therefore first present the basic concepts of catalysis/crystal growth theory translated to the case of carbon nanotube structures.

The growth of single-walled carbon nanotubes generally requires a catalyst. [16, 17, 123] A catalyst is a substance that increases the reaction rate, as it lowers the activation energy for the addition of carbon atoms to the growing nanotube. [124] The catalyst is a product of the reaction, meaning that it is not consumed during the reaction. [124] Common catalysts for the synthesis of carbon nanotubes involve Ni, [125] Fe, [126] and Co [17] or mixtures of these metals with themselves [3, 80, 127, 128] or other elements. [33, 36, 128] The nanotube growth rates vary in dependence of the chirality [2] and temperature, [129] $e.g.$ between 3 and 22 μm/s. [129] However, nanotubes have also been grown with a slow growth rate of 8.3 nm/s on a SiO_2 substrate, meaning without a metal catalyst, [130, 131] and the first growth of nanotubes (MWCNTs) was achieved without a catalyst. [4] The nanotube growth therefore needs only two basic ingredients, carbon and energy. [1, 4] The form of both ingredients depends on the growth method, which we present in the following.

Carbon nanotubes are commonly produced with three methods, the arc discharge, [4, 135, 136] the laser evaporation/vaporization, [137] and the chemical vapor deposition (CVD). [52, 123, 138, 139] In the arc discharge method a plasma consisting of metal and carbon atoms is created between an anode and cathode consisting of graphite, which is commonly mixed with a metal. [4, 140, 141] The nanotubes form during the cooling process of the plasma and precipitate to the walls of the arc discharge chamber. [141] In the laser vaporization method a high energy laser is focused on a metal-graphite composite target, which vaporizes the target and generates a

---

[8]Parts of this section are based on the diploma thesis of the author of this thesis, see Reference [1].
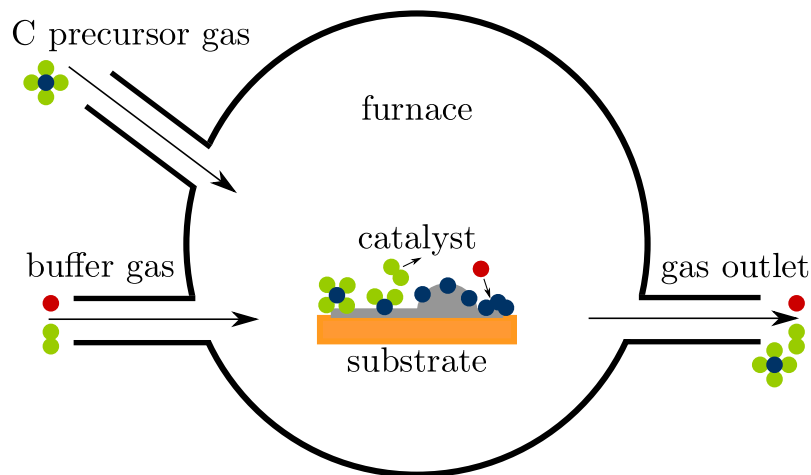
Figure 1.5: Schematic picture of an exemplary furnace for the CVD process. The catalyst (gray) is deposited on a substrate (orange) and forms clusters. A buffer/carrier gas, *e.g.*, Ar (red) + H_2 (green) [132, 133] and a carbon (blue) precursor gas, *e.g.*, methane [131, 134] are introduced into the furnace. The figure was inspired by Reference [1] of the author.

carbon-metal vapor. [137] The metal and carbon atoms in the vapor form clusters which grow nanotubes and get collected on a cooled metal-catalyst collector. [137] More details about the arc discharge and laser evaporation growth techniques can be found in the review articles in the References [140, 141]. We want to focus on the chemical vapor deposition (CVD) method in this thesis, as it is the most promising growth technique considering its scalability [142] and the possibility to control the parameters to enable chirality selective growth. [3] In the CVD growth method a carbon precursor gas is decomposed on a catalyst in a heating chamber/furnace, see Figure 1.5. [52, 140] The carbon precursor gases include CO, [139, 143] and the hydrocarbons C_2H_2, [134, 144], C_2H_4, [145] CH_4, [131, 134] CH_3OH, [38] and C_2H_5OH. [133] As we focus on the chirality of nanotubes, we do not consider the growth mechanism of multi-walled carbon nanotubes (MWCNTs) here, as it differs in many aspects from the growth process of single-walled carbon nanotubes (SWC-NTs). [1, 146] Details on the growth of multi-walled carbon nanotubes can be found in References [31, 136, 146–149].

A variety of chemical vapor deposition techniques exist, *e.g.*, thermal CVD, which often leads to spaghetti like/unaligned nanotubes, [134, 150] alcohol catalytic
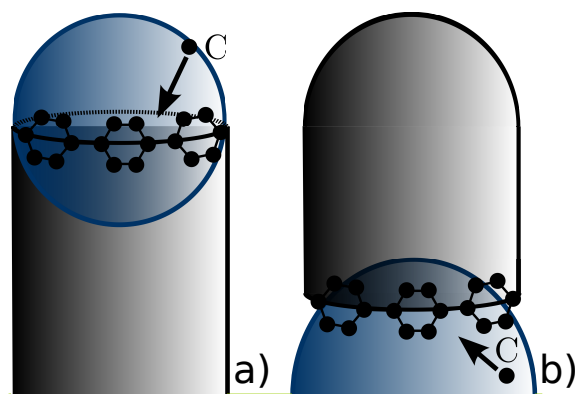
Figure 1.6: Sketch of the growth modes of nanotubes in the chemical vapor deposition. The substrate is green, the catalytic particle is blue and the carbon nanotube, and carbon atoms are in black. a) Tip growth mechanism, where the catalyst particle is lifted off the substrate by the elongating tube. [123, 149, 156] The carbon atoms add at the edge of the tube connected with the catalyst particle lifting the catalyst particle. b) Root/base growth mechanism, where the catalyst particle stays connected to the substrate and the carbon cap elongates from the catalyst particle. [123, 157]

CVD (ACCVD), [114, 151, 152] laser assisted CVD, [153], plasma enhanced CVD (PECVD), which leads to aligned nanotubes, [125, 150, 154] and time-programmed plasma CVD (TP-PCVD), which leads to narrow chirality distributions. [155] In the following we will introduce the basics in common for all of the chemical vapor deposition (CVD) growth techniques focusing on single-walled carbon nanotubes.

In the CVD method two general growth modes exist, the tip growth [9] [149, 158] and the root/base growth, [149, 157–160] see Figure 1.6. [123] In the tip growth model the carbon atoms push the metal particle away from the substrate, effectively lifting it during the nanotube elongation, see Figure 1.6 a). [123, 149, 156] There are two conditions for the tip growth, first the diffusion time of carbon atoms through the catalyst particle from its top to the bottom has to be shorter than the time it takes for the catalyst particle surface to be saturated by carbon atoms. [10] [149, 156]

---

[9]The tip growth has been observed for MWCNTs [149] and for horizontal growth of SWCNTs. [158]

[10]If the catalyst particle becomes saturated it will precipitate carbon atoms on its surface leading to a template for the nanotube formation resulting in base growth. [149] Further the diffusion time has to be smaller than the impingement time, as otherwise the surface would saturate and base growth would be initiated. [149, 156] We therefore expect the base growth mechanism

And second the energy gain from carbon transition from the catalyst particle to the nanotube has to be higher than the binding energy between the metal and the substrate. [123, 149, 156] In the base growth mode the catalyst particle stays on the substrate and the catalyst surface is saturated with carbon which grows into a nanotube, see Figure 1.6 b). [157] The base growth requires a moderate binding energy between the substrate and the catalyst, as strong interactions flatten the catalyst particle, disabling the particle as a template for a nanotube. [134] Too weak interactions can inhibit the growth, as the catalyst particles become too large for nanotube nucleation and get encapsulated by amorphous carbon. [134] The same requirement of moderate binding energy is imperative for the carbon-metal adhesion, [159, 161, 162] as too strong adhesion prevents the cap to lift off and elongate, [161] leading to amorphous carbon and too weak adhesion leads to carbon chain lift off before a cap can form or cap lift off without tube elongation, which stops the growth due to dome closure of the caps. [159, 162] We will focus on the root growth mechanism in this thesis, as the catalyst is easier to reuse for repeated growth cycles if it sticks to a substrate instead of the tips of the nanotubes. [132]

Two basic models have been suggested for the growth of nanotubes, the vapor-liquid-solid (VLS) model [11] [157, 165] and the screw-dislocation model. [4, 166–168] The vapor-liquid-solid (VLS) model was first developed for the growth of silicon whiskers, which do not contain an axial screw dislocation making an impurity essential for the growth. [165] The impurity allows to form a liquid silicon-gold alloy droplet, which becomes saturated with silicon leading to the precipitation and growth of silicon atoms to a whisker. [165] For the nanotube growth the liquid droplet corresponds to a metal-carbide particle, which after saturation precipitates carbon atoms that grow into the nanotube. [157] The screw-dislocation model is a standard model developed for the growth of crystals, which states that real crystals are not perfect. [12] [166, 167] The imperfections, *i.e.* dislocations ending in the surface with a screw component, serve as a site for the addition of a new layer and

---

if the carbon atoms do not diffuse into the catalyst particle and diffuse only on the surface (surface diffusion). [1]

[11]Besides the VLS models also vapor-solid-solid (VSS) models have been suggested. [163] Another recent idea is to model the growth of nanotubes by a nano Czochralski model. [164] In this model each catalyst particle serves as a nano crucible to grow a rotating nanotube with a chirality dependent growth rate. [164]

[12]On a perfect crystal surface the steps which are required for the crystal growth can only be produced under a highly supersaturated environment. [167]

avoid the high energy barrier occuring for completed planes. [166, 167] The main paper on carbon nanotubes by Iijima suggested to use a screw dislocation model to explain the growth of nanotubes, as the tubes can have spiral growth steps at the tube ends/rims. [4] Later Ding *et al.* used the model to derive a dependence between the chirality and the growth rate of the nanotube. [168] They identified kinks (see *aa.z* growth sites in Section 2.1.1) as low-energy-barrier addition sites for carbon atoms. [168] Following Ding *et al.* the growth is driven by a monotonous free energy decrease

$$\Delta G = -\Delta\mu \cdot N, \tag{1.14}$$

with $\Delta\mu$ "the driving chemical potential drop between the carbon dissolved in the catalyst and its bound state in the tube lattice", [13] [168] and N the number of added carbon atoms. [168] However, only chiral tubes contain kinks during the whole elongation process, achiral tubes (armchair and zigzag) grow in layers. [168] If a carbon layer is completed an activation energy G^* is required to initiate the growth of a new layer, which results from the under-coordinated carbon atoms at the newly emerging kinks. [168] This leads to the free energy decrease of

$$\Delta G = G^* - \Delta\mu \cdot N, \tag{1.15}$$

rendering the growth of achiral tubes significantly slower than compared to the growth of chiral tubes, if $G^* \gg k_bT$. [168]

In the following we present the detailed growth process of carbon nanotubes within the chemical vapor deposition following the description presented in the diploma thesis of the author, see Reference [1]. The growth process of carbon nanotubes in the CVD method can be divided in four phases. The preparation/pretreatment phase, in which the catalyst and substrate are prepared, [72, 169–171] the nucleation phase, in which the nanotube caps form, [172–175] the growth phase, in which the nanotubes elongate with a chirality dependent growth rate, [2, 43, 168] and a termination phase, in which the growth ends. [169, 176, 177]

The aim of the preparation phase is to grow small clusters on a substrate as templates for the nanotube caps. [53, 178, 179] Therefore a metal catalyst layer

---

[13] The carbon atoms that are not part of the nanotube have a higher energy than carbon atoms that are incorporated in the nanotube. [74] This drives the carbon atoms to add to the nanotube to lower the free energy of the system. [74, 168]

is epitaxially grown on a carefully chosen/designed substrate [35, 72] and a heat and/or plasma treatment [171] induces the nucleation of catalyst particles due to interatomic diffusion and the difference in the surface free energy of the substrate and the metal catalyst. [180] The pretreatment is often performed under a reducing gas atmosphere to increase the rate of reduction and sintering of metal clusters. [35]

The introduction of a carbon precursor gas, initiates the nucleation phase. The precursor gas is generally accompanied by an etching, [132] buffer, and/or carrier gas [132, 133] to generate a gas flow in the system and to prevent the encapsulation of the catalyst particle, [181] which likely terminates the growth. [169] The carbon precursor gas either impinges on the catalyst/substrate or it is partly decomposed in a plasma and the atoms impinge on the catalyst/substrate. [182] The precursor gas atoms adsorb at the catalyst surface to become decomposed in carbon atoms and a moiety of the precursor, [182] meanwhile the etching gas removes excess carbon feedstock [132] or prevents Ostwald ripening. [14] [176] The carbon atoms diffuse on the surface, [163, 182] sub-surface, [74] or through the bulk of the catalyst [163, 183] and start to form carbon structures, *e.g.* chains, Y-like carbon chain junctions, or seed pentagons. [184, 185] The carbon seed structures form curved graphene-like sheets through the curved template form of the catalyst. [184, 185] The curvature is induced by the pentagons in the graphene-like sheets, which were found to be energetically favorable in the nucleation phase, as the bond saturation is increased due to the curvature. [172]

The lift off of the graphene-like sheets in the form of a carbon nanotube cap [172, 184] ends the nucleation phase. The carbon nanotubes elongate with a chirality dependent growth rate [2, 43, 168] without changing their chirality, as rearrangements of the chirality are costly. [151, 179, 186] Carbon atoms therefore add at the edge of the nanotube [4, 168] and elongate the tube until the growth phase is ended due to a lack of carbon supply, named the termination phase. [169]

The lack of carbon supply can have various reasons. One reason might be, that a dense forest of nanotubes prevents carbon feedstock to directly reach the catalyst atoms and diffusion of carbon species along the tube surface becomes necessary

---

[14]Ostwald ripening corresponds to a process where a system of particles increases the system stability by an increase of the bulk-to-surface ratio (increase of volume and decrease of surface). [177] Smaller metal clusters decrease in size and larger clusters increase in size by a net diffusion of atoms of smaller clusters to larger clusters. [177]

to reach the catalyst. [156] Another reason is the encapsulation of the catalyst particle with amorphous carbon, often called catalyst poisoning. [169] It is also possible that the catalyst particles become too large to grow nanotubes [115] due to Ostwald ripening, which was found to be a chirality selective termination process of the nanotube growth. [177] The termination phase is generally ended with the extraction of the nanotubes from the catalyst/substrate. The extracted nanotubes are then processed in a post processing phase for experiments or industrial use, see Section 1.1.3. [78]

After we presented a model for the general growth mechanism in the chemical vapor deposition method, we now want to present some ideas to achieve chirality selective growth of single-walled carbon nanotubes discussed in the literature. All four phases and the post processing step, see Section 1.1.3 and Chapter 3, influence the chirality distribution of the nanotube sample. A good starting point for chirality selection is to reduce the number of possible chiralities that can be accessed with the specific experimental growth conditions. Therefore a first step towards chirality selective growth is the preparation of the catalyst particles, as a strong correlation between the catalyst size and nanotube diameters has been suggested. [52, 111, 114, 139, 187–189] This makes the small diameter carbon nanotubes especially interesting for chirality selective growth, as the number of accessible chiralities is limited for diameters in a small diameter range, see Section 1.1.2. A narrow catalyst particle size distribution therefore leads to a narrow chirality distribution, simplifying the problem to select a certain chirality.

An experimental study reported the enrichment of metallic tubes (91% up from 33%) due to the variation of the noble gas ambient during the thermal annealing of the catalysts. [39] The catalyst morphology changed in dependence of the nobel gas ambient, which was suggested to demonstrate a dependence between the catalyst morphology and the electronic structure of the grown carbon nanotubes. [39] Another study reported enrichment of semiconducting tubes (88% up from 67%), especially of the $(6,5)$ chirality (45%) due to the low temperature growth on a bimetallic FeCu/MgO catalyst. [90] A preferential growth of semiconducting nanotubes was suggested for smaller diameters, [15] as their formation energy was found

---

[15] A low temperature grows smaller diameter tubes, as higher temperature leads to larger catalyst particles. [35]

to be lower than the formation energy of semi-metallic and metallic tubes. [113] The use of bimetallic catalysts, *e.g.* NiFe [3, 127], CoMo [35] or FeRu [36], was observed to lead to a narrowing of the chirality distribution. [3, 36, 127] The reason for the narrowing of the chirality distribution for the NiFe bimetallic catalyst was studied with carbon nanotube caps of various chiralities on a flat surface model, [190] however, the initial cap structure and the lack of curvature renders the results unreliable, see our discussion on the nanotube cap structure in Section 2.1.2 and Section 2.3. The study suggested that the adhesion energy between the catalyst and the cap is higher for certain chiralities. [190] It had been previously suggested that the formation energy for caps on a catalyst particle depend on the fit between the cap and the catalyst surface, which would allow to design catalyst particles that enhance the yield of certain chiralities in the nucleation phase. [179, 186, 191] This follows, as the chirality of the nanotube grown from a specific nanotube cap is unique. [63] Another study, however, pointed out that only the diameter of the cap/nanotube can be controlled by the catalyst particle and excluded the chirality control. [192] The authors of the study argue, that the growth temperature required for the carbon diffusion on the catalyst would lead to a surface or bulk melting of the catalyst particle, preventing a lattice matched chirality selection mechanism. [192] They further argue, that the catalyst particles change their shape during the growth process even at low growth temperatures. [173, 192] The catalyst particle was found to act as a template for the cap, while the cap also shapes the catalyst, meaning an interplay of "template" and "inverse-template" effect, with a stronger effect from the catalyst on the nanotube. [53] Another study stated that the edge/surface energy of the nanotube (graphene sheet) on the catalyst decides the chirality of the tube during the nucleation phase, as armchair and zigzag edge energies are different for different catalysts. [193] The study, however, did not consider pentagons, [16] needed for the inclination of the cap [172] and neglected the change in the rim structure, especially the number of carbon addition sites, with every carbon addition, [43, 44, 63, 195] see Section 2.1. In an earlier study, the difference of the edge energy of armchair and zigzag sites on various metals had already been observed, [196] however, only

---

[16]In a very recent study the adhesion energy of the caps was found to be lower than the adhesion energy of the tube. [194] Combining this with the knowledge that nanotube caps often contain pentagons at the edge, leads to the conclusion, that the pentagons have to be considered to obtain meaningful adhesion energies.

small molecules were used to model the rim of the nanotube, neglecting, *e.g.* the curvature of the tube and catalyst, as well as the interaction of neighboring carbon atoms.

A recent study pointed out that the carbon solubility and wetting properties of catalyst nanoparticles are especially important to optimize the growth of nanotubes for specific chiralities. [197] The growth simulations of the study found that the wall of the nanotube cap grows parallel to the molten/surface-molten catalyst with addition of short carbon chains before the cap detaches and lifts off for elongation. [197] The nanotube stays connected to the catalyst through a diffuse carbon network, which serves as carbon addition site. [197] In-situ transmission electron microscopy footage of the nanotube nucleation indicates that this growth model might be applicable for certain growth conditions, [173] however, other growth conditions might lead to the conclusion that the cap elongates from the particle surface without the intermediate tangential growth step. [174] Another study which included the effect of the substrate found that the detachment of the cap depends on the adhesion energy between the catalyst and the substrate, as the capillary forces of the nanotube growth are counteracted by the substrate. [189] A high adhesion energy between the substrate and the catalyst particle were found to lead to a flattened shape of the catalyst particles with a low wetting angle. [189] The study further suggested that the occupation of hollow sites is a key factor to establish a good fit between the nanotube edge and the catalyst particle, which increases the interaction strength. [189] The interplay between the adhesion energy and the strain energy was found to be important for the lift-off step of the cap, which was suggested to be chirality selective. [198]

The chirality, however, does not necessarily need to remain constant during the nucleation process. [199, 200] In a reactive molecular dynamics/Monte Carlo simulation which applied a force field (ReaxFF) a change of the chirality was observed during the nucleation process of the cap, which resulted from the restructuring of the cap structure due to the interaction with the metal catalyst. [199] Another study, which simulated preformed nanotube caps without a catalyst (in vacuum), found that the change of the chirality is possible with the addition of single carbon atoms to the edge of the nanotube cap, while the caps/tubes are elongated for carbon dimer addition. [200]

If the chirality is "quenched in" in the nucleation phase, [179] the only way to change the yield of the chiralities during the elongation phase is by a chirality dependent growth rate. [43, 168] The theoretical model presented by Ding *et al.* considers kinks as carbon addition sites and finds a linear dependence of the growth rate on the chiral angle. [168] In our own growth model of a chirality dependent growth rate we extended the idea of the model and included the influence of more external parameters, *i.e.* temperature and catalyst, see Chapter 2. [17] [43] We suggested that the "key is to manipulate the energy difference between armchair and zigzag dangling bonds through the choice of metal catalyst and growth conditions". [43] Recently strong experimental evidence for the model of the chirality dependent growth rate was reported. [2] The experimental study used *in-situ* Raman spectroscopic measurements to determine the growth rates in dependence of the chirality and found that the growth rate of the tubes depends on their chirality. [2] A recent growth model for the island growth of graphene of the Yakobson group [201] can be regarded as an extension to their previous growth models presented in the papers of Ding *et al.* and Liu *et al.*. [168, 193] In the extended version of the model various edge structures are considered and their energetical stability is calculated. [201] This allows to simulate the atom addition to a graphene edge and derive the addition probability to a certain site from the energy of the calculated edge configurations. [201] They find that the first carbon addition to a zigzag edge is "strongly endoergic, and [the atom] is likely to fall back onto the substrate", which corresponds to a larger barrier for the growth of zigzag edges than for armchair edges. [201] After the first addition to the zigzag site the growth can occur very fast, as a kink site is created which grows without energy barrier. [201] The model uses the concentration (s_i) times the probability factors ($e^{\frac{E_i}{kT}}$) of the armchair (A), zigzag (Z) and kink sites (K) to determine a chirality dependent growth speed at the edge for tubes with $\nu(\chi) \propto s_K(\chi) \propto \sin(\chi)$, with χ the chiral angle. [201] For the chirality dependent growth rate theories to be valid the incorporation of carbon atoms into the nanotube wall has to be the threshold/rate limiting step for the single-walled carbon nanotube growth, as recently suggested. [74] The threshold barrier for the growth was calcu-

---

[17]A chirality dependent growth rate might not be observed for certain growth conditions, *e.g.* forest growth, as the tubes entangle, leading to the same growth speed [1, 74] or the addition of carbon atoms to the edge of the tubes is limited by the supply of carbon atoms to the tubes, [74] which is expected to be independent of the growth rate.

lated for the addition of two carbon atoms to the edge of the tube with about 2 eV for the common catalysts (Ni, Fe, Co), which is higher than the barriers for carbon diffusion on metal surfaces (*e.g.* 0.4 eV [182], respectively < 1.0 eV [74]) and the carbon decomposition on a metal (*e.g.* 1.4 eV [182], respectively < 1.5 eV [74]). [74] The study further applied transition state theory and determined the decomposition rate of the nanotube to estimate an upper limit of the armchair growth rate (corresponding to the difference of carbon addition to the nanotube and decomposition of nanotube atoms) with, *e.g.*, 1 mm/s for a growth temperature of 1300 K on Fe. [74]

Another study suggested the charge transfer between the nanotube edge and the catalyst particle to be important during the growth in general, as well as for the chirality selection during the growth process. [202] The charge transfer between the edge/rim and the metal catalyst clusters was suggested to increase the reactivity of the rim atoms. [202] The study used density functional theory to determine the charge transfer between nanotube caps (armchair, zigzag and $(6, 5)$) and a Ni cluster. [202] The kink site at the edge of the chiral $(6, 5)$ cap was suggested to be more reactive than other sites following from a higher charge distribution to the kink site. [202] It was proposed that the charge transfer property might be used to design chirality selective catalyst particles. [202] A follow up study on the charge transfer analysed various cap structures on a nickel catalyst particle. [194] The orientation and location of the frontier orbitals was identified with a high reactivity, which was suggested to lead to preferential growth of certain chiralities, *i.e.* $(6, 5)$ and $(7, 5)$. [194] Adhesion energies calculated in the study do not show a clear indication on the chirality selectivity and the authors state that the adhesion energy differences between the studied systems are only minor. [194] Especially, the elongation phase did not show a change in adhesion energy, meaning that the adhesion energy of the carbon nanotubes is independent of the length of the tube in the elongation phase. [194] Another study focused on the electric dipole moment induced in bimetallic clusters due to charge transfer of the different elements in dependence of the cluster composition. [203] The electric dipole moment was suggested to increase the carbon precursor landing probability at certain spots at the particle due to an electric field between the carbon precursor and the catalyst cluster. [203] The study suggested that the growth rate, alignment, and chirality show a close connection to the electric dipole moment and suggest that they can be controlled by the correct

choice of elemental composition and size of the catalyst particles. [203]

One chirality selective process during the nanotube growth might also be the defect annealing or the prevention of defects during the growth. [75, 204] The defect annealing process was suggested to influence the chirality distribution as armchair edges were found to more easily anneal defects than zigzag edges. [204] A chirality change is possible if the defects cannot be annealed which makes zigzag tubes "inferior in maintaining their chirality during" the growth process. [204] In contrast another theory study found efficient healing of defects, allowing the hypothetical growth of meter long nanotubes without chirality change. [75] The catalyst with the highest defect annealing efficiency was found to be iron. [75] High growth rates (commonly used in theoretical studies), however, were suggested to lead to defective structures, as the catalyst cannot anneal the defects until the next carbon atoms are incorporated in the tube wall. [75] Another study explicitly argued that the defect annealing process is not determining the chirality if no catalyst is present at the edge of the tube. [205]

At some point of time the nanotube growth ends. The termination of the nanotube growth was found to depend on the chirality, as nanotubes with stronger binding energy to the catalyst particle have a higher probability to survive the Ostwald ripening process, which terminates the growth. [177]

Besides the studies that tried to understand the chirality selective growth process in the chemical vapor deposition, other studies tried to generate chirality selection by other means. One idea to increase the yield of a certain chirality was to cut the nanotubes of the desired chiralities and add a catalyst to regrow the tubes. [145, 206] This increased the yield of the regrown chiralities, however, it seems that this approach is not followed anymore, as no research studies of newer date are known to the author. [145, 192, 206] Other approaches to the chirality selective synthesis of nanotubes, also aiming at the elongation phase, were tried by organic chemists. The Diels-Alder reaction [18] was suggested as a possible means to elongate a nanotube cap template into a nanotube. [207, 208] The first nanotube cap templates and short nanotubes have been synthesized, however, there is still a lack of template molecules to grow desired chiralities. [209] In another organic chemistry approach it was shown

---

[18]In the Diels-Alder reaction a hexagonal ring is formed by the addition of, *e.g.*, acetylene (C_2H_2) to the bay region of a carbon nanotube cap. [207]

that cycloparaphenylenes, which are strings/rings of benzene molecules, are possible seed and/or precursors to elongate armchair nanotubes. [210] The process was subsequently studied with quantum chemical simulations (density functional tight-binding method) and a strong dependence for a chirality dependent growth rate in a catalyst-free environment was observed. [211]

Even though extensive research effort has been put into the topic of chirality selective growth, as could be seen in this section, it is still not possible to grow a specific chirality. It is not even clear, if chirality selective growth is possible in the sense that certain growth conditions grow only one specific nanotube chirality. It has been shown, however, especially in the last few years, that the chirality distributions can be narrowed and certain control of the chirality is possible. [3, 36, 90, 127, 155, 212–215] Combined with post processing we are nowadays able to produce samples of only a few or even one chirality. [36, 41] However, we still do not understand the details of the chirality selection.

In this section we presented the growth techniques and methods to produce carbon nanotubes. We focused on the carbon vapor deposition (CVD) method and explained the nanotube growth mechanism in detail. Ideas and studies considering the chirality selective growth of carbon nanotubes were presented and assessed. We learned that the chirality selective growth is not fully understood despite many experimental and theoretical studies. We therefore study the chirality selective growth with our own models in Chapter 2.

1.2 Electronic Structure Theory

In this section we present the basics of electronic structure theory and the *ab-initio* program package SIESTA, [216] which we utilised for our calculations. In Section 1.2.1 we give a crude overview of the methodology we need to perform electronic structure calculations, following the introduction to electronic structure theory presented in the book of Richard Martin [92], which is a warmly suggested read for those who are interested in a deeper understanding of electronic structure theory. Section 1.2.2 gives a short introduction to the basics of the density functional theory, while Section 1.2.3 introduces the van der Waals dispersion interaction and the functional, which we use for our calculations of the dispersion between carbon nanotubes in a bundle, see Chapter 3. Section 1.2.4 presents the code/program package SIESTA [216] which we used for all density functional theory calculations presented in this thesis.

1.2.1 Introduction to Electronic Structure Theory

In this section [19] we present the necessary theoretical basics of electronic structure theory to understand the calculations that we performed in this thesis.

The starting point to derive the electronic structure of a system is the time-independent Schrödinger equation: [92]

$$\hat{H}|\phi\rangle = E|\phi\rangle. \tag{1.16}$$

The expectation value of an operator $\hat{O}$ involves the integration over all coordinates and yields the time-independent expression for any observable for an eigenstate. [92] "The total energy is the expectation value of the hamiltonian" $\hat{H}$, [92]

$$E = \frac{\langle\phi|\hat{H}|\phi\rangle}{\langle\phi|\phi\rangle}. \tag{1.17}$$

---

[19]This section is based on the book of Richard Martin, see Reference [92].

The hamiltonian for a system containing electrons and nuclei is given with:

$$\hat{H} = -\frac{\hbar^2}{2m_e} \sum_i \nabla_i^2 - \sum_{i,I} \frac{Z_I e^2}{|\vec{r}_i - \vec{R}_I|} + \frac{1}{2} \sum_{i \neq j} \frac{e^2}{|\vec{r}_i - \vec{r}_j|} - \sum_I \frac{\hbar^2}{2M_I} \nabla_I^2 + \sum_{I \neq J} \frac{Z_I Z_J e^2}{|\vec{R}_I - \vec{R}_J|},$$
(1.18)

with lower case indices for electrons and upper case indices for nuclei, *e.g.* the charge of nucleus I with Z_I. [92] The first term describes the kinetic energy of the electrons $\hat{T}$, the second term describes the Coulomb interaction between the electrons and nuclei, often regarded as an external potential $\hat{V}_{\text{ext}}$ due to the nuclei acting on the electrons, the third term describes the Coulomb interaction between the electrons, denoted as an internal potential $\hat{V}_{\text{int}}$, the fourth term describes the kinetic energy of the nuclei $\hat{T}_N$, and the last term describes the Coulomb interaction between the nuclei E_{II}. [92] This hamiltonian can be simplified using the assumption that electrons move on much faster timescales than protons and neutrons (atom core/nucleus). [92] The adiabatic or Born-Oppenheimer approximation states, that the electrons instantaneously achieve their ground state, if the nucleis change their position through, *e.g.* lattice vibrations or translations. [92, 217] This allows to neglect the kinetic energy term of the nucleis $\hat{T}_n \to 0$, if M_I is assumed to be infinite, and describe the interaction between the electrons and nuclei by an external potential of the nuclei acting on the electrons. [92] We want to study the cohesive energy (adhesion energy, excess energy), geometric structure, and band structure in this thesis. These are all ground state properties of the system, therefore we need to find the ground state wavefunction of the electrons. [92] The ground state wavefunction can be derived by minimization of the total energy, presented in Equation (1.17). [92]

To solve the time-independent Schrödinger equation, which allows to determine the total energy, a common approach is to assume that the electrons are independent-particles, which means that the complicated many-electron problem is replaced "by a one-electron problem in which electron-electron repulsion is treated in an average way". [92, 218] The electrons are uncorrelated except that they must obey the exclusion principle. [92] The Hartree-Fock approximation fulfills the condition by generating a antisymmetrized determinant wavefunction of N electron spin-orbitals (Slater determinant) and finding the single determinant that minimizes the total energy for the hamiltonian of Equation (1.18), where the fourth term is removed due to the Born-Oppenheimer approximation. [92, 219] To solve the Hartree-Fock equation,

in general a basis needs to be introduced. [92] A basis set is a set of functions (basis functions, spin orbitals), *e.g.* a linear combination of Gaussian functions or plane wave functions, which are combined to create molecular orbitals. [218] To describe an arbitrary function the basis set needs to be complete, meaning that an infinite set of functions is needed. [218] In general, however, the basis sets are finite, with a certain number of functions, which allows to reach a certain accuracy in describing the function. [218] As the Hartree-Fock equation is nonlinear, the solution has to be calculated iteratively using the self-consistent-field (SCF) method. [218] The idea of the SCF method is to make an initial guess at the spin orbitals, which allows to calculate the average field seen by the electrons generated by the spin orbitals of the electrons. [218] This average field is then used to determine new spin orbitals, which leads to an iterative procedure, which ends when the average field does not change anymore and the spin orbitals become eigenfunctions of the Fock operator. [218]

The problem with the Hartree-Fock approximation is the lack of correlation effects, which result from the repulsive interaction (Coulomb repulsion) for electrons of different spins. [92, 220] This is a consequence of the construction of the anti-symmetric total wave function (slater determinant) as a product of individual spin-orbitals. [220] The slater determinant vanishes for electrons of the same spin in the same orbital (Fermi hole), which is a consequence of the Pauli principle and can be regarded as a strong repulsion between particles of the same spin. [220] The energy resulting from this effect is commonly called exchange energy and it accounts for a large part of the correlation of parallel spins, however, the correlation of electrons with different spins is not included and has to be accounted for separately. [220] The exchange energy lowers the total energy and "may be interpreted as the interaction of each electron with a positive 'exchange hole' surrounding it". [92] The correlation effects can also be interpreted as a "correlation hole". [92] The correlation energy is "defined as the difference between the exact energy and the energy of an uncorrelated state" in the density functional theory, [92] which we will treat in the next section. The density functional theory approximates the correlation effects within its functionals. [221, 222]

In this section we presented a short overview on the basics of electronic structure theory. We introduced the Schrödinger equation, the hamiltonian for a general system containing electrons and nuclei, the Born-Oppenheimer approximation, the

Hartree-Fock approximation, the idea of basis sets, the self consistent field method, and the exchange and correlation energies and holes. For the interested reader, who wants to learn more about the details of electronic structure theory methods, we direct to the review article of Payne *et al.* [223], the book of Szabo and Ostlund [218], and the book of Richard Martin [92], which cover all methods used in our calculations, *e.g.* pseudopotentials, k-point sampling, supercells, and the conjugate gradient method.

1.2.2 Density Functional Theory

In this section we will give a short introduction to the fundamental ideas behind the density functional theory.

"The density functional theory [(DFT)] is a theory of correlated many-body systems", which has become one of the standard approaches for the calculation of electronic structure in condensed matter. [92] The DFT is based on the theorems of Hohenberg and Kohn, which yield as its most important result that the ground state density of a system fully determines the properties of the system. [92, 221] The hamiltonian of a system of interacting particles (considering the Born-Oppenheimer approximation) can be written

$$\hat{H} = -\frac{\hbar^2}{2m_e} \sum_i \nabla_i^2 - \sum_i V_{\text{ext}}(\vec{r}_i) + \frac{1}{2} \sum_{i \neq j} \frac{e^2}{|\vec{r}_i - \vec{r}_j|}, \tag{1.19}$$

see also Section 1.2.1. [92] The first Hohenberg-Kohn theorem states that the external potential is uniquely determined (except for a constant) by the ground state electron density $n_0(\vec{r})$. [92, 221] The *reductio ad adsurdum* proof of Hohenberg and Kohn shows an inconsistency for the assumption that two potentials $V_{\text{ext}}^{(1)}(\vec{r}) \neq V_{\text{ext}}^{(2)}(\vec{r})$ (differing by more than a constant) with different ground states $\Psi^{(1)} \neq \Psi^{(2)}$ have the same ground state density $n_0(\vec{r})$, which proofs the correctness of the first Hohenberg-Kohn theorem. [92, 221] This means $V_{\text{ext}}(\vec{r})$ "is (to within a constant) a unique functional of" the ground state density $n_0(\vec{r})$. [221] The hamiltonian is fixed by the external potential and therefore the full many-particle ground state is a unique functional of the ground state density, which completely determines the properties of the system. [92] The second theorem states that a *universal* energy functional

$F[n]$ exists, which leads to the lowest total energy for the correct ground state density. [92, 221] The functional can be used to define the energy functional for a given external potential with

$$E_{V_{\text{ext}}}[n] = \int V_{\text{ext}}(\vec{r})\, n(\vec{r})\, d\vec{r} + F[n], \qquad (1.20)$$

which can be shown to assume its minimum for the correct ground state density under the condition that $\int n(\vec{r})\, d\vec{r} = N$, with N the number of electrons in the system; [92, 221] Densities restricted by this conditions are called "V-representable" and define the space within which the functionals of the density can be constructed. [92, 221] An alternative approach due to Levy and Lieb allows the functional to be defined by "any density $n(\vec{r})$ derivable from a wavefunction Ψ_N for N electrons". [92, 224]

The problem is to derive the universal functional, as no method is known to derive an exact version. [92] The work of Kohn and Sham paved the way to derive approximate functionals by replacing the problem of an interacting system with an auxiliary independent-particle system that includes all many-body effects in an exchange-correlation functional. [92, 222] Therefore the energy functional can be rewritten by explicitly separating the classical Coulomb energy from the universal functional: [221]

$$E_{V_{\text{ext}}}[n] = \int V_{\text{ext}}(\vec{r})\, n(\vec{r})\, d\vec{r} + \frac{1}{2} \int \int \frac{n(\vec{r})\, n(\vec{r}')}{|\vec{r} - \vec{r}'|} d\vec{r} d\vec{r}' + G[n], \qquad (1.21)$$

where the new universal functional G[n] is defined by

$$G[n] = T_s[n] + E_{xc}[n], \qquad (1.22)$$

with $T_s[n]$ the kinetic energy of a system of non-interacting electrons with density $n(\vec{r})$ and $E_{xc}[n]$ "the exchange and correlation energy of an interacting system with density $n(\vec{r})$". [222] The exchange-correlation functional $E_{xc}[n]$ is not known and approximate functionals have to be used. [92] A method to explicitly include the exchange is to use the Hartree-Fock exchange energy and divide the exchange-

correlation energy into separate exchange and correlation energy: [222]

$$E_{xc}[n] = E_x[n] + E_c[n]. \tag{1.23}$$

The Kohn-Sham auxiliary system corresponds to a problem of minimization with respect to the density. [92] Therefore we can insert Equation (1.23) in Equation (1.22), Equation (1.22) in Equation (1.21), and use the "stationary property" of the resulting equation (variation of the density) subject to the condition $\int \delta n(\vec{r}) d\vec{r} = 0$ to obtain the Kohn-Sham variational equations. [92, 222] The Kohn-Sham equations have to be solved self-consistently, by starting with a guess for the initial density $n(\vec{r})$, which allows to construct the potentials that allow to find a new density, [222] see also SCF method in Section 1.2.1. The correlation energy can be approximated by a functional, *e.g.* the local density approximation (LDA), [222, 225] the generalized gradient approximation (GGA), [226] or a recent functional that is able to describe the van der Waals interaction, see Section 1.2.3. [227, 228]

In this section we presented the fundamental theorems of the density functional theory.

1.2.3 Van der Waals Density Functional

In this section we present the general idea behind the dispersion/long range interaction of microscopic systems. We start with the discussion of the Lennard-Jones potential and focus on the van der Waals density functional published by Dion, Rydberg, Schröder, Langreth, and Lundqvist [227, 228] in the second part of the section.

The attractive force of the long range interaction between microscopic systems is induced by dynamic polarization, which forms through the motion of electrons of one atom and couples with the atomic motion of electrons on an atom further away, meaning that they "tend to move in phase". [94] Using a simple model of a linear harmonic oscillator for the electron in a uniform electric field leads to a static polarization. [94] Considering a second electron as a parallel rigid dipole in a great distance r with a potential $-A/r^3$ acting as the external electric field leads to a polarization energy $\propto R^{-6}$. [94] Using the artificial assumption that the aforementioned electron oscillators are indeed fluctuating dipoles, Lennard-Jones states that

the two dipoles are not isolated systems. [94] In fact the one dipole is not fluctuating independently from the other (coupled through the electric field), it "will be subject to a dynamic polarization" and the two systems form one coupled system. [94] A more throughout, however, also more complicated treatment has been performed by Eisenschitz and London. [229] The analysis of the two coupled oscillators lead to a van der Waals polarization energy $-\frac{h\nu_0 e^4}{2k^2 R^6}$ and "an attractive force proportional to the inverse seventh power of the distance". [94] This corresponds to a potential proportional to R^{-6}, which is the attractive part of the Lennard-Jones potential.

The repulsive forces are induced by the exchange term, meaning that the van der Waals repulsive term is a quantum mechanical effect. [94] The repulsive force decreases very rapidly with distance, containing terms $\exp(-ar)$. [94] However, for distances most effective in atomic collisions, the dependence of $\lambda_{rep} r^{-n}$ allows to appropriately model the repulsive force, with a value of $n = 13$ found by comparison to experimental data. [94]

A convenient way to describe the van der Waals interaction is to use the Lennard-Jones potential [20]:

$$V_{LJ} = \frac{\lambda_{rep}}{r^{12}} - \frac{\lambda_{att}}{r^6}, \tag{1.24}$$

with the attractive term $\propto r^{-6}$ resulting from the aforementioned dynamic polarization and the repulsive term $\propto r^{-12}$ resulting from the exchange interaction. [94, 230] This potential can be rearranged by substitution of $\lambda_{rep} = 4\varepsilon\sigma^{12}$ and $\lambda_{att} = 4\varepsilon\sigma^6$, see Equation (3.10) page 66 in Reference [85]:

$$V_{LJ} = 4\varepsilon\left[\left(\frac{\sigma}{r}\right)^{12} - \left(\frac{\sigma}{r}\right)^6\right] = \varepsilon\left[\left(\frac{r_m}{r}\right)^{12} - 2\left(\frac{r_m}{r}\right)^6\right], \tag{1.25}$$

with ε the depth of the potential and with a final rearrangement $\sigma = 2^{-\frac{1}{6}}r_m$, where r_m is the distance for the minimal energy, see Figure 3.6 page 67 in Reference [85].

In the second part of this section we want to discuss the van der Waals density functional of Dion *et al.*. [227, 228] The problem of standard density functional

---

[20]The "Lennard-Jones" Potential in Reference [230] is given in form of the force $f(r) = \lambda_n/r^n - \lambda_m/r^m$, with $n = 14\frac{1}{3}, 21, 25$ for the repulsive force and $m = 5$ for the attractive force. [230] The potential can be obtained by integration $V(r) = -\int_r^\infty f(r)\,dr$. [230] In Reference [94] Lennard-Jones presents the "van der Waals polarization energy $= -\frac{h\nu_0 e^4}{2k^2 R^6}$" and the repulsive force with $n = 13$ and an attractive force with $m = 7$ corresponding to the $(12, 6)$-dependence we use for the potential.
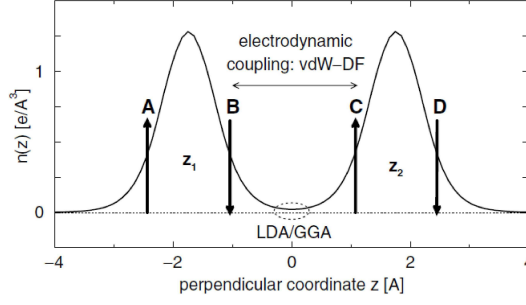
Figure 1.7: Long range dispersion interaction of two systems. Averaged electron density profile of two graphene sheets. [231] The overlap of the electron density does not yield a correct description of the van der Waals dispersion interaction (see dotted ellipse). [231] The figure was adapted from H. Rydberg *et al.* with permission of B. Lundqvist. [231]

theory (LDA and GGA) is that it does not explicitly consider the van der Waals interaction, which made the development of a new functional necessary. [231] Some flavors of the standard density functional theory, however, lead to an energy minimum for van der Waals systems, but this minimum occurs due to the small electron density overlap depicted in Figure 1.7. [231, 232] This overlap does not account for the physical binding between two van der Waals systems. [231] It is merely coincidental that the standard DFT leads to a binding. [231] Standard DFT also underestimates the binding energies. [231] A way to account for the physical van der Waals interaction is to include a nonlocal correlation energy term in the density functional. [231] The functional developed by Dion, Rydberg, Schröder, Langreth, and Lundqvist uses a nonlocal correlation energy, which is in its simplest form given by

$$E_c^{nl} = \frac{1}{2} \int d^3 r d^3 r' n\left(\vec{r}\right) \phi\left(\vec{r}, \ \vec{r}'\right) n\left(\vec{r}'\right), \tag{1.26}$$

with $\phi\left(\vec{r}, \ \vec{r}'\right)$ a general function depending on $\vec{r} - \vec{r}'$ and the densities n in the vicinity of $\vec{r}$ and $\vec{r}'$. [227, 228] The exchange-correlation part of the nonlocal energy functional proposed by Dion *et al.* can be given in the form [227, 233]:

$$E_{xc}\left[n\left(\vec{r}\right)\right] = E_x^{\mathrm{GGA}}\left[n\left(\vec{r}\right)\right] + E_c^{\mathrm{LDA}}\left[n\left(\vec{r}\right)\right] + E_c^{nl}\left[n\left(\vec{r}\right)\right], \tag{1.27}$$

where the exchange energy E_x^{GGA} is described by the generalized gradient approximation (GGA), [234] the local part of the correlation energy E_c^{LDA} is described by

the local density approximation (LDA), [222] and the nonlocal part E_c^{nl} is given with Equation (1.26). [227, 233] The idea for systems with planar symmetry is to determine the nonlocal-correlation energy by comparison of the solutions of the Poisson $[\nabla \cdot (\epsilon \nabla \Phi) = 0]$ and Laplace equation $[\nabla^2 \Phi = 0]$, where a simple plasmon-pole model is used for the dielectric function, with the plasma frequency and Fermi velocity depending on the local density. [231] For general geometries the determination of the nonlocal correlation energy is more involved and details can be found in the References [227, 235].

The exchange-correlation potential corresponding to the van der Waals density functional, which is needed to perform self-consistent calculations, was derived by Thonhauser *et al.*. [236] The potential can be derived by taking the functional derivative of the energy (Equation (1.26)) with respect to the density $v_c^{nl}\left(\vec{\vec{r}}\right) = \frac{\delta E_c^{nl}[n]}{\delta n(\vec{\vec{r}})}$. [236] An efficient implementation of the van der Waals density functional was presented by Roman-Perez *et al.*, which was also implemented in the SIESTA package, see Section 1.2.4. [227, 233] The implementation expresses the nonlocal correlation energy as a double spatial integral, which leads to a dramatic speedup (scaling with $\mathcal{O}(N \log N)$ instead of $\mathcal{O}(N^2)$ for the evaluation of the double integral). [233]

The van der Waals functional was recently shown to give adequate results for a potential energy curve of the adsorption of H_2 on Cu(111). [237] The calculation of nanotube bundles proved the applicability to nanotubes. [238] We calculate the properties of bundles of tubes with various chiralities using the van der Waals density functional in Chapter 3.

In this section we presented the dispersion interaction and ways to describe and treat it. One possibility is to use the Lennard-Jones potential. [94, 230] An alternative approach to account for the dispersion is the van der Waals density functional of Dion, Rydberg, Schröder, Langreth, and Lundqvist. [227, 228]

1.2.4 SIESTA - an ab-initio Software Package

In this section we present the method and the code, which is used to perform the calculations in this thesis.

We performed density functional theory calculations with the *ab-initio* package

SIESTA (Spanish Initiative for Electronic Simulations with Thousands of Atoms). [216, 233, 239] SIESTA is a selfconsistent density functional method that uses a numerical linear combination of atomic orbitals (LCAO) basis set. [216, 240] The atomic orbitals are a product of a numerical radial function and a spherical harmonic within a cutoff radius r_c and zero outside of the cutoff radius, which reduces the computational costs. [216] The number of orbitals per atom included in the basis, which is called multiple ζ, allows to increase the accuracy of the calculation. [216, 240] Polarization orbitals can be added to account for the deformation induced by bond formation. [216] SIESTA treats the core electrons by a pseudopotential, which allows to further reduce the computational costs, as only valence electrons need to be explicitly considered for the electron density. [216] The norm-conserving pseudopotentials used for our calculations are presented in the Appendix (see Section 5.1). They are generated by the scheme of Troullier and Martins and transformed into the fully nonlocal form proposed by Kleinman and Bylander for the calculations in SIESTA. [216, 241, 242] Various exchange-correlation functionals have been implemented in SIESTA including the standard LDA [222, 225] and GGA functionals, [226] but also van der Waals density functionals have been recently added. [216, 227, 233] The Hartree and exchange-correlation potentials and their matrix elements are calculated by projection of the basis functions and the electron density on a real-space grid. [216] The fineness of the grid is determined by a grid cutoff E_{cut} parameter that corresponds (not directly) to the energy cutoff in plane wave based methods. [216] The radial parts of all atomic orbitals at a certain grid point are interpolated from numerical tables and used (together with the spherical harmonics part) to calculate the valence density at the grid point. [216] The nonlocal core correction, which is a spherical charge density that simulates the atomic cores, is added to the valence density; [216] With this density the exchange potential can be determined. [216]

This section ends the introduction chapter with a short overview of the SIESTA method.

Die Schwingung

Hermann Ludwig Ferdinand ahnte nicht, was auf ihn zukam. Er wurde unvorbereitet getroffen, gepackt und fortgerissen. Erst hatte er sich noch an Ernest festgehalten, dann aber war die Kraft, die auf ihn wirkte doch stärker gewesen und er begann sich von Ernest zu entfernen. Er spürte wie die Kraft langsam nachließ, umschwang und ihn nun in die entgegengesetzte Richtung zu zerren begann. Er flog an Ernest vorbei, der nur unmerklich von dem Treiben beeinflusst wurde. Ernest war schließlich 1836 mal so schwer wie Hermann Ludwig Ferdinand. Durch sein hohes Gewicht konnte er ruhig auf seinem Platz hocken und beobachten, wie Hermann verzweifelt versuchte, sich an ihm festzuhalten. Ernest schaute belustigt zu, wie Hermann nichts gegen die Kraft ausrichten konnte und im Rhythmus der äußeren Kraft schwang. Hermann blieb nichts anderes übrig als sich hin- und herstoßen zu lassen. Er wartete und hoffte, dass sich die Situation beruhigen würde und das Ganze so plötzlich aufhören würde, wie es begonnen hatte. Doch die Kraft schien stärker zu werden und er wurde immer heftiger herumgewirbelt . . .

2 Chirality Selective Growth

In this chapter we present our studies on the chirality selective growth of carbon nanotubes. [1] The first section (Section 2.1) introduces the structure of the edge of carbon nanotubes, as well as the structure of nanotube caps. [2] In the literature two types of edges for the nanotube cap structures are commonly used for calculations to determine the adhesion energy between nanotube caps and catalyst particles. One is the edge derived from the circumferential vector, used, *e.g.*, in the studies of References [1, 45, 162, 179, 194, 200, 202], the other is an angled cut edge used in the studies of the References [160, 190, 195, 243]. We study and compare three edge structures, including the circumferential and angled cut edge, to determine the effect of the choice of the studied edge on the research results and conclusions of the research studies. Section 2.2 presents the model of the chirality dependent growth rate, which describes the chirality selective elongation process of the nanotube growth. [3] In Section 2.3 we calculate the parameters for the chirality dependent growth rate model on Ni, Fe and NiFe alloy particles. The parameters are then used to determine chirality selective growth rates on the particles to determine a possible chirality selection induced by the alloy particles observed experimentally. [3, 127] We study the effect of the charge transfer between nanotube

---

[1]Parts of the results, texts and figures of this chapter have been prepublished by the author of the thesis in References [43, 44]. The results are partly based on the research work performed by the author during his time as a diploma student and were partly included in the authors diploma thesis in Reference [1]. Acknowledgement to the references which were integrated are given for the specific sections of this chapter. The author felt it to be necessary to introduce the reader to the topic of the edge/rim structure of carbon nanotubes to be able to understand the extensions derived in this thesis, as well as the application of the growth rate model.

[2]Section 2.1.1 is based on Reference [44], which is based on the research work of the unpublished diploma thesis [1] of the author. Section 2.1.2 is an extension of the ideas of Reference [1] applied to nanotube caps. Reference [1] presented calculations on two different rim structures, however, the calculations were performed with a wrong pseudopotential (LDA instead of GGA).

[3]Section 2.2 is based on Reference [43], the general formalism was developed in the diploma thesis [1] of the author and extended in this thesis.

caps and NiFe clusters, which was recently reported to increase the reactivity of the rim atoms of nanotube caps [194, 202] and which also induces an electric dipole moment on the cap and cluster system.

2.1 Structure of Nanotubes During the Growth Process

In this section [4] we study the structures of carbon nanotubes, especially the structure of the edges/rims during the growth process. Before we go into the details, we want to remind on the basics of the growth process, see Section 1.1.4.

The structure of the carbon aggregates changes in various steps of the growth process. [159, 163, 170, 172, 182, 184, 244] The first structure/form of the carbon atoms is the precursor gas. [1, 170] The precursor gas is decomposed at the surface of a catalyst particle and the carbon atoms become individualised to diffuse into the particle to saturate it [1, 112, 163] or on the particle to form carbon chains. [1, 163, 182, 184] If the catalyst particle has the correct conditions, *e.g.* size, [134] shape, [134] and interaction strength with substrate and carbon, [1, 134, 161, 162] a graphene-like layer with pentagons in it transforms into a carbon nanotube cap structure. [172–175, 184] The formation of the nanotube cap ends the nucleation/formation stage. Here the form of the nanotube cap rim/edge, see Section 2.1.2, is especially interesting, as the form of the cap as well as pentagons as part of the rim might be defined by the structure of the catalyst particle. [53] Carbon addition to the rim elongates the nanotube, which is called the elongation stage. [200] During the elongation stage the structure of the rim is changing with every carbon addition, [1, 43, 44] see Section 2.1.1. In the last phase of the growth process, the termination phase, the growth ends and the nanotube either closes its growing end, encapsulates the particle with amorphous carbon or simply stops its growth, as the growth conditions do not allow further growth, *e.g.* no more heat/carbon supply. [169] We will only consider preformed caps and the elongation phase in this thesis and point to the References presented in Section 1.1.4 for informations about the other phases.

In the next section we will focus on the structure of the carbon nanotube edges and present a formalism depending only on the chiral indexes n and m to classify all rim structures of the nanotubes, see Section 2.1.1. The section also includes a calculation for the stability of the hexagonal rim structure in comparison to a structure with a

---

[4]The results presented in the first part of Section 2.1.1 are based on results of the unpublished diploma thesis of the author (Reference [1]), as well as on the results published by the author in References [43, 44]. The theoretical studies were performed by the author of this thesis under the supervision of the co author of the papers and the thesis advisor Stephanie Reich.
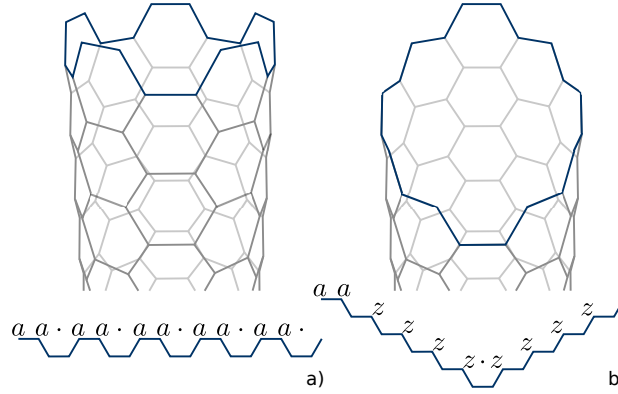
Figure 2.1: 3d wire model of a $(5,5)$ nanotube and unzipped 2d representation of its rim. The rim contains addition sites "." armchair "a", and zigzag dangling bonds "z". a) Rim expected from the circumferential vector construction. b) Angled rim. The figure was adapted from References [1, 44] of the author of this thesis.

Klein-edge, which can be obtained by carbon dimer rotation. Section 2.1.2 considers the rim structure of nanotube caps with a focus on different rim structures for the same cap. Various properties are studied to determine, if one of the cap structures is preferred. The section further includes a study on the bond length of carbon nanotube caps for armchair and zigzag edges, which is correlated with the bond strength between the carbon atoms.

2.1.1 Structures of the Edge

In this section [5] we present the possible configurations of the open ends (edges/rims) of carbon nanotubes and formulas to derive the number of armchair and zigzag-type dangling bonds contained in a specific rim of given chirality (n, m). In the second part of this section we calculate carbon rim structures to determine the stability of hexagonal rims.

In the following we discuss the essential properties of rims made up by hexagons.

---

[5]The first part of this section is based on the prepublished References [43, 44] of the author of this thesis. References [43, 44] are partly based on the diploma thesis of the author, see Reference [1]. Therefore the first part of this section is to be regarded as an introduction section, that is not part of the research work performed for this thesis. The analyses were performed by the author of this thesis under the supervision of the co author of the papers and the thesis advisor Stephanie Reich. The stability calculation of the rim in the second part of the section is original research work of the author and marked by a footnote.
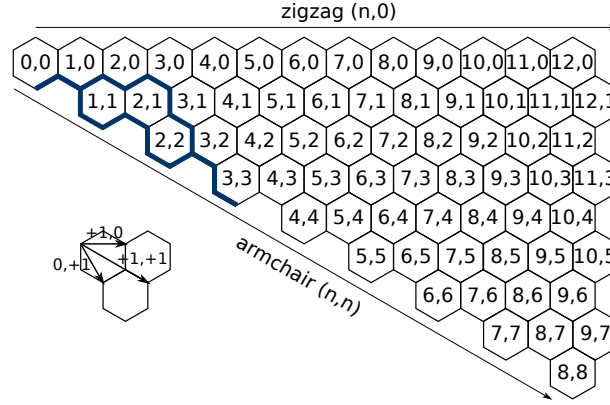
Figure 2.2: Rim creation sheet with the possible rim paths for a $(3,3)$ nanotube. Connecting the lower corner of the $(0,0)$ hexagon with the lower corner of the $(3,3)$ hexagon by any of the paths inside of the bold (blue) line border yields a $(3,3)$ rim. The figure was adapted from References [1, 44] of the author of this thesis.

All carbon nanotube rims consist of armchair a and zigzag-type dangling bonds z. Armchair dangling bonds a consist of one of two neighboring twofold C-C bonded atoms, see Figure 2.1 a). Zigzag dangling bonds z have two saturated C neighbors and are themselves twofold C-C bonded, see Figure 2.1 b). An addition site denoted by "." elongates the rim by a hexagon with C_2 addition. [245] The rim that follows most closely the circumferential vector (see Section 1.1.2) of a tube has

$$N_a = 2m, \qquad (2.1)$$

armchair and

$$N_z = n - m, \qquad (2.2)$$

zigzag dangling bonds, see Figure 2.1 a). For the $(5,5)$ tube we get $N_a = 10$ and $N_z = 0$ and the particular rim configuration $aa.aa.aa.aa.aa.$, if we follow the rim from left to right. The rim of Figure 2.1 b) is an angled rim with one side longer than the other side, it has $N_a = 2$ and $N_z = n + m - 2$, with $m \neq 0$.

Beneath the circumferential vector rim and the angled rim, there are many other possible rims. The nanotube rims can be derived from the rim creation sheet, see Figure 2.2 or for more details see the diploma thesis of the author (Reference [1]). The rims of the $(3,3)$ nanotube are shown bordered by bold (blue) lines. Following
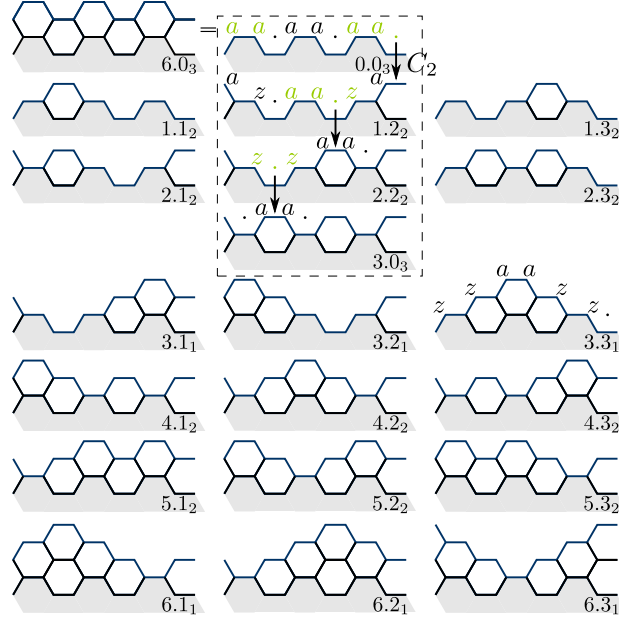
Figure 2.3: Rim configurations of the $(3,3)$-armchair nanotube from C_2 addition. The numbers at the bottom right of the rims are defined by $A.B_C$ with A the number of added C_2, B a counting variable for different rims (0 is special, as these are half or full layers) and C the number of addition sites. The gray shaded side represents the body of the tube. The figure was adapted from References [1, 44] of the author of this thesis.

the direct connection between the lower corner of the $(0,0)$ hexagon to the $(3,3)$ hexagon corresponds to the circumferential vector construction, see Figure 2.3 (0.0_3). An angled rim can be obtained by following the other bold (blue) line path between $(0,0)$ and $(3,3)$, see Figure 2.2. All the paths inside of the borders created by the bold (blue) lines in Figure 2.2 lead to different rim configurations, which have to fulfill the condition $N_a + N_z = n + m$. There are simple rules to derive a rim from the rim creation sheet: (i) The route must not go in circles, (ii) borders are not allowed to be crossed and (iii) paths only include ↑ up, ↙ down-left and ↖ up-left steps.

The $(3,3)$ nanotube has 20 different rims, see Figure 2.3. Only four of the rim configurations $(0.0_3, 1.1_2, 2.1_2,$ and $3.1_1)$ are unique, with the other rims having the same structure, e.g. $1.1_2 = 1.2_2 = 1.3_2 = 4.1_2 = 4.2_2 = 4.3_2$, which is true considering the application of simple symmetry operations like rotations and im-

proper rotations. The numbers at the bottom right of the rims are defined by $A.B_C$ where A denotes the number of added C_2 compared to the rim derived from the circumferential vector (0.0_3), B is a counting variable for different rims (0 is special, as these are half or full layers), and C is the number of addition sites. The amount of carbon atoms that needs to be added to complete a full layer depends on the chirality and is equal to the number of rim atoms $2 \cdot (n + m)$. For a $(3, 3)$ tube the addition of $n + m = 6$ C_2 to a rim structure can lead to an equivalent rim structure, e.g. $0.0_3 = 6.0_3$ or $1.3_2 = 7.3_2$.

The addition of C_2 to different addition/growth sites at the rim yields different transitions for the rim configuration. Three kinds of growth sites can be identified $aa.aa$, $aa.z$ and $z.z$, with $z.aa$ growth sites being identical to $aa.z$ by symmetry, see Figure 2.3 and Table 2.1. Additions to other rim sites, aa, az, za and zz do not add hexagons and are energetically less favorable. Addition of C_2 to an $aa.aa$ growth site induces a transition $aa.aa \rightarrow zaaz$ removing a growth site, see Figure 2.3 $(0.0_3 \rightarrow 1.2_2)$. For $aa.z$ we have a $aa.z \rightarrow zaa.$ transition with C_2 addition, which shifts the dangling bonds and the growth sites, see Figure 2.3 $(1.2_2 \rightarrow 2.2_2)$. The C_2 addition to $z.z$ induces a transition $z.z \rightarrow .aa.$ adding a growth site to the rim, see Figure 2.3 $(2.2_2 \rightarrow 3.0_3)$. It is also possible to create a different growth site type with C_2 addition to a growth site, as dangling bonds and growth sites are moved and transformed, see Figure 2.3 $(1.2_2 \rightarrow 2.2_2)$, where addition to $aa.z$ turns a $z.aa$ growth site to a $z.z$ growth site.

The number of growth sites of a rim depends on its chiral indexes (n, m) and the exact rim configuration. The number of growth sites in the rim configuration

Table 2.1: Overview of site types in a nanotube rim. "$\Delta.$" represents the change in addition site number and "transition" the change of the bond structure with C_2 addition.

site	$\Delta.$	transition	example
$aa.aa$	-1	$aa.aa \rightarrow zaaz$	Fig. 2.3 $(0.0_3 \rightarrow 1.2_2)$
$aa.z/z.aa$	0	$aa.z \rightarrow zaa./aa.z \rightarrow .aaz$	Fig. 2.3 $(1.2_2 \rightarrow 2.2_2)$
$z.z$	$+1$	$z.z \rightarrow .aa.$	Fig. 2.3 $(2.2_2 \rightarrow 3.0_3)$
aa	-	-	Fig. 2.3 (3.3_1)
az/za	-	-	Fig. 2.3 (3.3_1)
zz	-	-	Fig. 2.3 (3.3_1)

derived from the circumferential vector, *e.g.* 6.0_3 configuration in Figure 2.3, is

$$N_{aa.aa} = \max\left(2m - n, 0\right) = \begin{cases} 2m - n & \text{if } 2m - n > 0, \\ 0 & \text{otherwise,} \end{cases} \tag{2.3}$$

$$N_{aa.z} = \min\left(m, n - m\right), \tag{2.4}$$

and $N_{z.z} = 0$. All chiral tubes have at least one *aa.z* site in the rim configuration derived from the circumferential vector at which growth can occur without inducing so called armchair kinks. [1, 168] Details for the rims of chiral tubes can be found in the References [1, 44] of the author of this thesis, which show that the same considerations presented in this section are applicable for chiral and achiral rims, as both consist of armchair and zigzag bonds.

A pair of armchair kinks, corresponding to a C_2 addition between two armchair sites of the rim, [168] transforms two armchair bonds $2a$ into two zigzag bonds $2z$, see Figure 2.3 ($0.0_3 \rightarrow 1.2_2$), which corresponds to a *aa.aa* growth site with the transition *aa.aa* $\rightarrow$ *zaaz*; With the number of armchair kinks $k = 2 \cdot x$, ($x = 0, 1, \ldots, m - 2, m - 1$; $k_{max} = 2 \cdot (m - 1)$), we can derive all m possible rim configurations [6] in dependence of N_a the number of armchair bonds

$$N_a = 2 \cdot m - k, \tag{2.5}$$

and N_z the number of zigzag bonds

$$N_z = n - m + k. \tag{2.6}$$

The energetically most favorable rim structure depends on its environment. Rims in contact with other atomic species, *e.g.* a metallic catalyst, interact with the surface of the catalyst and the rims are deformed according to the surface structure. [179] Therefore the rim expected from the circumferential vector is not in every case the most likely rim, as a preformed contact can force the nanotube rim into a certain rim configuration. This is the starting point for the next section,

---

[6]The configurations of the rims derived by this formula are called standard rims, meaning rims, that do not change their total number of bond sites. For details see Reference [1] of the author of this thesis.

Section 2.1.2 where different rims of carbon nanotube caps are studied on an iron cluster to understand the interaction between the rim structure and the catalyst structure. The rim can also be deformed if its environment is taken into account. In vacuum the dangling bonds tend to bend out of the nanotube axis and the rim atoms decrease their nearest neighbor distances. [246, 247]

Before we study different rims on a catalyst particle, we first present calculations [7] of a Klein-edge configuration at a pentagon compared to the hexagon configuration on a graphene sheet model to determine the stability of the hexagonal rims presented in this section. The graphene sheet models the rim of a carbon nanotube neglecting the curvature, which can only give an approximation to the rim of a nanotube. The pentagon Klein-edge configuration corresponds to the hexagon configuration with rotation of the carbon dimer consisting of the edge atoms of the hexagon configuration.

We calculated the energy difference between the two structures and estimated the transition energy from the minimal energy path (MEP) between both configurations with density functional theory calculations utilising the *ab-initio* package SIESTA. [216, 239] The calculations used norm conserving nonlocal pseudopotentials generated by the Troullier-Martins scheme with the PBEsol functional. [241, 248] The carbon pseudopotential was generated in the ground state configuration of carbon $1s^2\ 2s^2\ 2p^2$ with cutoff radii $r_{s,p} = 1.29$ Bohr and $r_{d,f} = 1.50$ Bohr. The iron pseudopotential was generated in an excited configuration [Ar] $3d^7\ 4s^1$ with cutoff radii $r_{s,p,d,f} = 2.00$ Bohr and a pseudocore radius of 0.70 Bohr, more details on pseudopotentials can be found in the Appendix (Section 5.1). The calculation used the generalized gradient approximation within the PBEsol parametrization and a double-ζ basis set with polarization orbitals (DZP). [248] We chose cutoff radii for the s and p orbital of the carbon atoms with $r_s = 5.949$ Bohr and $r_p = 7.450$ Bohr and for the s and d orbital of the iron atoms we chose $r_s = 8.400$ Bohr and $r_d = 8.200$ Bohr. The mesh-cutoff for the real-space integration corresponded to about 750 Ry. We used a k-point sampling of 9x9x1 to calculate the total energies.

The carbon dimer rotation energy barrier is estimated by comparison of the total energies of the pentagon Klein-edge configuration, the hexagon configuration and in-

---

[7]The following part of the section has not been published before and represents original research work of the author of this thesis.
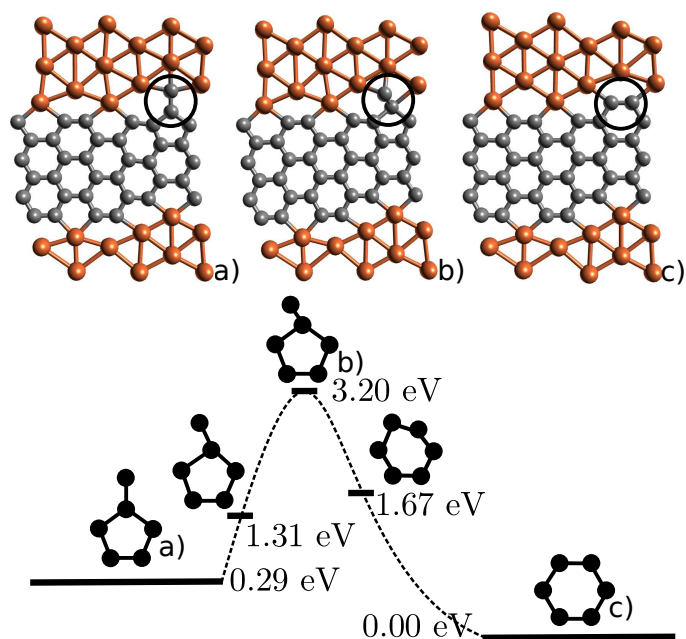
Figure 2.4: Top view on a ball and stick sketch model of a carbon (gray) dimer rotation in a graphene/nanotube edge near an iron (orange) catalyst in the top of the figure. The bottom shows the energy levels of the configurations normalized to the energy of the hexagon configuration. a) Pentagon configuration. b) Intermediate (transition) state. c) Hexagon configuration.

termediate configurations at the edge of a kinked graphene sheet on an iron catalyst, see Figure 2.4. The intermediate configurations allow to construct a potential energy surface, from which we can derive the rotation barrier height. The geometries of the configurations were optimized to a maximal atomic force of 0.01 eV/Å with fixed z-coordinates for all atoms and fixed dimer position for intermediate configuration calculations. [8]

The pentagon Klein-edge configuration is 0.29 eV higher in energy than the hexagon configuration. We find the energy barrier for the rotation of the carbon dimer at the edge of the carbon rim with 2.91 eV for the pentagon Klein-edge configuration and a barrier with 3.20 eV for the hexagon configuration, see the transition state in Figure 2.4 b). We can translate the two dimensional situation to the nanotube rim. If we consider a 90° rotated C-C bond in the wall of a nanotube instead of the edge of a flat graphene rim, we receive a defect composed of two pentagons and two heptagons, commonly denoted as Stone-Wales defect [9]. [251] The Stone-Wales defect was found to have a high energy barrier of about 9-11 eV in carbon nanotubes or graphene and about 6-7 eV in C_{60} fullerenes. [252] The activation energy, however, is decreased significantly near metal catalyst atoms, *e.g.* down to 3.25 eV in a $(6,6)$ nanotube cap with cobalt catalyst [253] or 3.15 eV in a fullerene with wolfram as catalyst, [254] which is comparable to our rotation barrier from the pentagon Klein-edge configuration to the hexagon configuration of 2.91 eV, see Figure 2.4 a) to b). A recent study on the annealing of defects in graphene showed that the defect annealing increases with higher temperature, which the authors suggested to be important for the chirality selective growth of carbon nanotubes, [255] see Section 1.1.4. The energy level difference between the hexagon configuration and the pentagon combined with a Klein-edge configuration is 0.29 eV, which is of the same order as the average nanotube cap formation energy (0.29 eV/atom). [63] Combining these observations and using the observation that the addition of single carbon atoms to pentagons lead to a chirality change of the cap, [200] points to a chirality selective mechanism in the nucleation stage of carbon nanotubes depending

---

[8]This method only allows a rough estimate for the rotation barrier. Improved results can be obtained by, *e.g.*, the (climbing image-) nudged elastic band (CI-NEB) approach, [249, 250] see *e.g.* Reference [75].

[9]Stone and Wales [251] actually studied rotations of carbon dimer bonds in a two pentagon and two hexagon environment in C_{60} molecules.

on temperature through the carbon addition to/annealing of pentagons.

2.1.2 Nanotube Cap Structures

In this section [10] we cover two important aspects of nanotube cap structures. First
we study the influence of the rim structure on the binding energies and charge
distribution, between an armchair carbon nanotube cap and an iron particle. A
second part considers the bond lengths at the edges of nanotube caps, which correlate
with the binding strength of the bonds.

  In the literature two kinds of rim structures (for non-zigzag caps) are commonly
used to calculate the interaction between nanotube caps and catalyst surfaces or
particles. One approach is to use maximally elongated rims which we call angled
rims, see References [1, 53, 190, 195, 243, 256] and Figure 2.5 c). The other approach
is to use the shortest possible cap structures, see References [1, 179, 194, 200, 202,
215, 256] and Figure 2.5 a), which correspond to the rim which is derived from the
circumferential vector and generally used in publications that study the interaction
between nanotubes and catalyst structures. [162, 194, 202] The motivation of this
section is to determine, if there is a preference of a certain rim structure of the
cap by comparison of three possible rim structures of a $(5,5)$ armchair cap, see
Figure 2.6. We consider the energetic stability, the electronic charge distribution at
the edges, the electric dipole moment, the HOMO-LUMO gap [11], the growth rates
and geometric arguments. To better understand the nanotube cap edges, which
only contain armchair and zigzag sites, we explicitly compare the bond length of
armchair and zigzag edges for the straight rims of the $(5,5)$ armchair cap and the
$(9,0)$ zigzag cap.

  We begin with a short analysis of the results of studies using elongated cap struc-
tures, which were presented in Reference [190] and Reference [195]. The study of
Dutta *et al.* models carbon nanotube caps on flat NiFe alloy surfaces. [190] As can
be seen from Figure 5 of Dutta *et al.* [190] they use caps with angled rims, *e.g.*, a
$(8,4)$ nanotube cap with 10 zigzag sites (z) and 2 armchair sites (a) at the edge
of the cap. The cap diameter of angled rims is increased, as angled rims have an

---

[10]A preliminary comparison between an angled rim and a straight cut rim has been conducted in
  the diploma thesis of the author, see Reference [1].

[11]HOMO means highest occupied molecular orbital and LUMO means lowest unoccupied molecular
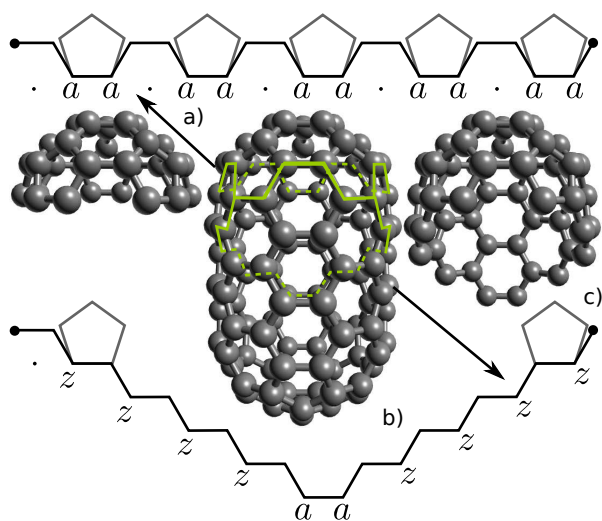 orbital. [194, 257]

Figure 2.5: C_{100}-fullerene and $(5,5)$ armchair caps in ball and stick model and reduced rim representations [1, 44] of the rims of the caps. The gray pentagons represent the positions of the pentagons in the rim. a) Straight rim/shortest cap with .aa.aa.aa.aa.aa rim configuration and 30 atoms. b) Short carbon nanotube/fullerene with two possible rims cut from it (green). c) Angled rim/longest cap with .zzzzaazzzz rim configuration and 50 atoms.
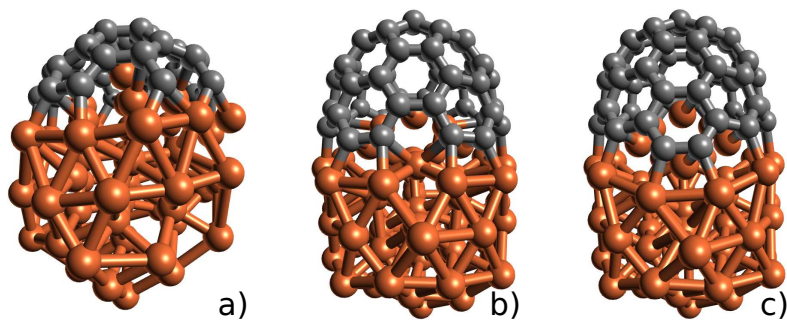

Figure 2.6: Ball and sticks sketch model of the three carbon nanotube caps on a Fe_{55} catalyst cluster on the *top* spot. Carbon atoms in gray and iron atoms in orange. a) The $(5,5)$ cap shows two Klein-edges through bond break of a pentagon at the rim. b) The intermediate $(5,5)$ cap. c) The angled $(5,5)$ cap.

elliptic area compared to the circle produced by straight rims. The $(8, 4)$ cap has an elliptical shape with two axes of $d_1 = 11.4$ Å and $d_2 = 7.6$ Å, leading to an area of about 68 Å^2. [190] For a straight rim, however, the $(8, 4)$ nanotube has an average diameter of 8.55 Å, see Table 3.1 in Section 3.2.1, leading to an area of about 57 Å^2 with the rim configuration $N_a = 2 \cdot m = 8$ armchair sites and $N_z = n - m = 4$ zigzag sites. As the calculation was performed on a flat surface, we do not expect a template effect of the catalyst structure. [53] The structure of the catalyst may be more stable for certain rim structures, which have a good fit to its surface. The diameter and rim structure of the cap do not seem adequate for a study on a flat surface, as the tube/cap "diameter" is increased compare to the nanotube diameter. The diameter of the tube is the only factor, which could be verified to show some correlation with the diameter of the catalyst particle. [52, 111, 114, 139, 187–189] Therefore the chirality selection should be studied with a cap that has a consistent diameter to the particle. An elongated rim seems only to be adequate for studies with steps or a three dimensional particle form.

Angled rim structure caps were also used in the study of Gómez-Gualdrón *et al.*, where they are erroneously used to find that the number of favorable growth sites increases for the $(6, 5)$ cap with increasing cap length. [12] [195] Carbon dimers are added to the cap until it finishes with a straight rim configuration. This rim configuration (without kinks) has the highest number of growth sites, see Section 2.1.1. The straight rim configuration is found to be the most stable configuration by following the energetically most favorable carbon addition path. [195] The study was performed in vacuum, therefore the excess energy for zigzag sites E_z is significantly larger than the excess energy for armchair sites E_a. [80, 258] The oscillatory pattern of the adhesion energy with adhesion of C_2 radicals observed by Gómez-Gualdrón *et al.* for the $(6, 6)$ cap [195] can be explained by the change of the rim structure (armchair into zigzag bonds and vice versa). The initial elongated cap starts with only one $z.z$ addition site, compare, *e.g.*, Figure 2.5 c) for a similar rim structure of a $(5, 5)$ rim, which through addition of C_2 transforms to one *.aa.* site. The energy is low, as the transformation of zigzag to armchair bonds is energetically favorable in the vacuum. Two possible *aa.z* addition sites can be found for addition step 2,

---

[12] The results of the Gómez-Gualdrón study have already been analysed in some detail in the diploma thesis of the author, see Reference [1], however, as the diploma thesis was not published the author considered it important to include the more throughout analysis here again.

the first addition to any of them does not change the number of zigzag or armchair bonds, however, it generates a $z.z$ site. Addition step 3 closes the intermediate layer through addition to the newly formed $z.z$ addition site and generates another $.aa.$ site accompanied with a low adhesion energy. Three addition sites are filled from step 4 to 6 leading to four addition sites for steps 7 to 10, at which the fifth addition site is generated. Five further carbon dimer additions would lead to a straight rim configuration with six addition sites, however, the study stopped after 10 steps. [195] The conclusion of the study seems wrong, as the initial cap in the vacuum is unlikely to be angled, as the number of zigzag sites is maximized for these caps. In the vacuum zigzag sites are energetically expensive, which suggests, that the cap should have a straight rim form with a minimum of zigzag sites and a maximum of armchair sites. If the structure was studied on a catalyst on the other hand, the number of growth sites would not be increased either with the length of the tube, as the initial rim structure was favorable from the beginning on the cluster. Therefore the rim structure would not change significantly during the growth and the number of growth sites would remain low on the angled rim. Only a catalyst-cap deformation would allow to change the rim structure.

In the following we study a straight, an angled and an intermediate rim structure of a $(5,5)$ carbon nanotube cap on an icosahedral iron nanoparticle containing 55 atoms, see Figure 2.6. The computational details of the density functional theory calculations performed for this section are described in Section 2.3.1. The nanotube cap structures were derived from geometry optimized fullerene structures, see Section 2.3.1. The fullerenes were divided into single caps by cutting either straight in Figure 2.5 a) to obtain the circumferential vector rim structure or cutting with an angle to obtain the angled rim in Figure 2.5 c). The intermediate structure was obtained by removal of the lowest carbon dimer of the angled rim cap, see Figure 2.6 b) and Figure 2.7 b). The single caps were transferred on three different spots of a catalyst particle, $e.g.$, on the top spot, see Figure 2.6 and Section 2.3.1 for more details about the catalyst particle. The adhesion energies, excess energies and Bader charge distributions were derived as described in Section 2.3.1. The bond lengths were derived from the atom positions contained in the ".xyz" files with the help of the program $Avogadro$, which was also used to produce the ball and stick models in the figures of this thesis. [57]

Table 2.2: Comparison of adhesion energies, carbon-metal bond energies, excess electron charges at the rim, electric dipole moments, and HOMO-LUMO gaps of $(5, 5)$ nanotube caps with straight, intermediate and angled rim on an iron cluster. The asterisk denotes the system with at least one Klein-edge at the rim.

cap	spot	E_{ad} (eV)	E_{CM} (eV)	rim charge (e)	Δ (D)	HL-gap (eV)
straight	1	-21.2	4.3	4.1	13.7	0.23
straight	2	-	-	4.1	13.1	0.18
straight	3*	-21.2	4.3	4.3	10.3	0.18
intermediate	1	-20.7	3.6	3.6	15.8	0.16
intermediate	2	-19.4	5.0	3.8	15.0	0.12
intermediate	3	-21.4	3.0	3.7	14.4	0.22
angled	1	-21.5	3.8	3.5	15.1	0.13
angled	2	-20.8	4.6	3.7	14.6	0.10
angled	3	-22.9	2.5	3.5	14.4	0.12

The adhesion energies and excess (carbon-metal bond) energies show no significant trend, see Table 2.2. Even though the adhesion energy increases from straight to angled rim, the increase of adhesion energy with only a few eV is negligible for the cap properties. One of the reasons for the increase is the increase of the number of zigzag bonds, which is 0 for the straight rim and 8 for the angled rim. In the vacuum (dissociated cap) the zigzag sites need more energy, as they have dangling bonds compared to armchair sites which tend to form triple bonds. [258] The energy difference between the armchair and zigzag bonds at the edge of the cap, however, was found to be small, see Section 2.3.1. The number of pentagons at the edge may influence the adhesion energy of the edge, which is only two for the intermediate and angled rim, while there are five pentagons at the edge of the straight rim. The adhesion energy describes the energy needed for the cap to lift off of the particle into the vacuum. The barriers of about -20 eV are large enough to prevent the caps to lift off into the vacuum, which would end the growth, as the caps would likely form fullerenes. [159, 162] Therefore a small adhesion energy change of a few eV is negligible for the stability of the caps on the clusters. The excess energies vary with spot and rim structure between 2.5 eV and 5.0 eV. No rim structure can be identified to be preferable for all spots from the excess energies. For example the
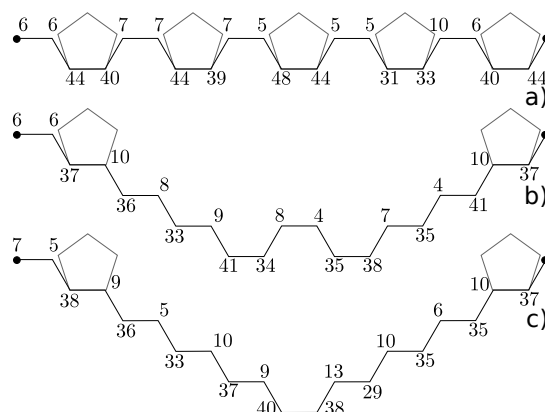
Figure 2.7: Representation of the straight, intermediate and angled $(5,5)$ carbon nanotube rims with excess electron charges next to the edge atoms in 10^{-2} e. The excess electron charges are averaged over three different cap-catalyst systems, with the cap being connected to different spots on the catalyst particle. The *top* spot 3 of the straight rim was excluded, as it contains a broken pentagon bond resulting in two Klein-edges, see Figure 2.6. a) Straight rim. b) Intermediate rim. c) Angled rim.

angled rim has a good fit with spot 3 (*top*) following from the low excess energy. The low excess energy alone, however, does not allow a conclusion about the formation probability of a certain cap structure on a catalyst, as the catalyst particle shape for real systems is expected to be significantly deformed by the substrate and the cap structure, as the metal atoms are expected to be molten or surface molten. [192] Therefore the binding energy or surface fit between a catalyst and the cap is not a good parameter to determine the stability or formation probability of a cap on a specific catalyst cluster. [192, 194]

The electron charge on the edge atoms establishes a trend, see Table 2.2. If the carbon nanotube cap is attached to a catalyst particle some charge is transfered from the metal catalyst atoms to the carbon atoms in the nanotube cap. [202, 256] The charge transfer is a common phenomenon as the tendency to attract electrons depends on the element. [51, 259] The tendency to attract electrons is called electronegativity, which is 1.6 or 1.8 for iron and 2.5 for carbon. [51, 259] The charge transfer induces a dipole moment on the system, which depends on the amount of transfered electrons and the geometry of the system. [51, 259] The frontier orbital theory states that "reaction sites with higher frontier electron density are more

reactive". [202, 257] In the study of Wang *et al.* for the $(5,5)$ cap on a Ni cluster of 55 atoms it was found that the "negative charged outermost edge carbon atoms have significantly higher electron density near the Fermi level than inner atoms", [202] which means that they are more reactive. [202] The charge induced by the metal catalyst particle was suggested to activate the nanotube edge for the growth. [202] Another important parameter for the reactivity is the gap between the highest occupied molecular orbital (HOMO) and the lowest unoccupied molecular orbital (LUMO), where a small gap points to higher reactivity. [194, 257] Atomic orbitals can only form molecular orbitals, if the energies and geometries of the orbitals are not too different, [51] a small HOMO-LUMO gap means a small difference in orbital energy. [194, 257]

The straight cap has the highest electron charge on the edge atoms (4.1 e), which decreases to the lowest value on the angled rim (3.6 e), see Table 2.2. The electron charge is nearly independent of the spot, which points to an intrinsic property of the rim structure. We show the charges for the individual atoms of the edge in Figure 2.7. All charge values are excess values compared to the valence charge of carbon of 4 e. We average the charge values for individual atoms on the three different spots to derive the charge redistribution. The atoms that form carbon-metal bonds (outer edge atoms) receive the major part of the electron charge, while the carbon atoms connected to the outer edge atoms receive only a smaller amount of charge, see Figure 2.7. The values of the inner straight rim are between 0.05 e and 0.10 e. The values on the outer rim are more volatile ranging from 0.31 e to 0.48 e with an average value of (0.41 ± 0.07) e. The intermediate rim has an average charge redistribution from the iron atoms to the carbon nanotube outer edge atoms of (0.37 ± 0.04) e. The average charge redistribution of the angled rim atoms is slightly smaller than the value of the straight rim with (0.36 ± 0.04) e, however, the zigzag sites have an average value of (0.35 ± 0.04) e, while the two armchair sites of the rim have (0.39 ± 0.03) e. This points to a possible influence of the edge structure on the charge redistribution and therefore the reactivity of the edge atoms.

For the caps that contain only zigzag sites the electron charge redistribution has about 70% of the charge at the outer edge $((9,0)$ cap), which is lower than for caps that contain only armchair sites, where about 83% of the electron redistributed charge is at the edge $((5,5)$ cap with straight rim). The intermediate $(5,5)$ rim

structure cap has 76% of its charge distributed at the outer edge, while the angled cap has only 71% at the outer edge, which is likely a result of the high number of zigzag sites in the angled cap. The higher electron charge on armchair edges allows them to be more reactive than zigzag edges, which is accompanied by a higher growth rate.

The electric dipole moments depend on the spot and the rim structure. There is a small tendency for smaller dipole moments on the straight rim, as well as a tendency of decreasing dipole moments from spot 1 to spot 3, see Table 2.2. A maximum occurs for the intermediate rim structure, which has a dipole moment of 15.8 Debye on the *square* spot 1. The smallest dipole moment of 10.3 Debye on the *top* spot 3 for the straight rim results from the special structure of the rim with a broken pentagon bond, which developed two Klein-edges. The dipole moments of the isolated iron cluster are small and lay between 0.2 and 1.2 Debye. The dipole moments are directed along the axis between the catalyst particle and the nanotube cap, which corresponds to the nanotube growth direction. This corresponds to the result of the theoretical model of Mohammad, which suggested that the electric dipole of bimetallic clusters might be important for the vertical alignment during the growth of carbon nanotubes. [203] Further the study suggested that the electric field resulting from the dipole moment is the driving force for the graphene layer nucleation, as the field causes an increased graphene layer bending and the carbon precursors preferentially land on the catalyst particle due to the electrostatic attraction. [203]

The HOMO-LUMO gaps are small for the cap-catalyst systems, pointing to a high reactivity, see Table 2.2. The lowest gap is found for the angled rim, which slightly increases to the straight rim. The gap of the isolated caps is high for the straight rim with about 1.3 eV, lower for the angled rim with about 0.5 eV and lowest for the intermediate cap with 0.3 eV. The isolated clusters have the lowest gaps between 0.04 eV and 0.21 eV. As pointed out by Wang *et al.* the density functional parametrization of Perdew, Burke and Ernzerhof [226] used for our calculations is not able to predict energy gaps well, meaning that the results have to be regarded with care. [194] With this problem in mind we want to try an interpretation of the results. The electrons of an incoming carbon atom occupy certain energy states, depending on the chemical potential of the system. A lower gap therefore means that the chemical potential needed to include the carbon atom to the tube can be lower.
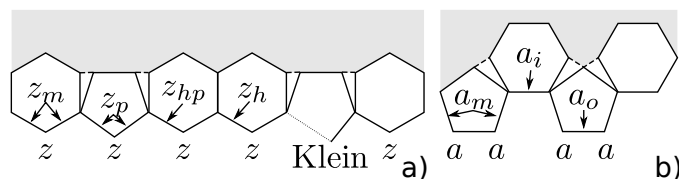
Figure 2.8: Carbon nanotube cap edges/rims projected on a two dimensional surface. a) Zigzag cap rim with z_m bonds between two carbon atoms which can be either at a pentagon z_p, between a hexagon and a pentagon z_{hp}, or at a hexagon z_h. A Klein-edge forms through bond break at a pentagon. b) Armchair cap rim with a_m, a_i, and a_o bonds between the carbon atoms.

Here the energy of the electron of the incoming carbon atom would be lower and a lower gap value would therefore allow easier integration of incoming carbon atoms. However, we further have to regard the geometry of the system, which means that the incorporation of a new carbon atom might cost energy due to transformation of the rim structure, *e.g.* addition of a single carbon atom to a zigzag site creates a Klein-edge which is only bonded to one carbon atom with its four possible bonds. The carbon-carbon bond strength is stronger than the carbon-metal bond strength, see excess energies in Table 2.2, which could prevent the carbon incorporation. Also the orbital geometry has to be regarded, as only a high orbital overlap of the HOMO-LUMO pair leads to an energetically favorable formation of molecular orbitals from the atomic orbitals. The geometry of the orbitals for straight rim caps of various chiralities has been studied in more detail by Wang *et al.* in Reference [194].

In the following we want to compare the bond lengths of the edge atoms between the straight rim $(5, 5)$ cap and the $(9, 0)$ cap. The edges/rims of the nanotube caps contain armchair and zigzag sites, see Figure 2.8 a) and b). The edge atoms of the caps can belong to a hexagon and/or a pentagon. The bond length between the carbon atoms at the rim of the cap depend on the neighboring atoms. This leads to a high volatility of bond lengths at the rim, however, we can derive trends for certain standard configurations.

Zigzag edges form z_m bonds between carbon atoms at the inner and outer edge, see Figure 2.8 a). Outer edge zigzag atoms have two z_m bonds and a carbon-metal bond. Inner edge zigzag atoms have two z_m bonds and a carbon-carbon bond not belonging to the edge. For caps the edge contains pentagons, which have an influence

on the bond length between the carbon atoms. Therefore we classify the bonds in z_p for bonds at a pentagon, z_{hp} for the bond at a hexagon next to a pentagon, and z_h for a bond at a hexagon. Armchair atoms can form a_o bonds between two outer edge atoms, a_m bonds between an outer edge and an inner edge atom, and a_i bonds between two inner edge atoms, see Figure 2.8 b). The outer edge atoms are next to the metal and form one carbon-metal bond, one a_o, and one a_m bond. The inner atoms form a carbon-carbon bond, which is not part of the edge, an a_i, and an a_m bond.

The average bond length of the edge atoms is $d = 1.475$ Å. [13] The bond length of a single bond is $d_{diamond} = 1.54$ Å for diamond. [51] The bond length for a double bond is $d_{C=C} = 1.34$ Å. [51] The average bond length of the rim atoms lies between the value of a double bond and a single bond. Small changes in the bond lengths can significantly change the bond energies. The bond lengths show a trend of shorter bond lengths for armchair type chiralities. In detail $d_{a_o}^{(5,5)} = (1.464 \pm 0.023)$ Å, $d_{a_i}^{(5,5)} = (1.442 \pm 0.020)$ Å, and $d_{a_m}^{(5,5)} = (1.490 \pm 0.011)$ Å. Showing that the inner carbon-carbon bonds tend to have lower bond length values, resulting in higher bond energies than the outer and middle bonds. The middle bonds have the lowest carbon-carbon bond energies and longest bond lengths, pushing the outer armchair atoms further away from the inner cap atoms and lowering their binding energies. The bond lengths of the $(9,0)$ cap are $d_{z_p}^{(9,0)} = (1.506 \pm 0.004)$ Å, $d_{z_{hp}}^{(9,0)} = (1.502 \pm 0.010)$ Å, and $d_{z_h}^{(9,0)} = (1.471 \pm 0.010)$ Å. The bond lengths of the bonds of the hexagons are smaller than the other bond lengths. Klein-edges occur at broken pentagon carbon-carbon bonds, as the increased bond length weakens the bonds and allows the carbon atom to form a carbon-metal bond by rearrangement of the structure at the rim. The Klein-edges were found to occur especially on spot 1 (*square*). The $(5,5)$ cap rim exclusively contains armchair sites formed by pentagons. The Klein-edges occur especially on spot 3 (*top*).

After we collected informations about the rims and their structures, we want to add some more geometric facts for armchair and zigzag structures. The number of growth sites is always lower on angled rims that include a high number of zigzag sites, as the addition to the zigzag sites contains a barrier. [168] Therefore from

---

[13] The average bond length was derived from all edge bonds of various caps on various clusters, including the alloy clusters in Section 2.3. The other values in this Section correspond to the $(5,5)$ and $(9,0)$ cap on the iron cluster.

a growth rate point of view the straight rim growth is preferable to obtain higher growth rates. A higher growth rate means a higher yield of certain chiralities. The shape of the particle and cap are changing during the growth process [173], therefore also the energetically preferred rim structure of the cap/nanotube can change. Our excess energy results show that no rim structure is preferable for all spots, which accompanied with a changing particle structure gives evidence, that there is no preferred rim structure on the catalyst spot and further that the nucleation is mainly diameter selective and not especially chiral angle selective.

Summary

In summary we presented the edge/rim of carbon nanotubes in a model, that describes hexagonal carbon nanotube rims by armchair and zigzag sites. [1, 43, 44] The rims contain three different addition sites that keep the hexagon structure intact if carbon dimers are added. [1, 43, 44] The carbon addition changes the rim structure and can even add or remove growth sites. [1, 43, 44] To determine the stability of the hexagon rim the calculation of dimer rotations at the rim was performed. We found a energy difference between the hexagon and Klein-edge pentagon configuration of only 0.29 eV, which corresponds to a dimer rotation or Stone-Wales defect at the nanotube edge. The rotation barrier between the two configurations was estimated with 2.91 eV, respectively 3.20 eV. The rotation process can be used to incorporate carbon atoms at the edge of the nanotube cap, transforming between pentagons with a dangling carbon atom and hexagons, which is relevant during the growth process of the nanotubes. A more realistic picture can be derived from carbon nanotube cap rim structure calculations on a catalyst particle, which we performed for three distinct armchair rims on an iron catalyst particle. We found no preference for any of the studied rim structures from the adhesion or excess energy, as the energy differences are small or do not yield a preferred rim structure for all studied spots. The fit between the cap and the catalyst particle influences the energies, however, as deformations of the catalyst and cap structure occur during the geometry optimization process, a metastable equilibrium has to be expected, which especially under real conditions (high temperature), does not allow to use the catalyst particle structure as a template for the nanotube cap. Another property, the electron charge at the edge of the nanotube cap seems to be an intrinsic property of the edge structure,

with a difference between the straight and the angled rim configuration of the nanotube cap of 0.6 e. The electric dipole moment of the intermediate rim was found to be the highest, while the dipole moments align along the cap-catalyst axis, which supports the suggestion that the dipole moment influences the vertical alignment of the tube. [203] HOMO-LUMO gaps decrease from straight to angled rim, however, the addition of a carbon atom changes the edge structure and a conclusion for the preference of a certain rim is not possible from this parameter alone. One plausible argument for the preference of straight rims is the number of growth sites, which is minimal for the angled rim, leading to a low growth rate, as only few energetically favorable carbon addition sites exist.

2.2 Chirality Dependent Growth Rate

In this section [14] we present a model for the elongation process of the carbon nanotubes. The model follows the general idea, that the nanotube chirality abundance is partially determined during the nanotube elongation process, which was proposed by Ding *et al.*. [168] This idea is combined with the observation by Gómez-Gualdrón *et al.* that the number of growth sites can change during the growth process. [195] We propose that the growth of a nanotube proceeds through the conversion of armchair bonds to zigzag bonds and vice versa. This is elucidated by a calculated chirality distribution derived from our model which we compare to experimental data. We will show that the growth rate depends on the rim structure (chirality), the energy barriers for the bond conversion, and the growth temperature. A recent study found evidence that supports the chirality dependent growth rate model. [2]

2.2.1 Carbon Addition Barrier

Before we consider the chirality dependent growth rate, we want to remind you on the structure of the edge/rim, see Section 2.1.1. Starting from the rim structure we can schematically describe the growth of a carbon nanotube, see Figure 2.9 and compare to Figure 2.3 in Section 2.1.1. The growth proceeds by addition of C_2. [245] The first carbon atom adds exothermically [74] and is followed endothermically by a second carbon atom. [15] The pentagon created in the first step is energetically less favorable than a hexagon. [172] We, therefore, expect the next carbon atom to be added to the pentagon to form a hexagon, see Section 2.1.1. Also, the creation of more and more pentagons would close the tube [16] [246] and terminate the growth. [260] Alternatively, a carbon dimer is added. [245]

---

[14]A major part of the following text and results has been published by the author of this dissertation in Reference [43]. The model was developed mainly in the unpublished diploma thesis of the author [1] and extended in the published paper of Reference [43]. The research was performed by the author of this thesis under the supervision of the co author of the paper and the thesis advisor, for the diploma and PhD thesis, Stephanie Reich. We will focus on the new results that were not included in the diploma thesis of the author in Section 2.2.2, the necessary basics were presented in Section 2.1.1 to create an understanding for the growth model. More details of the growth model can be found in the diploma thesis of the author, see Reference [1].

[15]An exothermic process is a process, where energy is released, *e.g.* in form of heat, while an endothermic process is a process, where heat is absorbed.

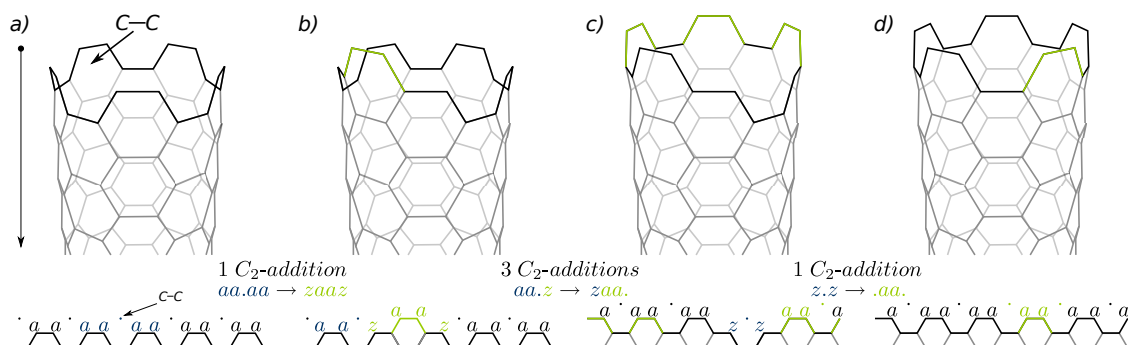[16]A fullerene cap consists of six pentagons. [62]

Figure 2.9: Three dimensional (top) and reduced rim (bottom) representations of half layer growth of a $(5, 5)$ tube. The reduced rim representations at the bottom are obtained by unzipping the 3d wire model (top). The "." denotes a growth site for C_2 addition, the a stands for an armchair and the z for a zigzag dangling bond. The arrow at the left denotes the growth direction. We assume root growth, but the picture is turned upside down and a catalyst was omitted for clarity of the C_2 addition. a) A C_2 adds at the rim. The induction of a new layer is accompanied by a barrier. [168] b) 3 C_2 additions follow without experiencing an energy barrier leading to tube c). The last C_2 addition leads to a stable rim or closed layer. d) A half layer is grown compared to a). This process continues until the growth is terminated. The figure was adapted from Reference [43] of the author of this thesis.

Going through the series of tubes in Figure 2.9 a) to d) a layer of carbon atoms is grown, which corresponds to half a unit cell of the $(5,5)$ tube. The continuation of the process - until growth is terminated - leads to an armchair carbon nanotube. [245]

The first C_2 addition to the rim starts a new layer by converting two a into z dangling bonds, which is accompanied by an energy barrier, [168] compare Figure 2.9 a) and b) (addition to $aa.aa$ site, see Table 2.1). The following three C_2 additions do not change the energy of the rim, since they only move a and z dangling bonds leading to Figure 2.9 c) (addition to $aa.z$ sites, see Table 2.1). The final C_2 addition to Figure 2.9 c) yields a finished armchair layer presented in d) (addition to $z.z$ site, see Table 2.1). We argue that the conversion and movement of the growth sites and the energetic barriers for the conversion determine the chirality-specific growth speed of carbon nanotubes.

During the growth the total number of dangling bonds in the rim remains constant $N_a + N_z = n + m$, while N_a and N_z vary. By this condition we include all reasonable configurations of a growing nanotube and exclude obviously unreasonable configurations, $e.g.$, one side of the tube being much longer than the other side, see Figure 2.1 b).

In the starting configuration the number of growth sites in a rim of an (n, m) nanotube is $N_{aa.aa} = \max{(2m - n, 0)}$ with "max" the maximum, $N_{aa.z} = \min{(m, n - m)}$ with "min" the minimum, and $N_{z.z} = 0$, see Section 2.1.1. Note that for tubes with $2m - n \leq 0$ there are only $aa.z$ growth sites and zigzag tubes $(m = 0)$ do not contain any growth sites at all. The growth of zigzag tubes is supressed in our model and needs an intermediate addition of C or C_3 to induce a growth site for C_2 addition, that we do not consider here, for more details on a possible zigzag growth process see Reference [1] of the author. [17] The zigzag sites zz are therefore considered to yield no growth sites. A C_2 addition to the rim will change the type and the number of growth sites, see Table 2.1 in Section 2.1.1.

The rim of an (n, m) nanotube with $n > m > n/2$ can be divided into a part with a chiral vector $(2m - n, \ 2m - n)$ that contains $aa.aa$ growth sites and a part with a vector $(2n - 2m, \ n - m)$ that consists exclusively of $aa.z$ sites. Therefore, all nanotube rims, except pure zigzag rims, can be divided in $aa.aa$ containing rim

---

[17] In a recent study of Artyukhov $et\ al.$ the carbon addition to a zigzag rim was studied in more detail. [201]

parts and *aa.z* containing rim parts. During the growth the number of growth sites contributed by a rim part containing exclusively *aa.z* sites remains constant. [18] The number of growth sites contributed by a rim part containing exclusively *aa.aa* sites, however, changes continously during the growth as is best illustrated by the example of an armchair tube. Growing a full layer of an armchair rim requires the addition of $2 \cdot (2m - n) = n + m$ carbon dimers. The maximum number of *aa.aa* growth sites $2m - n$ occurs only at half and full armchair layers. The other $2 \cdot (2m - n) - 2$ growth steps have one growth site less. [19] Summing up the number of growth sites in each step and dividing by the number of C_2 additions yields the average growth site number

$$\Lambda_{aa.aa}(n, m) = 2m - n - 1 + \frac{1}{2m - n}. \tag{2.7}$$

Similarly, we find the average growth site number for the rim part containing *aa.z* sites $\Lambda_{aa.z} = N_{aa.z}$. [20] Adding the contributions of *aa.aa* and *aa.z* rim parts yields the average number of growth sites as a function of chiral indexes n and m

$$\Lambda(n, m) = \begin{cases} \Lambda_{aa.aa} + \Lambda_{aa.z} & \text{if } 2m - n > 0, \\ \Lambda_{aa.z} & \text{otherwise.} \end{cases} \tag{2.8}$$

The addition of C_2 to the different growth sites will experience varying energy barriers, as zigzag dangling bonds ($E_z = 2.90\,\text{eV}$) require much more energy than armchair dangling bonds ($E_a = 2.10\,\text{eV}$) in vacuum. [80] The armchair configuration is energetically favorable because it consists of two dangling bonds on neighboring C atoms that form a triple bond. [258] To model experimental growth conditions we need to consider a metal catalyst in most growth scenarios. [196] The energetic difference between a and z dangling bonds is reduced by the presence of a metal, as carbon-metal bonds are formed. [168, 179, 196] However, the difference remains non-zero, as electrons of carbon neighbors influence the total bond energy of the

---

[18]The aforementioned statements contain strong assumptions which are considered in more detail in the diploma thesis of the author (Reference [1]).

[19]This assumes an optimal growth path with only one addition to an *aa.aa* growth site and addition to *aa.z* sites in every subsequent addition until the layer is closed by an addition to a *z.z* site. More details, especially for other less likely growth pathes are presented in the diploma thesis of the author of this thesis (Reference [1]).

[20]We assume that the addition to *aa.z* sites does not create other growth sites, or if they are created no addition to them occurs, but only to *aa.z* sites.

carbon-metal bonds, rendering a lower in energy than z. [196]

The energy barrier for the C_2 addition to an $aa.aa$ site depends on the conversion of $aa.aa$ into $zaaz$ dangling bonds (see Table 2.1 in Section 2.1.1). The conversion requires an energy

$$\Delta_a \;=\; |E_{zaaz} - E_{aa.aa}| = |2E_z - 2E_a| = 2E_a\,|r - 1|, \tag{2.9}$$

with E_a the energy of an armchair and E_z the energy of a zigzag dangling bond. [21] With $r = E_z/E_a$ we denote the ratio between the two energies. The total dangling bond energies as well as their ratio depend on the catalyst. Changing $z.z$ into $.aa.$ we gain Δ_a, if $E_z > E_a$. Growing at an $aa.z$ site will cost no energy; this growth happens without an energetic barrier. This energetically different behavior allows to affect the chirality distribution of carbon nanotubes through external parameters such as the metal catalyst and the growth temperature.

2.2.2 Gamma - Growth Rate Function

The addition of C_2 dimers to the $\Lambda(n, m)$ sites will lead to a lengthening of the tube with $n + m$ C_2 additions for a single full layer. If we define the abundance of a certain nanotube chirality to depend on the number of full carbon layers, we find the growth speed of a tube to be proportional to

$$\Gamma(n, m) = \frac{\Lambda(n, m)}{n + m}. \tag{2.10}$$

The growth factor $\Gamma(n, m)$ allows us to understand why chiral selectivity occurs during the nanotube elongation phase. In the following we will show how we can influence the chirality distribution during the elongation of a nanotube. Therefore we first add some weight factors (Arrhenius like factor, see Reference [51]) to the

---

[21]The formula is modified compared to the one presented in References [1, 43], as the barrier occurs for the initiation of a new layer as well as for the closing of a layer, which previously had not been considered. If a layer is finished by a C_2 addition, the last $z.z$ site that remained in the rim configuration is converted to an $.aa.$ configuration, see Table 2.1. This requires a transformation of 2 z bonds to 2 a bonds, which leads to a barrier, if the zigzag bond energy E_z is lower than the armchair bond energy E_a.
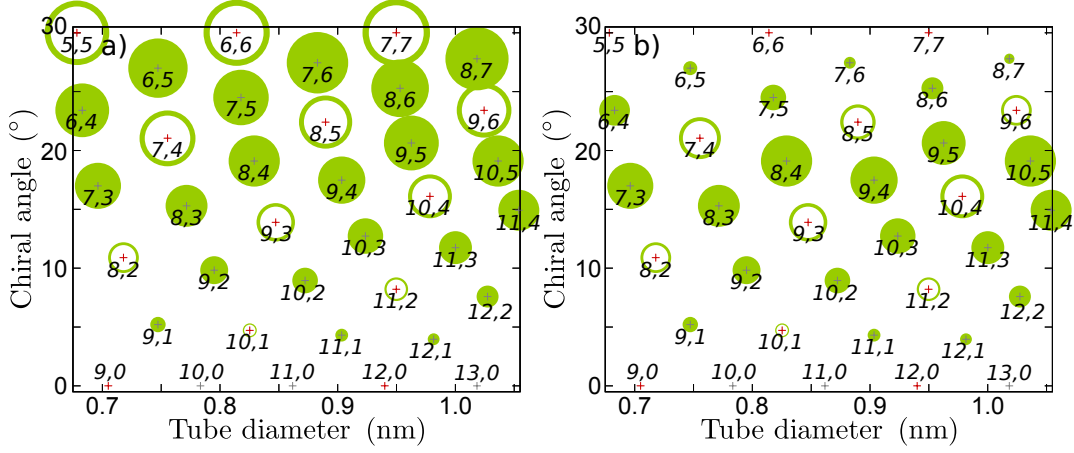
Figure 2.10: Comparison of $\Gamma(n,m)$ for tube diameters $d = 0.675\text{-}1.055\,\text{nm}$ for a) $\Delta_a \ll k_B T \leftrightarrow \delta_a = 1$. b) $\Delta_a \gg k_B T \leftrightarrow \delta_a = 0$. The abundance of metallic/semi-metallic tubes (open circle, red cross) decreases compared to semiconducting tubes (full circle, gray cross) from a) to b). The figure was adapted from Reference [43].

growth rate factor equation: [22]

$$\Gamma(n,m) = \begin{cases} \frac{\Lambda_{aa.aa}(n,m)\cdot\delta_a + \Lambda_{aa.z}(n,m)\cdot\delta_{az}}{n+m} & \text{if } 2m - n > 0, \\ \frac{\Lambda_{aa.z}(n,m)\cdot\delta_{az}}{n+m} & \text{otherwise,} \end{cases} \qquad (2.11)$$

where $\delta_a = \exp\left(-\Delta_a/k_b T\right)$ is an exponential factor to account for the temperature dependence of the addition barrier to armchair sites and $\delta_{az} = \exp\left(-\Delta_{az}/k_b T\right) = 1$, as an addition barrier for $aa.z$ sites (kinks) is negligible ($\Delta_{az} = 0$). [43, 168] The growth rate factor Γ can have values between 0.5 and 0, in dependence of the chirality.

We can insert Equation (2.7) and $\Lambda_{aa.z} = N_{aa.z} = \min\left(m, n - m\right)$ in Equation (2.11) to determine Γ. Figure 2.10 shows the growth speed factor Γ as area size in chiral angle and diameter dependence for diameters $d = 0.675\text{-}1.055\,\text{nm}$. If the addition to $aa.aa$ sites has a negligible barrier, meaning $\delta_a = 1$ ($r = E_z/E_a \approx 1$ or $\Delta_a \ll k_B T$), all growth sites can contribute to the growth speed, see Figure 2.10 a). The highest Γ occur for (n,n) armchair tubes. A small trend for increasing Γ exists for larger

---

[22]The inclusion of the weight factors is an extension compared to the formula derived in the diploma thesis [1] of the author, as well as to the formula presented in Reference [43].

diameter tubes, resulting from the fractional term of Equation (2.7), as the comparison of the armchair tubes shows. Changing the environment (*e.g.* another catalyst with another r or adjustment of temperature) so that $\Delta_a \gg k_B T$, the *aa.aa* growth sites will not contribute anymore; Equation (2.11) yields $\Gamma = \Lambda_{aa.z} / (n + m)$, which leads to a different growth speed distribution, see Figure 2.10 b). In that case the highest Γ occurs for $\left(n, \frac{n}{2}\right)$ chiral tubes.

For real samples we expect a distribution of growth speed factors Γ to be between the two limiting cases presented in Figure 2.10. The thermal energy of nanotube growth is on the order of $k_B T \approx 0.05$-0.11 eV. [133, 144] Δ_a depends on the catalyst material, its composition and - less pronounced - on the position of the carbon with respect to the metal atom. The barriers for metal catalysts are on the order of $\Delta_a \approx 0$-0.12 eV for various metals [168, 179] and thus comparable to the thermal energy. Therefore, the addition to the *aa.aa* site is not suppressed. This agrees with the results of Ding *et al.*, that the barrier for armchair kink introduction - which corresponds to C_2 addition to *aa.aa* - is negligible. [168] Recently, other materials like SiO_2 were found to catalyze nanotube growth. [131] Further, bimetallic/alloy catalysts contain different barriers and may be extremely interesting for influencing the chirality distribution, [3] which we study in Section 2.3.

Up to now we concentrated on the growth/elongation of an existing nanotube nucleus. Using Equation (2.11) we can derive chirality distributions in dependence of catalyst composition and growth temperature. The chirality distribution of a sample, however, will also depend on the nucleation phase, *i.e.*, whether a particular tube cap is nucleated or not. [63] We assume the tube diameters (and also the chirality) to be fixed by the nucleation. [179, 186] The diameter of a carbon nanotube is determined in the nucleation phase. [111, 186] To consider the dependence of nanotube diameters on the diameter of the catalyst particles, [111, 114, 188] we therefore multiply Equation (2.11) by a Gaussian distribution of the nanotube diameters $f(d; \mu, \sigma^2)$ [96] and obtain a growth rate factor Γ^* which leads to a more realistic chirality distribution,

$$\Gamma^*(n, m) = \frac{1}{\sigma\sqrt{2\pi}} e^{-\frac{(d-\mu)^2}{2\sigma^2}} \cdot \Gamma(n, m). \tag{2.12}$$

The tube diameter distribution might also include additional effects that do not

result from the particle diameters and which might not be covered by the Gaussian distribution, however, the distribution serves the simplicity of the model.

In the following comparison to experimental data we assume the barrier to *aa.aa* growth sites to be negligible ($\Delta_a \ll k_B T \leftrightarrow \delta_a = 1$). Figure 2.11 a) compares the chirality distribution of semiconducting nanotubes with $d = (0.93 \pm 0.3)$ nm to the experimental distribution in HiPco tubes; Figure 2.11 b) is for tubes with $d = (0.75 \pm 0.15)$ nm and ACCVD samples. [151] The agreement between theory and experiment in Figure 2.11 b) is striking. Our model very well predicts the overall increase of the number of tubes with increasing chiral angle. The strong discrepancies for selected chiralities - *e.g.* the strong luminescence of the $(10, 2)$ tube - is most likely due to a high quantum yield for some nanotubes. [261] On the other hand, the nucleation phase might also prefer certain chiralities. [179] It would be highly desirable to establish an unambigious chirality distribution experimentally to clarify these points, as different techniques yield different chirality distributions. [89]

The barrier δ_a is not negligible for the HiPco sample as the deviation between the theoretical and experimental part of Figure 2.11 a) shows. Better results for the HiPco sample could therefore be obtained if the barrier was included. The barrier is negligible, however, for the growth conditions presented in Figure 2.11 b), as the theory perfectly reproduces the trend with only considering the contribution of the Γ^* factor for $\delta_a = 1$. We conclude that different growth conditions have indeed an influence on the chirality distributions which result during the elongation of the nanotubes.

At the end of this section we want to consider how the growth speed factor Γ can be included into a real growth rate. Therefore we use the results derived by Yuan *et al.*, which found that the threshold barrier for the growth of carbon nanotubes is the incorporation of the carbon atoms into the nanotube wall through the catalyst-nanotube interface. [74] They derive energy barriers G_0^* of 1.85 eV on Fe and 2.27 eV on Ni for the diffusion and incorporation of two carbon atoms into the nanotube. [74] This allow to estimate a growth rate, if one considers that the carbon atoms on the catalyst have a higher chemical potential than the carbon atoms in the tube. [74] The difference is given with $2\Delta\mu$ leading to an overall barrier of $G^* = G_0^* - 2\Delta\mu$. [74] Yuan *et al.* further consider the decomposition of the nanotube in single carbon atoms, which has the barrier G_0^*. [74] This leads to the chemical reaction rates (from
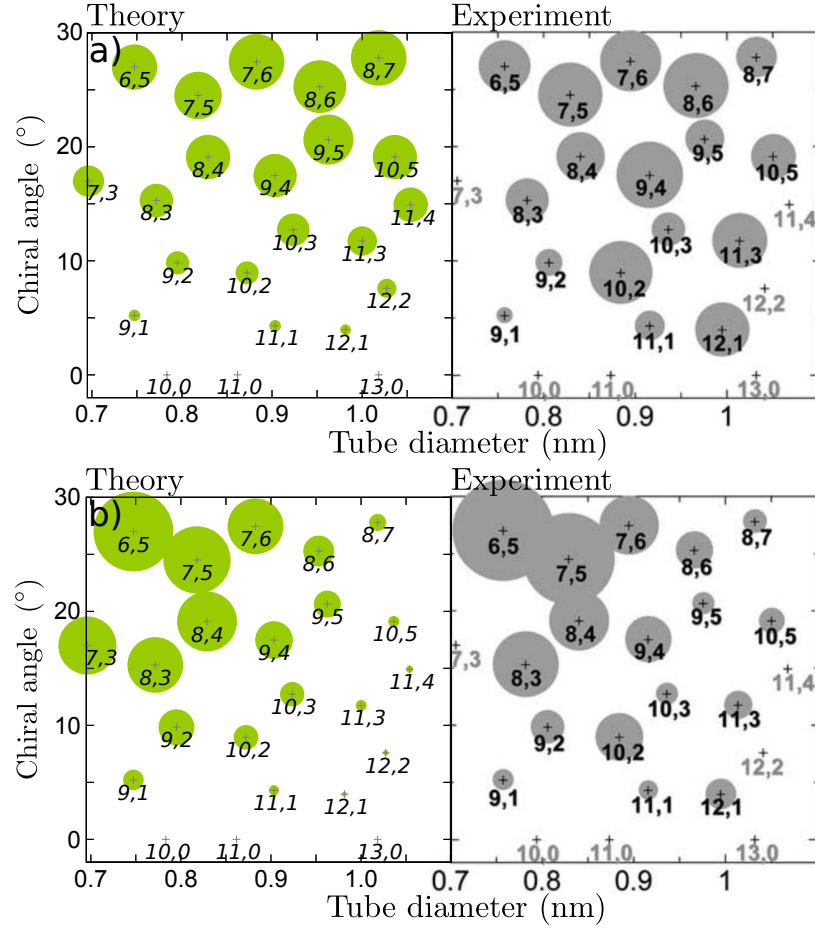
Figure 2.11: Comparison of chirality distributions. The theoretically calculated distributions were determined by Equation (2.12) for $\Delta_a \ll k_B T \leftrightarrow \delta_a = 1$. The experimentally determined chirality distributions are adapted from Miyauchi *et al.* (Reference [151]). a) Theory: $d = (0.93 \pm 0.3)$ nm. [42] Experiment: HiPco sample. b) Theory: $d = (0.75 \pm 0.15)$ nm. Experiment: ACCVD sample grown at $650\,°\text{C}$ with Fe/Co catalyst. The figure was adapted from Reference [43] of the author of this thesis.

transition state theory)

$$K^+ = \frac{k_B T}{h} \cdot \exp\left[-\frac{(G_0^* - 2\Delta\mu)}{k_B T}\right], \tag{2.13}$$

$$K^- = \frac{k_B T}{h} \cdot \exp\left[-\frac{G_0^*}{k_B T}\right], \tag{2.14}$$

where k_B is the Boltzmann constant, T is the temperature, K^+ is the carbon incorporation rate to the nanotube and K^- is the carbon decomposition rate from the nanotube. [74] The nanotube growth rate of Yuan *et al.* was then estimated by a model that considered the number of active armchair sites at the tube end, [74] we want to include our growth rate factor Γ instead, which leads to:

$$R(n,m) = 2 \cdot \Gamma^* \left(K^+ - K^-\right) \cdot \kappa, \tag{2.15}$$

with the factor 2 to normalize the prefactor, as Γ^* has values between 0 and 0.5, and $\kappa = 0.1$ nm, which follows from the comparison to the experimental growth rates, which are considered with $R \approx 250$ μm/s at $T = 1200$ K ($\Delta\mu = 0.1$ eV).

Summary

In summary, we presented a model for the chirality selective nanotube growth and elongation process through the structure of the rim. [1, 43, 44] Depending on the tube chirality the rim contains three different growth sites *aa.aa*, *aa.z* and *z.z*. [1, 43, 44] Geometric considerations yield the growth factor Γ^*, which in turn determines the chirality distribution of carbon nanotube samples. [1, 43] We showed that chiral selectivity can be obtained through the combination of external parameters, *i.e.* catalyst and temperature. [1, 43] We combine our growth rate factor Γ with the results of Yuan *et al.* [74] to derive a growth rate which can be compared to experimental growth rates. In the next section (Section 2.3) we will calculate the armchair and zigzag bond energies needed as input for the growth factor presented in this section. We especially focus on alloy particles of Ni and Fe.

2.3 Growth on Ni, Fe and NiFe Alloy Particles

In this section [23] we present density functional theory calculations of carbon nanotube caps on Ni, Fe and Ni_xFe_{1-x} alloy particles to determine the a and z bond energies for the chirality dependent growth rate (see Section 2.2.2) and barrier energies Δ_a. We describe the system and computational methods for our calculations in Section 2.3.1. Section 2.3.2 studies the adhesion energies and carbon-metal bond energies of the caps. In Section 2.3.3 we study the charge distribution at the carbon atoms and the catalyst particle atoms, as well as the resulting electric dipole moments. Section 2.3.4 discusses our results in comparison to other theoretical and experimental results and combines the results of Section 2.3.2 with the growth model we developed in Section 2.2.2 to estimate some exemplary chirality distributions.

In recent experimental studies it was found that growth on alloy NiFe particles leads to an enrichment of certain chiralities. [3, 127] A recent theoretical study attempted to explain the chirality enrichment on the NiFe alloy particles. [190] It, however, considered plane surfaces and elongated nanotube caps (non-minimal seed caps with only an inferior number of growth sites/kinks), which does not seem to be appropriate to describe the chirality selection on a catalyst particle, [190, 256] see the discussion in Section 2.1.2. Another theoretical study on a nickel particle suggested that electronic charge transfer might be important to control the chirality-selective growth process. [202] We study the binding, as well as the charge transfer properties of the nanotube caps on NiFe alloy particles to solve the puzzle.

2.3.1 Methodology and Catalyst Particles

In this section we present the catalyst particles and nanotube caps used for our calculations and further present the details of the computational methods. More details about the caps used for the study can also be found in Section 2.1.2.

We performed spin polarized density functional theory calculations with the *ab-initio* package SIESTA. [216, 239] We used the generalized gradient approximation parameterized by Perdew, Burke and Ernzerhof, [226] as the bias towards compact cluster structures is reduced compared to the local density approximation. [262] The

---

[23]A major part of the texts and results of this section is based on Reference [45]. The calculations and analyses were performed by the author of this thesis under the supervision of the co authors of the paper, especially by the thesis advisor Stephanie Reich.
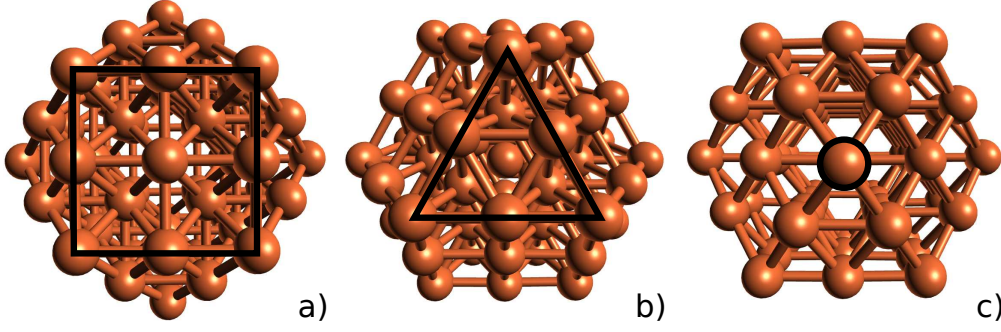
Figure 2.12: Top view on a ball and stick sketch model of the spots of a 55 atom (iron) cluster. The atoms that form the top of the cluster are marked. a) Spot 1, fcc(100) with a 3 times 3 atom *square* (9 atoms). b) Spot 2, fcc(111) with a 3 atom sided *triangle* (6 atoms). c) Spot 3, with only 1 atom at the *top* of the cluster. The figure is similar to Fig. 63 of the diploma thesis of the author (see Ref. [1]).

calculations used the norm conserving nonlocal pseudopotentials presented in Section 5.1.1. [241] To balance the computational time and the accuracy to a reasonable level, we used a double-ζ polarized (DZP) basis set. The cutoff radii of the orbitals were determined by the parameter "PAO.EnergyShift" with 7 meV. This leads to cutoff radii $r_s = 6.099$ Bohr and $r_p = 7.832$ Bohr for the s and p orbital of the carbon atoms, $r_s = 9.649$ Bohr and $r_d = 6.001$ Bohr for the s and d orbital of the iron atoms, and $r_s = 9.187$ Bohr and $r_d = 5.572$ Bohr for the s and d orbital of the nickel atoms. The mesh-cutoff for the real-space integration corresponded to about 350 Ry. We used only the Γ-point to calculate the total energies, as all studied systems have finite dimensions.

For our calculations we consider the situation, where a carbon nanotube cap has already formed on a catalyst particle, but is not elongated. The systems studied in this section therefore consist of two parts, a catalytic particle and a carbon nanotube cap. We consider the Fe_{55}, $Ni_{12}Fe_{43}$, $Ni_{27}Fe_{28}$, and Ni_{55} clusters to understand the influence of alloy systems and chiralities on the cap-cluster interaction.

Our (deformed) icosahedral catalyst particles consists of 55 atoms [263] that initially form a higly symmetric structure containing six fcc(100), eight fcc(111) surfaces, and three distinctive spots to add a carbon nanotube cap, see Figure 2.12 a) to 2.12 c). The icosahedral particles have been found to be the most stable configura-

Table 2.3: Comparison of total energies (E_{tot}) and excess energies (ΔE_{tot}) of various clusters compared to the lowest total energy configuration of a specific cluster and the absolute value of the electric dipole moments Δ of the clusters. The initial cluster structures for the geometry optimization were used from the specified combined system and the energies of the geometry optimized clusters are presented. The calculations of the $Ni_{12}Fe_{43}$ cluster have been performed for two different initial configurations.

cap	particle	spot	E_{tot} (eV)	ΔE_{tot} (eV)	Δ (Debye)
$(5,5)$	Fe_{55}	1	-41238.69	2.01	1.1
$(5,5)$	Fe_{55}	2	-	-	-
$(5,5)$	Fe_{55}	3	-41239.71	0.99	0.5
$(9,0)$	Fe_{55}	1	-	-	-
$(9,0)$	Fe_{55}	2	-	-	-
$(9,0)$	Fe_{55}	3	-41240.69	0.0	0.2
$(5,5)$	$Ni_{12}Fe_{43}$	1	-46366.09	1.52	0.3
$(5,5)$	$Ni_{12}Fe_{43}*$	1	-46365.96	1.65	0.6
$(5,5)$	$Ni_{12}Fe_{43}$	2	-46366.97	0.64	0.9
$(5,5)$	$Ni_{12}Fe_{43}*$	2	-46367.19	0.42	1.3
$(5,5)$	$Ni_{12}Fe_{43}$	3	-46366.45	1.16	0.8
$(5,5)$	$Ni_{12}Fe_{43}*$	3	-46367.61	0.00	0.6
$(9,0)$	$Ni_{12}Fe_{43}$	1	-46365.54	2.06	0.8
$(9,0)$	$Ni_{12}Fe_{43}*$	1	-46366.98	0.63	1.1
$(9,0)$	$Ni_{12}Fe_{43}$	2	-46366.96	0.65	0.8
$(9,0)$	$Ni_{12}Fe_{43}*$	2	-46365.94	1.66	1.1
$(9,0)$	$Ni_{12}Fe_{43}$	3	-	-	-
$(9,0)$	$Ni_{12}Fe_{43}*$	3	-46365.96	1.65	0.5
$(5,5)$	$Ni_{27}Fe_{28}$	1	-	-	-
$(5,5)$	$Ni_{27}Fe_{28}$	2	-52774.82	1.44	0.6
$(5,5)$	$Ni_{27}Fe_{28}$	3	-52774.48	1.78	1.0
$(9,0)$	$Ni_{27}Fe_{28}$	1	-52775.40	0.86	1.9
$(9,0)$	$Ni_{27}Fe_{28}$	2	-52776.26	0.00	0.5
$(9,0)$	$Ni_{27}Fe_{28}$	3	-52776.10	0.16	1.1
$(5,5)$	Ni_{55}	1	-64732.44	3.19	1.0
$(5,5)$	Ni_{55}	2	-64732.31	3.32	0.7
$(5,5)$	Ni_{55}	3	-64733.05	2.58	0.9
$(9,0)$	Ni_{55}	1	-64734.50	1.13	0.5
$(9,0)$	Ni_{55}	2	-	-	-
$(9,0)$	Ni_{55}	3	-64735.63	0.00	0.0

tion with a magnetic moment of 40 μ_B for Ni and 150 μ_B for Fe. [24] [263] The relaxed particle structures do not keep the icosahedral symmetry and are not expected to represent the global minimum, as it is not feasible to find the global minimum of the clusters in density functional theory. [25] [192, 262] The trend, however, is expected to be correct, see discussion in Reference [192], respectively our calculations of the same catalyst compositions of $Ni_{12}Fe_{43}$ particles in slightly different initial configurations, see Section 2.3.2. Further we used the energies of the geometry optimized catalyst structures from the initial structures of the combined system to be consistent, see Table 2.3.

The carbon nanotube caps were created with the program code CaGe using the isolated pentagon rule (IPR), which states that caps are energetically most stable, if all six pentagons needed for the cap inclination are isolated from each other. [62, 63, 265] CaGe derives cap structures from a graphtheoretical method. [62] We created and geometry optimized fullerene structures starting from the graphtheoretically generated caps from CaGe to get to a decent cap structure. Studying a certain cap of a given chirality does not allow to draw straight forward conclusions for that chirality, as there exist many possible cap configurations for a certain chirality. [62, 63] The isolated pentagon rule used for the generation of our caps, however, allows to reduce the number of possible caps, by only considering energetically favorable structures. [63] Especially the $(5, 5)$ (30 atom cap) and $(9, 0)$ (39 atom cap) chiralities only have one possible cap structure which fulfills the isolated pentagon rule, [191] making them perfect candidates for our study.

The caps were transferred on the three different spots of the catalyst particles,

---

[24]Smaller nickel particles (13 atoms) on the walls of CNTs were suggested as single-molecule sensors, as the addition of a benzene molecule changed the magnetic moment of the system from 8 μ_B to 6 μ_B. [29] This renders the study of the magnetic properties of the system during the growth interesting, as the nanotube caps are all unique molecules, which might have a chirality dependent influence on the magnetic properties of the system, see Section 2.3.3.

[25]The energy values deviate between the different relaxed catalyst structures, depending on the initial structure, see Table 2.3. Zhu *et al.* report energy differences between 2-3 eV between different geometry optimized catalyst cluster structures, [192] which corresponds well to our results. The catalyst clusters can have various morphologies for the same particle size and it was found that 10^{21} local minima exist for a 55 atom (Lennard-Jones) cluster, which was compared to the problem of finding the global minimum in protein folding. [262, 264] Considering the composition, it becomes even harder, which makes it nearly impossible to find the global minimum for the clusters of two elements and 55 atoms. Another problem in the comparison to the experiment may be that the clusters are liquid like or the growth time is smaller than the morphological relaxation time. [262]
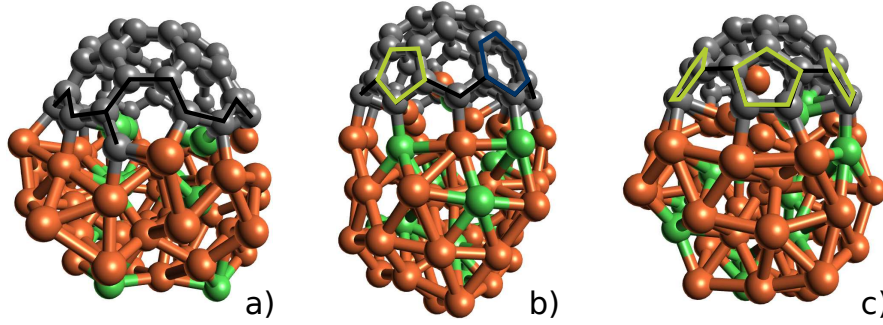
Figure 2.13: Ball and sticks sketch model of carbon nanotube caps on a $Ni_{12}Fe_{43}$ alloy cluster on three different spots. Carbon atoms in grey, Nickel atoms in green, and iron atoms in orange. a) Spot 1: $(9,0)$ cap shows a Klein-edge through bond break of a pentagon at the rim. b) Spot 2: $(9,0)$ cap showing a hexagon (blue) and pentagon (green) at the zigzag rim. c) Spot 3: $(5,5)$ cap showing an armchair rim formed exclusively by pentagons (green).

see Figure 2.12. The fit of the rims of the carbon nanotube caps to the spots of the clusters were performed by hand. In Figure 2.13 we show geometry optimized structures of the $(9,0)$ and $(5,5)$ cap bound to the three spots of the $Ni_{12}Fe_{43}$ catalyst as examples for all the systems we studied. The atoms at the rim of the cap bind to the cluster, see Figure 2.13. The deformation (structure change) of the cluster is significant for the presented alloy systems. The atoms in the rim of the cap also adjusted their positions, which suggests a dynamic process of carbon and metal reshaping, which was studied in detail in Reference [53]. The edges/rims of the caps are composed of only armchair and zigzag sites, which is true for all nanotubes. [18] If a pentagon bond gets broken at the edge, a Klein-edge can form and offer a site for addition of a single carbon to close the edge with a hexagon, see Figure 2.13 a). The Klein-edge configuration occurs commonly for the $(9,0)$ cap and might be a possible way to avoid the initiation barrier for a new layer. [168] The configuration with the Klein-edge was recently suggested to be energetically favorable for the graphene growth, however, it was suggested to be relevant for the armchair growth, see A5' site in Reference [201]. In general there is a nearly continuous number of ways to combine the cap with the cluster in dependence of the chirality of the cap, however, the chosen spots are expected to allow the best comparison.

All optimized geometries were relaxed to a maximal atomic force of 0.04 eV/Å.

The total energy of the combined system as well as the energy of the cluster and cap were calculated in various structures and basis sets to account for the basis set superposition error. [26] The SIESTA basis set is incomplete, therefore a BSSE occurs and we calculated the counterpoise correction term [267, 268] to remove the basis set superposition error (BSSE):

$$E^{BSSE} = E_{cap}^{ghost} - E_{cap} + E_{cluster}^{ghost} - E_{cluster}, \tag{2.16}$$

with E_{cap}^{ghost} the energy of the cap in the structure of the combined system with a cluster of ghost atoms, corresponding to a calculation with the basis of the combined system, E_{cap} the energy of the cap in the structure of the combined system with removed cluster atoms, corresponding to a calculation with the basis of the cap, $E_{cluster}^{ghost}$ the energy of the cluster in the structure of the combined system with a cap of ghost atoms, and $E_{cluster}$ the energy of the cluster in the structure of the combined system with removed cap atoms. [266–269] The basis set superposition errors for our calculations range between 2.0 eV and 3.0 eV with an average error of (2.5 ± 0.3) eV. Using the BSSE correction we can calculate the adsorption energy between the carbon nanotube cap and the catalyst cluster with:

$$E_{ad} = E_{tot} - E_{cap}^{relax} - E_{cluster}^{relax} - E^{BSSE}, \tag{2.17}$$

where E_{tot} is the energy of the geometry optimized combined system of the cap and the catalyst cluster, E_{cap}^{relax} is the energy of the geometry optimized cap, and $E_{cluster}^{relax}$ is the energy of the geometry optimized cluster, see *e.g.*, total energy in Reference [194] or binding (adhesion) energy in Reference [192].

Another way to assess the stability of the combined system is by the comparison with other systems that contain the same number of carbon and metal atoms. This leads to formulas for the excess energy:

$$E_x^i = E_{tot} - E_{cluster}^{relax} - n_C E_C^i - E^{BSSE}, \tag{2.18}$$

---

[26]In calculations that use localized atomic orbitals, each of the orbitals uses a unique incomplete basis set, see Section 1.2.1. [266, 267] The "basis set superposition error" results from the problem that the basis set of an adsorbed atom in a molecule uses the basis set of the neighboring atom, which lowers the energy for all atoms that use the basis sets of neighbors. [266, 267]

Table 2.4: Comparison of total energies (E_{tot}) and excess energies (ΔE_{tot}^i) per atom of various carbon systems. The third row compares the excess energies of the systems to the energy of graphene. The fourth row compares the excess energies of the fullerenes to the associated nanotubes, meaning the energy of $C_{60,100}$ is compared to the energy of the $(5,5)$ tube and the energy of C_{78} is compared to the energy of the $(9,0)$ tube.

system	E_{tot}/atom	$\Delta E_{tot}^{\text{graphene}}$/atom	$\Delta E_{tot}^{\text{tube}}$/atom
graphene	-154.865	0.00	-
$(5,5)$	-154.702	0.16	0.00
$(9,0)$	-154.711	0.15	0.00
C_{60}	-154.510	0.36	0.19
C_{100}	-154.591	0.27	0.11
C_{78}	-154.554	0.31	0.16

with E_{C}^i the energy per carbon atom for various systems and n_{C} the number of carbon atoms in the cap of the combined system. [172, 179, 192] In detail we calculate the excess energy per atom in comparison to the energy of a system of an isolated metal cluster and an infinitely long carbon nanotube, a fullerene, or an infinite graphene sheet, see Table 2.4 for a comparison between the total energies of the carbon systems. This allows to determine which system configuration is expected to be lower in energy and therefore more stable. [172, 179, 192] It follows immediately that the graphene structure has the lowest energy of the studied structures, see Table 2.4, which means that it is the most stable structure. This, however, is only true for an infinite graphene sheet, as edges with dangling bonds would significantly increase the total energy of a graphene flake. A detailed study for various carbon systems by Fan *et al.* found that the nanotube cap structure is energetically favorable on a metal surface, as the dangling bonds are saturated. [172]

Another possibility to obtain the excess energy compared to the fullerene structure is to remove the dangling bond contributions of the adhesion energy. This leads to

$$E_x^{\text{fullerene}} = E_{CM} = E_{ad} - 2 \cdot m \cdot E_a^{vac} - (n - m) \cdot E_z^{vac}, \qquad (2.19)$$

where E_{ad} is the adhesion energy, E_a^{vac} is the armchair bond energy in the vacuum, and E_z^{vac} is the zigzag bond energy in the vaccum. The factor $2 \cdot m$ results from the

number of armchair bonds at the rim of the nanotube cap and the factor $(n - m)$ results from the number of zigzag bonds at the rim of the cap, see Section 2.1.1 or References [43, 44]. The vacuum bond energies (for a straight cut rim) can be derived with the equations

$$E_a^{vac} = \frac{E_{C_{60}}/2 - E_{cap}^{(5,5)}}{2 \cdot m}, \tag{2.20}$$

$$E_z^{vac} = \frac{E_{C_{78}}/2 - E_{cap}^{(9,0)}}{n - m}, \tag{2.21}$$

where E_{C_i} is the energy of a fullerene formed from two (n, m) caps. The armchair edges in the vacuum have lower absolute bond energies than zigzag edges, as armchair edges form triple bonds between two edge armchair atoms. [258] Zigzag edge atoms have dangling bonds, which are energetically even more unpreferable than the triple bonds of the armchair edge atoms. [258] We find the average armchair bond energy in the vacuum with $E_a^{vac} = (2.61 \pm 0.04)$ eV [27] ($E_{a,\text{lit}}^{vac} = 2.1$ eV). [80] The average zigzag bond energy in the vacuum is $E_z^{vac} = (2.69 \pm 0.01)$ eV ($E_{z,\text{lit}}^{vac} = 2.9$ eV). [80] The deviation to the literature values results from the deformation energy of the edge of the cap compared to the edge of the nanotube, as the cap contains more curvature and pentagons at the edge. Especially the considered armchair cap has five pentagons at the edge, while the zigzag cap only contains three. We used the system specific vacuum bond energies to determine the carbon-metal bond energies. To determine the carbon-metal bond energies per bond we divided through the number of bonds $n + m$.

An error for the energies was estimated from the standard deviation by averaging over identical systems with small changes in their initial configuration. The standard deviations are rather large, as only two values were included which does not have a statistical significance, however, it allows to estimate the order of the error with at least 0.1 eV for the excess energy from the comparison of the $(5, 5)$ cap on spot 1 and 2 of the $Ni_{12}Fe_{43}$ cluster, see Table 2.5 in Section 2.3.2. The error for the adhesion energy is estimated to be slightly higher with about 0.7 eV. The errors in the total energy for the combined system following from the eggbox effect ($\Delta \approx 0.02$ eV) and

---

[27]Only edges with armchair sites were considered, therefore edges which contained a Klein-edge were neglected.

the unit cell size ($\Delta \approx 0.004$ eV) are negligible compared to the error resulting from the non global minimum catalyst particle structure.

Besides the energies it is also interesting to study the electron distribution to understand the combined system of a cap and a cluster. We therefore performed Bader population analysis calculations on the cap-cluster systems to determine the electron charge transfer between the carbon cap atoms and the catalyst particle atoms. [270–273] The charge transfer between nanotube edges and nickel catalyst particles has been suggested to be important for the nanotube growth, as it increases the reactivitiy of the carbon edge atoms creating reactive sites. [194, 202] Another study suggested that the electric dipole moment, which is induced by the charge transfer in bimetallic clusters affects the nanotube growth, as carbon precursor atoms preferentially land on specific spots of the catalyst due to the electric field. [203] We do not find a significant difference for the electric dipole moments between monometallic and bimetallic clusters, see Table 2.3. If the caps connect to the cluster, however, the charge transfer between the edge of the cap and the clusters induces electric dipole moments, see Section 2.3.3.

2.3.2 Carbon Metal Energies

In this section we determine the adhesion and excess energies between the nanotube caps and the metal catalyst clusters.

The adhesion energies are high with slightly more than -20 eV, varying about a few eV in dependence of the spot, catalyst and cap, see Table 2.5. The armchair caps have adhesion energies that are a few eV higher than the zigzag energies, which is a result of the number of dangling bonds at the edge of the caps. The zigzag caps have $n+m = 9+0 = 9$ dangling bonds. The armchair caps have $n+m = 5+5 = 10$ dangling bonds. Therefore the adhesion energy of the armchair cap is higher than the adhesion energy of the zigzag cap, even though the energy per dangling bond is lower for the armchair compared to the zigzag bond, [258] see Section 2.3.1.

Averaging the adhesion energies over the alloy compositions we find $E_{ad}^{\mathrm{Fe}_{55}} = (-21.0 \pm 0.3)$ eV, $E_{ad}^{\mathrm{Ni}_{12}\mathrm{Fe}_{43}} = (-22.3 \pm 1.4)$ eV, $E_{ad}^{\mathrm{Ni}_{27}\mathrm{Fe}_{28}} = (-22.3 \pm 1.5)$ eV, and $E_{ad}^{\mathrm{Ni}_{55}} = (-22.4 \pm 1.5)$ eV. [28] Two effects account for the adhesion energy. One is

---

[28]The results have to be regarded with care, as the number of considered armchair and zigzag caps is not the same for all average adhesion energies.

Table 2.5: Comparison of adhesion energies and carbon-metal bond energies of nanotube caps on various catalyst clusters. The asterisks denote systems with at least one Klein-edge at the rim.

cap	particle	spot	E_{ad} (eV)	E_{CM} (eV)
$(5,5)$	Fe_{55}	1	-21.2	4.3
$(5,5)$	Fe_{55}	2	-	-
$(5,5)$	Fe_{55}	3*	-21.2	4.3
$(9,0)$	Fe_{55}	1	-	-
$(9,0)$	Fe_{55}	2	-	-
$(9,0)$	Fe_{55}	3	-20.7	3.6
$(5,5)$	$Ni_{12}Fe_{43}$	1	-23.2	2.6
$(5,5)$	$Ni_{12}Fe_{43}*$	1	-23.9	2.5
$(5,5)$	$Ni_{12}Fe_{43}$	2	-24.2	2.2
$(5,5)$	$Ni_{12}Fe_{43}*$	2	-24.0	2.3
$(5,5)$	$Ni_{12}Fe_{43}$	3*	-22.4	3.6
$(5,5)$	$Ni_{12}Fe_{43}*$	3	-21.3	5.0
$(9,0)$	$Ni_{12}Fe_{43}$	1*	-20.8	3.4
$(9,0)$	$Ni_{12}Fe_{43}*$	1*	-20.4	3.9
$(9,0)$	$Ni_{12}Fe_{43}$	2	-20.7	3.5
$(9,0)$	$Ni_{12}Fe_{43}*$	2	-22.6	1.7
$(9,0)$	$Ni_{12}Fe_{43}$	3	-	-
$(9,0)$	$Ni_{12}Fe_{43}*$	3	-21.6	2.6
$(5,5)$	$Ni_{27}Fe_{28}$	1	-23.6	2.7
$(5,5)$	$Ni_{27}Fe_{28}$	2	-24.4	2.0
$(5,5)$	$Ni_{27}Fe_{28}$	3*	-22.5	3.4
$(9,0)$	$Ni_{27}Fe_{28}$	1*	-20.3	3.9
$(9,0)$	$Ni_{27}Fe_{28}$	2	-21.7	2.4
$(9,0)$	$Ni_{27}Fe_{28}$	3	-22.6	1.6
$(5,5)$	Ni_{55}	1	-22.9	3.4
$(5,5)$	Ni_{55}	2	-23.4	2.9
$(5,5)$	Ni_{55}	3	-23.2	3.2
$(9,0)$	Ni_{55}	1	-20.2	4.1
$(9,0)$	Ni_{55}	2	-	-
$(9,0)$	Ni_{55}	3	-20.2	4.1

Table 2.6: Comparison of adhesion energies and carbon-metal bond energies of nanotube caps on metallic/alloy clusters in eV. The errors are standard deviations from averaging over the spots.

cap	particle	E_{ad} (eV)	E_{CM}/bond (eV)	E_{CM} (eV)
$(5,5)$	Fe_{55}	(-21.2 ± 0.0)	(0.43 ± 0.00)	4.3
$(5,5)$	$Ni_{12}Fe_{43}$	(-23.2 ± 1.1)	(0.30 ± 0.11)	3.0
$(5,5)$	$Ni_{27}Fe_{28}$	(-23.5 ± 1.0)	(0.27 ± 0.07)	2.7
$(5,5)$	Ni_{55}	(-23.2 ± 0.3)	(0.32 ± 0.03)	3.2
$(9,0)$	Fe_{55}	$(-20.7 \pm \text{-.-})$	$(0.40 \pm \text{-.-})$	3.6
$(9,0)$	$Ni_{12}Fe_{43}$	(-21.2 ± 0.9)	(0.33 ± 0.10)	3.0
$(9,0)$	$Ni_{27}Fe_{28}$	(-21.5 ± 1.1)	(0.30 ± 0.13)	2.7
$(9,0)$	Ni_{55}	(-20.2 ± 0.0)	(0.46 ± 0.00)	4.1

the structure and the other is the material. The mixture of two materials distorts the catalyst structure as they have different electronic structure resulting in different bond lengths and lattice constants. The adhesion energy shows no significant effect in dependence of the alloy composition.

The adhesion energies averaged on the three spots introduced in Figure 2.12, show no obvious trend, with $E_{ad}^1 = (-22.0 \pm 1.5)$ eV for the *square* spot 1, $E_{ad}^2 = (-23.0 \pm 1.4)$ eV for the *triangle* spot 2, and $E_{ad}^3 = (-21.7 \pm 1.0)$ eV for the *top* spot 3. We use this result and average over different spots when calculating adhesion energies as a function of the cap and alloy composition, see Table 2.6. The *triangle* spot shows the highest adhesion energy, but the adhesion energies calculated for the other spots are within the standard deviation of spot 2.

The average adhesion energies for the different compositions of Ni and Fe, show higher energies for the armchair cap than the zigzag cap, which we already described as the general trend of the calculations. We further observe an increase of adhesion energy for the NiFe alloy systems compared to the pure Ni and Fe clusters, see Table 2.6. The adhesion energy difference is not significant, however, it shows that the caps are slightly more stable on the NiFe alloy systems compared to the pure elemental catalyst clusters.

The excess/carbon-metal bond energies decrease non monotonically with increasing Ni content from Fe to Ni, see Table 2.6. The Ni cluster shows the highest excess

Table 2.7: Charge redistributions between the carbon nanotube caps and the metallic/alloy clusters. q_C^{rim} is the total charge shift of the carbon atoms at the rim of the nanotube cap, q_C is the total charge shift considering all carbon atoms of the cap, q_{Fe} is the total charge shift considering all iron atoms, and q_{Ni} is the total charge shift considering all nickel atoms of the catalyst particle.

cap	particle	q_C^{rim} (e)	q_C (e)	q_{Fe} (e)	q_{Ni} (e)
$(5,5)$	Fe_{55}	(4.15 ± 0.14)	(5.31 ± 0.72)	(-5.32 ± 0.72)	
$(5,5)$	$Ni_{12}Fe_{43}$	(4.08 ± 0.31)	(5.06 ± 0.52)	(-7.18 ± 0.65)	(2.12 ± 0.46)
$(5,5)$	$Ni_{27}Fe_{28}$	(3.67 ± 0.24)	(4.36 ± 0.36)	(-6.46 ± 0.20)	(2.10 ± 0.32)
$(5,5)$	Ni_{55}	(2.90 ± 0.06)	(3.32 ± 0.36)		(-3.33 ± 0.38)
$(9,0)$	Fe_{55}	$(3.26 \pm \text{-.-})$	$(4.68 \pm \text{-.-})$	$(-4.68 \pm \text{-.-})$	
$(9,0)$	$Ni_{12}Fe_{43}$	(3.39 ± 0.17)	(4.62 ± 0.22)	(-6.71 ± 0.42)	(2.09 ± 0.59)
$(9,0)$	$Ni_{27}Fe_{28}$	(2.99 ± 0.05)	(3.96 ± 0.02)	(-6.48 ± 0.29)	(2.52 ± 0.28)
$(9,0)$	Ni_{55}	(2.34 ± 0.08)	(3.11 ± 0.42)		(-3.11 ± 0.42)

energy for the $(9,0)$ cap. The lowest excess energy is observed for the $Ni_{27}Fe_{28}$, which also showed the highest adhesion energy, suggesting that the $Ni_{27}Fe_{28}$ alloy cluster yields the best growth conditions for the systems compared in this study.

2.3.3 Charge Redistribution

In this section we study the charge redistribution from the catalyst atoms to the edge atoms of the carbon nanotube cap, which was suggested to increase the reactivity of the edge atoms [194, 202] and induce an electric dipole moment, which was suggested to be relevant for the nanotube growth process. [203]

We study the charge population on the atoms in the rim of the cap and for the metal atoms in the catalyst particle, see Table 2.7. All charge values are excess charges compared to the ideal valence electron situation with 8 charges on each Fe atom, 10 charges on each Ni atom and 4 charges on each C atom. The metal atoms partially loose their electrons to the carbon atoms in the cap, with whom they form carbon-metal bonds. The amount of electron charge transfer to the carbon atoms depends on the catalyst element and on the bond type of the edge atom (zigzag or armchair). The charge on the rim of the armchair cap is higher than on the rim

of the zigzag cap. The trend weakens, but does not vanish, if the charge transfer per bond is considered, as the number of carbon-metal bonds is 10 for the armchair and only 9 for the zigzag cap. Considering the charge transfer to the whole cap and dividing through the number of bonds leads to an equal charge transfer to the armchair and zigzag caps per bond. The highest layer of the catalyst atoms supplies the major part of the electrons to the carbon nanotube cap. The carbon atoms of the cap that are not part of the rim have an average valence charge of about 4 e, with low deviations (below 0.1 e), which means that they do not take part in the charge redistribution process between the metal catalyst and the carbon cap. The electron charge redistribution is localised at the outer rim atoms of the cap that form the carbon-metal bonds. The localisation is slightly higher for the armchair edges with about 80% of the charge localised at the outer rim atoms compared to about 74% at the outer edge zigzag cap atoms, which is the reason why the armchair rim atoms yield a higher charge per bond.

The charge on the cap increases with Fe content and becomes maximal for the elemental Fe cluster. We observe the same behaviour at the rim, with the exclusion of the $(9, 0)$ cap on Fe, which, however, may be an artifact, as only one cap was considered on spot 3. The higher charge points to a higher reactivity on Fe compared to Ni, which likely leads to a faster growth rate on iron compared to nickel.

The Fe atoms do not only supply their electron charge to C, but also to the Ni atoms, see the charge transfer for the NiFe alloy systems in Table 2.7. The iron atoms loose about 5-7 electron charges. The nickel atoms either gain about 2-2.5 e in the alloy systems or loose about 3 e if Ni is the only element in the catalyst particle. The carbon atoms in the cap always receive electron charges, see Table 2.7. The total amount of charge received by the carbon cap is about 3-5 e. The amount of charge supplied to the rim is slightly lower with about 2-4 e.

Following from the reactivity argument, which results from the increased charge on the edge atoms, we can give a geometric argument for the preference of armchair over zigzag structures in the following. It follows from the number of edge sites. We consider the line density of edge sites, which corresponds to the number of edge sites divided by the circumference of the nanotube rim

$$\lambda = \frac{N_a + N_z}{\left|\vec{C}_h\right|} = \frac{n + m}{a_0 \cdot \sqrt{n^2 + nm + m^2}}, \qquad (2.22)$$

with $N_a + N_z$ the number of armchair and zigzag sites and $\left|\vec{C}_h\right|$ the circumference of the tube. The righternmost equation follows for straight rim configurations. Equation (2.22) leads to a line density of $\lambda_a = 2/\left(\sqrt{3}a_0\right)$ for $(n = m)$ armchair and $\lambda_z = 1/a_0$ for $(n \in \mathbb{N}^+,\ m = 0)$ zigzag tubes, for all other tubes $(n \neq m \neq 0)$ the value of the line density is between λ_a and λ_z $(\lambda_a > \lambda_c > \lambda_z)$. Considering the fact that a higher density of edge sites increases the number of carbon metal bonds, directly gives the argument why armchair tubes are prefered compared to zigzag tubes, as the number of electrons at the edge is increased, yielding a higher reactivity. An easy example is the case of the $(5,5)$ compared to the $(9,0)$ tube, which have nearly identical diameters, see Table 3.1. The number of edge sites on the $(5,5)$ tube is $N = N_a + 0 = 2m = 10$. The number of edge sites on the zigzag tube is $N = 0 + N_z = n - m = 9$. The increased number of sites with higher chiral angles leads to an enrichment of armchair/near-armchair tubes in nanotube samples from simple geometric reasoning. This geometric argument can also be translated to the growth rate of nanotubes, as the edge contains more possible sites for carbon atoms to dock, independent of addition sites the geometry already dictates that armchair tubes will have a faster growth rate than zigzag tubes, see also Section 2.2.2.

The charge transfer also induces a dipole moment in the nanotube cap and cluster system. The dipole moments for the clusters without the caps are about 1 Debye or lower, see Table 2.3 in Section 2.3.1. If a nanotube cap is connected to the cluster, however, the dipole moment significantly increases due to the charge transfer between the cap and the cluster, see Table 2.8. The highest electric dipole moment can be found with 14.7 Debye for the $(9,0)$ cap on spot 3 of the Fe cluster and the lowest electric dipole moment is 7.4 Debye for the $(5,5)$ cap on the Ni cluster. A decrease of the electric dipole moment is correlated with the Ni content in the composition of the catalyst particle, where higher Ni content leads to lower electric dipole moments. The zigzag caps have higher electric dipole moments compared to the armchair caps, which is likely a result of the weaker localisation of electron charge at the carbon-metal bond forming atoms for the zigzag caps. The difference of the average electric dipole moments of a certain catalyst composition between armchair and zigzag caps decreases with increasing Ni content, with the highest difference of 2.3 Debye on Fe and the lowest difference of 1.1 Debye on Ni. The electric dipole moments generate an electric field, which was suggested to increase

Table 2.8: Electric dipole moments Δ between the nanotube caps and metallic clusters in Debye. The last column of the table shows electric dipole moments for the armchair/zigzag caps averaged over the spots of a specific catalyst composition. The asterisks denote systems with at least one Klein-edge at the rim.

cap	particle	spot	Δ (Debye)	Δ_{avg} (Debye)
$(5,5)$	Fe_{55}	1	13.7	$\downarrow$
$(5,5)$	Fe_{55}	2	13.1	12.4
$(5,5)$	Fe_{55}	3*	10.3	$\uparrow$
$(9,0)$	Fe_{55}	1	-	$\downarrow$
$(9,0)$	Fe_{55}	2	-	14.7
$(9,0)$	Fe_{55}	3	14.7	$\uparrow$
$(5,5)$	$Ni_{12}Fe_{43}$	1	10.5	$\downarrow$
$(5,5)$	$Ni_{12}Fe_{43}*$	1	10.7	$\downarrow$
$(5,5)$	$Ni_{12}Fe_{43}$	2	9.9	10.6
$(5,5)$	$Ni_{12}Fe_{43}*$	2	12.5	$\uparrow$
$(5,5)$	$Ni_{12}Fe_{43}$	3*	9.5	$\uparrow$
$(5,5)$	$Ni_{12}Fe_{43}*$	3	10.5	$\uparrow$
$(9,0)$	$Ni_{12}Fe_{43}$	1*	12.2	$\downarrow$
$(9,0)$	$Ni_{12}Fe_{43}*$	1*	12.0	$\downarrow$
$(9,0)$	$Ni_{12}Fe_{43}$	2	13.0	12.1
$(9,0)$	$Ni_{12}Fe_{43}*$	2	11.5	$\uparrow$
$(9,0)$	$Ni_{12}Fe_{43}$	3	-	$\uparrow$
$(9,0)$	$Ni_{12}Fe_{43}*$	3	10.6	$\uparrow$
$(5,5)$	$Ni_{27}Fe_{28}$	1	10.4	$\downarrow$
$(5,5)$	$Ni_{27}Fe_{28}$	2	10.3	10.0
$(5,5)$	$Ni_{27}Fe_{28}$	3*	9.3	$\uparrow$
$(9,0)$	$Ni_{27}Fe_{28}$	1*	12.0	$\downarrow$
$(9,0)$	$Ni_{27}Fe_{28}$	2	11.5	11.4
$(9,0)$	$Ni_{27}Fe_{28}$	3	10.6	$\uparrow$
$(5,5)$	Ni_{55}	1	10.4	$\downarrow$
$(5,5)$	Ni_{55}	2	7.4	8.6
$(5,5)$	Ni_{55}	3	7.8	$\uparrow$
$(9,0)$	Ni_{55}	1	9.9	$\downarrow$
$(9,0)$	Ni_{55}	2	-	9.7
$(9,0)$	Ni_{55}	3	9.4	$\uparrow$

the landing probability of carbon atoms on the catalyst particle. [203] Therefore the landing probability on Fe is higher than on Ni, leading to a higher growth rate on catalysts containing Fe.

2.3.4 Comparison to the Experiment

In this section we derive chirality distributions based on the carbon-metal energies calculated in Section 2.3.2 and the formalism developed in Section 2.2.2 and compare our results to other theoretical and experimental studies.

There are two important results, that can be derived from the carbon-metal bond energies. First, the energies are important for the nucleation phase, as lower excess (carbon-metal bond) energies point to more stable cap structures leading to a higher formation probability. [162, 179] Second, a carbon addition barrier Δ_a can be derived from the carbon-metal bond energies for the growth phase, which was found to influence the chirality dependent growth rate. [2, 43, 168] Both phases determine the chirality of the carbon nanotube ensemble which is grown during the nanotube synthesis. The energy barrier for the carbon addition to an armchair rim was presented in Equation (2.9), $\Delta_a = 2 \cdot |E_z - E_a|$, where E_a is the energy of an armchair carbon-metal bond and E_z is the energy of a zigzag carbon-metal bond (E_{CM}/bond in Table 2.6), see Section 2.2.1. [43] We determine the barrier energies, by using $E_a = E_{CM}^{(5,5)}$/bond and $E_z = E_{CM}^{(9,0)}$/bond from Table 2.6 in Equation (2.9). The barriers result from small deviations between armchair and zigzag bond energies. Previous studies considered flat metallic surfaces as catalysts and tried to optimize the fit between catalyst surface and the edge of the cap. [179, 190] On a curved particle, as in this thesis, a perfect fit between the edge of the nanotube cap and the catalyst particle is impossible, which might increase the carbon-metal bond energies. The bond energies for armchair edges from Reich *et al.*, derived for a flat Ni surface, range from $E_a = 0.12$ eV to $E_a = 1.12$ eV, comparing well to our average value $E_a^{\mathrm{Ni}_{55}} = (0.32 \pm 0.04)$ eV. [179] The values for zigzag edges from Reich *et al.* range from $E_z = 0.16$ eV to $E_z = 1.44$ eV, which are also comparable to our value $E_z^{\mathrm{Ni}_{55}} = 0.46$ eV. [179] The caps connect to various spots on the catalyst clusters which increases the deviation of the bond energies and therefore renders the chiral selectivity even harder. The large standard deviations point to a general problem for *ab-initio* studies of carbon nanotube growth. The quantitative reproducibility is
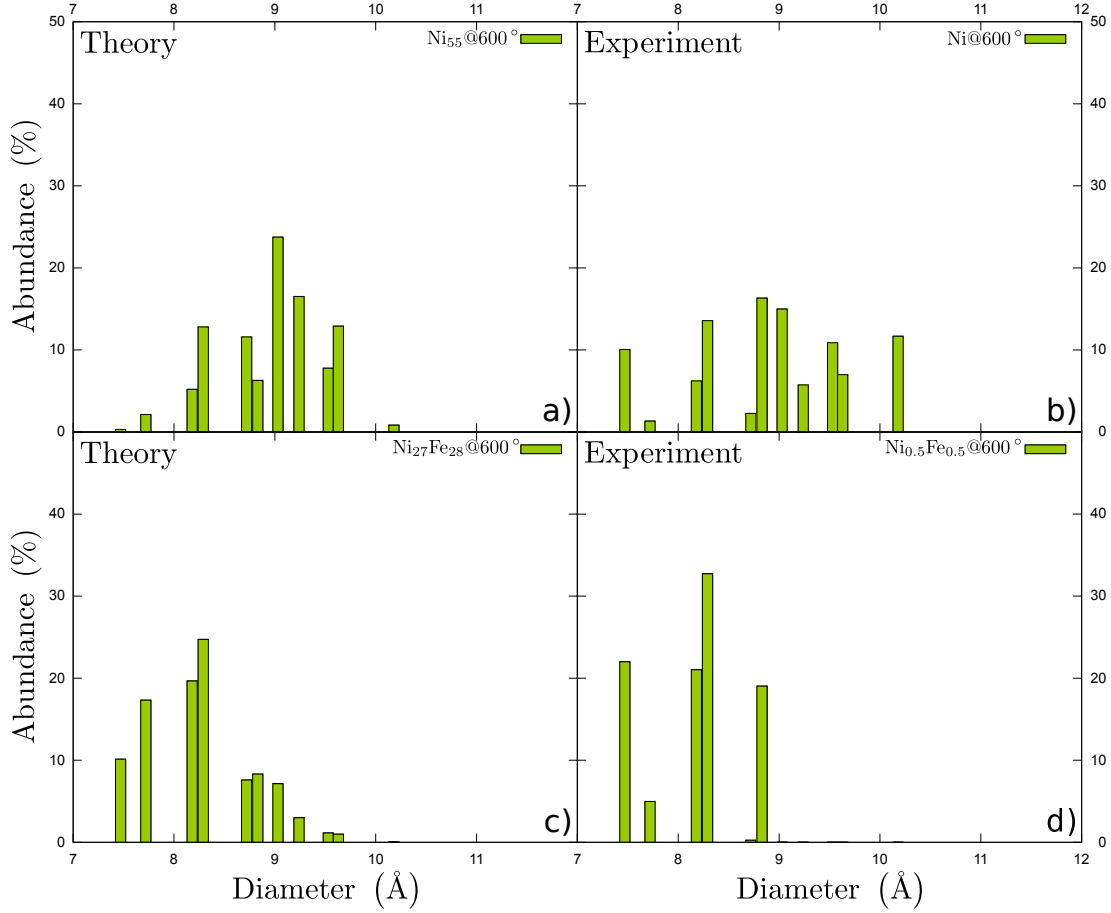
Figure 2.14: Normalized abundances in dependence of the tube diameter; a) $\left(\mu = 9.0\ \text{Å}, \sigma = 0.6\ \text{Å}\right)$ and c) $\left(\mu = 8.1\ \text{Å}, \sigma = 0.6\ \text{Å}\right)$ estimated from our theoretical growth model, see Equation (2.12); b) and d) from experimental photoluminescence data by Chiang *et al.* for nanotubes grown on Ni and on a nickel-iron alloy at 600° C. [3]

rather weak and it should be desired to test various systems with slightly different configurations/parameters. The energy barriers for the studied catalyst compositions are calculated with $\Delta_a^{\text{Fe}55} = 0.06$ eV, $\Delta_a^{\text{Ni}12\text{Fe}43} = 0.06$ eV, $\Delta_a^{\text{Ni}27\text{Fe}28} = 0.06$ eV, and $\Delta_a^{\text{Ni}55} = 0.28$ eV. The barriers are equal for all iron containing catalyst compositions, which might be coincidental. A study with more statistical relevance is desired to determine bond energies with smaller errors, leading to more reliable values for the carbon addition barriers.

The barriers can be inserted in Equation (2.12) to determine the chirality distributions, where the contribution of Γ (Equation (2.11)) is the same for all systems

that mainly contain iron atoms ($\delta_a = 0.45$ for $600°$ C) and only the gaussian diameter distribution factor changes the chirality distribution. This corresponds well to experimental results for NiFe alloy systems, where the chirality distributions derived from nanotube ensembles grown on catalysts with the composition $Ni_{0.27}Fe_{0.73}$ and $Ni_{0.5}Fe_{0.5}$ were found to be almost identical. [3] The Ni catalyst particle has a significantly larger barrier energy, leading to a suppression of armchair growth sites, as, *e.g.* $\delta_a = 0.024$ for $600°$ C.

Chiang *et al.* grew nanotubes on NiFe alloy systems to analyse the influence of the catalyst composition on the chirality distribution of a nanotube ensemble. [3, 127] They derived chirality distributions from photoluminescence data using calculated photoluminescence intensities. [3, 87] The chirality distributions satisfactorily fit the results derived from our growth model, see Figure 2.14. [3] Nanotubes grown on a Ni catalyst show a relatively wide chirality distribution with a peak for $(9,4)$. [3, 127] Especially important seems to be the diameter region of the nanotubes with 9.0 Å for $(9,4)$ and 8.8 Å for $(7,6)$ which have the highest intensity/abundance in the experimental study. [3] A slight descent of intensity occurs for chiralities with diameters that have smaller/higher tube diameters than about 9.0 Å, pointing to a lower number of catalyst particles, or other unknown effects, to grow tubes of that higher/lower diameters. Increasing the iron content of the composition of the catalyst particles until iron becomes the major component, leads to a significant narrowing of the chirality distribution to only a few chiralities at lower diameters, compared to the Ni catalyst particle, see Figure 2.14 c) and Figure 2.14 d). The fcc-lattice constant of iron $a_{\text{Fe}} = 3.45$ Å is lower than the lattice constant of nickel $a_{\text{Ni}} = 3.63$ Å, [1] which leads to smaller diameter alloy catalyst particles with increasing Fe content, which might be a reason for the shift of the chirality distribution to lower diameter nanotubes ($(7,6)$ and $(8,4)$ abundance increased), as the diameters of the grown nanotubes depend on the diameters of the catalyst particles on which they are grown in the tangential growth mode/under growth conditions close to thermodynamic equilibrium. [111, 114, 188] The experimental study, however, tried to obtain equal particle diameters through the preparation process, pointing to a dependence on the material instead of the catalyst diameters. [3] An enrichment of a small number of chiralities occurs, which is partially reproduced by our growth model, see Figure 2.14 c), as tubes with armchair growth sites have a higher

contribution on Fe containing particles. Our model was not intended to perfectly reproduce all abundances, however, it still gives a fair approximation to the experimental results and successfully reproduces the significant change in the chirality distribution by the change of the catalyst.

Besides the chirality distributions obtained from our growth model we also want to compare our charge transfer results to the literature. Wang *et al.* suggested that the short ranged charge distribution on nanotube edge atoms and catalyst atoms might be important for the chirality-selective growth of carbon nanotubes, as electron charges would increase their reactivity. [202] We observe an increase of electron charge on the carbon edge atoms with charge supply by the metal atoms in agreement with Wang *et al.*. [202] The average charge values on the carbon rim atoms, see Table 2.7, compare well to the values calculated by Wang *et al.* for, *e.g.*, the $(5, 5)$ nanotube cap on nickel we find an average value of 0.29 e which compares to the slightly higher values of Wang *et al.* between 0.31 e and 0.38 e. [202] To determine the effect of the charges on chirality distributions, we also put a focus on alloy systems. In alloy systems a charge distribution between two metallic species leads to an electron accumulation not only on the carbon edge atoms, but also on the nickel atoms. We find higher charges on armchair than on zigzag edges, which was suggested by Wang *et al.* to be used to influence the chirality. [202] The alloy composition has a significant effect on the charge distribution. We find an increase of electron charge on the carbon cap edge atoms from Ni to Fe with increasing Fe content in the alloy, pointing to an increased growth rate of nanotubes through increased reactivity of the nanotube edge atoms, which compares well to the higher growth rates found for iron compared to nickel. [74] Another relevant factor for the growth rate was found to be the metal d orbital energy. [274] The charge distribution patterns suggested by Wang *et al.* [202] resemble the edge structure of armchair and zigzag sites, see, *e.g.*, Section 2.1.1.

Theoretical studies can only model some aspects of the nanotube growth, neglecting other aspects, *e.g.*, the effect of Ostwald ripening, [177] that influence the chirality distribution as well. Further the chirality distributions determined in experiments have to be regarded with care as huge differences for the abundances of the chiralities might arise through the method used to determine the abundances, *i.e.* the intensity of a measured entity is not directly proportional to the abundance

of the tube. [87, 89, 261] Therefore we did not expect to obtain results that perfectly match our growth model, however, we see it as a success that the model correctly describes the qualitative features of the chirality selective growth process, which suggests, that the model might include some part of the truth to solve the puzzle of chirality selective growth.

Summary

In summary we calculated adhesion energies, excess energies, and electronic charge redistributions between carbon nanotube caps and NiFe alloy systems using density functional theory. The highest adhesion energies and lowest excess energies are found for the $Ni_{27}Fe_{28}$ alloy cluster, for both armchair and zigzag caps. The energy differences between armchair and zigzag, however, were found to be low. The curved form of the catalyst particle can be regarded as a constraint to the fit between the nanotube edge and the catalyst, which tends to lower the energy difference between armchair and zigzag caps. The small energy difference between the armchair and zigzag caps allows to derive a carbon addition barrier, which leads to a chirality distribution that compares satisfactorily with experimental results. The charge transfer between the cap and the catalyst particles increases with increasing Fe content, which further induces a dipole moment. The charge transfer to the armchair caps is higher than to the zigzag caps, in contrast to the electric dipole moment, which is higher for zigzag than for armchair caps and has a maximum of about 15 Debye on the iron particle. The excess electron charges on the carbon rim atoms increase with Fe content of the catalyst particle from (2.90 ± 0.06) e for Ni to (4.15 ± 0.14) e for Fe. The excess electron charges increase the reactivity of the carbon cap atoms, which explains why the nanotube growth rate on iron is higher than on nickel.

Die Vereinigung

Alles schien zu strahlen. Hermann sah sich selbst, aber war er es ? Oder war es sein Spiegelbild ? Heftig schüttelte es ihn hin und her. Es schien ihm so als würde er sich von aussen selbst beobachten können, als wäre er nicht mehr er selbst. Und dann erkannte er, dass er selbst strahlte. Ihm lief der Schweiss herunter, erst jetzt hatte er bemerkt, wie heiss es um ihn herum geworden war. Plötzlich tauchte in kurzer Entfernung neben ihm William auf. Dann riss es ihn wieder fort und es zog ihn zu Ernest zurück. Ernest hatte nicht mit der Anwesenheit von William gerechnet und stemmte sich mit aller Kraft von ihm weg, während er überrascht zur Kenntnis nahm, Hermann doppelt zu sehen. Hermann begriff erst jetzt, dass auch er einen Zwilling hatte, der ihm aber so sehr glich, dass sie ununterscheidbar waren. Hermann versuchte noch einmal sich von seinem Zwilling zu trennen, musste aber feststellen, dass er sich dafür von William und Ernest entfernen müsste. Dies führte dazu, dass er noch einige Male heftig hin- und herschwang bevor er sich schlussendlich seinem Schicksal ergab und seine Runden im vertrakten Muster wiederaufnahm, wobei es ihm sein Zwilling in gebührendem Abstand gleichtat.

3 Carbon Nanotube Bundles

After studying a possible path to enrich certain chiralities through the growth process in the previous chapter (Chapter 2), we now want to focus on bundles of carbon nanotubes, which is a common form of occurrence of nanotubes, as nanotube walls attract each other through van der Waals forces. [80] Before nanotubes can be effectively studied in experiments or used in devices, often, a first step is to separate the bundled tubes in individual tubes. [78]

In this chapter we will analyse the binding energies of various nanotube bundles under the aspect of their structure, in detail, the intertube orientation and chirality.

Section 3.1 presents the computational methods of our study on bundles of nanotubes.

In Section 3.2 [1] the general properties of bundles are studied, *e.g.*, the intertube distance and binding energy between tubes in a bundle. This is a starting point to understand the bundling and debundling processes of nanotubes, which is important for post processing separation methods and to understand under which conditions (*e.g.*, temperature, tube diameter) carbon nanotubes form bundles.

Compared to Section 3.3 [2] all previous sections considered the question of how nanotubes of a single chirality can be isolated. In the last part of the results of this thesis (Section 3.3) we study the electronic structure of monochiral bundles in dependence of the orientation of the tubes in the bundle, which serves as an example for the fascinating properties which can arise from monochiral nanotube samples. Therefore we first consider the symmetry of monochiral bundles. In the last section of this chapter we focus on the chiralities that experience a symmetry breaking through the change of the intertube orientation and the influence this symmetry break has on the electronic properties, *i.e.*, the band structure and density of states.

---

[1] The section is based on results prepublished in Reference [48].
[2] The section is based on results prepublished in Reference [46].

Before we present our results we give a short refresher about bundles of carbon nanotubes (see also Section 1.1.3) and a motivation, why it is worthwhile to study the binding energies of nanotube bundles. [3]

Nanotubes tend to form bundles, [80] this, *e.g.*, quenches their fluorescence. [78] However, isolated tubes are desired to study the extraordinary properties of nanotubes which are induced by their one dimensionality. [18] Therefore the bundles need to be destroyed and tubes have to be isolated. [78] This is achieved by the use of a combination of sonication or centrifugation and surfactants, *e.g.*, sodium dodecyl sulfate (SDS). [37, 118, 122, 275] These processes of bundling and debundling are not well understood. Especially the influence of the chirality of the tubes on the binding strength is interesting, as this might help to explain the selectivity of certain surfactants or debundling methods for certain chiralities. [91, 276–278] Section 3.2 adresses the question if the binding strength of the tubes depends on the chirality of the tubes.

It was suggested that the orientation of the tubes in a bundle can be compared to the stacking of graphene layers (*e.g.* bernal/AB stacked). [107, 279] The binding energy and intertube distance of AB and AA stacked graphene show a significant difference, pointing to a structural dependence of nanotubes in dependence of the intertube orientation. For nanotube bundles, we have to additionally consider the chirality of the tubes. The structural influence on the bundle properties is especially interesting for bundles of tubes that consist of only one chirality (monochiral bundles), as these have uniform properties, which are not averaged over mixed structural surfaces. The mechanical and electronic properties of bundles were already studied theoretically and experimentally. [65, 80, 83, 95, 99–101] However, there is little knowledge about the influence of the structure (chirality) of the tubes on, *e.g.*, the electronic structure of the bundle. [102, 107, 108] Monochiral bundles, have not been experimentally produced yet, even though their production is expected in the near future. [40, 41, 91, 122] The studies performed on bundles of nanotubes so far lack in the level of applied theory. Nanotube bundles and their electronic structure were studied with density functional theory within the local density approximation (LDA), which allows to consider the structure of the tubes

---

[3]The motivation is a modified version of the introductions of the papers published by the author of this thesis in References [46, 48].

in the bundle. [102, 107, 108] The local density approximation, however, fails in modeling the van der Waals interaction between tubes. [231] Another approach is to use continuum approximations involving the Lennard-Jones potential. [280–283] The continuum approximation, however, does not account for the specific configuration of the carbon atoms (structure). [280–283] Other approaches that consider the structure as well as the van der Waals interaction, do not reach the accuracy of density functional theory calculations. [284, 285] The van der Waals functional developed by Dion *et al.* was shown to be able to model bundles of carbon nanotubes in density functional theory, however, only one chirality $(8, 0)$ has been studied so far. [227, 238]

3.1 Computational Methods

This section [4] presents the computational methods for the calculations on bundles of carbon nanotubes presented in the following two Sections 3.2 and 3.3.

The calculations were performed with the trunk-version 387 of SIESTA, [216, 239] which supports calculations using the van der Waals density functional developed by Dion *et al.* (Section 1.2.3). [227, 233] The calculation used the norm-conserving carbon van der Waals pseudopotential presented in the Appendix (Section 5.1.2), which was generated by the scheme proposed by Troullier and Martins. [241] We used a double-ζ (DZ) basis set to describe the valence electrons. Cutoff radii for the s and p orbital of the carbon atoms were $r_s = 5.949$ Bohr and $r_p = 7.450$ Bohr. The mesh cutoff for the real-space integration corresponded to about 350 Ry. We used a k-point sampling between 1x1x10 and 1x1x14 k-points in the Monkhorst-Pack scheme [286] to calculate the total energies; the z-axis was chosen as the tube-axis. The calculation of band structures requires a better k-point sampling. Therefore the k point sampling for the band structure calculations of the bundled tubes were 20 k-points in x and y direction and 300 k-points in the z-direction, leading to a k point sampling of 20x20x300 k-points. The band structure was plotted for certain high symmetry directions of the hexagonal Brillouin zone, *e.g.* $AHLA\Gamma KM\Gamma$, see Figure 3.1 and Section 3.3.3. We used the whole k-sampled zone to derive the density of states at an electronic temperature of 20 K.

To derive a decent bundle geometry we first improved the geometry of isolated tubes. Therefore we optimized the lattice constant of isolated tubes by minimization of the total energy in dependence of the lattice constant. A geometry optimization was then performed within the conjugate gradient method to a maximal force tolerance of 0.04 eV/Å. The optimized coordinates of the isolated tubes were used to calculate the properties (binding strength and intertube distance) of the carbon nanotube bundles. We placed the relaxed tube in a hexagonal unit cell with periodic boundaries to simulate the trigonal bundle structure, see Figure 3.2 a) for the example of a bundle of $(6,6)$-tubes. All tubes are studied as oriented parallel to

---

[4] A major part of the methods section has been published by the author of this dissertation in References [48] and [46]. The calculations of the manuscripts [46, 48] were wrongly performed with a LDA pseudopotential. An erratum was published in Reference [47]. The data presented in this thesis were derived from calculations using the correct van der Waals pseudopotential presented in Section 5.1.2.
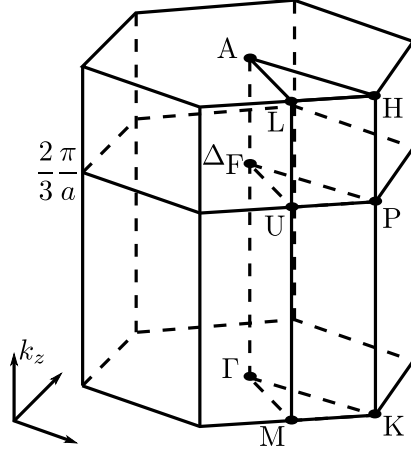
Figure 3.1: Hexagonal Brillouin zone with high symmetry points A, H, L, Δ_F, P, U, Γ, K, and M. The point Δ_F is found at about $\frac{2}{3}\frac{\pi}{a}$, and corresponds to the band intersection in metallic armchair carbon nanotubes. [93] The figure was inspired by the figure of Reference [107].

each other and perpendicular to the xy-plane, this is justified, as the formation of helical bundles is only expected for chiral tubes with low pitch angle χ due to high coiling energy costs for tubes with mediocre and high pitch angles. [103] The bundle has an infinite number of tubes (bulk-bundle/nanotube crystal). Our calculation is a good approximation for inner tubes (I in Figure 3.2 a)) of the bundle, as bundles have a trigonal structure where inner tubes I have six neighbors ($E_1, \ldots, E_6$). External tubes E_i have less than six neighbors, $e.g.$, three interacting neighbors ($e.g.$, E_1 interacts with E_6, I, E_2) for the structure presented in Figure 3.2 a). Triangle like interaction holes exist at the area where three tube surfaces meet ($e.g.$ between E_1, E_2 and I in Figure 3.2 a)), see Figure 3.2 b). The length of a side of the equilateral triangle of the triangle hole can be derived with

$$t = \frac{d + D}{2}, \tag{3.1}$$

with the tube diameter d and intertube distance D, see Figure 3.2 b) for a geometric derivation. Twice the length of the triangle side corresponds to the lattice constant of the hexagonal unit cell, in which the tube is enclosed, see Figure 3.2 b) right bottom. The lattice constant of the hexagonal unit cell is given by the diameter of the tube d plus the inter tube distance D. The intertube distance is independent
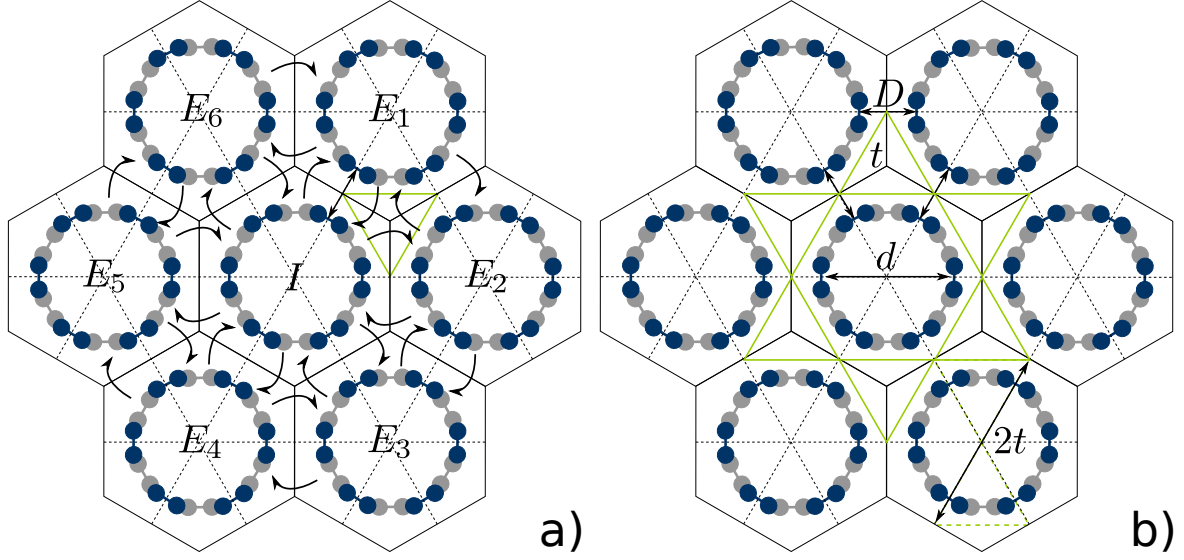
Figure 3.2: Sketch of a bundle of seven $(6,6)$-tubes based on References [46, 48]. The hexagon in the middle represents the unit cell for our bundle calculations. Lines connecting the middle points of the hexagons are added to better illustrate the symmetry of the system, which is trigonal. The upper carbon atoms of the tube are in blue and the lower carbon atoms are in gray; only one unit cell in z-direction is shown. a) Triangle holes (green) exist between three adjacent tubes, $e.g.$ E_1, E_2, and I. External tubes E_i interact with three neighbors, inner tubes I interact with six neighbors. b) Sketch of the triangle holes around the inner tube of a bundle of seven $(6,6)$-tubes. The tube diameter d is connected with the length of the side of the equilateral triangle of the triangle hole by $t = \frac{d+D}{2}$, as $2t$ correspond to the hexagonal lattice constant $d + D$ (geometric derivation from the figure). The hexagonal lattice constant consists of the tube diameter d and $2 \cdot \frac{D}{2}$.

of the tube diameter d (see Section 3.2.1). Therefore the size of the triangle hole will increase for an increase of the tube diameter and the interaction of neighboring tubes is reduced, as the distance between atoms of neighboring tubes is increased/a smaller fraction of atoms of the tube will have a significant contribution to the intertube interaction. Therefore the intertube binding energy per atom decreases to a constant, small value for larger diameter tubes (see Section 3.2.2). The triangle holes have been suggested as channels for doping with one dimensional chains of atoms to change the electronic properties of the system. [109]

The inner tube was rotated in steps of $1°$ or $5°$ starting from $0°$ to $60°$ in its unit cell for certain chiralities (see Section 3.3.1) to include effects that arise from the orientation of the tubes (details can be found in Section 3.3). [5] Therefore we did not perform a relaxation of the bundle structure, as this leads to energetically lowest states, which does not allow to consider energetically unstable orientations of the tubes of the bundle. As we did not relax the bundled structure some stress remains in the systems. The distortion caused by the bundling has little or no effect on the properties for tubes with diameters below 15 Å. [79, 102] A polygonalization/hexagonal deformation suggested [109] and observed [110] for large diameter nanotubes $(d \geq 25 Å)$ is negligible in our case, as the tubes studied in our calculation have diameters in the range of 6-17 Å, with the only exception of the $(20, 20)$ chirality which has a diameter of 27.8 Å. Special care is taken for the large diameter $(20, 20)$ bundle. The maximal forces for the atoms in the bundle range from 0.05 eV/Å up to 0.15 eV/Å for all the chiralities, except the $(8, 6)$ chirality which has a slightly higher maximal atomic force of 0.22 eV/Å. The low forces of 0.10 eV/Å observed for the $(20, 20)$ chirality point to only small effects of a possible hexagonal deformation induced by the bundling.

The difference between minimal total energy of the bundle and total energy of the isolated tube is regarded as total van der Waals energy. The minimal total energy of the bundle was derived by variation of the lattice constant of the hexagonal unit cell, which corresponds to a variation of the intertube distance. The total energy was plotted in dependence of the intertube distance/hexagonal lattice constant and a fourth order polynomial fit was conducted in the attractive region (potential well)

---

[5]The rotation of the inner tube corresponds to a simultaneous rotation of all tubes of the bundle as periodic boundary conditions were applied.
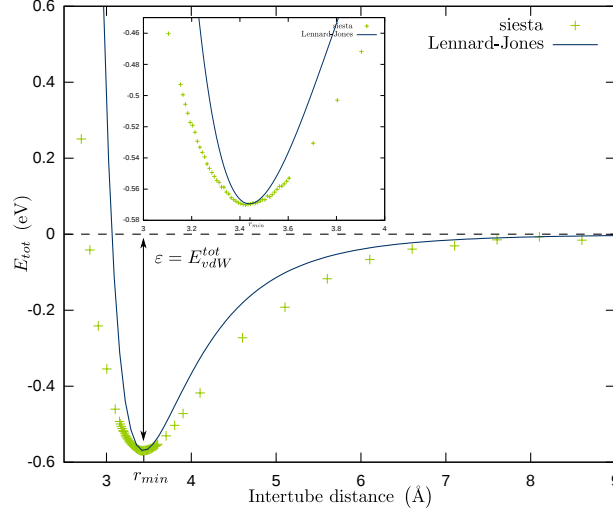
Figure 3.3: Total energy in dependence of the intertube distance calculated for a bundle of $(6,6)$ tubes. The energy is normalized to the energy of an isolated tube, which corresponds to "infinitely" distant neigboring tubes. The data points were obtained with SIESTA, see Section 1.2.4. A Lennard-Jones potential is plotted with ε and r_{min} parameters fitted to our data. The figure was inspired by Reference [46].

to find the intertube distance which minimizes the total energy, see Figure 3.3. A Lennard-Jones potential

$$V_{LJ} = \varepsilon \left[\left(\frac{r_m}{r} \right)^{12} - 2 \left(\frac{r_m}{r} \right)^6 \right], \tag{3.2}$$

with ε the depth of the potential and r_m the distance for the minimal energy, is plotted with ε and r_{min} parameters fitted to our data, see also Section 1.2.3. [85, 94, 230] The Lennard-Jones potential shows a smaller width in the attractive region compared to the calculated data points, see Figure 3.3. The total energy of the isolated tube was simulated by the calculation of very high intertube distances. Therefore the average total energy of two to three intertube distances of about 30-40Å was calculated, which showed only differences in energy on the order of 10^{-4} meV. Dividing the total van der Waals energy through the number of atoms of the unit cell yields the van der Waals energy per atom. Dividing the total van der Waals energy through the length of the unit cell yields the van der Waals energy per length. The intertube distance can be derived from the optimized xy/hexagonal unit

cell length by subtraction of the diameter of the tube. The optimized xy/hexagonal unit cell length was derived by minimization of the total energy in dependence of xy/hexagonal unit cell length. We derived the diameters of the tubes from the averaged values of the distances between the individual tube atoms to the center axis of the geometrically optimized tube.

3.2 Separation of Carbon Nanotube Bundles

In this section [6] we study the intertube distance (Section 3.2.1) and binding strength (Section 3.2.2) for inner tubes of carbon nanotube bundles in dependence of their structure (chirality) with van der Waals density functional theory. [227] We try to understand the bundling and debundling process of nanotube bundles and test whether an influence of chirality exists for the binding energy and/or intertube distance.

3.2.1 Intertube Distances

In this subsection we determine the intertube distance of monochiral carbon nanotube bundles as a function of chirality.

Table 3.1 presents an overview of the intertube distances between the tubes of the bundle in dependence of their chirality and diameter, as well as intertube binding energies; the values for chiralities marked by an asterisk correspond to average values for various orientations of the tubes in the bundle, corresponding to the way described in Dumlich and Reich [46], respectively Section 3.3.2. The orientation only affects achiral tubes which share symmetry operations with the bundle, *e.g.* $(6,6)$ with a C_6-axis. [46]

The intertube distance has no systematic dependence on chirality and diameter, which agrees with the major part of the literature. [65, 109, 281] The lack of chirality dependence results from the imperfect matching of the atomic structure of the neighboring tubes in the bundle. [83] Each inner tube I has six neighbors in the trigonal lattice, see Figure 3.2 a). This leads to an averaged interaction between neighboring tubes, as an optimal arrangement of all surfaces between neighboring tubes is not geometrically possible, except for achiral C_6-axis tubes, see Section 3.3.2 or Reference [83].

---

[6]A major part of the texts and results of this section, including the subsections, has been published by the author of this dissertation in Reference [48]. The calculations and analyses were performed by the author of this thesis under the supervision of one of the co authors of the paper and the thesis advisor Stephanie Reich. All parts that have not been calculated/analysed by the author of this thesis have been omitted. Further all calculations of the manuscript [48] were wrongly performed with a LDA pseudopotential. An Erratum was published in Reference [47]. The data presented in this thesis were derived from calculations using the correct van der Waals pseudopotential presented in Section 5.1.2.

Table 3.1: Intertube distances D and binding energies for bundles of tubes of various chiralities (n, m)/chiral angles (θ) (calculated using Equation (1.6)) and diameters d. For chiralities marked with an asterisk the values were derived by averaging over values for various orientations of the tubes in the bundle as presented in Dumlich and Reich [46], respectively Section 3.3.2. The diameters d are for the single tubes of the bundles, the intertube distance D is the nearest distance between the walls of two neighboring tubes of the bundle, E_{vdW}^{atom} is the intertube binding energy per atom and E_{vdW}^{length} is the intertube binding energy per length.

(n, m)	θ (°)	$d(\text{\AA})$	$D(\text{\AA})$	$E_{vdW}^{atom}(\text{meV})$	$E_{vdW}^{length}\left(\frac{\text{eV}}{\text{\AA}}\right)$
$(7, 0)$	0	5.73	3.32	34.4	0.221
$(8, 0)^*$	0	6.52	3.32	32.4	0.238
$(5, 5)^*$	30	7.03	3.35	30.3	0.241
$(9, 0)^*$	0	7.30	3.24	32.7	0.271
$(8, 2)^*$	10.9	7.43	3.32	29.8	0.251
$(7, 4)$	21.1	7.80	3.29	29.9	0.265
$(10, 0)$	0	8.11	3.33	28.2	0.263
$(6, 6)^*$	30	8.40	3.26	30.2	0.288
$(8, 4)$	19.1	8.55	3.29	28.4	0.276
$(11, 0)$	0	8.90	3.34	26.4	0.266
$(12, 0)^*$	0	9.69	3.33	25.6	0.283
$(7, 7)$	30	9.77	3.31	26.1	0.291
$(8, 6)$	25.3	9.80	3.32	26.2	0.293
$(8, 8)$	30	11.15	3.31	24.6	0.313
$(14, 0)^*$	0	11.30	3.31	24.2	0.316
$(9, 9)$	30	12.53	3.39	21.6	0.308
$(12, 6)^*$	19.1	12.76	3.29	23.6	0.344
$(10, 10)^*$	30	13.91	3.30	22.9	0.364
$(20, 0)$	0	16.05	3.29	20.5	0.376
$(12, 12)^*$	30	16.68	3.29	20.8	0.396
$(20, 20)$	30	27.75	3.29	15.8	0.504
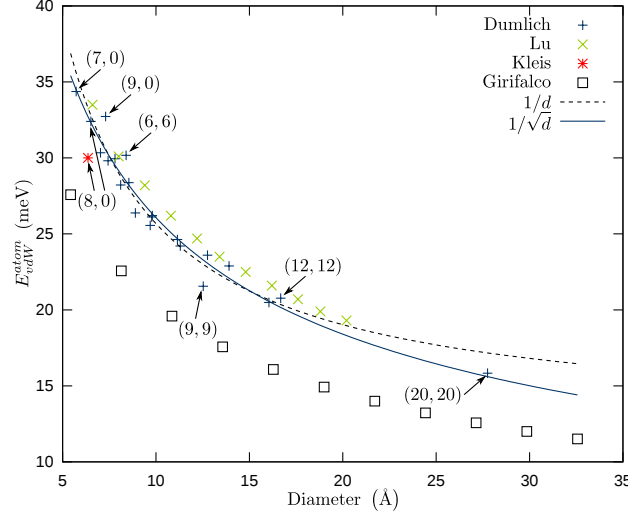
Figure 3.4: Calculated van der Waals energy per atom plotted over single tube diameter for various nanotube bundles. The calculated values are compared to literature values; for those that are available. [65, 238, 281] The chiralities that share symmetry operations with the bundle, *e.g.* $(6,6)$ and $(9,0)$, have slightly higher binding energies than expected from the fit, see Section 3.3.2. The $(12,12)$ value is only slightly higher, as the effect due to the shared bundle symmetry weakens with increasing diameters. The figure was reproduced from Reference [48] with new values.

The intertube distances vary in a small range of 3.24-3.39 Å independently of chiral angle and diameter with an average diameter of (3.31 ± 0.03) Å, see Table 3.1. Our results compare quite well to the intersheet distance for graphite of 3.35 Å (Ref. [280]) and also to intertube distances of 3.2-3.4 Å reported previously. [16, 65, 80, 103, 106]

3.2.2 Intertube Binding Energies

In this subsection we study the intertube binding energy of inner tubes of bundles for various chiralities. We start with the calculation and analysis of the intertube binding energy per atom.

Therefore we first calculate the binding energy per atom as described in Section 3.1. A $1/d$ and $1/\sqrt{d}$ fit is applied on the calculated van der Waals energy per atom, see Figure 3.4. The adjusted R^2 value[7], which is a measure of how good the model

---

[7]All adjusted R^2 values of this section were calculated using the *Mathematica* software pack-

fits the data, [287, 288] was found with $\bar{R}^2_{1/d} = 0.954$ for $1/d$ and for $1/\sqrt{d}$ it is $\bar{R}^2_{1/\sqrt{d}} = 0.960$. The fitted functions for both models are

$$E_{vdW}^{atom}\left(d\left(\text{Å}\right)\right) = \frac{133.0}{d} + 12.4 \ (\text{meV}), \tag{3.3}$$

and

$$E_{vdW}^{atom}\left(\sqrt{d\left(\text{Å}\right)}\right) = \frac{82.7}{\sqrt{d}} - 0.09 \ (\text{meV}). \tag{3.4}$$

Both models describe the correlation between the van der Waals energy per atom E_{vdW}^{atom} and d about equally well, with the $1/\sqrt{d}$-dependence being slightly better. The strongest deviations occur for chiralities that share symmetry operations with the bundle, see Section 3.3.2. Especially the $(6,6)$ and $(9,0)$, have too high energies, which is a consequence of their symmetry and averaging over various orientations of the tubes. Only one orientation was considered for the $(9,9)$ bundle, which lead to a value lower in energy than the fit would suggest. The intertube distance found for the $(9,9)$ bundle is higher than for all other chiralities, which leads to a lower intertube binding energy, see Table 3.1. The value of the $(6,6)$ tube in high symmetry configuration was found to be $E_{vdW}^{DZ} = 23.7$ meV/atom $\left(D = 3.44 \ \text{Å}\right)$ compared to the average value of $E_{vdW}^{(6,6)} = 30.2$ meV/atom $\left(D = 3.26 \ \text{Å}\right)$, which shows that the average value of the $(9,9)$ bundle can be expected to lie higher in energy if an average value of all orientations is considered, as the $(9,9)$ bundle shares symmetry with the bundle. For higher diameters the tube orientation effect on the binding energy diminishes, *e.g.*, for the $(12,12)$ bundle. A calculation considering a higher number of basis functions, *i.e.* double zeta polarized, lead to a binding energy of $E_{vdW}^{DZP} = 21.7$ (meV/atom) for the high symmetry configuration of the monochiral $(6,6)$ bundle. All binding energies can therefore be expected to be slightly (about 2 meV) lower in energy. [8]

Increasing the tube diameters increases the size of the triangle holes, reducing

---

age, utilising the Program routine "LinearModelFit". [287] The adjusted R^2 values $\left(\bar{R}^2\right)$ are defined as $\bar{R}^2 = 1 - (n-1)/(n-p)\left(1-R^2\right)$, with n the number of data points and p the number of parameters, [287] while R^2 is the coefficient of determination, see Bestimmtheitsmaß/Determinationskoeffizient R^2 on page 159 ff. in Reference [288].

[8] The shift is expected to be of about the same size for all studied bundles; considering the weak influence of chirality and diameter the change should be slightly smaller for larger diameter tubes and slightly larger than 2 meV for smaller diameter tubes with higher binding energies per atom.

the van der Waals binding energy per atom, see Figure 3.2 b). As a Gedanken-experiment, neglecting the effect of a possible polygonalization, [109, 110] we can estimate the minimal binding energy of the largest nanotubes and find a limiting energy needed for bundles of circular tubes to be stable. We get a rough estimate of $E_{min}^{SWCNT} =$ 8-14 meV/atom for the intertube binding energy of the largest single-walled carbon nanotubes, with diameters of at least 10 nm. [71, 72] The E_{min}^{SWCNT} value was extracted from the fitted functions in Equation (3.3) and Equation (3.4). In an experiment by Ma *et al.* it was observed, that some large diameter single-walled carbon nanotubes did not form bundles at room temperature, however, bundles were observed for small diameter tubes of up to 2 nm. [71] We find a binding energy per atom of $E_{min}^{bundle} =$ 18.4-19.1 meV/atom for tubes with diameters of 2 nm, which might be regarded as a threshold for these bundles to be stable at room temperature. The reason, why the large diameter tubes do not form bundles at room temperature might be the thermal energy $k_B T_{300°K}/2 \approx 13$ meV of each degree of freedom of the system, which is on the order of the binding energy per atom between large diameter tube bundles. We therefore expect the large diameter tubes reported by Ma *et al.* to bundle at low temperatures, *e.g.*, with the largest diameters becoming bundled at about $T_{bundle} \approx$ 160°-175° K.

Our results for the binding energies per atom show good agreement for the $(8,0)$-bundle with $E_{vdW}^{atom} =$ 32.4 meV compared to $E_{vdW}^{atom} =$ 30 meV [238] [9] and for armchair-bundles reported by Lu [65], see Figure 3.4.

The binding energies per atom of carbon nanotube bundles are lower than in graphite; Experimental values for the van der Waals energy per atom were derived from graphite with $\left(35_{-10}^{+15}\right)$ meV [280] and more recently (52 ± 5) meV. [289] The lower binding energy results from the packing of the tubes, which contain vast "empty" spaces (triangle holes) induced by the curvature of the tubes compared to

---

[9]Kleis *et al.* used the same van der Waals density functional and a non-self-consistent (post-GGA) implementation, in detail they replaced the GGA description of the correlation and used the electron density calculated in the GGA calculation for the evaluation of a nonlocal correlation energy that includes the "nature of the van der Waals binding". [227, 238] We use a self consistent approach [233] in our study, meaning that the density used to evaluate the nonlocal correlation energy is fully self-consistent. [236] The utilisation of a larger basis set, *i.e.* doubly zeta polarized, leads to an energy shift of about 2 meV lower in binding energy, which would lead to a value of about $E_{vdW}^{atom} =$ 30.4 meV for the binding energy of the $(8,0)$-bundle. Therefore the size of the basis set is regarded as the most important factor for the slightly higher binding energies we observe. The agreement between the results of the two methods concurs to previous results that the effect of the self-consistency is low. [236]
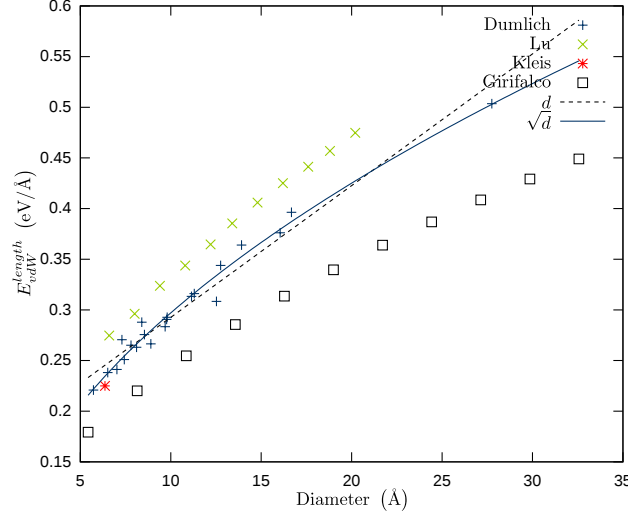
Figure 3.5: Van der Waals energy per length plotted in dependence of diameter for various nanotube bundles. The calculated values are compared to literature values; for those that are available. [65, 238, 281] The figure was reproduced from Reference [48] with new values.

the graphite systems, which are flat and have a more compact packing.

The next quantity of interest is the binding energy per length, calculated as described in Section 3.1. We find a linear or $\sqrt{d}$ dependence between diameter and the van der Waals energy per length, see Figure 3.5. The adjusted R^2 value, for d is $\bar{R}_d^2 = 0.963$ and for $\sqrt{d}$ it is $\bar{R}_{\sqrt{d}}^2 = 0.977$. The fitted functions for both models are

$$E_{vdW}^{length}\left(d\left(\text{Å}\right)\right) = 0.0130 \cdot d + 0.162635 \ \left(\text{eV/Å}\right), \tag{3.5}$$

and

$$E_{vdW}^{length}\left(\sqrt{d\left(\text{Å}\right)}\right) = 0.0978 \cdot \sqrt{d} - 0.0121 \ \left(\text{eV/Å}\right). \tag{3.6}$$

Both models succeed to describe the behavior for growing values of d as increasing tube diameters lead to increasing tube circumferences with more atoms (linear increase [290])/larger areas participating in the binding between the tubes. [10] There-

---

[10]The area density of the carbon atoms $\sigma = 2/A_{hex} = \frac{4}{\sqrt{3}a_0^2}$, with $a_0 = 2.461$ Å the graphene lattice constant, can be derived from the hexagonal unit cell area $A_{hex} = \frac{\sqrt{3}}{2}a_0^2$, [96] which includes two $\left(6 \cdot \frac{1}{3}\right)$ carbon atoms. Multiplication with the area of the cylinder/nanotube surface $A = \pi dl$, [96] where d is the tube diameter and l is the tube length, leads to the linear dependence between the number of carbon atoms and the diameter: $N_C = \sigma \cdot A = \frac{4\pi}{\sqrt{3}}\frac{l}{a_0^2} \cdot d \propto d$.

fore the binding energy per length increases with increasing diameter. However, the triangle holes increase with increasing tube diameter, see Section 3.1, which lowers the binding energy per atom and the effective interaction area, therefore the order of divergence is lowered. We only considered the small diameter regime here $\left(d \leq 25 \text{ Å}\right)$, for larger diameter tubes the structural transition to the polygonized/hexagonal structure has to be considered, that changes the expected dependence. [109, 110] The small diameter regime applies for all of our studied bundles, as even the deformation of the largest diameter tube bundle with $(20, 20)$ chirality is very small. The increase in binding energy per atom in comparison between the circular and hexagonal form is about 0.8 meV for the $(20, 20)$ bundle and negligible for all smaller tubes we studied, if the error of the calculation ± 0.2 meV/atom is considered, see Section 3.3.2 or the error induced by the use of the DZ basis set instead of a larger basis set.

Our result of $E_{vdW}^{length} = 0.238$ eV/Å shows good agreement for the $(8, 0)$-bundle compared to $E_{vdW}^{length} = 0.225$ eV/Å reported previously. [238] For the $(10, 10)$-bundle we derive a value of $E_{vdW}^{length} = 0.364$ eV/Å, which lies between $E_{vdW}^{length} = 0.286$ eV/Å (Ref. [281]) and $E_{vdW}^{length} = 0.377$ eV/Å derived for a bulk-bundle of tubes. [65]

In the following we want to give some details of previous studies and the differences to our study, especially why using the van der Waals density functional is superior compared to previous studies. In Reference [281] the interaction between the tubes was modeled by a continuum model and Lennard-Jones potentials with Lennard-Jones constants derived from graphite. The electron density was continuously/uniformly distributed on the surfaces of cylindrical tubes to model a bundle of nanotubes with various chiralities and same diameter. [281] A fit to their data lead to an energy function of $E_{vdw}^{length}(\sqrt{d\left(\text{Å}\right)}) = -0.0803\sqrt{d} + 9.39 \cdot 10^{-3} \left(\text{eV/Å}\right)$. [281] In Reference [65] the van der Waals interaction was modeled by Lennard-Jones pair potentials with parameters derived from a measurement on single crystal graphite. Each atom was assumed to be the center of a spherically symmetric electron distribution. [65] The structure of the nanotubes was obtained by conformal mapping of a graphite strip onto a cylindrical surface. [65] The total intertube interaction was minimized in dependence of the intertube distance to obtain a fit

---

Compare also to the number of atoms per length of tube, presented by Tersoff and Ruoff with $2\pi R/A_a$, where $A_a = 2.62$ Å is the area per atom and R is the tube radius. [109]

of $E_{vdW}^{atom}(\sqrt{d\,(\text{Å})}) = 87.0/\sqrt{d}$ (meV) for the van der Waals binding energy per atom. [65] In Reference [109] the atomic interaction within the tube is modeled with a valence-force model, the van der Waals interaction between the tubes is modeled by a Lennard-Jones $(6, 12)$ potential in a parametrization used to describe inter-layer forces in graphite and the "interactions are averaged along the atom columns parallel to the cylinder axis". [109] The small diameter regime in Reference [109] leads to a cohesive energy per atom of $E_{vdW}^{atom}(\sqrt{d\,(\text{Å})}) = 62.5/\sqrt{d}$ (meV), with the dependence derived by a consideration of the interaction between two parallel cylinders. [11] [109]

All three models, the continuum models and discrete atom-atom model, contain rough assumptions, in opposing directions. [65, 109, 281] Our van der Waals density functional calculation should lead to results which are closer to reality as non-uniformly distributed electron densities are used and the discrete atomic structure is considered. This agrees with the result that our values are between the values of the discrete and continuum model. Even though, we did not receive straight forward dependences, the adjusted R^2 values were slightly better for the $1/\sqrt{d}$-dependence [65] of the binding energy per atom and for the $\sqrt{d}$-dependence [281] of the binding energy per length, as previously suggested within the lower level of theory; This supports the previous suggestions. If we consider a larger basis set, a slight shift to lower binding energies per atom would be observable, shifting our curves closer to the middle between the previously published results. [65, 281]

An experimentally based value for the binding energy between two double walled carbon nanotubes of 4 nm diameter was derived with $E_{vdW}^{length} = 0.225$ eV/Å, [291] which is roughly comparable to our values for the van der Waals energy per length that lie between 0.221 eV/Å and 0.504 eV/Å. Another experimental value was derived more recently with peeling force spectroscopy by determining the interaction of a single-walled carbon nanotube with a highly oriented pyrolitic graphite surface (HOPG). [292] The peeling force spectroscopy study found a binding energy per length of (0.612 ± 0.044) eV/Å for a nanotube with a diameter of $d = (37 \pm 4)$ Å,

---

[11]The consideration allows to derive the cohesive energy per atom $E_a = -\frac{U_0 A_a}{2\pi\sqrt{R}}$, with $U_0 = U(b_0)$ where $b_0 = 3.42$ Å is the interlayer distance, $U(b) = \int V(b + \eta^2)\,d\eta$, with $\eta = x/R^{1/2}$ and $V(y)$ is the interaction per unit area between two graphite planes at separation y. [109] The interaction energy per length of tube is presented with $E(b) = U(b)R^{1/2}$. [109] For more details see Reference [109].

for which our values of both models are in the standard deviation (0.644 eV/Å for the d model and 0.583 eV/Å for the $\sqrt{d}$ model). [292]

Summary

In summary we presented van der Waals binding energies per atom/per length of various chiralities for inner carbon nanotubes of monochiral bundles. We find a diameter dependence for the van der Waals energy, meaning the curvature of the carbon nanotubes is the most important factor for the intertube binding strengths. The binding strengths between the tubes are independent of the chiral angle. However, this result applies only for inner tubes of the bundle, especially only for the intertube interaction, neglecting external influences like surfactants. Postprocessing methods generally try to separate the nanotubes using structurally selected molecules in a peeling like approach, tube by tube from the outside to the inside. [121] Therefore the results of our study cannot be directly applied to those postprocessing methods. An external tube would have to be studied to see the effect of the binding of its neighbors to it. Further its binding strength would have to be compared with other structurally preferable molecular systems (surfactants), to find a system with stronger binding to the tube than its neighboring tubes. As this would call for large unit cells with an even larger amount of atoms, we used an alternative approach to show, that the structure has a significant impact for the intertube binding. In the next section we will show that for certain chiralities a significant influence of the structure exists, which can be seen as an indicator for the possibility to use specific molecules to separate nanotubes of a desired chirality.

3.3 Monochiral Bundles

In this section [12] we study the binding energy, intertube distance and electronic structure of monochiral bundles of single-walled carbon nanotubes in dependence of the orientation of the tubes within the bundle to each other. The details on the computational methodology can be found in Section 3.1.

In Section 3.3.1 we study the symmetry of the bundles. We discuss the van der Waals energies and intertube distances of bundles in orientational dependence and the meaning of our results for mixed chirality bundles in Section 3.3.2. At the end of Section 3.3.2 we discuss the influence of using a local density approximation (LDA) pseudopotential instead of a van der Waals pseudopotential. In Section 3.3.3 we discuss the electronic properties, *i.e.* the electronic band structure and density of states around the Fermi level, for a selection of bundles $((8,0)$, $(9,0)$, and $(6,6))$ as a function of their tube orientation. We further discuss the effect of tube orientation for applications of monochiral bundles.

3.3.1 Symmetry of Bundles

Bundles were experimentally observed in triangular lattices that contain up to hundreds of tubes. [80, 293] A comparison between the stability of a nanotube bundle composed of $(6,6)$ tubes in tetragonal and hexagonal configuration has been performed using the local density approximation (LDA). [93] The study found that the hexagonal packing yields a better stability than the tetragonal packing for the case of a nanotube crystal. [93] We focus our study on large bundles, meaning bundles that have more than seven tubes. These bulk-bundles are expected to form trigonal structures based on the aforementioned experimental observations [80, 293] and theoretical calculations. [93] If bundles with less tubes are considered other preferable structures might be possible, see Section 1.1.3. A trivial example of two tubes leads

---

[12]A major part of the texts and results of this section, including the subsections, has been published by the author of this dissertation in Reference [46]. The calculations and analyses were performed by the author of this thesis under the supervision of the co author of the paper and the thesis advisor Stephanie Reich. All calculations of the manuscript [46] were wrongly performed with a LDA pseudopotential. An Erratum has been recently published in Reference [47] to account for the previous use of a LDA pseudopotential, which is discussed at the end of Section 3.3.2. The data presented in this thesis were derived from calculations using the correct van der Waals pseudopotential presented in Section 5.1.2.

to a parallel arrangement of the tubes for achiral tubes, [238] however, for chiral tubes it is possible to find helical structures, if the energy gain of the orientational alignment of the tubes is larger than the energy costs of bending the tubes into a helix. [103] If only two tubes are considered the influence of the arrangement of the surface atoms of the tubes to each other becomes important for the stability of the tube, [238] especially Figure 3 in Reference [238] shows the impact of the tube-tube orientation on the intertube distance of about 0.16 Å for two possible configurations of a pair of $(8,0)$ tubes (The intertube binding energy per length changes only by about 0.006 eV/Å). The $(8,0)$ tube has a fourfold symmetry following from the atomic positions around the circumference. [238] Kleis $et\ al.$ found a periodicity in the variation of the van der Waals binding energy with the relative rotation angle θ between the tubes, which lead to a reproduction of the binding energies for θ and $\theta + \pi$ at the sub meV level, following from the symmetry. [238] This can be seen as an indication for the importance of the structural fit between adjacent tubes and their relative tube orientation for the binding between the tubes, which makes it interesting for the bundling/debundling process of tubes. It was further observed that achiral C_{3n}-axis tubes $(n \in \mathbb{N}^+)$ have the largest interaction energy in bundles, as they can form close-packed bundles. [83]

In our calculations we model the triangular lattice of the bundle by a hexagonal unit cell, compare Figure 3.2 a) or Figure 3.6. A symmetry breaking occurs, if the individual tube and the bundle do not share all symmetry operations. The bundle structure has in general a D_{6h} symmetry, this means it has symmetry axes (2 C_6, 2 C_3, C_2, 3 C'_2, 3 C''_2), mirror planes (3 σ_v, 3 σ_d, σ_h), one inversion center (i), rotation-reflection axes (2 S_3, 2 S_6) and one identity element (E). [295] The tubes have symmetry operations depending on their chirality. [18] The level of symmetry breaking depends on the number of shared symmetry elements between the bundle structure and the chirality of the individual tube. [18] For example, a tube in the bundle has to have the same atom configuration every 60° on the circumference of the tube to share the full rotational symmetry with the bundle, see Figure 3.6. If the chirality and bundle structure share the rotation-reflection symmetry, we say that the chirality has a S_6-axis and symmetry breaking is lifted in high symmetry configurations ($e.g.$ 0° in Figure 3.6 a), which is a C_6 axis). The high symmetry configuration has all symmetry operations of the D_{6h} symmetry, especially mirror
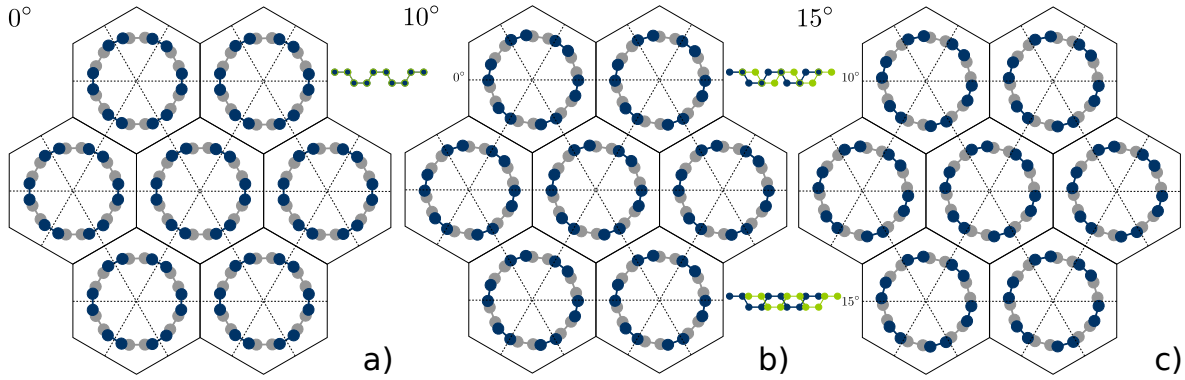
Figure 3.6: Ball and stick model of unit cells of a monochiral bundle of $(6,6)$ tubes. The color coding in the main pictures is blue for upper layer atoms and gray for lower layer atoms. For the insets the front tube atoms are in blue and the rear tube atoms are in green. a) $0°$ configuration; The inset shows the planar projection, corresponding to AA stacked graphite. b) $10°$ configuration; The inset shows the planar projection, corresponding to AB stacked graphite. [279] c) $15°$ configuration; The inset shows a configuration that can be described as an AA' configuration of graphite, [294] as one layer is relativly shifted by half a unit cell in the z-direction to the other.

planes.

The $0°$ configuration of the monochiral $(6,6)$ bundle can be identified with the AA stacking of graphite, [107] see the planar projection of the tube stack in the upper right part of Figure 3.6 a). A simultaneous rotation of all tubes to the $10°$ configuration can be identified as AB stacking graphite, [107, 279] see upper right part of Figure 3.6 b). A further rotation to the $15°$ configuration leads to a high symmetry configuration equivalent to AA' stacked graphite, [294] where the nanotube unit cells are relatively shifted by a half unit cell, see lower left part of Figure 3.6 c).

For our calculations we consider the $(6,6)$, $(12,12)$, $(9,0)$, $(12,0)$ and $(12,6)$ [13] S_6-axis chiralities. The $(12,0)$-tube structure, for example, has the same atomic configuration every $15°$ around the circumference (considering screw operations), as the full circumference contains $360°$ and there are 24 atom positions on the

---

[13]As we do not study helical configurations, the $(12,6)$ bundle is expected to show the same behavior as if it had no C_6/S_6-axis, as the symmetry is broken due to the helical structure of the individual $(12,6)$ tubes.

Table 3.2: Comparison of the intertube distance D, van der Waals energy per atom $|E_{vdW}^{atom}|$, and their variations $\Delta(D, E_{vdW}^{atom})$ for various chiralities (n, m), chiral angles θ and tube diameters d. The table presents the dependence of the fundamental properties on the orientation (rotation) of the tubes in the bundle with minimal and maximal values. Errors for intertube distances are ± 0.02 Å and for binding energies the errors are ± 0.2 meV/atom.

(n, m)	θ (°)	d (Å)	D (Å)	ΔD	$\|E_{vdW}^{atom}\|$ (meV)	ΔE_{vdW}^{atom}
$(8, 0)$	0	6.52	3.31-3.33	0.02	32.3-32.5	0.2
$(5, 5)$	30	7.03	3.34-3.36	0.02	30.2-30.5	0.3
$(9, 0)$	0	7.30	3.16-3.35	0.19	29.6-35.4	5.7
$(8, 2)$	10.9	7.43	3.31-3.32	0.01	29.7-29.9	0.2
$(6, 6)$	30	8.40	3.16-3.44	0.28	23.6-33.7	10.0
$(12, 0)$	0	9.69	3.26-3.41	0.15	24.1-27.1	3.0
$(14, 0)$	0	11.30	3.30-3.32	0.02	24.1-24.3	0.3
$(12, 6)$	19.1	12.76	3.28-3.31	0.03	23.4-23.7	0.3
$(10, 10)$	30	13.91	3.29-3.31	0.02	22.7-23.0	0.3
$(12, 12)$	30	16.68	3.22-3.38	0.16	19.2-22.0	2.8

circumference of the tube. This also means that the $(12, 0)$-tube has the same atomic configuration at the angles $0°/360°$, $60°$, $120°$, $180°$, $240°$ and $300°$, therefore it has a C_6-axis. To study the effect of intertube orientation on non S_6-axis chiralities we further study the chiral $(8, 2)$-bundle, the two zigzag bundles $(8, 0)$ and $(14, 0)$ and the two armchair bundles $(5, 5)$ and $(10, 10)$, which have nearly no common symmetry elements with the bundle structure. We use the same handedness for all the tubes, which, however, is only relevant for the chiral bundles $(12, 6)$ and $(8, 2)$, as the achiral tubes do not have a handedness.

3.3.2 Influence of the Tube Orientation

In this subsection we present the intertube binding energies and intertube distances of monochiral bundles of various chiralities in dependence of their relative intertube orientation.

The minimal values, maximal values and variation in dependence of the orientation of the tubes (rotation angle) for the intertube distance D and van der Waals energy per atom $|E_{vdW}^{atom}|$ for various chiralities and tube diameters are compared in
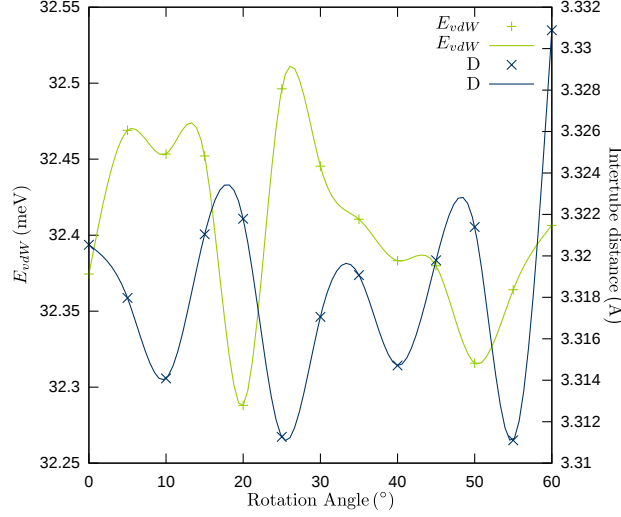
Figure 3.7: Van der Waals binding energy per atom E_{vdW} (green) and intertube distance D (blue) of a monochiral carbon nanotube bundle of $(8,0)$ tubes. The cubic spline fits (lines) are meant to serve as a guide to the eye. No clear pattern arises from the rotation of the tubes. The energy differences and intertube differences are of the size of the calculation error, which shows how small the effect of orientation is for the $(8,0)$ bundle.

Table 3.2. We only see small variations for the values of non S_6-axis chiralities, *e.g.* for the bundle of $(8,2)$-tubes. The intertube distance of the $(8,2)$-bundle varies by $\Delta D \approx 0.01$ Å and E_{vdW}^{atom} varies by ≈ 0.2 meV, meaning by less than 1%. Our results correspond well to results of the $(10,10)$-bundle, with our maximal difference between lowest and highest van der Waals energy per atom $\Delta E_{vdW} = 0.3$ meV and the activation barrier for rotations of $\Delta E_{vdW} = 0.15$ meV reported previously. [99] The activation barrier results from the reduction in symmetry from D_{2h} to C_{2h} due to rotation. [100] The properties of bundles made from non S_6-axis chiralities show hardly any dependence on orientation.

Comparing the intertube distance for the $(8,0)$ and the $(14,0)$ tube, we find a variation of less than 1%, whereas the tube diameter increases by ≈ 73 %. The van der Waals energy per atom decreases about 25 % for the same diameter comparison. The tube diameter has a strong influence on the binding strength, but does not influence the intertube distance, see also Section 3.2.1 and Section 3.2.2.

The van der Waals binding energy, as well as the intertube distance in dependence

of the orientation for the $(8,0)$ bundle shows no periodic pattern, see Figure 3.7. [14] A weak correlation can be extracted from the figure with higher van der Waals binding energies for smaller intertube distances, which is most likely an effect of the attractive r^{-6} potential. The periodic pattern with $\theta + \pi$ periodicity observed by Kleis for a pair of two $(8,0)$ tubes is broken through the trigonal symmetry of the bundle, which permits an optimal arrangement of the tubes. [238]

For the S_6-axis chiralities, we receive a radically different result for the dependence of the properties of the bundles on the rotation angle. We observe a variation of the bundle properties in dependence of the orientation for all achiral S_6-axis chiralities, compare Table 3.2. Starting with the zigzag chirality $(9,0)$; The intertube distance varies by $\Delta D \approx 0.19$ Å, corresponding to about 6 % variation, which is at least six times higher than the variation observed for non S_6-axis chiralities and about six to 19 times higher than the variation associated with tube diameter. Furthermore $\Delta E_{vdW}^{atom} \approx 5.7$ meV, corresponding to about 17 % variation, which is at least 17 times higher than the variation observed for non S_6-axis chiralities and only slightly smaller than the variation accounted to the tube diameter. For the $(12,0)$ chirality the orientational dependence on the properties weakens, with $\Delta D \approx 0.15$ Å ($\approx 5\%$) and $\Delta E_{vdW}^{atom} \approx 3.0$ meV ($\approx 12\%$). The rotation energy barrier $\Delta E_{vdW}^{atom} \approx 3.0$ meV corresponds well to the barrier of 3.0 meV previously reported by LDA calculations, [107] this is most likely a coincidence in the LDA calculation. The influence of the orientation on the bundle properties decreases with increasing tube diameter limiting the occurrence of the special properties of the S_6-axis bundles to small diameter nanotubes. We suppose that the increase in low distance interaction area lowers the influence of the local symmetry. The low distance interaction area increases through the reduced curvature of larger-diameter tubes.

The $(6,6)$ armchair bundle shows the strongest orientation dependence with $\Delta D \approx 0.28$ Å ($\approx 9\%$). The rotation energy barrier $\Delta E_{vdW}^{atom} \approx 10.0$ meV ($\approx 33\%$) is larger than ≈ 5.0 meV previously reported by LDA calculations. [107] Interestingly, the variations of the bundle parameters in dependence of the orientation are smaller for the zigzag bundles than for the armchair bundles of comparable tube diameter.

For S_6-axis bundles of chiral tubes (*e.g.* $(12,6)$) we see only a very small depen-

---

[14]The cubic spline fits presented in Figure 3.7 were performed with the option "with csplines" in the gnuplot software package. (http://www.gnuplot.info)
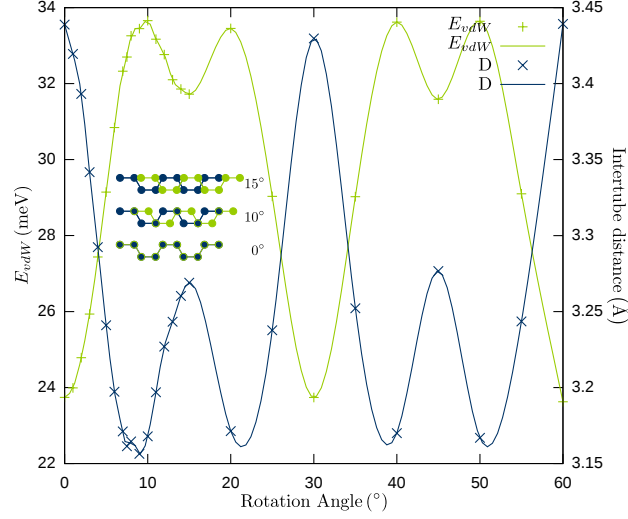
Figure 3.8: Van der Waals binding energy per atom E_{vdW} (green) and intertube distance D (blue) as a function of rotation angle for a bundle of $(6,6)$ tubes. E_{vdW} and D show a specific (Mexican-hat like) structure in dependence of the orientation of the tubes. The tubes of the bundle are rotated starting from the high symmetry position ($0°$, see Figure 3.6 a)). The lines are cubic spline fits and show symmetry breaking behavior. Global extrema occur every $10°$. Maximum binding energies occur at $10°+30°\cdot n$ and $20°+30°\cdot n$ with integer n. Global minima of the binding energy occur every $30°$ starting from $0°$ and local minima occur every $30°$ starting from $15°$. The binding energy and intertube distance are clearly anti-correlated. The insets show the three exemplary configurations of $0°$, $10°$, and $15°$ rotation of the tubes in the bundle, see also Figure 3.6.

dence on the van der Waals energy ($\Delta E_{vdW}^{atom} \approx 0.3$ meV ($\approx 1\%$)) and the intertube distance ($\Delta D \approx 0.03$ Å ($\approx 1\%$)). In chiral S_6-axis bundles alignment of neighboring tubes is impossible due to the handedness of chiral tubes. [83] Neighboring tubes with the same handedness have opposing surfaces with different handedness leading to mismatched surface structures of neighboring surface atom layers. [83] It is not possible to interchange handedness of neighboring tubes to generate alignment for all neighbors as neighbors with the same handedness remain caused through the trigonal structure of the bundle. [83]

The intertube distance of achiral S_6-axis nanotubes depends on their orientation and varies by as much as 9%. The binding strength of S_6-axis bundles is influenced through the variation of the intertube distance but at the same time by the orien-
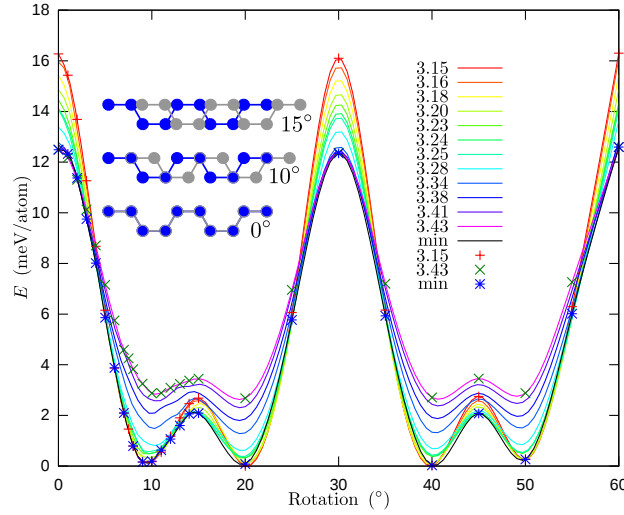
Figure 3.9: Total energy difference for various intertube distances as a function of rotation angle for a bundle of (6, 6)-tubes, with energies normalized to the highest binding energy. The total energy depends on the intertube distance as well as the orientation of the tubes. The inset shows a side view sketch of the atomic configuration for the three most interesting rotation angles, see Figure 3.6. The front tube has blue atoms, the tube in the back is in gray. The results were calculated with a wrong LDA pseudopotential, however, the difference to the results calculated with the van der Waals pseudopotential are small. Figure adapted from Reference [46].

tation; see Figure 3.8 or Figure 3.9. The influence of the intertube distance on the total energy has a strong impact for 0° (AA-stacked) and around 10° (AB-stacked), but is weaker around 4°, see Figure 3.9.

We use the example of the $(6,6)$-bundle to discuss the physical properties of a S_6-axis bundle. In this bundle the properties depend most strongly on rotational orientation. The van der Waals energy per atom of the $(6,6)$-bundle as a function of rotation angle shows symmetry breaking behavior, see Figure 3.8. Symmetry is initially D_{6h} (0°) and reduces to C_{6h} (loss of mirror planes) due to rotation. The high symmetry configuration of 0°, corresponding to AA stacking in graphite [107], is not energetically stable, see Figure 3.8. It has one of the highest intertube distances of 3.44 Å. The magnitude of the van der Waals energy increases up to a maximum at $\approx 10°$, corresponding to AB stacking in graphite [107], see Figure 3.8. This is in contrast to previous LDA findings, where a configuration about 2.5° off the AB stacking lead to a maximum at about 7.5°. [107] The configuration at 10° has one of the smallest intertube distances observed in our calculations with 3.17 Å. At 15° the rotation leads to an interesting configuration (AA') that has glide reflection planes, with a local binding energy minimum and a moderate intertube distance of 3.27 Å. Further rotations only reproduce the behavior that is contained in the first 15° rotation, see Figure 3.8. For other S_6 axis bundles the periodicity is changed, *e.g.* the periodicity of the $(12,12)$ bundle is contained in the first 7.5° rotation starting from the high symmetry configuration and for the $(9,0)$ bundle it is contained in a 10° rotation. [15] The 5° configuration of the $(9,0)$ bundle can be identified with the AA' stacked graphite configuration, while the 15° configuration can be identified with the AA stacked graphite configuration. All other configurations are intermediate between the two stackings, however, no AB stacked configurations can be obtained for the rotation of zigzag tubes, which is the reason for the lower rotation barrier compared to the $(6,6)$ bundle, as the AB configuration is the lowest energy configuration for carbon systems, see Table 3.2. [16]

---

[15]The number of "atom configurations" on the surface is $n + m$ for the armchair tubes and $2 \cdot n$ for the zigzag tubes. Another factor 2 is gained from the symmetry, see rotation of 0° to 15° in Figure 3.8, which is then reproduced for a rotation of 30° to 15°. Therefore for $(12,12)$ the 360° rotation is divided by 48 leading to a need of only a 7.5° rotation sampling, starting from the high symmetry position to sample the whole rotational behavior of the $(12,12)$ bundle.

[16]The non-AB stacking of zigzag tubes is not a mere artifact of the calculation. It is possible to shift the unit cells of the zigzag tubes which allows to create AB stacking, however, this

The error in our calculation can be estimated by comparing two identical configurations, *e.g.* $10°$, $20°$, $40°$, and $50°$ in Figure 3.8. We obtain an error of ± 0.2 meV/atom for the total energy. An error of ± 0.02 Å for the intertube distance can be estimated from the data in Figure 3.8.

The smaller activation barrier for rotations between $15°$ and $20°$ has a value of $\Delta E = 1.8$ meV/atom and the second, larger activation barrier for rotations between all orientations (*e.g.* between $0°$ and $10°$) is $\Delta E = 10.0$ meV/atom. Rotations of a solid made from C_{60} fullerenes were experimentally and theoretically found to be hindered below $T \approx 260$ K, implicating that a hinderance of rotations for nanotubes in a bundle might also be possible. [99, 296–298]

We want to discuss our findings and the implications for mixed chirality carbon nanotube bundles in the following paragraph. Most carbon nanotube bundles contain nanotubes of various chiralities (n, m). [83] The binding strength and intertube distance depend in general on the orientation of the tubes in the bundle. [83] But the orientational dependence of the aforementioned properties is suppressed by symmetry breaking induced by mismatch of the bundle and tube symmetry. [83] We can conclude from our calculations, that the properties of bundles of mixed chiralities have a negligible dependence on tube orientation, which confirms previous results of Reference [83]. This results from the non S_6-axis chirality observations, which show only a weak dependence on the orientation for the bundle properties (about or less than 1% variation in orientation dependence). The tube diameter (curvature) otherwise has a strong influence on the binding strength, but does not influence the intertube distance. Recently Crochet *et al.* and others succeeded in producing nearly mono chirality single-walled carbon nanotube bundles, highlighting the possibility to produce monochiral samples in the near future which would allow to experimentally test the theoretically predicted properties. [40, 41, 91, 122] Only the monochiral S_6-axis tubes preserve the symmetry in the higher symmetry configurations. Chiralities with S_6-axis can exhibit special properties, *e.g.* binding energy and intertube distance are influenced in orientational dependence in contrast to the tube diameter which only influences the binding energy. Considering real monochiral bundles at room temperature, however, we have to consider the effect

---

is limited through the trigonal bundle structure and the AB stacking cannot be achieved for every neighbor, compare also to the similar discussion on handedness in Reference [83].
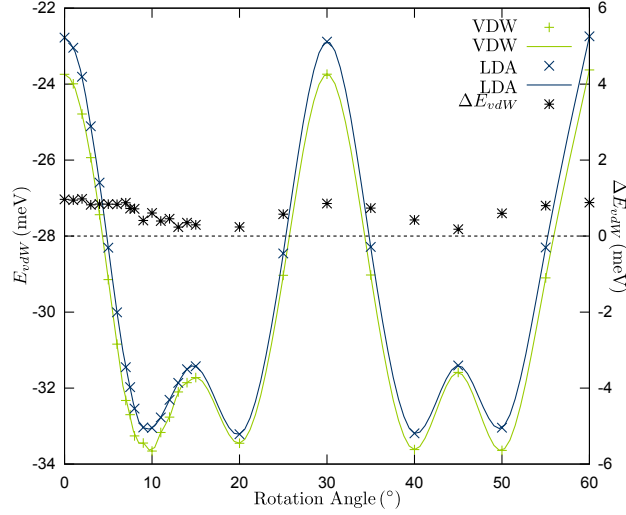
Figure 3.10: Comparison between the density functional theory calculations utilising a LDA pseudopotential (blue) and the van der Waals pseudopotential (green) (see Section 5.1.2), using the same van der Waals density functional. The differences (black) are only small in a range between 0.2 meV and 1.0 meV with a periodic pattern resembling the periodic pattern of the binding energy results. The difference of the binding energies per atom by using a larger basis set (about 2 meV) is higher than the difference by using the wrong LDA pseudopotential, especially no qualitative feature changes by wrongly using a LDA pseudopotential. The results of the calculation of the LDA pseudopotential were published in Reference [46]. An erratum including the new results considering the van der Waals pseudopotential has been published in Reference [47].

of rotations, vibrations, twists and defects which reduce effects of chirality.

At the end of this section we want to compare our results calculated with the van der Waals pseudopotential of Section 5.1.2 with the calculation using a local density approximation (LDA) pseudopotential ($r_{s,p} = 1.29$ a.u., $r_{d,f} = 1.50$ a.u.) published by us in Reference [46]. The comparison between the binding energies per atom shows only a small deviation between both pseudopotentials, see Figure 3.10 The deviations are between 0.2 meV and 1.0 meV with higher deviations for higher binding energy per atom. Therefore the deviation pattern resembles the pattern observed in dependence of the orientation. The pseudopotential therefore only has a weak effect on the results, especially if we compare the results presented in this thesis with
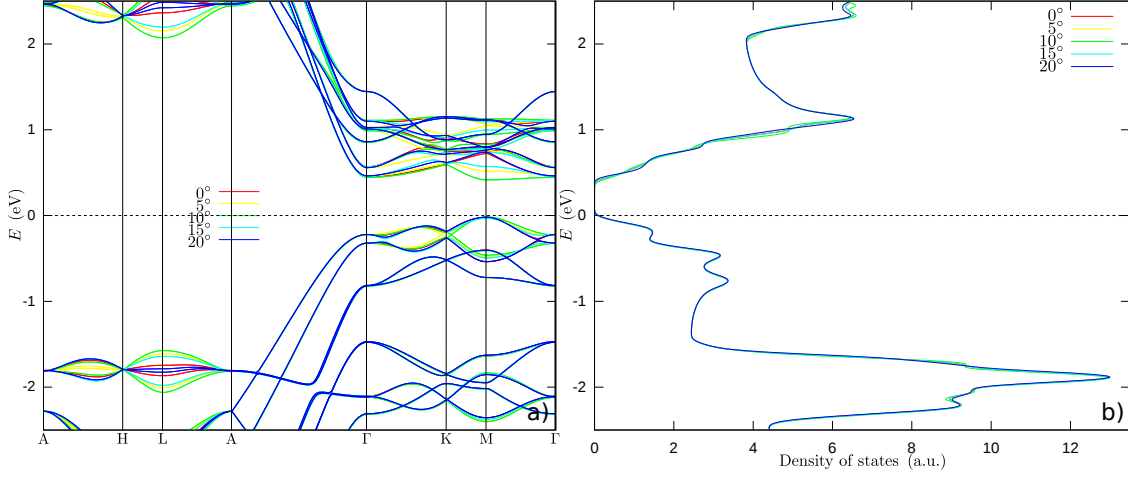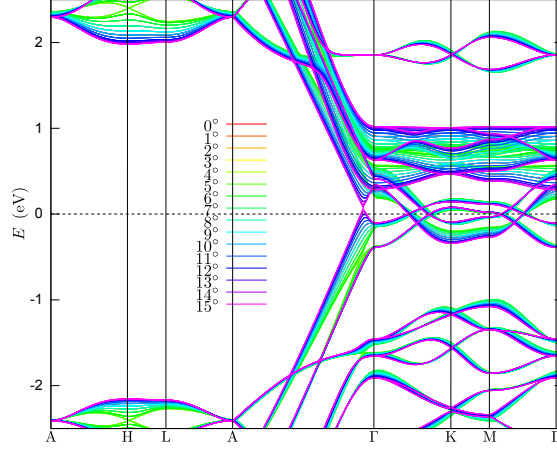
Figure 3.11: a) Band structure along high symmetry directions of a bundle of $(8,0)$-tubes rotated for configurations between $0\,^\circ$ and $20\,^\circ$ in rainbow colors. The band structure diagrams are normalized to the Fermi levels and high symmetry points of the $0\,^\circ$ configuration are shown. b) Density of states of the same bundle of $(8,0)$-tubes and the same configurations.

the results published in Reference [46] we find only small quantitative differences. The qualitative features remain the same independent of the pseudopotential used for the calculation, even though it is unphysical to use a pseudopotential generated from a LDA functional in a calculation using another (van der Waals, VDW-DRSLL, see Section 1.2.3) functional. A stronger dependence on the binding energy can be observed for the basis set, which lead to a change of 2 meV for the binding energy per atom in the AA stacked configuration of the $(6,6)$ bundle.

3.3.3 Electronic Structure of Monochiral Bundles

In this section we study the band structure and density of states in dependence of the inter tube orientation at the example of the monochiral bundles of $(8,0)$, $(9,0)$ and $(6,6)$ chirality. [17] At the end of the section we compare our results to other theoretical and experimental studies and discuss the influence of rotation barriers on the electronic properties of bundles.

---

[17]The figures for the $(6,6)$ bundle presented in this section are similar to the figures published by the author of this thesis in Reference [46], however, all figures were generated with the results of calculations performed with the van der Waals pseudopotential.

Figure 3.12: Band structure along high symmetry directions of a bundle of $(9,0)$-tubes rotated for configurations between $0\,^\circ$ and $15\,^\circ$ in rainbow colors. The band structure diagrams are normalized to the Fermi levels and high symmetry points of the $0\,^\circ$ configuration are shown. The $5\,^\circ$ configuration corresponds to AA' stack and the $15\,^\circ$ configuration corresponds to AA stacked graphite. All band structure diagrams in dependence of mutual intertube orientation are contained between the $5\,^\circ$ configuration and the $15\,^\circ$ configuration, with $e.g.$ the $0\,^\circ$ configuration leading to the same band structure as the $10\,^\circ$ configuration.

We start our discussion with the band structure and density of states of the $(8,0)$ bundle, as the orientation was shown to have only a minor effect on the intertube binding energy for bundles that share only few symmetry operations with the bundle structure, see Section 3.3.2. Therefore we expect the same behavior for the electronic properties. The band structure along the symmetry points presented in Figure 3.1 is nearly unaffected by the inter tube orientations for a large number of bands, see Figure 3.11 a). Especially close to the Fermi level only the $10\,^\circ$ configuration shows a slightly lower conduction band leading to a smaller energy gap. This can be seen in the density of states, which was derived from the whole Fermi surface, see Figure 3.11 b). The density of states shows no notable change for energies below the Fermi level. Above the Fermi level only minor changes occur, which lower the band gap and change the shape of the density of states. The small effect on the electronic properties for non S_6 axis bundles becomes apparent, if we study the effect of the orientation on S_6 axis bundles in the following.

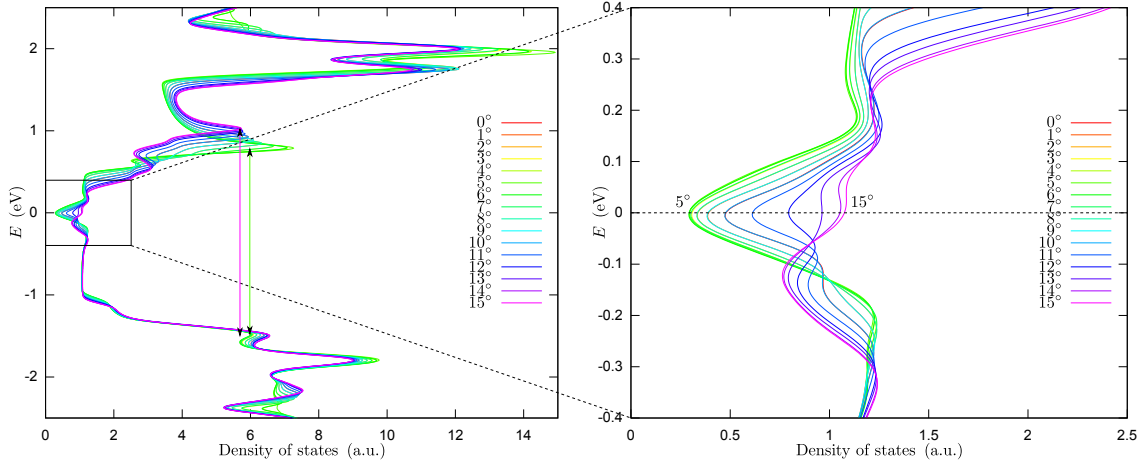The bundle of $(9,0)$-tubes shares the symmetry with the bundle as it contains a S_6

Figure 3.13: Density of states of a bundle of $(9, 0)$-tubes rotated for configurations between $0\,°$ and $15\,°$ in rainbow colors. The density of states diagrams are normalized to the Fermi levels. The inset (right panel) shows the shift of the pseudogap minimum with respect to the Fermi level (0 eV).

axis. The band structure in dependence of intertube orientation shows that all band diagrams are contained within the AA' $(5\,°)$ and AA $(15\,°)$ stacked configurations, *e.g.* the $4\,°$ configuration and the $6\,°$ configuration have the same band structure, see Figure 3.12. A band crossing develops along the AΓ-direction for the AA stacked configuration.

The band crossing for the AA stacked configuration is likely the reason for the increase of the density of states at the Fermi level for the AA configuration $(15\,°)$, see Figure 3.13 and its inset. The density of states at the Fermi level is 1.07 a.u. for the AA and 0.29 a.u. for the AA' configuration, meaning more than three times larger for AA compared to AA'. The valence side of the density of states shows only small changes in the density of states in dependence of the intertube orientation. The conduction side on the other hand shows some interesting shifts of the density of states maxima. The AA stacked configuration $(15\,°)$ has a maximum of 5.72 a.u. at 1.03 eV that is higher in energy than the AA' configuration $(5\,°)$ with 7.27 a.u. at 0.79 eV, while the valence side is nearly unchanged. This corresponds to a change in transition energy of about 0.26 eV with a transition energy of 2.53 eV for AA and 2.27 eV for AA'.

Band structure diagrams of a bundle of $(6, 6)$-tubes for orientations of $0\,°$ to $15\,°$
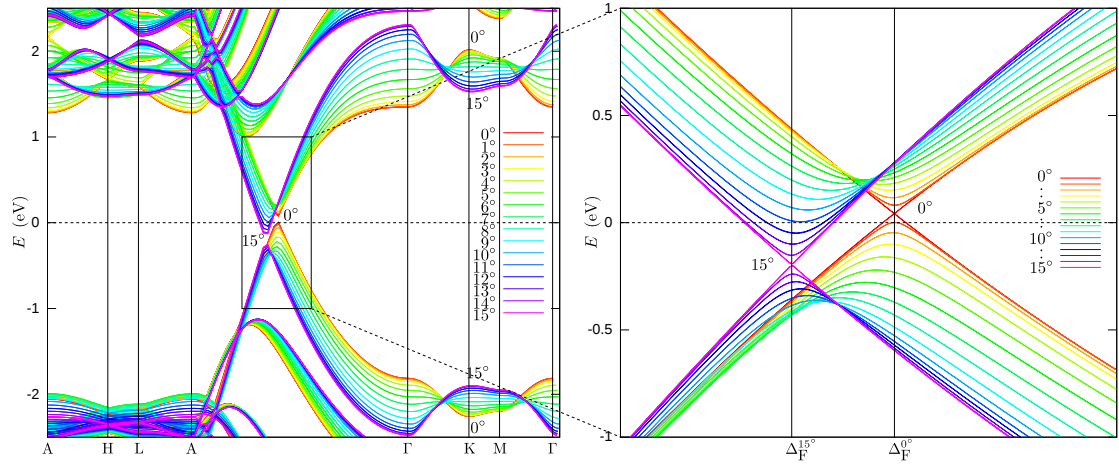
Figure 3.14: Band structure along high symmetry directions of a bundle of $(6,6)$-tubes rotated starting from its high symmetry configuration $0\,°$/AA to $15\,°$/AA' in rainbow colors. The band structure diagrams are normalized to the Fermi levels and the symmetry points for the AA configuration are used as labels on the x-axis. The inset shows a close up view of the crossing region with the symmetry points Δ_F (see Figure 3.1) for the AA and AA' configuration. The Δ_F points for the intermediate configurations are between those of the AA and AA' configuration.

show that the bands change their slope with orientation, see Figure 3.14. The valence band maximum and conduction band minimum shift in energy- and k-direction through the change in orientation. This is accompanied by a shift of the Fermi level, as can be seen between A and Γ (all Fermi levels were normalized to 0 eV). The Fermi levels shift through the changed electron density of each orientation, which result from a volume change induced by the orientational specific intertube distances. For the high symmetry configuration ($0°$, D_{6h}) the valence band and conduction band cross at about 42 meV above the Fermi level for the AΓ direction, [18] which corresponds well to the value of about 70 meV calculated within LDA calculations; the Fermi level is shifted compared to the Fermi level of the isolated tube. [102] The k_z value for the position of the valence band maximum and conduction band minimum is between $k_z = 0.606 \cdot \frac{\pi}{a}$ for $0°$ and $k_z = 0.669 \cdot \frac{\pi}{a}$ for $15°$, where $a = 2.515$ Å is the lattice constant along the tube. Our k_z-values correspond well to the value in isolated tubes of $k_z = 2/3 \cdot \frac{\pi}{a}$. [93] There is no band splitting in the orientations at $0°$ and $15°$ along the AΓ direction. The different parity of the bands allows the crossing of the bands. [93] An equivalent behavior has been reported in a DFT calculation within the local density approximation (LDA) for the $10°$ orientation corresponding to AB-stacked graphene for the HK-direction, [93] in contrast to the previous result we find a band gap of 0.24 eV for the AB-stack along the HK-direction. [19] The band splits by rotating the tubes of the bundle as little as $1°$ out of the high symmetry position, which opens up a band gap of $E_g = 79$ meV along the AΓ-direction. The mirror symmetry for rotated configurations is broken, which leads to anticrossing. The band gap increases until $\approx 7.5°$ ($E_g = 511$ meV) and then becomes smaller again until it vanishes at $15°$.

Comparing the behavior along the $\Delta_\mathrm{F}PU\Delta_\mathrm{F}$ path, see Figure 3.1, where Δ_F is chosen as the k_z vector where the valence and conduction band cross, we find a flattening of the valence band in dependence of the orientation, see Figure 3.15. The Fermi level touches the $1°$ valence band at Δ_F and is lower for all higher $°$

---

[18]The sampling in the main picture of Figure 3.14 is not good enough to resolve the crossing, therefore the inset of Figure 3.14 presents a detailed view around the crossing of the valence band and conduction band.

[19]Charlier *et al.* find band gaps of 0.46 eV along the AΓ direction and 0.25 eV along the ML direction, [93] comparing to our band gaps of 0.42 eV and 0.16 eV. As our study explicitly includes van der Waals interactions we believe our results to be more accurate than the results obtained using the LDA.
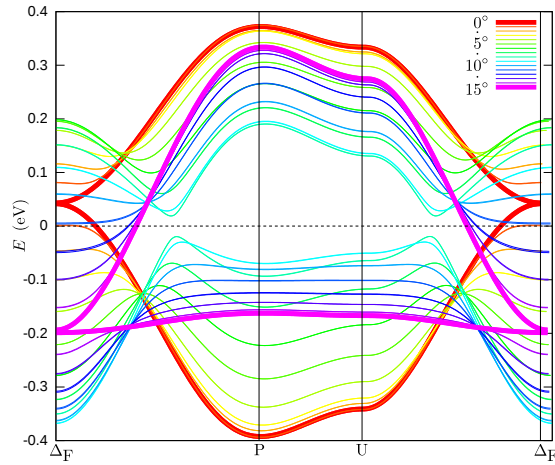
Figure 3.15: Band structure along high symmetry directions of a bundle of $(6,6)$-tubes starting from the position of the valence and conduction band crossing in rainbow colors, see also Figure 3.1 and inset of Figure 3.14. The band structure diagrams are normalized to the Fermi levels. The valence band flattens by a change in orientation while the influence on the conduction band is smaller and it mostly keeps its shape. The bands for the orientations with metallic behavior (without pseudogap) are highlighted (AA and AA' configuration).
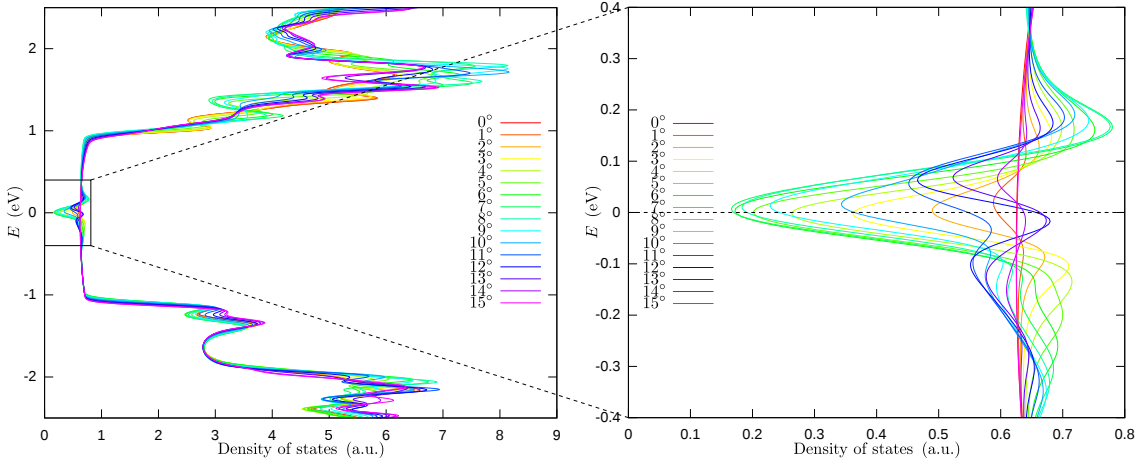
Figure 3.16: Density of states of a bundle of $(6,6)$-tubes rotated starting from its high symmetry position $(0\,°)$ in rainbow colors. The density of states diagrams are normalized to the Fermi levels. The inset (right panel) shows the shift of the pseudogap minimum with respect to the Fermi level (0 eV), which can also be observed in Figure 3.14.

orientations. However, starting with the $12\,°$ orientation the conduction bands dive below the Fermi level and increase the conductivity until the gap closes for the $15\,°$ orientation, see Figure 3.15.

The high symmetry configuration $(0\,°)$ shows metallic behavior while an increase of rotation angle of the tubes in the bundle increases a pseudogap, which is maximal at $\approx 7\,°$, see density of states in Figure 3.16. The pseudogap diminishes with further rotation until it closes at $15\,°$, which can be accounted for by the symmetry of the configuration. The $15\,°$ configuration looses mirror planes, but has glide reflection planes, which keeps the configuration metallic, see Figure 3.15 and inset of Figure 3.16. Furthermore, the density of states minima shift around the Fermi level from about -2.5 meV to 65 meV in dependence of the orientation, with the global minimum at 7.5 meV see right panel in Figure 3.16. The shift of the density of states maxima leads to increased density of states at the Fermi level for orientations between $12\,°$ and $14\,°$, compared to the metal like behavior of the $0\,°$ orientation. This can partly be understood by comparison to the behavior observed by the band structure, see the conduction band dive for these orientations below the Fermi level in the inset of Figure 3.14 and Figure 3.15.

The orientation has a smaller influence on the valence side than on the conduction

side of the band structure, see Figure 3.16, which has already been observed for the non S_6 axis bundles, see Figure 3.11 b). The first peak of the conduction side shifts between 1.03 eV and 1.20 eV through rotation; for certain rotation angles (*e.g.* 15°) it becomes a shoulder. The valence band shows only small variation for the first two peaks.

We conclude that the most exciting properties of S_6-axis bundles can be found in the band structure and density of states. Achiral S_6-axis bundles can be metallic. Certain orientations possess higher density of states at the Fermi level than the metallic configurations. The minima of the density of states meanwhile shift around the Fermi level in dependence of the orientation. The band structure shows a dive of the conduction band minimum below the Fermi level along the high symmetry direction accompanied by a pseudogap opening which closes again for higher symmetry configurations that have mirror planes or glide reflection planes.

We now want to compare our results to other theoretical studies. The density of states of the high symmetry and rotated $(10, 10)$ monochiral nanotube bundles were shown to have very similar behavior, which agrees with our results. [99, 100] For S_6-axis bundles, however, we find a strong coupling between the electronic states near the Fermi level and the rotational motion, which was suggested to lead to superconducting behavior previously. [99] In contrast to previous studies we find metallic behavior for achiral C_6-axis bundles (*e.g.* $(6, 6)$, $(12, 12)$) for multiple orientations. [107] We were able to show, that no energy gap, but a pseudogap opens in dependence of orientation of the tubes in the bundle in contrast to previous studies, which showed an energy gap in the density of states for AB-stacked $(6, 6)$ bundles as well as for the 8° orientation. [107] Furthermore our results show a shift of the density of state extrema around the Fermi level, corresponding to previously reported results. [100] We also find, however, an increased density of states at the Fermi level compared to the metallic configurations for certain orientations. We find good agreement in comparison to experimentally derived density of states with the general trend of pseudogaps opening due to the bundling. [101]

At the end of the section we want to discuss the influence of rotation barriers on the electronic properties of monochiral achiral S_6-axis bundles. At low temperatures, certain configurations of monochiral S_6-axis bundles can be stable, *e.g.* the orientation at $\approx 10°$ for the $(6, 6)$-bundle. At room temperature thermal energy is

likely to lead to rotations and vibrations of the tubes in the bundle. A complex electronic behavior is expected, as rotations (orientational changes) and absorption and emission occur time averaged over the experiment. Especially the slope flipping behavior and shifts of the bands lead to a further broadening [20] of the width of the bands, which further broadens the density of states and therefore also the optical-absorption bands for the S_6-axis chiralities. The high symmetry configuration (AA) with metallic behavior is the energetically most unstable configuration and therefore semi-metallic behavior has to be expected for bundles of metallic tubes. The $15°$ configuration (AA') is a local maximum in total energy and therefore also expected to be an unstable configuration, even though it is lower in energy than the high symmetry configuration. For larger diameter tubes the rotation barriers flatten, allowing metallic behavior in C_6-axis bundles of large diameter armchair tubes. The next paragraph summarizes our study on monochiral bundles.

Summary

In summary we presented van der Waals energies and intertube distances of various chiralities of carbon nanotube bundles in dependence of the orientation of the tubes inside of the bundle. Furthermore the electronic structure of the monochiral bundles was studied in dependence of the tube orientation. The intertube distances are between 3.2 Å and 3.4 Å but independent of orientation for non S_6-axis tubes. For tubes with a S_6-axis the orientation of the tubes in the bundle becomes a new degree of freedom to adjust the bundle properties. The intertube distance ($\pm$5-9%) as well as the binding strength ($\pm$12-33%) vary in dependence of the tube orientation. This dependence decreases with increasing tube diameter. Therefore this effect is mainly important for bundles composed of small diameter tubes with high curvature. The S_6-axis bundles experience rotation barriers for the tubes that are induced by the configuration of the atoms on the tube surfaces. The barriers can be as high as $\Delta E = 10.0$ meV/atom. Rotation barriers for tubes that do not share the trigonal symmetry of the bundle are less than $\Delta E = 0.3$ meV/atom. By variation of the orientation of the tubes in a $(6,6)$ C_6 axis bundle a pseudogap opens and increases until it vanishes at the next configuration which preserves the

---

[20]A broadening of the bandwidths has been reported for bundles previously, which was accounted to the broken symmetry. [102]

symmetry. C_6 axis bundles of armchair tubes have metallic configurations. Certain configurations (between AB and AA' stack) show a higher density of states at the Fermi level than the metallic configurations. As recent progress suggests monochiral C_6/S_6 axis bundles will soon be experimentally available, [40, 41, 91, 122] which will give access to study the newly arisen bundle properties.

Die Seele des Entdeckers

Denn was der Neugier noch verwehrt,
ist was der Mensch erst recht begehrt.
Das unentdeckte Wissen zu erlangen,
trotzt er allem Frust und Bangen.

Denn eines gibt dem Menschen Kraft,
es ist das Wissen,
das Neugier stets Erkenntnis schafft.

4 Conclusion

In this thesis we presented a step towards the explanation of chirality selective production of carbon nanotubes and studied the properties of bundles containing only tubes of one chirality with a focus on the tube orientation. In this section we want to summarize our results, draw conclusions, [1] and give an outlook for future research directions.

In order to study the growth process we presented a formalism to describe the hexagonal edges/rims of the carbon nanotubes that considers armchair and zigzag sites. We suggest that carbon nanotube edges that contains only hexagons have the lowest energy. From this idea we find three different addition sites ($aa.aa$, $aa.z$, and $z.z$) that keep the hexagon structure intact if carbon dimers are added. The addition of single carbon atoms is suggested to lead to an intermediate state with a pentagonal or dangling atom at the edge, which is transformed to a hexagon by a second carbon atom addition. The rotation barrier for a carbon dimer formed by a carbon atom at a pentagon edge was estimated with 2.91 eV, which allows to slowly incorporate carbon dimers in an atom by atom mechanism. The high barrier points to the preference of an intermediate dangling atom configuration at the nanotube edge, which is stabilized by metal atoms. This allows to obtain a faster growth rate.

Density functional theory calculations of various initial cap structures of nanotubes on an iron catalyst particle allow to study a possible preference for a rim structure on the catalyst surface. The adhesion and excess energy do not yield an energetically prefered structure, as the cap and catalyst structure deform each other to optimize their fit. Under realistic growth conditions the particle cannot be expected to be used as a template for a certain rim structure, which means that no chiral angle selectivity is expected from the fit between the rim of the cap and

---

[1] As we summarize our results we will not cite other works in this section, with the exception where we think it to be necessary and refer to the main text for the references.

the catalyst structure. The electron charge at the edge of the nanotube cap, which describes the polar binding character between the edge and the catalyst, was found to be an intrinsic property of the edge structure. The excess electron charge on a straight rim is about 0.6 e higher than on an angled rim. The electric dipole moment which results from the polar binding and a small charge transfer to the inner cap atoms reaches up to about 15 Debye for the angled rim and decreases slightly for the straight rim. One argument for the preference of a straight rim is the higher number of addition sites compared to the angled rim, which leads to a significantly higher growth rate.

We used geometric and energetical considerations to derive a growth rate factor Γ^*. The growth rate factor depends on a combination of external parameters, *i.e.* catalyst and temperature. Combining Γ^* with the results of Yuan *et al.* [74] allows to derive a growth rate which can be compared to experimental growth rates.

To derive the catalyst dependent parameters for Γ^* we calculated carbon nanotube caps on various catalyst compositions using density functional theory. The calculation was further used to calculate the formation energies of nanotube caps on catalysts of various compositions to determine if the structural fit between the catalyst and the nanotube cap lead to a preference of certain chiralities. We did not find any evidence for a preference of certain chiralities. Considering the catalyst composition we found the highest adhesion energies and lowest excess energies on the $Ni_{27}Fe_{28}$ alloy cluster, for both armchair and zigzag caps. A small energy difference can be derived between armchair and zigzag caps, which allows to derive a carbon addition barrier for the growth factor. A chirality distribution, which models the relative abundance of the tubes satisfactorily compares to the experiment.

The number of carbon edge atoms was found to decrease from armchair to zigzag edges, which could be used as a simple geometric argument for a lower growth rate of low chiral angle (zigzag) tubes, as the number of carbon atoms that can add at the edge is reduced compared to higher chiral angle (*e.g.* armchair) tubes.

We analysed the charge transfer/polar bonding between the caps and the catalysts and found an increasing charge redistribution with increasing iron content in the catalyst cluster, from (2.90 ± 0.06) e for Ni to (4.15 ± 0.14) e for Fe. The excess electron charges increase the reactivity of the carbon cap atoms, which explains why the nanotube growth rate on iron is higher than on nickel. The charge transfer to

the armchair caps was found to be higher than to the zigzag caps, in contrast to the electric dipole moment, which was found to be higher for zigzag than for armchair caps and has a maximum of about 15 Debye on the iron particle, corresponding to the mainly zigzag site containing angled rim of an armchair cap.

The second part of the thesis studied bundles of nanotubes of the same chirality. We presented the van der Waals binding energies per atom/per length of various chiralities. A diameter dependence was observed for the van der Waals energy. The binding strengths and intertube distances between the inner tubes were found to be independent of the chiral angle. The properties of the inner tubes that share symmetry operations with the bundle show a significant dependence on the intertube orientation. The intertube distance ($\pm$5-9%) as well as the binding strength ($\pm$12-33%) vary in dependence of the tube orientation for tubes that share the symmetry of the bundle, $e.g.$ tubes with a S_6-axis or C_6-axis. This dependence was found to decrease with increasing tube diameter. The change of binding strength with rotation leads to barriers, which can be as large as $\Delta E = 10.0$ meV/atom. Rotation barriers for tubes that do not share the trigonal symmetry of the bundle are smaller than $\Delta E = 0.3$ meV/atom. The fit of the structure between the tubes is found as the reason for the dependence of the binding strength and intertube distance on the intertube orientation. This can be regarded as an indication for the possibility to use specific molecules to separate nanotubes of a desired chirality.

The change of the orientation of the tubes in a $(6,6)$ bundle was found to open a pseudogap which increases with rotation to a maximum, decreases again and vanishes at the next configuration which preserves the symmetry. C_6 axis bundles of armchair tubes were found to have metallic character for certain configurations. A higher density of states at the Fermi level compared to the metallic configurations was found for stacks between AB and AA'.

In conclusion we were able to show evidence, that the abundance of carbon nanotubes of a certain chiral angle depends on their chirality dependent growth rate during the elongation phase, while the nucleation phase only determines the diameter of the tubes. The monochiral bundles which share symmetry operations with the bundle have fascinating electrical properties, which may become accessible in the near future. [40, 41, 91, 122]

The quest to understand the chirality selective growth of carbon nanotubes is still

going on. There is still a lot left to understand, *e.g.*, how the substrate influences the growth process, the height of the barriers for carbon addition to the nanotube on non-metal catalysts, or if the carbon addition to the nanotube edge is the rate limiting step. A large number of publications already discussed questions on the general nanotube growth process and also the chirality selective growth process has been discussed in many publications, see Section 1.1.4, however, one of the biggest problems is that the results do not converge to one general model. The nanotube formation process is very complex and the number of parameters is high, which makes it a hard task to include all of the parameters. The idea for a general growth model is to find the rate limiting step of the nanotube growth, which was recently suggested to be the carbon atom incorporation into the nanotube edge. [74] The verification of this result and further studying the addition process would be an interesting project for the future, as this step could possibly be used to model the system in a way to select desired chiralities.

In a future work it would also be interesting to study the properties of an external tube of a nanotube bundle, which interacts with only three or less neighbors and has a lower influence from its neighbors than an inner tube. The binding strength of external tubes is expected to depend on the structure, *i.e.* the chirality of the tubes.

At the end we want to thank you for spending the last few hours with the lecture of this thesis. We hope that it added to your knowledge on the chirality selection of carbon nanotubes and monochiral bundles.

May the enlightenment rise in those who seek the eternal wisdom provided by science.

Bibliography

[1] Heiko Dumlich. Growth of carbon nanotubes on catalytic metal particles. Master's thesis, Free University of Berlin, December 2009.

[2] Rahul Rao, David Liptak, Tonya Cherukuri, Boris I. Yakobson, and Benji Maruyama. In situ evidence for chirality-dependent growth rates of individual carbon nanotubes. *Nature Materials*, 11:213–216, 2012.

[3] Wei-Hung Chiang and R. Mohan Sankaran. Linking catalyst composition to chirality distributions of as-grown single-walled carbon nanotubes by tuning nixfe1-x nanoparticles. *Nature Materials*, 8:882–886, 2009.

[4] Sumio Iijima. Helical microtubules of graphitic carbon. *Nature*, 354:56–58, 1991.

[5] VL. Dumitrescu. *The Prehistory of the Balkans; and the Middle East and the Aegean world, tenth to eighth centuries B.C.* Cambridge University Press, 1982. Editors: John Boardman, I. E. S. Edwards, N. G. L. Hammond, and E. Sollberger; page 31-32.

[6] P. J. Lu, N. Yao, J. F. So, G. E. Harlow, J. F. Lu, G. F. Wang, and P. M. Chaikin. The earliest use of corundum and diamond, in prehistoric china*. *Archaeometry*, 47:1–12, 2005.

[7] L. V. Radushkevich and V. M. Lukyanovich. -. *Soviet Journal of Physical Chemistry*, 26:88–95, 1952.

[8] H. W. Kroto, J. R. Heath, S. C. O'Brien, R. F. Curl, and R. E. Smalley. C60: Buckminsterfullerene. *Nature*, 318:162–163, 1985.

[9] Harold Kroto. Space, stars, c60, and soot. *Science*, 242:1139–1145, 1988.

[10] W. Kraetschmer, Lowell D. Lamb, K. Fostiropoulos, and Donald R. Huffman. Solid c60: a new form of carbon. *Nature*, 347:354–358, 1990.

[11] Peter R. Buseck, Semeon J. Tsipursky, and Robert Hettich. Fullerenes from the geological environment. *Science*, 257:215–217, 1992.

[12] Jan Cami, Jeronimo Bernard-Salas, Els Peeters, and Sarah Elizabeth Malek. Detection of c60 and c70 in a young planetary nebula. *Science*, 329:1180–1182, 2010.

[13] Liming Yuan, Kozo Saito, Chunxu Pan, F.A. Williams, and A.S. Gordon. Nanotubes from methane flames. *Chemical Physics Letters*, 340:237–241, 2001.

[14] L. E. Murr, J. J. Bang, D. A. Lopez, P. A. Guerrero, E. V. Esquivel, A. R. Choudhuri, M. Subramanya, M. Morandi, and A. Holian. Carbon nanotubes and nanocrystals in methane combustion and the environmental implications. *Journal of Materials Science*, 39:2199–2204, 2004.

[15] L.E. Murr, J.J. Bang, E.V. Esquivel, P.A. Guerrero, and D.A. Lopez. Carbon nanotubes, nanocrystal forms, and complex nanoparticle aggregates in common fuel-gas combustion sources and the ambient air. *Journal of Nanoparticle Research*, 6:241–251, 2004.

[16] Sumio Iijima and Toshinari Ichihashi. Single-shell carbon nanotubes of 1-nm diameter. *Nature*, 363:603–605, 1993.

[17] D. S. Bethune, C. H. Klang, M. S. de Vries, G. Gorman, R. Savoy, J. Vazquez, and R. Beyers. Cobalt-catalysed growth of carbon nanotubes with single-atomic-layer walls. *Nature*, 363:605–607, 1993.

[18] Stephanie Reich, Christian Thomsen, and Janina Maultzsch. *Carbon Nanotubes*. Wiley-VCH, 2004.

[19] Riichiro Saito, Mitsutaka Fujita, G. Dresselhaus, and M. S. Dresselhaus. Electronic structure of graphene tubules based on c60. *Phys. Rev. B*, 46:1804–1811, 1992.

[20] Noriaki Hamada, Shin-ichi Sawada, and Atsushi Oshiyama. New one-dimensional conductors: Graphitic microtubules. *Phys. Rev. Lett.*, 68:1579–1581, 1992.

[21] Ryusuke Matsunaga, Kazunari Matsuda, and Yoshihiko Kanemitsu. Observation of charged excitons in hole-doped carbon nanotubes using photoluminescence and absorption spectroscopy. *Phys. Rev. Lett.*, 106:037404, Jan 2011.

[22] Ray H. Baughman, Anvar A. Zakhidov, and Walt A. de Heer. Carbon nanotubes–the route toward applications. *Science*, 297:787–792, 2002.

[23] Hongjie Dai. Carbon nanotubes: opportunities and challenges. *Surface Science*, 500:218, 2002.

[24] Philip G. Collins, Michael S. Arnold, and Phaedon Avouris. Engineering carbon nanotubes and nanotube circuits using electrical breakdown. *Science*, 292:706–709, 2001.

[25] Alan B. Dalton, Steve Collins, Edgar Munoz, Joselito M. Razal, Von Howard Ebron, John P. Ferraris, Jonathan N. Coleman, Bog G. Kim, and Ray H. Baughman. Super-tough carbon-nanotube fibres. *Nature*, 423:703, 2003.

[26] Mei Zhang, Shaoli Fang, Anvar A. Zakhidov, Sergey B. Lee, Ali E. Aliev, Christopher D. Williams, Ken R. Atkinson, and Ray H. Baughman. Strong, transparent, multifunctional, carbon nanotube sheets. *Science*, 309:1215–1219, 2005.

[27] Walt A. de Heer, A. Chatelain, and D. Ugarte. A carbon nanotube field-emission electron source. *Science*, 270:1179–1180, 1995.

[28] Yun Jung Lee, Hyunjung Yi, Woo-Jae Kim, Kisuk Kang, Dong Soo Yun, Michael S. Strano, Gerbrand Ceder, and Angela M. Belcher. Fabricating genetically engineered high-power lithium-ion batteries using multiple virus genes. *Science*, 324:1051–1055, 2009.

[29] Zeila Zanolli and J.-C. Charlier. Single-molecule sensing using carbon nanotubes decorated with magnetic clusters. *ACS Nano*, 6:10786–10791, 2012.

[30] Márcio D. Lima, Na Li, Mônica Jung de Andrade, Shaoli Fang, Jiyoung Oh, Geoffrey M. Spinks, Mikhail E. Kozlov, Carter S. Haines, Dongseok Suh, Javad Foroughi, Seon Jeong Kim, Yongsheng Chen, Taylor Ware, Min Kyoon Shin, Leonardo D. Machado, Alexandre F. Fonseca, John D. W. Madden, Walter E. Voit, Douglas S. Galvão, and Ray H. Baughman. Electrically, chemically, and photonically powered torsional and tensile actuation of hybrid carbon nanotube yarn muscles. *Science*, 338:928–932, 2012.

[31] Yahachi Saito. Nanoparticles and filled nanocapsules. *Carbon*, 33:979–988, 1995.

[32] Ting Guo, Pavel Nikolaev, Andrew G. Rinzler, David Tomanek, Daniel T. Colbert, and Richard E. Smalley. Self-assembly of tubular fullerenes. *J. Phys. Chem.*, 99:10694–10697, 1995.

[33] D.E. Resasco, W.E. Alvarez, F. Pompeo, L. Balzano, J.E. Herrera, B. Kitiyanan, and A. Borgna. A scalable process for production of single-walled carbon nanotubes (swnts) by catalytic disproportionation of co on a solid catalyst. *Journal of Nanoparticle Research*, 4:131–136, 2002.

[34] Michael S. Arnold, Samuel I. Stupp, and Mark C. Hersam. Enrichment of single-walled carbon nanotubes by diameter in density gradients. *Nano Lett.*, 5:713–718, 2005.

[35] Giulio Lolli, Liang Zhang, Leandro Balzano, Nataphan Sakulchaicharoen, Yongqiang Tan, and Daniel E. Resasco. Tailoring (n,m) structure of single-walled carbon nanotubes by modifying reaction conditions and the nature of the support of como catalysts. *J. Phys. Chem. B*, 110:2108–2115, 2006.

[36] Xiaolin Li, Xiaomin Tu, Sasa Zaric, Kevin Welsher, Won Seok Seo, Wei Zhao, and Hongjie Dai. Selective synthesis combined with chemical separation of single-walled carbon nanotubes for chirality selection. *J. Am. Chem. Soc.*, 129:15770–15771, 2007.

[37] Mark C. Hersam. Progress towards monodisperse single-walled carbon nanotubes. *Nature Nanotechnology*, 3:387–394, 2008.

[38] Lei Ding, Alexander Tselev, Jinyong Wang, Dongning Yuan, Haibin Chu, Thomas P. McNicholas, Yan Li, and Jie Liu. Selective growth of well-aligned semiconducting single-walled carbon nanotubes. *Nano Lett.*, 9:800–805, 2009.

[39] Avetik R. Harutyunyan, Gugang Chen, Tereza M. Paronyan, Elena M. Pigos, Oleg A. Kuznetsov, Kapila Hewaparakrama, Seung Min Kim, Dmitri Zakharov, Eric A. Stach, and Gamini U. Sumanasekera. Preferential growth of single-walled carbon nanotubes with metallic conductivity. *Science*, 326:116–120, 2009.

[40] Erik H. Haroz, William D. Rice, Benjamin Y. Lu, Saunab Ghosh, Robert H. Hauge, R. Bruce Weisman, Stephen K. Doorn, and Junichiro Kono. Enrichment of armchair carbon nanotubes via density gradient ultracentrifugation: Raman spectroscopy evidence. *ACS Nano*, 4:1955, 2010.

[41] Huaping Liu, Daisuke Nishide, Takeshi Tanaka, and Hiromichi Kataura. Large-scale single-chirality separation of single-wall carbon nanotubes by simple gel chromatography. *Nature Communications*, 2:309, 2011.

[42] Sergei M. Bachilo, Michael S. Strano, Carter Kittrell, Robert H. Hauge, Richard E. Smalley, and R. Bruce Weisman. Structure-assigned optical spectra of single-walled carbon nanotubes. *Science*, 298:2361–2366, 2002.

[43] Heiko Dumlich and Stephanie Reich. Chirality-dependent growth rate of carbon nanotubes: A theoretical study. *Phys. Rev. B*, 82:085421, 2010, Copyright Physical Review B, http://dx.doi.org/10.1103/PhysRevB.82.085421.

[44] Heiko Dumlich and Stephanie Reich. Rims of carbon nanotubes - influence of chirality. *Phys. Status Solidi B*, 247:2722–2725, 2010, Copyright Wiley-VCH Verlag GmbH & Co. KGaA. Reproduced with permission.

[45] Heiko Dumlich, John Robertson, and Stephanie Reich. Nanotube caps on fe, nife, ni nano particles: A path to chirality selective growth. *arXiv:*, 1305.0145:v1, 2013.

[46] Heiko Dumlich and Stephanie Reich. Nanotube bundles and tube-tube orientation: A van der waals density functional study.

Phys. Rev. B, 84:064121, 2011, Copyright Physical Review B, http://dx.doi.org/10.1103/PhysRevB.84.064121.

[47] Heiko Dumlich and Stephanie Reich. Erratum: Nanotube bundles and tube-tube orientation: A van der waals density functional study [phys. rev. b 84, 064121 (2011)]. *Phys. Rev. B*, 86:179905(E), 2012, Copyright Physical Review B, http://dx.doi.org/10.1103/PhysRevB.86.179905.

[48] Heiko Dumlich, Michael Gegg, Frank Hennrich, and Stephanie Reich. Bundle and chirality influences on properties of carbon nanotubes studied with van der waals density functional theory. *Phys. Status Solidi B*, 248:2589–2592, 2011, Copyright Wiley-VCH Verlag GmbH & Co. KGaA. Reproduced with permission.

[49] Carter T. White and John W. Mintmire. Fundamental properties of single-wall carbon nanotubes. *J. Phys. Chem. B*, 109:52, 2005.

[50] K. S. Novoselov, A. K. Geim, S. V. Morozov, D. Jiang, Y. Zhang, S. V. Dubonos, I. V. Grigorieva, and A. A. Firsov. Electric field effect in atomically thin carbon films. *Science*, 306:666–669, 2004.

[51] Erwin Riedel. *Anorganische Chemie.* de Gruyter, 6th edition, 2004.

[52] M. Jose-Yacaman, M. Miki-Yoshida, L. Rendon, and J. G. Santiesteban. Catalytic growth of carbon microtubules with fullerene structure. *Appl. Phys. Lett.*, 62:657–659, 1993.

[53] Diego A. Gómez-Gualdrón, Jin Zhao, and Perla B. Balbuena. Nanocatalyst structure as a template to define chirality of nascent single-walled carbon nanotubes. *J. Chem. Phys.*, 134:014705, 2011.

[54] Simon M. Sze and Kwok K. NG. *Physics of Semiconductor Devices.* Wiley & Sons, 3rd edition, 2006.

[55] Martin Dienwiebel, Gertjan S. Verhoeven, Namboodiri Pradeep, Joost W. M. Frenken, Jennifer A. Heimberg, and Henny W. Zandbergen. Superlubricity of graphite. *Phys. Rev. Lett.*, 92:126101, 2004.

[56] Michael Gegg. Van der waals interaction in bilayer graphene. Bachelor thesis, Freie Universität Berlin, April 2011.

[57] Marcus D. Hanwell, Donald E. Curtis, David C. Lonie, Tim Vandermeersch, Eva Zurek, and Geoffrey R. Hutchison. Avogadro: An advanced semantic chemical editor, visualization, and analysis platform. *Journal of Cheminformatics*, 4:17, 2012.

[58] Gary G. Tibbetts. Lengths of carbon fibers grown from iron catalyst particles in natural gas. *Journal of Crystal Growth*, 73:431–438, 1985.

[59] Daniel Ugarte. Curling and closure of graphitic networks under electron-beam irradiation. *Nature*, 359:707–709, 1992.

[60] S. Iijima, M. Yudasaka, R. Yamada, S. Bandow, K. Suenaga, F. Kokai, and K. Takahashi. Nano-aggregates of single-walled graphitic carbon nano-horns. *Chemical Physics Letters*, 309:165–170, 1999.

[61] J.W. Mintmire, D.H. Robertson, and C.T. White. Properties of fullerene nanotubules. *Journal of Physics and Chemistry of Solids*, 54:1835, 1993.

[62] G. Brinkmann, P. W. Fowler, D. E. Manolopoulos, and A. H. R. Palser. A census of nanotube caps. *Chemical Physics Letters*, 315:335–347, 1999.

[63] S. Reich, L. Li, and J. Robertson. Structure and formation energy of carbon nanotube caps. *Phys. Rev. B*, 72:165423, 2005.

[64] Teri Wang Odom, Jin-Lin Huang, Philip Kim, and Charles M. Lieber. Atomic structure and electronic properties of single-walled carbon nanotubes. *Nature*, 391:62, 1998.

[65] Jian Ping Lu. Elastic properties of carbon nanotubes and nanoropes. *Phys. Rev. Lett.*, 79:1297, 1997.

[66] M. Terrones, N. Grobert, J. Olivares, J. P. Zhang, H. Terrones, K. Kordatos, W. K. Hsu, J. P. Hare, P. D. Townsend, K. Prassides, A. K. Cheetham, H. W. Kroto, and D. R. M. Walton. Controlled production of aligned-nanotube bundles. *Nature*, 388:52, 1997.

[67] K. S. Novoselov, D. Jiang, F. Schedin, T. J. Booth, V. V. Khotkevich, S. V. Morozov, and A. K. Geim. Two-dimensional atomic crystals. *PNAS*, 102:10451–10453, 2005.

[68] A. H. Castro Neto, F. Guinea, N. M. R. Peres, K. S. Novoselov, and A. K. Geim. The electronic properties of graphene. *Rev. Mod. Phys.*, 81:109–162, 2009.

[69] Alexander A. Green and Mark C. Hersam. Colored semitransparent conductive coatings consisting of monodisperse metallic single-walled carbon nanotubes. *Nano Lett.*, 8:1417, 2008.

[70] E. Menéndez-Proupin, Ana L. Montero-Alejo, and J. M. García de la Vega. Ultrathin carbon nanotube with single, double, and triple bonds. *Phys. Rev. Lett.*, 109:105501, Sep 2012.

[71] Jie Ma, Jian Nong Wang, and Xiao Xia Wang. Large-diameter and water-dispersible single-walled carbon nanotubes: synthesis, characterization and applications. *J. Mater. Chem.*, 19:3033, 2009.

[72] Zhao Jun Han and Kostya (Ken) Ostrikov. Uniform, dense arrays of vertically aligned, large-diameter single-walled carbon nanotubes. *J. Am. Chem. Soc.*, 134:6018–6024, 2012.

[73] L. X. Zheng, M. J. O'Connell, S. K. Doorn, X. Z. Liao, Y. H. Zhao, E. A. Akhadov, M. A. Hoffbauer, B. J. Roop, Q. X. Jia, R. C. Dye, D. E. Peterson, S. M. Huang, J. Liu, and Y. T. Zhu. Ultralong single-wall carbon nanotubes. *Nature Materials*, 3:673–676, 2004.

[74] Qinghong Yuan, Hong Hu, and Feng Ding. Threshold barrier of carbon nanotube growth. *Phys. Rev. Lett.*, 107:156101, 2011.

[75] Qinghong Yuan, Zhiping Xu, Boris I. Yakobson, and Feng Ding. Efficient defect healing in catalytic carbon nanotube growth. *Phys. Rev. Lett.*, 108:245505, 2012.

[76] Léon Van Hove. The occurrence of singularities in the elastic frequency distribution of a crystal. *Phys. Rev.*, 89:1189–1193, 1953.

[77] J. W. Mintmire and C. T. White. Universal density of states for carbon nanotubes. *Phys. Rev. Lett.*, 81:2506–2509, 1998.

[78] Michael J. O'Connell, Sergei M. Bachilo, Chad B. Huffman, Valerie C. Moore, Michael S. Strano, Erik H. Haroz, Kristy L. Rialon, Peter J. Boul, William H. Noon, Carter Kittrell, Jianpeng Ma, Robert H. Hauge, R. Bruce Weisman, and Richard E. Smalley. Band gap fluorescence from individual single-walled carbon nanotubes. *Science*, 297:593–596, 2002.

[79] Rodney S. Ruoff, J. Tersoff, Donald C. Lorents, Shekhar Subramoney, and Bryan Chan. Radial deformation of carbon nanotubes by van der waals forces. *Nature*, 364:514, 1993.

[80] Andreas Thess, Roland Lee, Pavel Nikolaev, Hongjie Dai, Pierre Petit, Jerome Robert, Chunhui Xu, Young Hee Lee, Seong Gon Kim, Andrew G. Rinzler, Daniel T. Colbert, Gustavo E. Scuseria, David Tomanek, John E. Fischer, and Richard E. Smalley. Crystalline ropes of metallic carbon nanotubes. *Science*, 273:483–487, 1996.

[81] C. T. White, D. H. Robertson, and J. W. Mintmire. Helical and rotational symmetries of nanoscale graphitic tubules. *Phys. Rev. B*, 47:5485–5488, 1993.

[82] H. Kataura, Y. Kumazawa, Y. Maniwa, I. Umezu, S. Suzuki, Y. Ohtsuka, and Y. Achiba. Optical properties of single-wall carbon nanotubes. *Synthetic Metals*, 103:2555–2558, 1999.

[83] Ágnes Szabados, László P. Biró, and Péter R. Surján. Intertube interactions in carbon nanotube bundles. *Phys. Rev. B*, 73:195404, 2006.

[84] Brett I. Dunlap. Relating carbon tubules. *Phys. Rev. B*, 49:5643, 1994.

[85] C. Kittel. *Einführung in die Festkörperphysik*. Oldenbourg Verlag München Wien, 14th edition, 2006.

[86] Luca Ortolani, Florent Houdellier, Marc Monthioux, and Vittorio Morandi. Chirality dependent surface adhesion of single-walled carbon nanotubes on graphene surfaces. *Carbon*, 48:3050, 2010.

[87] Y. Oyama, R. Saito, K. Sato, J. Jiang, Ge. G. Samsonidze, A. Grüneis, Y. Miyauchi, S. Maruyama, A. Jorio, G. Dresselhaus, and M.S. Dresselhaus. Photoluminescence intensity of single-wall carbon nanotubes. *Carbon*, 44:873, 2006.

[88] A. Jorio, R. Saito, J. H. Hafner, C. M. Lieber, M. Hunter, T. McClure, G. Dresselhaus, and M. S. Dresselhaus. Structural (n,m) determination of isolated single-wall carbon nanotubes by resonant raman scattering. *Phys. Rev. Lett.*, 86:1118, 2001.

[89] Sebastian Heeg, Ermin Malic, Cinzia Casiraghi, and Stephanie Reich. Quantitative composition of a single-walled carbon nanotube sample: Raman scattering versus photoluminescence. *Phys. Status Solidi b*, 246:2740–2743, 2009.

[90] Maoshuai He, Bilu Liu, Alexander I. Chernov, Elena D. Obraztsova, Inkeri Kauppi, Hua Jiang, Ilya Anoshkin, Filippo Cavalca, Thomas W. Hansen, Jakob B. Wagner, Albert G. Nasibulin, Esko I. Kauppinen, Juha Linnekoski, Marita Niemelä, and Juha Lehtonen. Growth mechanism of single-walled carbon nanotubes on iron–copper catalyst and chirality studies by electron diffraction. *Chem. Mater.*, 24:1796, 2012.

[91] Carolin Blum, Ninette Stuerzl, Frank Hennrich, Sergei Lebedkin, Sebastian Heeg, Heiko Dumlich, Stephanie Reich, and Manfred M. Kappes. Selective bundling of zig-zag single-walled carbon nanotubes. *ACS Nano*, 5:2847, 2011.

[92] Richard M. Martin. *Electronic Structure Basic Theory and Practical Methods.* Cambridge University Press, 2004.

[93] J.-C. Charlier, X. Gonze, and J.-P. Michenaud. First-principles study of carbon nanotube solid-state packings. *EPL (Europhysics Letters)*, 29:43, 1995.

[94] J. E. Lennard-Jones. Cohesion. *Proc. Phys. Soc.*, 43:461, 1931.

[95] Min-Feng Yu, Bradley S. Files, Sivaram Arepalli, and Rodney S. Ruoff. Tensile loading of ropes of single wall carbon nanotubes and their mechanical properties. *Phys. Rev. Lett.*, 84:5552, 2000.

[96] I. N. Bronstein, K. A. Semendjajew, G. Musiol, and H. Mühlig. *Taschenbuch der Mathematik*. Verlag Harri Deutsch, 2001.

[97] Brian Ley. Diameter of a human hair. The Physics Factbook, (accessed via http://hypertextbook.com/facts/1999/BrianLey.shtml on Tue 06 Nov 2012 11:31:09 AM CET), 1999.

[98] Marc Bockrath, David H. Cobden, Paul L. McEuen, Nasreen G. Chopra, A. Zettl, Andreas Thess, and R. E. Smalley. Single-electron transport in ropes of carbon nanotubes. *Science*, 275:1922–1925, 1997.

[99] Young-Kyun Kwon, Susumu Saito, and David Tománek. Effect of intertube coupling on the electronic structure of carbon nanotube ropes. *Phys. Rev. B*, 58:R13314, 1998.

[100] Paul Delaney, Hyoung Joon Choi, Jisoon Ihm, Steven G. Louie, and Marvin L. Cohen. Broken symmetry and pseudogaps in ropes of carbon nanotubes. *Phys. Rev. B*, 60:7899–7904, 1999.

[101] Min Ouyang, Jin-Lin Huang, Chin Li Cheung, and Charles M. Lieber. Energy gaps in "metallic" single-walled carbon nanotubes. *Science*, 292:702, 2001.

[102] S. Reich, P. Ordejon, and C. Thomsen. Electronic band structure of isolated and bundled carbon nanotubes. *Phys. Rev. B*, 65:155411, 2002.

[103] David Teich, Gotthard Seifert, Sumio Iijima, and David Tománek. Helicity in ropes of chiral nanotubes: Calculations and observation. *Phys. Rev. Lett.*, 108:235501, 2012.

[104] Reinhard J. Maurer and Alexander F. Sax. Solvation of carbon nanotubes by aniline calculated with density functional tight binding. *Phys. Chem. Chem. Phys.*, 12:9893–9899, 2010.

[105] Wen Hui Duan, Quan Wang, and Frank Collins. Dispersion of carbon nanotubes with sds surfactants: a study from a binding energy perspective. *Chem. Sci.*, 2:1407–1413, 2011.

[106] Paul Delaney, Hyoung Joon Choi, Jisoon Ihm, Steven G. Louie, and Marvin L. Cohen. Broken symmetry and pseudogaps in ropes of carbon nanotubes. *Nature*, 391:466–468, 1998.

[107] Susumu Okada, Atsushi Oshiyama, and Susumu Saito. Pressure and orientation effects on the electronic structure of carbon nanotube bundles. *J. Phys. Soc. Jpn.*, 70:2345, 2001.

[108] H. J. Liu, Y. W. Wen, L. Miao, and Y. Hu. Structural and electronic properties of bundles of 4 Å carbon nanotubes. *Nanotechnology*, 18:445708, 2007.

[109] J. Tersoff and R. S. Ruoff. Structural properties of a carbon-nanotube crystal. *Phys. Rev. Lett.*, 73:676–679, Aug 1994.

[110] M. J. López, A. Rubio, J. A. Alonso, L.-C. Qin, and S. Iijima. Novel polygonized single-wall carbon nanotube bundles. *Phys. Rev. Lett.*, 86:3056–3059, 2001.

[111] Yiming Li, Woong Kim, Yuegang Zhang, Marco Rolandi, Dunwei Wang, and Hongjie Dai. Growth of single-walled carbon nanotubes from discrete catalytic nanoparticles of various sizes. *J. Phys. Chem.*, 105:11424–11431, 2001.

[112] Feng Ding, Arne Rosen, and Kim Bolton. Molecular dynamics study of the catalyst particle size dependence on carbon nanotube growth. *J. Chem. Phys.*, 121:2775–2779, 2004.

[113] Yiming Li, Shu Peng, David Mann, Jien Cao, Ryan Tu, K. J. Cho, and Hongjie Dai. On the origin of preferential growth of semiconducting single-walled carbon nanotubes. *J. Phys. Chem. B.*, 109:6968–6971, 2005.

[114] Shuhei Inoue and Yoshihiro Kikuchi. Diameter control and growth mechanism of single-walled carbon nanotubes. *Chemical Physics Letters*, 410:209–212, 2005.

[115] Eric W. Wong, Michael J. Bronikowski, Michael E. Hoenk, Robert S. Kowalczyk, and Brian D. Hunt. Submicron patterning of iron nanoparticle monolayers for carbon nanotube growth. *Chem. Mater.*, 17:237–241, 2005.

[116] Nobuo Ohmae. Shaping carbon nanotube bundles during growth using a magnetic field. *Carbon*, 46:544–546, 2008.

[117] Sangeeta Sahoo, Ravi Maranganti, Sarah Lastella, Govind Mallick, Shashi Karna, Pradeep Sharma, and Pulickel M. Ajayan. Reversible separation of single-walled carbon nanotubes in bundles. *Appl. Phys. Lett.*, 93:083120, 2008.

[118] W. Wenseleers, I. I. Vlasov, E. Goovaerts, E. D. Obraztsova, A. S. Lobach, and A. Bouwen. Efficient isolation and solubilization of pristine single-walled nanotubes in bile salt micelles. *Adv. Func. Mater.*, 14:1105, 2004.

[119] Xiaomin Tu, Suresh Manohar, Anand Jagota, and Ming Zheng. Dna sequence motifs for structure-specific recognition and separation of carbon nanotubes. *Nature*, 460:250, 2009.

[120] Atsushi Hirano, Takeshi Tanaka, and Hiromichi Kataura. Thermodynamic determination of the metal/semiconductor separation of carbon nanotubes using hydrogels. *ACS Nano*, 6:10195–10205, 2012.

[121] Michael S. Strano, Valerie C. Moore, Michael K. Miller, Mathew J. Allen, Erik H. Haroz, Carter Kittrell, Robert H. Hauge, and R.E. Smalley. The role of surfactant adsorption during ultrasonication in the dispersion of single-walled carbon nanotubes. *J. Nanosci. Nanotech.*, 3:81, 2003.

[122] Jared J. Crochet, Jay D. Sau, Juan G. Duque, Stephen K. Doorn, and Marvin L. Cohen. Electrodynamic and excitonic intertube interactions in semiconducting carbon nanotube aggregates. *ACS Nano*, 5:2611, 2011.

[123] K. B. K. Teo, C. Singh, M. Chhowalla, and W. I. Milne. *Encyclopedia of nanoscience and nanotechnology*, chapter Catalytic synthesis of carbon nanotubes and nanofibres, page 665. American Scientific Publisher, 2004.

[124] A. D. McNaught and A. Wilkinson. *IUPAC. Compendium of Chemical Terminology*. Blackwell Scientific Publications, Oxford (1997), 2nd edition, 1997. XML on-line corrected version: http://goldbook.iupac.org (2006-) created by M. Nic, J. Jirat, and B. Kosata; updates compiled by A. Jenkins. doi:10.1351/goldbook. Last update: 2012-08-19; version: 2.3.2. DOI of the term "catalyst": doi:10.1351/goldbook.C00876.

[125] K. B. K. Teo, M. Chhowalla, G. A. J. Amaratunga, W. I. Milne, D. G. Hasko, G. Pirio, P. Legagneux, F. Wyczisk, and D. Pribat. Uniform patterned growth of carbon nanotubes without surface carbon. *Appl. Phys. Lett.*, 79:1534–1536, 2001.

[126] Michael J. Bronikowski, Peter A. Willis, Daniel T. Colbert, K. A. Smith, and Richard E. Smalley. Gas-phase production of carbon single-walled nanotubes from carbon monoxide via the hipco process: A parametric study. *J. Vac. Sci. Technol. A*, 19:1800–1805, 2001.

[127] Wei-Hung Chiang, Mohammed Sakr, Xuan P. A. Gao, and R. Mohan Sankaran. Nanoengineering nixfe1-x catalysts for gas-phase, selective synthesis of semiconducting single-walled carbon nanotubes. *ACS Nano*, 3:4023, 2009.

[128] Sailaja Tetali, Mujtaba Zaka, Ronny Schoenfelder, Alicja Bachmatiuk, Felix Boerrnert, Imad Ibrahim, Jarrn H. Lin, Gianaurelio Cuniberti, Jamie H. Warner, Bernd Buechner, and Mark H. Ruemmeli. Unravelling the mechanisms behind mixed catalysts for the high yield production of single-walled carbon nanotubes. *ACS Nano*, 3:3839–3844, 2009.

[129] Yagang Yao, Ran Liu, Jin Zhang, Liying Jiao, and Zhongfan Liu. Raman spectral measuring of the growth rate of individual single-walled carbon nanotubes. *J. Phys. Chem. C*, 111:8407–8409, 2007.

[130] Shaoming Huang, Qiran Cai, Jiangying Chen, Yong Qian, and Lijie Zhang. Metal-catalyst-free growth of single-walled carbon nanotubes on substrates. *J. Am. Chem. Soc.*, 131:2094–2095, 2009.

[131] Bilu Liu, Wencai Ren, Chang Liu, Cheng-Hua Sun, Libo Gao, Shisheng Li, Chuanbin Jiang, and Hui-Ming Cheng. Growth velocity and direct length-sorted growth of short single-walled carbon nanotubes by a metal-catalyst-free chemical vapor deposition process. *ACS Nano*, 3:3421–3430, 2009.

[132] Kenji Hata, Don N. Futaba, Kohei Mizuno, Tatsunori Namai, Motoo Yumura, and Sumio Iijima. Water-assisted highly efficient synthesis of impurity-free single-walled carbon nanotubes. *Science*, 306:1362–1364, 2004.

[133] Lianxi Zheng, B. C. Satishkumar, Pingqi Gao, and Qing Zhang. Kinetics studies of ultralong single-walled carbon nanotubes. *J. Phys. Chem. C*, 113:10896–10900, 2009.

[134] Robert Seidel, Georg S. Duesberg, Eugen Unger, Andrew P. Graham, Maik Liebau, and Franz Kreupl. Chemical vapor deposition growth of single-walled carbon nanotubes at 600 c and a simple growth model. *J. Phys. Chem. B*, 108:1888–1893, 2004.

[135] T. W. Ebbesen and P. M. Ajayan. Large-scale synthesis of carbon nanotubes. *Nature*, 358:220–222, 1992.

[136] Yahachi Saito, Tadanobu Yoshikawa, Motonori Inagaki, Masato Tomita, and Takayoshi Hayashi. Growth and structure of graphitic tubules and polyhedral particles in arc-discharge. *Chemical Physics Letters*, 204:277–282, 1993.

[137] T. Guo, P. Nikolaev, A. Thess, D. T. Colbert, and R. E. Smalley. Catalytic growth of single-walled nanotubes by laser vaporization. *Chemical Physics Letters*, 243:49–54, 1995.

[138] Morinobu Endo, Kenji Takeuchi, Susumu Igarashi, Kiyoharu Kobori, Minoru Shiraishi, and Harold W. Kroto. The production and structure of pyrolytic carbon nanotubes (pcnts). *Journal of Physics and Chemistry of Solids*, 54:1841–1848, 1993.

[139] Hongjie Dai, Andrew G. Rinzler, Pasha Nikolaev, Andreas Thess, Daniel T. Colbert, and Richard E. Smalley. Single-wall nanotubes produced by metal-catalyzed disproportionation of carbon monoxide. *Chemical Physics Letters*, 260:471–475, 1996.

[140] Erik T. Thostenson, Zhifeng Ren, and Tsu-Wei Chou. Advances in the science and technology of carbon nanotubes and their composites: a review. *Composites Science and Technology*, 61:1899–1912, 2001.

[141] Peter J.F. Harris. Solid state growth mechanisms for carbon nanotubes. *Carbon*, 45:229–239, 2007.

[142] Satoshi Yasuda, Don N. Futaba, Takeo Yamada, Junichi Satou, Akiyoshi Shibuya, Hirokazu Takai, Kouhei Arakawa, Motoo Yumura, and Kenji Hata. Improved and large area single-walled carbon nanotube forest growth by controlling the gas flow direction. *ACS Nano*, 3:4164–4170, 2009.

[143] Sergei M. Bachilo, Leandro Balzano, Jose E. Herrera, Francisco Pompeo, Daniel E. Resasco, and R. Bruce Weisman. Narrow (n,m)-distribution of single-walled carbon nanotubes grown using a solid supported catalyst. *J. Am. Chem. Soc.*, 125:11186–11187, 2003.

[144] Mirco Cantoro, Stephan Hofmann, Simone Pisana, Vittorio Scardaci, Atlus Parvez, Caterina Ducati, Andrea C. Ferrari, Arthur M. Blackburn, Kai-You Wang, and John Robertson. Catalytic chemical vapor deposition of single-wall carbon nanotubes at low temperatures. *Nano Lett.*, 6:1107–1112, 2006.

[145] Richard E. Smalley, Yubao Li, Valerie C. Moore, B. Katherine Price, Ramon Jr. Colorado, Howard K. Schmidt, Robert H. Hauge, Andrew R. Barron, and James M. Tour. Single wall carbon nanotube amplification: En route to a type-specific growth mechanism. *J. Am. Chem. Soc.*, 128:15824–15829, 2006.

[146] Santiago Esconjauregui, Caroline M. Whelan, and Karen Maex. The reasons why metals catalyze the nucleation and growth of carbon nanotubes and other carbon nanomorphologies. *Carbon*, 47:659–669, 2009.

[147] Sumio Iijima, P. M. Ajayan, and T. Ichihashi. Growth model for carbon nanotubes. *Phys. Rev. Lett.*, 69:3100 – 3103, 1992.

[148] Shoushan Fan, Michael G. Chapline, Nathan R. Franklin, Thomas W. Tombler, Alan M. Cassell, and Hongjie Dai. Self-oriented regular arrays of carbon nanotubes and their field emission properties. *Science*, 283:512–514, 1999.

[149] Oleg A. Louchev, Thomas Laude, Yoichiro Sato, and Hisao Kanda. Diffusion-controlled kinetics of carbon nanotube forest growth by chemical vapor deposition. *J. Chem. Phys.*, 118:7622–7634, 2003.

[150] Chris Bower, Wei Zhu, Sungho Jin, and Otto Zhou. Plasma-induced alignment of carbon nanotubes. *Appl. Phys. Lett.*, 77:830–832, 2000.

[151] Yuhei Miyauchi, Shohei Chiashi, Yoichi Murakami, Yasunori Hayashida, and Shigeo Maruyama. Fluorescence spectroscopy of single-walled carbon nanotubes synthesized from alcohol. *Chemical Physics Letters*, 387:198–203, 2004.

[152] Rong Xiang, Erik Einarsson, Jun Okawa, Yuhei Miyauchi, and Shigeo Maruyama. Acetylene-accelerated alcohol catalytic chemical vapor deposition growth of vertically aligned single-walled carbon nanotubes. *J. Phys. Chem. C*, 113:7511–7515, 2009.

[153] Y. Gao, Y. S. Zhou, W. Xiong, M. Mahjouri-Samani, M. Mitchell, and Y. F. Lu. Controlled growth of carbon nanotubes on electrodes under different bias polarity. *Appl. Phys. Lett.*, 95:143117, 2009.

[154] Yiming Li, David Mann, Marco Rolandi, Woong Kim, Ant Ural, Steven Hung, Ali Javey, Jien Cao, Dunwei Wang, Erhan Yenilmez, Qian Wang, James F. Gibbons, Yoshio Nishi, and Hongjie Dai. Preferential growth of semiconducting single-walled carbon nanotubes by a plasma enhanced cvd method. *Nano Lett.*, 4:317–321, 2004.

[155] Toshiaki Kato and Rikizo Hatakeyama. Direct growth of short single-walled carbon nanotubes with narrow-chirality distribution by time-programmed plasma chemical vapor deposition. *ACS Nano*, 4:7395, 2010.

[156] Oleg A. Louchev, Yoichiro Sato, and Hisao Kanda. Growth mechanism of carbon nanotube forests by chemical vapor deposition. *Appl. Phys. Lett.*, 80:2752, 2002.

[157] J. Gavillet, A. Loiseau, C. Journet, F. Willaime, F. Ducastelle, and J.-C. Charlier. Root-growth mechanism for single-wall carbon nanotubes. *Phys. Rev. Lett.*, 87:275504, 2001.

[158] Simone Pisana, Alain Jungen, Can Zhang, Arthur M. Blackburn, Renu Sharma, Felipe Cervantes-Sodi, Christoph Stampfer, Caterina Ducati, Andrea C. Ferrari, Christofer Hierold, John Robertson, and Stephan Hofmann. Flying and crawling modes during surface-bound single wall carbon nanotube growth. *J. Phys. Chem. C*, 111:17249–17253, 2007.

[159] Jean-Yves Raty, Francois Gygi, and Giulia Galli. Growth of carbon nanotubes on metal nanoparticles: A microscopic mechanism from ab initio molecular dynamics simulations. *Phys. Rev. Lett.*, 95:096103, 2005.

[160] Diego A. Gómez-Gualdrón and Perla B. Balbuena. Growth of chiral single-walled carbon nanotube caps in the presence of a cobalt cluster. *Nanotechnology*, 20:215601, 2009.

[161] Feng Ding, Arne Rosen, and Kim Bolton. Md simulations of catalytic carbon nanotube growth: Important features of the metal-carbon interactions. *AIP Conf. Proc.*, 723:364–367, 2004.

[162] Feng Ding, Peter Larsson, J. Andreas Larsson, Rajeev Ahuja, Haiming Duan, Arne Rosen, and Kim Bolton. The importance of strong carbon-metal adhesion for catalytic nucleation of single-walled carbon nanotubes. *Nano Lett.*, 8:463–468, 2008.

[163] Feng Ding, Arne Rosen, and Kim Bolton. Dependence of swnt growth mechanism on temperature and catalyst particle size: Bulk versus surface diffusion. *Carbon*, 43:2215–2217, 2005.

[164] Jingyu Lu and Jianmin Miao. Growth mechanism of carbon nanotubes: a nano czochralski model. *Nanoscale Research Letters*, 7:356, 2012.

[165] R. S. Wagner and W. C. Ellis. Vapor-liquid-solid mechanism of single crystal growth. *Appl. Phys. Lett.*, 4:89–90, 1964.

[166] W. K. Burton, N. Cabrera, and F. C. Frank. Role of dislocations in crystal growth. *Nature*, 163:398–399, 1949.

[167] W. K. Burton, N. Cabrera, and F. C. Frank. The growth of crystals and the equilibrium structure of their surfaces. *Philosophical Transactions of the Royal Society of London. Series A, Mathematical and Physical Sciences*, 243:299–358, 1951.

[168] Feng Ding, Avetik R. Harutyunyan, and Boris I. Yakobson. Dislocation theory of chirality-controlled nanotube growth. *PNAS*, 106:2506–2509, 2009.

[169] Chris Bower, Otto Zhou, Wei Zhu, D. J. Werder, and Sungho Jin. Nucleation and growth of carbon nanotubes by microwave plasma chemical vapor deposition. *Appl. Phys. Lett.*, 77:2767–2769, 2000.

[170] C. Mattevi, S. Hofmann, M. Cantorod, A.C. Ferrari, J. Robertson, C. Castellarin-Cudia, S. Dolafi, A. Goldoni, and C. Cepek. Surface-bound chemical vapour deposition of carbon nanotubes: In situ study of catalyst activation. *Physica E*, 40:2238–2242, 2008.

[171] S. Esconjauregui, B. C. Bayer, M. Fouquet, C. T. Wirth, C. Ducati, S. Hofmann, and J. Robertson. Growth of high-density vertically aligned arrays of carbon nanotubes by plasma-assisted catalyst pretreatment. *Appl. Phys. Lett.*, 95:173115, 2009.

[172] X. Fan, R. Buczko, A. A. Puretzky, D. B. Geohegan, J. Y. Howe, S. T. Pantelides, and S. J. Pennycook. Nucleation of single-walled carbon nanotubes. *Phys. Rev. Lett.*, 90:145501, 2003.

[173] Stephan Hofmann, Renu Sharma, Caterina Ducati, Gaohui Du, Cecilia Mattevi, Cinzia Cepek, Mirco Cantoro, Simone Pisana, Atlus Parvez, Felipe Cervantes-Sodi, Andrea C. Ferrari, Rafal Dunin-Borkowski, Silvano Lizzit, Luca Petaccia, Andrea Goldoni, and John Robertson. In situ observations of catalyst dynamics during surface-bound carbon nanotube nucleation. *Nano Lett.*, 7:602–608, 2007.

[174] Hideto Yoshida, Seiji Takeda, Tetsuya Uchiyama, Hideo Kohno, and Yoshikazu Homma. Atomic-scale in-situ observation of carbon nanotube growth from solid state iron carbide nanoparticles. *Nano Lett.*, 8:2082–2086, 2008.

[175] H. Amara, C. Bichara, and F. Ducastelle. Understanding the nucleation mechanisms of carbon nanotubes in catalytic chemical vapor deposition. *Phys. Rev. Lett.*, 100:056105, 2008.

[176] Placidus B. Amama, Cary L. Pint, Laura McJilton, Seung Min Kim, Eric A. Stach, P. Terry Murray, Robert H. Hauge, and Benji Maruyama. Role of water in super growth of single-walled carbon nanotube carpets. *Nano Lett.*, 9:44–49, 2009.

[177] Anders Börjesson and Kim Bolton. First principles studies of the effect of ostwald ripening on carbon nanotube chirality distributions. *ACS Nano*, 5:771, 2011.

[178] Yasushi Shibuta and Shigeo Maruyama. Molecular dynamics simulation of formation process of single-walled carbon nanotubes by ccvd method. *Chemical Physics Letters*, 382:381–386, 2003.

[179] Stephanie Reich, Lan Li, and John Robertson. Control the chirality of carbon nanotubes by epitaxial growth. *Chemical Physics Letters*, 421:469–472, 2006.

[180] Qiang Fu and Thomas Wagner. Interaction of nanostructured metal overlayers with oxide surfaces. *Surface Science Reports*, 62:431–498, 2007.

[181] Stig Helveg, Carlos Lopez-Cartes, Jens Sehested, Poul L. Hansen, Bjerne S. Clausen, Jens R. Rostrup-Nielsen, Frank Abild-Pedersen, and Jens K. Norskov. Atomic-scale imaging of carbon nanofibre growth. *Nature*, 427:426–429, 2004.

[182] S. Hofmann, G. Csanyi, A. C. Ferrari, M. C. Payne, and J. Robertson. Surface diffusion: The low activation energy path for nanotube growth. *Phys. Rev. Lett.*, 95:036101, 2005.

[183] Julio A. Rodriguez-Manzo, Mauricio Terrones, Humberto Terrones, Harold W. Kroto, Litao Sun, and Florian Banhart. In situ nucleation of carbon nanotubes by the injection of carbon atoms into metal particles. *Nature Nanotechnology*, 2:307–311, 2007.

[184] Yasuhito Ohta, Yoshiko Okamoto, Alister J. Page, Stephan Irle, and Keiji Morokuma. Quantum chemical molecular dynamics simulation of single-walled carbon nanotube cap nucleation on an iron particle. *ACS Nano*, 3:3413–3420, 2009.

[185] Erik C. Neyts, Yasushi Shibuta, Adri C. T. van Duin, and Annemie Bogaerts. Catalyzed growth of carbon nanotube with definable chirality by hybrid molecular dynamics-force biased monte carlo simulations. *ACS Nano*, 4:6665–6672, 2010.

[186] S. Reich, L. Li, and J. Robertson. Epitaxial growth of carbon caps on ni for chiral selectivity. *Phys. Status Solidi*, 243:3494–3499, 2006.

[187] H. Duan, F. Ding, A. Rosén, A. Harutyunyan, T. Tokune, S. Curtarolo, and K. Bolton. Initial growth of single-walled carbon nanotubes on supported iron clusters: a molecular dynamics study. *Eur. Phys. J. D*, 43:185–189, 2007.

[188] M.-F. C. Fiawoo, A.-M. Bonnot, H. Amara, C. Bichara, J. Thibault-Pénisson, and A. Loiseau. Evidence of correlation between catalyst particles and the single-wall carbon nanotube diameter: A first step towards chirality control. *Phys. Rev. Lett.*, 108:195503, 2012.

[189] Diego A. Gómez-Gualdrón, Gilbert D. McKenzie, Juan F. J. Alvarado, and Perla B. Balbuena. Dynamic evolution of supported metal nanocatalyst/carbon structure during single-walled carbon nanotube growth. *ACS Nano*, 6:720, 2012.

[190] Debosruti Dutta, Wei-Hung Chiang, R. Mohan Sankaran, and Venkat R. Bhethanabotla. Epitaxial nucleation model for chiral-selective growth of single-walled carbon nanotubes on bimetallic catalyst surfaces. *Carbon*, 50:3766, 2012.

[191] L. Li, S. Reich, and J. Robertson. Modelling the nucleation and chirality selection of carbon nanotubes. *Journal of Nanoscience and Nanotechnology*, 6:1–8, 2006.

[192] Wuming Zhu, Anders Börjesson, and Kim Bolton. Dft and tight binding monte carlo calculations related to single-walled carbon nanotube nucleation and growth. *Carbon*, 48:470–478, 2010.

[193] Yuanyue Liu, Alex Dobrinsky, and Boris I. Yakobson. Graphene edge from armchair to zigzag: The origins of nanotube chirality? *Phys. Rev. Lett.*, 105:235502, 2010.

[194] Qiang Wang, Hong Wang, Li Wei, Shuo-Wang Yang, and Yuan Chen. Reactive sites for chiral selective growth of single-walled carbon nanotubes: A dft study of ni55–cn complexes. *J. Phys. Chem. A*, 116:11709–11717, 2012.

[195] Diego A. Gómez-Gualdrón and Perla B. Balbuena. The role of cap chirality in the mechanism of growth of single-wall carbon nanotubes. *Nanotechnology*, 19:485604, 2008.

[196] Oleg V. Yazyev and Alfredo Pasquarello. Effect of metal elements in catalytic growth of carbon nanotubes. *Phys. Rev. Lett.*, 100:156102, 2008.

[197] M. Diarra, A. Zappelli, H. Amara, F. Ducastelle, and C. Bichara. Importance of carbon solubility and wetting properties of nickel nanoparticles for single wall nanotube growth. *Phys. Rev. Lett.*, 109:185501, 2012.

[198] Dmitri Schebarchov, Shaun C. Hendy, Elif Ertekin, and Jeffrey C. Grossman. Interplay of wetting and elasticity in the nucleation of carbon nanotubes. *Phys. Rev. Lett.*, 107:185503, 2011.

[199] Erik C. Neyts, Adri C. T. van Duin, and Annemie Bogaerts. Changing chirality during single-walled carbon nanotube growth: A reactive molecular dynamics/monte carlo study. *J. Am. Chem. Soc.*, 133:17225, 2011.

[200] Qiang Wang, Man-Fai Ng, Shuo-Wang Yang, Yanhui Yang, and Yuan Chen. The mechanism of single-walled carbon nanotube growth and chirality selection induced by carbon atom and dimer addition. *ACS Nano*, 4:939–946, 2010.

[201] Vasilii I. Artyukhov, Yuanyue Liu, and Boris I. Yakobson. Equilibrium at the edge and atomistic mechanisms of graphene growth. *PNAS*, 109:15136–15140, 2012.

[202] Qiang Wang, Shuo-Wang Yang, Yanhui Yang, Mary B. Chan-Park, and Yuan Chen. Charge transfer between metal clusters and growing carbon structures in chirality-controlled single-walled carbon nanotube growth. *J. Phys. Chem. Lett.*, 2:1009, 2011.

[203] S Noor Mohammad. A possible role of the dipole moment of the catalyst droplet in nanotube growth, alignment, chirality, and characteristics. *Nanotechnology*, 23:085701, 2012.

[204] Joonghan Kim, Alister J. Page, Stephan Irle, and Keiji Morokuma. Dynamics of local chirality during swcnt growth: Armchair versus zigzag nanotubes. *J. Am. Chem. Soc.*, 134:9311, 2012.

[205] M. Diarra, H. Amara, C. Bichara, and F. Ducastelle. Role of defect healing on the chirality of single-wall carbon nanotubes. *Phys. Rev. B*, 85:245446, 2012.

[206] Yuhuang Wang, Myung Jong Kim, Hongwei Shan, Carter Kittrell, Hua Fan, Lars M. Ericson, Wen-Fang Hwang, Sivaram Arepalli, Robert H. Hauge, and Richard E. Smalley. Continued growth of single-walled carbon nanotubes. *Nano Lett.*, 5:997–1002, 2005.

[207] Eric H. Fort, Patrick M. Donovan, and Lawrence T. Scott. Diels-alder reactivity of polycyclic aromatic hydrocarbon bay regions: Implications for metal-free growth of single-chirality carbon nanotubes. *J. Am. Chem. Soc.*, 131:16006–16007, 2009.

[208] Graham J. Bodwell. Carbon nanotubes: Growth potential. *Nature Nanotechnology*, 5:103–104, 2010.

[209] Lawrence T. Scott, Edward A. Jackson, Qianyan Zhang, Brian D. Steinberg, Mihail Bancu, and Bo Li. A short, rigid, structurally pure carbon nanotube by stepwise chemical synthesis. *J. Am. Chem. Soc.*, 134:107, 2012.

[210] Haruka Omachi, Sanae Matsuura, Yasutomo Segawa, and Kenichiro Itami. A modular and size-selective synthesis of [n]cycloparaphenylenes: A step toward the selective synthesis of [n,n] single-walled carbon nanotubes. *Angewandte Chemie International Edition*, 49:10202, 2010.

[211] Hai-Bei Li, Alister J. Page, Stephan Irle, and Keiji Morokuma. Single-walled carbon nanotube growth from chiral carbon nanorings: Prediction of chirality and diameter influence on growth rates. *Journal of the American Chemical Society*, 134:15887–15896, 2012.

[212] Matthieu Paillet, Jannik C. Meyer, Thierry Michel, Vincent Jourdain, Philippe Poncharal, Jean-Louis Sauvajol, Nadege Cordente, Catherine Amiens, Bruno

Chaudret, Siegmar Roth, and Ahmed Zahab. Selective growth of large chiral angle single-walled carbon nanotubes. *Diamond and Related Materials*, 15:1019–1022, 2006.

[213] Zohreh Ghorannevis, Toshiaki Kato, Toshiro Kaneko, and Rikizo Hatakeyama. Narrow-chirality distributed single-walled carbon nanotube growth from non-magnetic catalyst. *J. Am. Chem. Soc.*, 132:9570–9572, 2010.

[214] M. Fouquet, B. C. Bayer, S. Esconjauregui, R. Blume, J. H. Warner, S. Hofmann, R. Schlögl, C. Thomsen, and J. Robertson. Highly chiral-selective growth of single-walled carbon nanotubes with a simple monometallic co catalyst. *Phys. Rev. B*, 85:235411, 2012.

[215] Hong Wang, Li Wei, Fang Ren, Qiang Wang, Lisa D. Pfefferle, Gary L. Haller, and Yuan Chen. Chiral-selective coso4/sio2 catalyst for (9, 8) single walled carbon nanotube growth. *ACS Nano*, 7:614–626, 2012.

[216] Jose M. Soler, Emilio Artacho, Julian D. Gale, Alberto Garcia, Javier Junquera, Pablo Ordejon, and Daniel Sanchez-Portal. The siesta method for ab initio order-n materials simulation. *J. Phys.: Condens. Matter*, 14:2745–2779, 2002.

[217] M. Born and R. Oppenheimer. Zur quantentheorie der molekeln. *Annalen der Physik*, 389:457–484, 1927.

[218] Attila Szabo and Neil S. Ostlund. *Modern Quantum Chemistry: Introduction to Advanced Electronic Structure Theory*. Dover Books on Chemistry, 1996.

[219] V. Fock. Näherungsmethode zur lösung des quantenmechanischen mehrkörper-problems. *Zeitschrift für Physik*, 61:126–148, 1930.

[220] Per-Olov Löwdin. Quantum theory of many-particle systems. iii. extension of the hartree-fock scheme to include degenerate systems and correlation effects. *Phys. Rev.*, 97:1509–1520, Mar 1955.

[221] P. Hohenberg and W. Kohn. Inhomogeneous electron gas. *Phys. Rev.*, 136:B864–B871, 1964.

[222] W. Kohn and L. J. Sham. Self-consistent equations including exchange and correlation effects. *Phys. Rev.*, 140:A1133–A1138, 1965.

[223] M. C. Payne, M. P. Teter, D. C. Allan, T. A. Arias, and J. D. Joannopoulos. Iterative minimization techniques for *ab initio* total-energy calculations: molecular dynamics and conjugate gradients. *Rev. Mod. Phys.*, 64:1045–1097, 1992.

[224] Mel Levy. Universal variational functionals of electron densities, first-order density matrices, and natural spin-orbitals and solution of the v-representability problem. *PNAS*, 76:6062–6065, 1979.

[225] J. P. Perdew and Alex Zunger. Self-interaction correction to density-functional approximations for many-electron systems. *Phys. Rev. B*, 23:5048, May 1981.

[226] John P. Perdew, Kieron Burke, and Matthias Ernzerhof. Generalized gradient approximation made simple. *Phys. Rev. Lett.*, 77:3865–3868, 1996.

[227] M. Dion, H. Rydberg, E. Schröder, D. C. Langreth, and B. I. Lundqvist. Van der waals density functional for general geometries. *Phys. Rev. Lett.*, 92:246401, 2004.

[228] M. Dion, H. Rydberg, E. Schröder, D. C. Langreth, and B. I. Lundqvist. Erratum: Van der waals density functional for general geometries [phys. rev. lett. 92, 246401 (2004)]. *Phys. Rev. Lett.*, 95:109902(E), 2005.

[229] R. Eisenschitz and F. London. Über das verhältnis der van der waalsschen kräfte zu den homöopolaren bindungskräften. *Zeitschrift für Physik A Hadrons and Nuclei*, 60:491–527, 1930.

[230] John Edward Jones. On the determination of molecular fields. ii. from the equation of state of a gas. *Proc. R. Soc. Lond. A*, 106:463–477, 1924.

[231] H. Rydberg, M. Dion, N. Jacobson, E. Schröder, P. Hyldgaard, S. I. Simak, D. C. Langreth, and B. I. Lundqvist. Van der waals density functional for layered structures. *Phys. Rev. Lett.*, 91:126402, 2003.

[232] Henrik Rydberg. *Nonlocal Correlations in Density Functional Theory.* PhD thesis, Department of Applied Physics Chalmers University of Technology and Göteborg University, 2001.

[233] G. Roman-Perez and J. M. Soler. Efficient implementation of a van der waals density functional: application to double-wall carbon nanotubes. *Phys. Rev. Lett.*, 103:096102, 2009.

[234] Yingkai Zhang and Weitao Yang. Comment on "generalized gradient approximation made simple". *Phys. Rev. Lett.*, 80:890–890, 1998.

[235] D. C. Langreth, M. Dion, H. Rydberg, E. Schröder, P. Hyldgaard, and B. I. Lundqvist. Van der waals density functional theory with applications. *International Journal of Quantum Chemistry*, 101:599, 2004.

[236] T. Thonhauser, Valentino R. Cooper, Shen Li, Aaron Puzder, Per Hyldgaard, and David C. Langreth. Van der waals density functional: Self-consistent potential and the nature of the van der waals bond. *Phys. Rev. B*, 76:125112, 2007.

[237] Kyuho Lee, Andre K. Kelkkanen, Kristian Berland, Stig Andersson, David C. Langreth, Elsebeth Schröder, Bengt I. Lundqvist, and Per Hyldgaard. Evaluation of new density functional with account of van der waals forces by use of experimental h2 physisorption data on cu(111). *Phys. Rev. B*, 84:193408, 2011.

[238] Jesper Kleis, Elsebeth Schröder, and Per Hyldgaard. Nature and strength of bonding in a crystal of semiconducting nanotubes: van der waals density functional calculations and analytical results. *Phys. Rev. B*, 77:205422, 2008.

[239] Pablo Ordejon, Emilio Artacho, and Jose M. Soler. Self-consistent order-n density-functional calculations for very large systems. *Phys. Rev. B*, 53:R10441–R10444, 1996.

[240] Javier Junquera, Oscar Paz, Daniel Sanchez-Portal, and Emilio Artacho. Numerical atomic orbitals for linear-scaling calculations. *Phys. Rev. B*, 64:235111, 2001.

[241] N. Troullier and Jose Luriaas Martins. Efficient pseudopotentials for plane-wave calculations. *Phys. Rev. B*, 43:1993–2006, 1991.

[242] Leonard Kleinman and D. M. Bylander. Efficacious form for model pseudopo-tentials. *Phys. Rev. Lett.*, 48:1425–1428, 1982.

[243] Diego A. Gómez-Gualdrón and Perla B. Balbuena. Effect of metal cluster-cap interactions on the catalyzed growth of single-wall carbon nanotubes. *J. Phys. Chem. C*, 113:698–709, 2009.

[244] Yasuhito Ohta, Yoshiko Okamoto, Stephan Irle, and Keiji Morokuma. Density-functional tight-binding molecular dynamics simulations of swcnt growth by surface carbon diffusion on an iron cluster. *Carbon*, 47:1270–1275, 2009.

[245] Mickal Marchand, Catherine Journet, Dominique Guillot, Jean-Michel Benoit, Boris I. Yakobson, and Stephen T. Purcell. Growing a carbon nanotube atom by atom : "and yet it does turn". *Nano Lett.*, 9:2961–2966, 2009.

[246] M. Zubaer Hossain. Structural instability of single wall carbon nanotube edges from first principles. *Appl. Phys. Lett.*, 95:153104, 2009.

[247] Naokazu Kitamura and Atsushi Oshiyama. Open edge growth mechanisms of single wall carbon nanotubes. *J. Phys. Soc. Jpn.*, 70:1995–2011, 2001.

[248] John P. Perdew, Adrienn Ruzsinszky, Gábor I. Csonka, Oleg A. Vydrov, Gus-tavo E. Scuseria, Lucian A. Constantin, Xiaolan Zhou, and Kieron Burke. Restoring the density-gradient expansion for exchange in solids and surfaces. *Phys. Rev. Lett.*, 100:136406, Apr 2008.

[249] Graeme Henkelman, Blas P. Uberuaga, and Hannes Jonsson. A climbing image nudged elastic band method for finding saddle points and minimum energy paths. *J. Chem. Phys.*, 113:9901, 2000.

[250] Jiri Klimes, David R. Bowler, and Angelos Michaelides. A critical assessment of theoretical methods for finding reaction pathways and transition states of surface processes. *J. Phys.: Condens. Matter*, 22:074203, 2010.

[251] A.J. Stone and D.J. Wales. Theoretical studies of icosahedral c60 and some related species. *Chemical Physics Letters*, 128:501, 1986.

[252] Pablo Jensen, Julian Gale, and X. Blase. Catalysis of nanotube plasticity under tensile strain. *Phys. Rev. B*, 66:193403, 2002.

[253] J.-C. Charlier, H. Amara, and Ph. Lambin. Catalytically assisted tip growth mechanism for single-wall carbon nanotubes. *ACS Nano*, 1:202, 2007.

[254] Chuanhong Jin, Haiping Lan, Kazu Suenaga, Lianmao Peng, and Sumio Iijima. Metal atom catalyzed enlargement of fullerenes. *Phys. Rev. Lett.*, 101:176102, 2008.

[255] Sondes Karoui, Hakim Amara, Christophe Bichara, and Francois Ducastelle. Nickel-assisted healing of defective graphene. *ACS Nano*, 4:6114, 2010.

[256] Heiko Dumlich and Stephanie Reich. Stability of armchair carbon nanotube caps with different edges on an iron cluster. *to be submitted*, x:x, 2013.

[257] Kenichi Fukui. Role of frontier orbitals in chemical reactions. *Science*, 218:747–754, 1982.

[258] D.-H. Oh and Young Hee Lee. Stability and cap formation mechanism of single-walled carbon nanotubes. *Phys. Rev. B*, 58:7407–7411, 1998.

[259] Manfred Hoffmann, Heinz Gascha, Horst Schaschke, and Harald Gärtner, editors. *Compact Grosses Handbuch - Mathe Physik Chemie Formeln*. Compact Verlag München, 1999.

[260] Young Hee Lee, Seong Gon Kim, and David Tomanek. Catalytic growth of single-wall carbon nanotubes: An ab initio study. *Phys. Rev. Lett.*, 78:2393–2396, 1997.

[261] Stephanie Reich, Christian Thomsen, and John Robertson. Exciton resonances quench the photoluminescence of zigzag carbon nanotubes. *Phys. Rev. Lett.*, 95:077402, 2005.

[262] Francesca Baletto and Riccardo Ferrando. Structural properties of nanoclusters: Energetic, thermodynamic, and kinetic effects. *Rev. Mod. Phys.*, 77:371–423, 2005.

[263] Ranber Singh and Peter Kroll. Structural, electronic, and magnetic properties of 13-, 55-, and 147-atom clusters of fe, co, and ni: A spin-polarized density functional study. *Phys. Rev. B*, 78:245404, 2008.

[264] Jonathan P. K. Doye and David J. Wales. Calculation of thermodynamic properties of small lennard-jones clusters incorporating anharmonicity. *J. Chem. Phys. 102, 9659*, 102:9659, 1995.

[265] G. Brinkmann, O. Delgado Friedrichs, S. Lisken, A. Peeters, and N. Van Cleemput. Cage - a virtual environment for studying some special classes of plane graphs - an update. *MATCH Commun. Math. Comput. Chem.*, 63:533–552, 2010.

[266] B. Liu and A. D. McLean. Accurate calculation of the attractive interaction of two ground state helium atoms. *J. Chem. Phys.*, 59:4557, 1973.

[267] Frans B. van Duijneveldt, Jeanne G. C. M. van Duijneveldt-van de Rijdt, and Joop H. van Lenthe. State of the art in counterpoise theory. *Chemical Reviews*, 94:1873–1885, 1994.

[268] S. F. Boys and F. Bernardi. The calculation of small molecular interactions by the differences of separate total energies. some procedures with reduced errors. *Molecular Physics*, 19:553–566, 1970.

[269] B. Liu and A. D. McLean. The interacting correlated fragments model for weak interactions, basis set superposition error, and the helium dimer potential. *J. Chem. Phys.*, 91:2348, 1989.

[270] R. S. Mulliken. Electronic population analysis on lcao-mo molecular wave functions. i. *J. Chem. Phys.*, 23:1833–1840, 1955.

[271] Graeme Henkelman, Andri Arnaldsson, and Hannes Jonsson. A fast and robust algorithm for bader decomposition of charge density. *Comput. Mater. Sci.*, 36:354–360, 2006.

[272] Edward Sanville, Steven D. Kenny, Roger Smith, and Graeme Henkelman. Improved grid-based algorithm for bader charge allocation. *Journal of Computational Chemistry*, 28:899–908, 2007.

[273] W. Tang, E. Sanville, and G. Henkelman. A grid-based bader analysis algorithm without lattice bias. *J. Phys.: Condens. Matter*, 21:084204, 2009.

[274] John Robertson. Heterogeneous catalysis model of growth mechanisms of carbon nanotubes, graphene and silicon nanowires. *Journal of Materials Chemistry*, 22:19858–19862, 2012.

[275] Pascal Bluemmel, Antonio Setaro, Chris S. Popeney, Rainer Haag, and Stephanie Reich. Dispersion of carbon nanotubes using an azobenzene derivative. *Phys. Status Solidi B*, 247:2891, 2010.

[276] Renaud Marquis, Carla Greco, Izabela Sadokierska, Sergei Lebedkin, Manfred M. Kappes, Thierry Michel, Laurent Alvarez, Jean-Louis Sauvajol, Stephane Meunier, and Charles Mioskowski. Supramolecular discrimination of carbon nanotubes according to their helicity. *Nano Lett.*, 8:1830, 2008.

[277] Sang-Yong Ju, Jonathan Doll, Ity Sharma, and Fotios Papadimitrakopoulos. Selection of carbon nanotubes with specific chiralities using helical assemblies of flavin mononucleotide. *Nature Nanotechnology*, 3:356, 2008.

[278] A. Setaro, C.S. Popeney, B. Trappmann, V. Datsyuk, R. Haag, and S. Reich. Polyglycerol-derived amphiphiles for single walled carbon nanotube suspension. *Chemical Physics Letters*, 493:147, 2010.

[279] J. D. Bernal. The structure of graphite. *Proc. R. Soc. Lond. A*, 106:749–773, 1924.

[280] Lorin X. Benedict, Nasreen G. Chopra, Marvin L. Cohen, A. Zettl, Steven G. Louie, and Vincent H. Crespi. Microscopic determination of the interlayer binding energy in graphite. *Chemical Physics Letters*, 286:490, 1998.

[281] L. A. Girifalco, Miroslav Hodak, and Roland S. Lee. Carbon nanotubes, buckyballs, ropes, and a universal graphitic potential. *Phys. Rev. B*, 62:13104, 2000.

[282] Cheng-Hua Sun, Gao-Qing Lu, and Hui-Ming Cheng. Simple approach to estimating the van der waals interaction between carbon nanotubes. *Phys. Rev. B*, 73:195414, 2006.

[283] Alexander I. Zhbanov, Evgeny G. Pogorelov, and Yia-Chung Chang. Van der waals interaction between two crossed carbon nanotubes. *ACS Nano*, 4:5937–5945, 2010.

[284] Rick F. Rajter, Rudi Podgornik, V. Adrian Parsegian, Roger H. French, and W. Y. Ching. van der waals–london dispersion interactions for optically anisotropic cylinders: Metallic and semiconducting single-wall carbon nanotubes. *Phys. Rev. B*, 76:045417, 2007.

[285] M. Seydou, Y. J. Dappe, S. Marsaudon, J.-P. Aimé, X. Bouju, and A.-M. Bonnot. Atomic force microscope measurements and lcao-s2 + vdw calculations of contact length between a carbon nanotube and a graphene surface. *Phys. Rev. B*, 83:045410, 2011.

[286] Hendrik J. Monkhorst and James D. Pack. Special points for brillouin-zone integrations. *Phys. Rev. B*, 13:5188–5192, 1976.

[287] Wolfram Research Inc. *Mathematica Edition: Version 7.0.1.0.* Wolfram Research, Inc., Champaign, Illinois, 2008.

[288] Ludwig Fahrmeir, Rita Künstler, Iris Pigeot, and Gerhard Tutz. *Statistik Der Weg zur Datenanalyse.* Springer-Lehrbuch, 6th edition, 2007.

[289] Renju Zacharia, Hendrik Ulbricht, and Tobias Hertel. Interlayer cohesive energy of graphite from thermal desorption of polyaromatic hydrocarbons. *Phys. Rev. B*, 69:155406, 2004.

[290] Daniel Sanchez-Portal, Emilio Artacho, Jose M. Soler, Angel Rubio, and Pablo Ordejon. Ab initio structural, elastic, and vibrational properties of carbon nanotubes. *Phys. Rev. B*, 59:12678–12688, 1999.

[291] B. Chen, M. Gao, J. M. Zuo, S. Qu, B. Liu, and Y. Huang. Binding energy of parallel carbon nanotubes. *Appl. Phys. Lett.*, 83:3570, 2003.

[292] J. Buchoux, L. Bellon, S. Marsaudon, and J. Aimé. Carbon nanotubes adhesion and nanomechanical behavior from peeling force spectroscopy. *The European Physical Journal B - Condensed Matter and Complex Systems*, 84:69–77, 2011.

[293] J. M. Cowley, Pavel Nikolaev, Andreas Thess, and Richard E. Smalley. Electron nano-diffraction study of carbon single-walled nanotube ropes. *Chemical Physics Letters*, 265:379, 1997.

[294] Jae-Kap Lee, So-Hyung Lee, Jae-Pyoung Ahn, Seung-Cheol Lee, and Wook-Seong Lee. Aa' stacked graphite and fabrication method thereof, U.S. Patent 20100028573, published on 4th February 2010.

[295] David M. Bishop. *Group Theory and Chemistry*. Dover Publications, Inc. New York, 1973.

[296] C. S. Yannoni, R. D. Johnson, G. Meijer, D. S. Bethune, and J. R. Salem. Carbon-13 nmr study of the c60 cluster in the solid state: molecular motion and carbon chemical shift anisotropy. *J. Phys. Chem.*, 95:9, 1991.

[297] R. Tycko, R. C. Haddon, G. Dabbagh, S. H. Glarum, D. C. Douglass, and A. M. Mujsce. Solid-state magnetic resonance spectroscopy of fullerenes. *J. Phys. Chem.*, 95:518, 1991.

[298] Jian Ping Lu, X.-P. Li, and Richard M. Martin. Ground state and phase transitions in solid c60. *Phys. Rev. Lett.*, 68:1551, 1992.

[299] Freie Universität Berlin. Promotionsordnung des fachbereichs physik. *Amtsblatt der Freien Universität Berlin*, 5/2010:32–40, Februar 2010.

[300] H. Hellmann. A new approximation method in the problem of many electrons. *J. Chem. Phys.*, 3:61, 1935.

[301] G. P. Kerker. Non-singular atomic pseudopotentials for solid state applications. *J. Phys. C: Solid State Phys.*, 13:L189, 1980.

[302] Ilya Grinberg, Nicholas J. Ramer, and Andrew M. Rappe. Quantitative criteria for transferable pseudopotentials in density functional theory. *Phys. Rev. B*, 63:201102, 2001.

[303] Atom, a program for dft calculations in atoms and pseudopotential generation, distributed as part of the siesta software package. see http://www.icmab.es/siesta/atom.

[304] Stephanie Reich, Janina Maultzsch, Christian Thomsen, and Pablo Ordejon. Tight-binding description of graphene. *Phys. Rev. B*, 66:035412, 2002.

[305] Y. Baskin and L. Meyer. Lattice constants of graphite at low temperatures. *Phys. Rev.*, 100:544, 1955.

[306] Jun-Hyung Cho and Matthias Scheffler. Ab initio pseudopotential study of fe,co, and ni employing the spin-polarized lapw approach. *Phys. Rev. B*, 53:10685–10689, 1996.

[307] Jing Zhu, X. W. Wang, and Steven G. Louie. First-principles pseudopotential calculations of magnetic iron. *Phys. Rev. B*, 45:8887–8893, 1992.

[308] Jiri Klimes, David R. Bowler, and Angelos Michaelides. Van der waals density functionals applied to solids. *Phys. Rev. B*, 83:195131, 2011.

5 Appendix

The first section of the Appendix (Section 5.1) presents more details on pseudopotentials. The detailed parameters used for the generation of pseudopotentials used in the thesis and test calculations for them are presented. In Section 5.2 we present a list of people, institutions, and software who/which were essential in the creation of this thesis in one way or the other. The Section 5.3 includes the mandatory "Selbstständigkeitserklärung", following from § 7 IV Promotionsordnung des Fachbereichs Physik der Freien Universität Berlin. [299]

5.1 Pseudopotentials

In this section we present the pseudopotentials generated for our calculation and study their quality, *i.e.* their transferability. Before we go into the details, we will start with a reasoning, why the pseudopotential approximation is physically justifyable and what the pseudopotential approximation does. The idea behind the pseudopotential approximation is, that an artificial potential can be used to replace the core electrons of an atom to reduce the computational costs by reduction of the number of electrons which need to be considered for a calculation. [241, 300, 301] The pseudopotential approximation is therefore especially useful for larger atoms with many core electrons, however, it is not always straight forward to decide which electrons of the core can be neglected and which electrons have to be taken into account, as they have mayor contributions to the binding process between different atoms. The duty of a pseudopotential is to effectively reproduce the effects of the core electrons on the valence electron wavefunctions, *i.e.* to enforce the orthogonality of the valence electron wavefunctions to the core states. [241] A method to generate norm-conserving pseudopotentials was described by Troullier and Martins in Reference [241]. It is based on the work of Kerker with the general idea to replace the real wavefunction inside of the core region by a smooth analytical function, *e.g.*, a polynomial or exponential, while a nodeless radial pseudo-valencefunction identically reproduces the real wavefunction outside the core region. [301] The coefficients of the analytical core pseudo wavefunction are determined by constraints/conditions to the wavefunction. [301] The number and type of conditions slightly varies between Kerker (four constraints) [301] and Troullier and Martins (seven constraints). [241] The conditions given by Kerker are that the eigenvalues of pseudo and atomic wavefunctions are identical, the pseudo-wavefunction has to be nodeless and identical to the real valence wavefunction behind the cutoff radius r_c, the first and second derivatives of the wavefunctions have to be matched at r_c (continuity), and the pseudo-charge in a sphere around r_c has to be identical to the real charge contained in that sphere. [301] The "only significant difference between the [Troullier and Martins] study and old schemes is in the use of an even polynomial instead of a mixed polynomial in" [241] the equation for the polynomial contained in the exponential function which forms part of the pseudo-wavefunction defined by Kerker, [241, 301]

this is:

$$R_l^{PP}(r) = \begin{cases} R_l^{AE}(r) & \text{if } r \geq r_c, \\ r^l \cdot \exp[p(r)] & \text{if } r \leq r_c, \end{cases} \qquad (5.1)$$

where $p(r) = c_0 + \sum_{i=2}^{n} c_i r^i$ is the aforementioned polynomial and l is the angular momentum quantum number. [241, 301] The study of Troullier and Martins increased the order n of the polynomial in the exponential compared to Kerker, which increased the variational freedom and allowed to study smoothness properties. [241, 301] Details on the methods can be found in Reference [301] and Reference [241]. The method of Troullier and Martins can be regarded as superior to, *e.g.*, the method of Kerker [301], as larger cut off radii can be used to generate pseudopotentials with comparable transferability properties. [241] The pseudopotentials are generated from the pseudo wavefunctions by inversion of the radial Schrödinger equation. [241]

To perform adequate calculations, it is most important to generate accurate pseudopotentials, meaning pseudopotentials, which reproduce the all-electron wavefunction beyond a cutoff radius r_c for all atomic configurations. [302] The results of calculations with the newly generated pseudopotentials have to be compared to results of all-electron calculations, especially important are the eigenvalue agreement for all atomic configurations, as well as the norm conversation in other than the reference configuration. [241, 302] Further it is common in the literature to perform calculations of bulk moduli and lattice constants using the pseudopotentials to assess the quality of the pseudopotential. [302] We will determine the orbital eigenvalues of various electron configurations and the total energy differences by all-electron calculations and calculations using the pseudopotentials. Further we will compare the lattice constants calculated with pseudopotentials to experimental values as well as other values derived by density functional theory calculations using pseudopotentials.

5.1.1 GGA-PBE

In the following we present and study the quality of the pseudopotentials for carbon, nickel and iron generated within the Troullier-Martins scheme using the generalized

Table 5.1: List of parameters used to generate our generalized gradient approximation (GGA) pseudopotentials in the program package ATOM. [303] All GGA pseudopotentials were generated using the functional of Perdew, Burke and Ernzerhof (PBE) [226] considering relativistic effects (option: pbr) within the generation scheme of Troullier-Martins [241] (option: tm2). The metallic species were generated with a core correction.

atomic species	configuration	r_s	r_p	r_d	r_f	$r_{pseudocore}$
C	[He] $2s^2 2p^2$	1.29	1.29	1.50	1.50	-
Ni	[Ar] $3d^8 4s^2$	2.00	2.30	2.55	2.55	0.75
Fe	[Ar] $3d^6 4s^2$	2.30	2.40	2.70	2.70	0.75

gradient approximation (GGA) functional of Perdew, Burke and Ernzerhof. [226, 241] The parameters used to generate all of our GGA pseudopotentials are presented in Table 5.1. The cutoff radii of iron and nickel are rather large, which makes the pseudopotentials smoother/softer, however, it reduces the transferability. [241] A softer pseudopotential will lead to faster convergence in the calculations, which lead to our decision to trade off accuracy for speed, as numerous and demanding calculations had to be performed using the pseudopotentials. However, we will show in this section, that the agreement between experimental results and calculations utilising the pseudopotentials lead to good agreement, *e.g.*, the lattice constants were overestimated by just a few percent. The generalized gradient approximation tends to overestimate bond lengths/the experimental lattice constants, [302] which we account for by considering the pseudopotential to be decent for slightly higher lattice constant values than the experimental lattice constant. We start our in depth discussion of the pseudopotentials with carbon.

First we compare the orbital eigenvalues of the carbon pseudopotential calculation with the orbital eigenvalues of the all-electron calculation. The difference for the reference configuration [He] $2s^2 2p^2$ for the $2s$ orbitals is very small with 0.06 mRy, as well as for the $2p$'s (spin) with 0.03-0.05 mRy. To be able to model the valence binding of the electrons it is important for the pseudopotential to be able to model other than the reference configuration. [302] We test the [He] $2s^1 2p^3$, [He] $2s^2 2p^1 3s^1$, [He] $2s^1 2p^2 3s^1$, and [He] $2s^0 2p^3 3s^1$ configurations by calculation of orbital eigenvalues and total energies of these systems with our pseudopotential derived from the
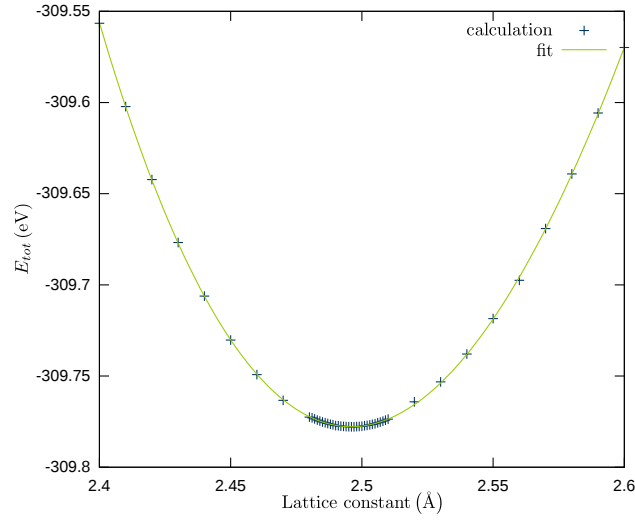
Figure 5.1: Graph of the minimisation of the total energy in dependence of the lattice constant to determine the lattice constant of graphene to test the GGA-PBE pseudopotential for carbon.
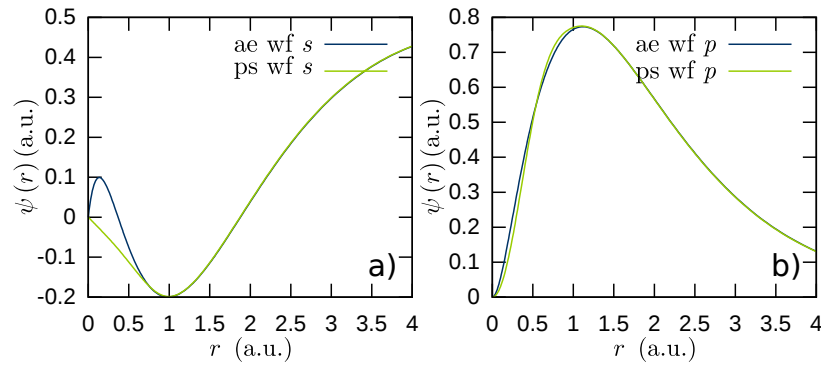

Figure 5.2: Comparison of the s and p wavefunctions for all electrons of carbon (blue) and the wavefunctions of the GGA-PBE pseudopotential of carbon (green). The pseudopotential wavefunctions reproduce the all-electron wavefunctions behind the cutoff radii.
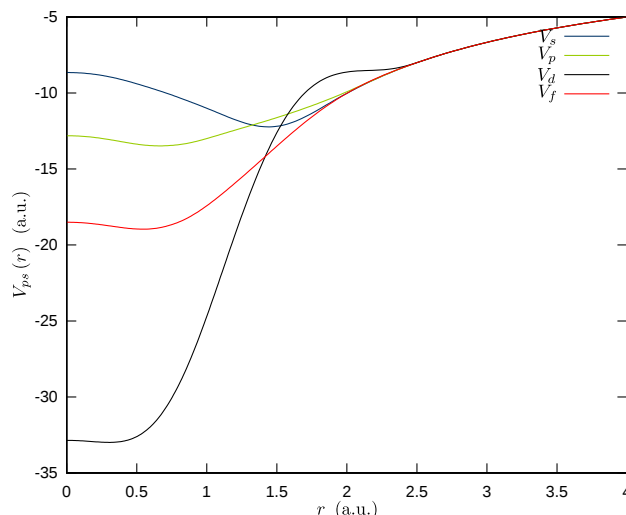
Figure 5.3: Plot of the s, p, d and f GGA-PBE pseudopotentials of nickel.

reference configuration. The highest orbital eigenvalue difference was found with 0.77 mRy for the 2s orbital of the $[\mathrm{He}]\,2s^2 2p^1 3s^1$ configuration, which is still low. [1] The maximal total energy difference was found between the reference configuration and $[\mathrm{He}]\,2s^2 2p^1 3s^1$, with a difference of 1.1 mRy, which should "not (be) much larger than 1 mRy" to generate a good pseudopotential. [303] However, the "*real* proof of good transferability [...] can only come from a molecular or solid-state calculation", [303] therefore we tested the carbon pseudopotential in a calculation of graphene.

Graphene is a small and simple reference system with only two atoms in the unit cell. The lattice constant calculated with our pseudopotential $a = 2.496$ Å is - as expected for GGA functionals - slightly larger than the common literature value $a_{lit} = 2.461$ Å [304] or the measured lattice constant for graphite (corresponding to AB-stacked multi layer graphene) 2.4589 ± 0.0005 Å, [305] see Figure 5.1. A calculation of the lattice constant using the local density approximation with the Perdew-Zunger functional lead to $a = 2.468$ Å, [304] however, LDA generally tends to lead to smaller/better lattice constants than GGA. [241, 302] The wavefunctions of the pseudopotential for the s and p orbital follow the structure of the all-electron wavefunctions behind the cutoff radii, see Figure 5.2.

---

[1] The ATOM user manual states that eigenvalue differences "should be of around 1 mRyd for a good pseudopotential". [303]
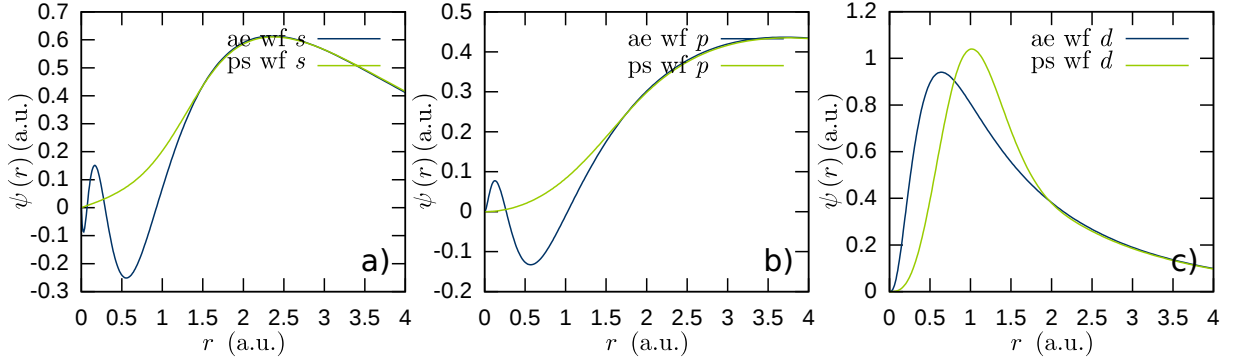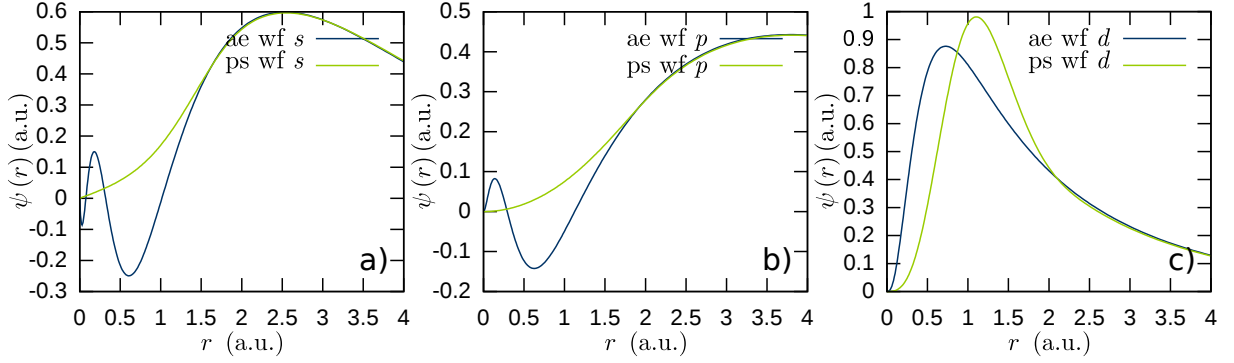
Figure 5.4: Comparison of the s, p, and d wavefunctions for all electrons of nickel
(blue) and the wavefunctions of the GGA-PBE pseudopotential of nickel
(green).

The second pseudopotential we generated is the nickel pseudopotential, see Figure 5.3 and Figure 5.4 for the wavefunctions. We decided to use the electron configuration of $[\mathrm{Ar}]\,3d^8 4s^2$ as the ground state/reference configuration, even though the configuration $[\mathrm{Ar}]\,3d^9 4s^1$ was found to be lower in energy, however, for a pseudopotential to be transferable, the reference configuration should not change the quality of the pseudopotential significantly. [241] The eigenvalues, compared by all electron and pseudopotential calculation, for the reference configuration deviate by 0.05 mRy for the s orbital and by 0.51 mRy for the d orbitals. As non reference configurations we tested the excitations $[\mathrm{Ar}]\,3d^8 4s^1 4p^1$, $[\mathrm{Ar}]\,3d^8 4s^1$, and $[\mathrm{Ar}]\,3d^9 4s^1$. The highest eigenvalue difference was found with 11.77 mRy for the d orbital of the $[\mathrm{Ar}]\,3d^9 4s^1$ configuration, which is quite high, however, the s to d transfer of the metal systems is rather tricky, making it hard to get to low values. Pseudopotentials from the SIESTA pseudopotential database, [2] which is based on the AB-INIT pseudopotential database, [3] lead to eigenvalue differences of up to 11.8 mRy and total energy differences of up to 3.7 mRy. Our total energy differences on the other hand have a maximal difference of only 1.1 mRy for the reference configuration compared to $[\mathrm{Ar}]\,3d^8 4s^1$. To have a better impression of the effect of the eigenvalue difference, especially for the $[\mathrm{Ar}]\,3d^9 4s^1$ configuration, we test the pseudopotential in a model system.

---

[2] http://www.icmab.es/dmmis/leem/siesta/Databases/Pseudopotentials/periodictable-intro.html as of 16th October 2012

[3] http://www.abinit.org/downloads/psp-links/pseudopotentials as of 16th October 2012

Figure 5.5: Comparison of the s, p, and d wavefunctions for all electrons of iron (blue) and the wavefunctions of the GGA-PBE pseudopotential of iron (green).

The nickel pseudopotential was tested in a fcc bulk calculation, leading to a lattice constant of $a = 3.590$ Å, compared to an experimental value of $a = 3.52$ Å [4] and $a = 3.535$ Å derived by a density functional theory calculation using the GGA functional PW91. [85, 306] The deviation from the experimental value is about 2%, being decent enough for our calculations and the trade off we expected, as we chose larger cut off radii for the orbitals to generate smoother pseudopotentials.

The last GGA-PBE pseudopotential we generated is the pseudopotential of iron, see Figure 5.5 for the pseudo wavefunctions. We decided to use the groundstate electron configuration of $[\text{Ar}]\,3d^6 4s^2$ as the reference configuration, even though we found the configuration of $[\text{Ar}]\,3d^7 4s^1$ to be lower in energy. Comparison of the eigenvalues of all electron and pseudopotential calculations for the reference configuration lead to a deviation of 0.04 mRy for the s orbital and 0.36 mRy for the d orbitals. As non reference configurations we tested the excitations $[\text{Ar}]\,3d^6 4s^1 4p^1$, $[\text{Ar}]\,3d^6 4s^1$, and $[\text{Ar}]\,3d^7 4s^1$. The highest eigenvalue difference was found with 10.14 mRy for the d orbital of the $[\text{Ar}]\,3d^7 4s^1$ configuration. Non-relativistically generated pseudopotentials from the SIESTA pseudopotential database yield eigenvalue differences of up to 13.0 mRy and total energy differences of up to 6.6 mRy. Even a pseudopotential generated with a small cutoff of $r_c^{s,p,d,f} = 1.60$ a.u. [5], lead to eigenvalue

---

[4]From Table 1.3 "Kristallstrukturen der Elemente" Page 24 in Reference [85].

[5]The pseudopotential was generated relativistically with all parameters according to our used pseudopotential, only the cutoff radii were changed, the core correction had a pseudo core of $r_{pseudo} = 0.75$ a.u..

Table 5.2: List of parameters used to generate our van der Waals (VDW) pseudopotentials in the program package ATOM [303] using the functional of Dion, Rydberg, Schröder, Langreth, and Lundqvist (DRSLL) [227] (option: vw) within the generation scheme of Troullier-Martins [241] (option: tm2).

atomic species	configuration	r_s	r_p	r_d	r_f
C	$[He] 2s^2 2p^2$	1.29	1.29	1.50	1.50

differences of up to 7.8 mRy, being slightly better than the value of our used pseudopotential, however, we found a maximal total energy differences of 6.6 mRy. The total energy differences of our used pseudopotential are even lower than in the case of the Ni pseudopotential with a maximal difference of only 0.8 mRy for the reference configuration compared to $[Ar] 3d^6 4s^1$. The transferability is again tested with a calculation on a reference system and comparison to experimental and other theoretical values.

The iron pseudopotential was tested in a bcc bulk configuration with a lattice constant of $a = 2.936$ Å, compared to an experimental value of $a = 2.87$ Å and $a = 2.858$ Å or $a = 2.963$ Å for other calculation by density functional theory using GGA functionals. [85, 306, 307] The deviation from the experimental value is therefore about 2.4%, which is in between the values calculated by other theoretical calculations.

5.1.2 VDW-DRSLL

In the following we present and study the quality of the carbon pseudopotential generated within the Troullier-Martins scheme using the van der Waals density functional (VDW) of Dion, Rydberg, Schröder, Langreth, and Lundqvist (DRSLL). [227, 241] We used the same parameters for the generation of the GGA-PBE and VDW-DRSLL pseudopotential and changed only the functional for the generation of the pseudopotential, see Table 5.2.

The difference for the eigenvalues of the reference configuration $[He] 2s^2 2p^2$ for the $2s$ orbitals is again, as for the GGA-PBE carbon pseudopotential, very small with 0.03 mRy, as well as for the $2p$ with 0.06 mRy. We tested the same excitation configurations as for the GGA-PBE pseudopotential of carbon, namely the
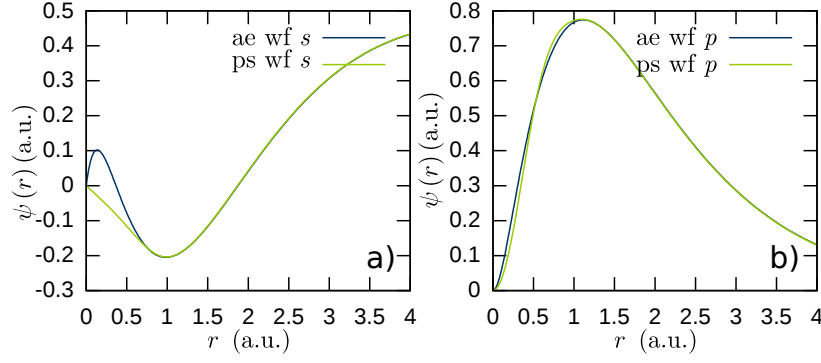
Figure 5.6: Comparison of the s and p wavefunctions for all electrons of carbon (blue) and the wavefunctions of the VDW-DRSLL pseudopotential of carbon (green). The pseudopotential wavefunctions reproduce the all-electron wavefunctions behind the cutoff radii, showing an overall good agreement.

[He] $2s^1 2p^3$, [He] $2s^2 2p^1 3s^1$, [He] $2s^1 2p^2 3s^1$, and [He] $2s^0 2p^3 3s^1$ configurations. The highest orbital eigenvalue difference was found with 3.7 mRy for the 2p orbital of the [He] $2s^2 2p^1 3s^1$ configuration. The maximal total energy difference was found between the reference configuration and [He] $2s^0 2p^3 3s^1$, with a difference of 3.8 mRy. As the values are higher than the GGA-PBE values, the transferability check for a reference system is important.

We performed a test calculation of the pseudopotential on graphene. The lattice constant was found with $a = 2.509$ Å, slighly higher than the GGA-PBE ($\approx 1.7\%$), and literature values ($\approx 2\%$). [304, 305] It was found, however, that the van der Waals density functional tends to overestimate lattice constants (*e.g.* for out of plane carbon), which agrees with our result. [236, 308]

The calculation time for the exchange correlation potential was estimated to be about 10 times larger for the van der Waals functional compared to the calculation with a generalized gradient approximation (GGA). [233] Comparing to the previous results for the GGA-PBE calculation, we find an increase of about 20% in total calculation time for the van der Waals functional calculation (361s) compared to the GGA-PBE calculation (308s), showing that the calculations performed by the van der Waals functional are computationally more demanding than standard DFT (LDA, GGA) calculations, however, they are still manageable.

5.2 Acknowledgments

- Andre Boden: I want to thank Andre for being an always friendly and communicative colleague and room neighbor. He knows everything about sports and I especially enjoyed drifting away from physics during the walks to the Mensa and talk about the mayor sports events, *e.g.* soccer championships, . . .

- Pascal Blümmel: Thank you Pascal, it was always a pleasure to have you around. The discussions were always interesting, even if they sometimes did not cover condensed matter physics (discussions on golf). I want to especially acknowledge Pascal here, as Pascal believes that it does not make sense to acknowledge people that "you might not even know anymore in a few years". I still have the hope that you will know me when I open this thesis in a far far future, as well as I hope to remember you.

- Michael Gegg: Michael was my bachelor student and did a project on bilayer graphene under my supervision. I especially thank him for the fruitful discussion on the differences and equivalency between the structure of bilayer graphene and carbon nanotube bundles and for the calculations on bilayer graphene and graphite. The discussions helped to improve our collaboratively published manuscript.

- Roland Gillen: I thank Roland for our interesting projects in Berlin and Cambridge. He was able to give me some insight into CASTEP and how it can be recoded to perform calculations of defects, which, however, did not became a part of this dissertation. I especially enjoyed our pub crawls around Cambridge, as well as in depth discussions on electronic structure theory, that opened my mind and gave me motivation to start reading more papers and books on the topic.

- Benjamin Hatting: My office mate which had the worst place with his back to the door. He was always open to useful discussions on the recent topics. I want to thank him for always taking care on our room plant and the awesome time we had in the office. I hope you enjoy "my" desk for the time until you finish your PhD.

- Sebastian Heeg: My other office mate sitting at the other "good" spot. He shared the office with me for my full time of four years in the group, including

my time as a diploma student. We had a lot of useful discussions and I want to thank him again for the good time we had. Even though our first plant did not make it till the end of our PhDs, he still had enough faith in us to buy a second one. I hope this one will outlive us and bring joy and a good climate to all following PhD generations of the AG-Reich.

- Frank Hennrich: Frank is one of our collaborators from Karlsruhe, who had a significant influence on the direction of my studies by the suggestion to study the debundling of carbon nanotubes during a conference in Kirchberg. Thank you for your input and discussions.

- Christian Lehmann: I want to thank Christian for the discussions we shared and for being the IT supervisor of the group. He was always helpful and friendly. I especially enjoyed sharing the same home district with him "Spandau", even though the other group members did not quite understand what it means to be from Spandau.

- Rohit Narula: Rohit left me his prior spot in our room after he had finished his PhD, so I finally did not have the door in my back. I also want to thank him for being a nice and smart guy with constructive questions and criticism that were always able to open my eyes for problems that I was not able to see before.

- Antonio Setaro: Antonio was always a great help with *Mathematica* [287] and my source for finding papers on postprocessing methods for carbon nanotubes. His skills in *Mathematica* will never be forgotten, which saved me a lot of time. I especially enjoyed sharing the duty of being a guest editor for the IWEPNM 2010 and 2011 with him. Here the *Mathematica* skills were very useful, by creating a *Mathematica* notebook, which delivered the personalized mails to all of the about 200 different authors. I also want to thank him for the time we spend together watching mystery movies or driving around in town.

- I would also like to thank all other people from the research groups in Berlin and Cambridge that shared their time with me in scientific and private discussions.

- A special thanks goes to Jens Dreger and Philipp Neuser and the whole ZEDV team that were available day and night for problems with software, hardware and especially the computer cluster system. Therefore I would also like to thank "aramis" and later "sheldon" for giving me access to their minions to perform my calculations.

- Regina Dumlich and Joachim Dumlich: Danke, dass ihr mir ermöglicht habt der Mensch zu werden, der ich geworden bin. Danke dafür, dass ihr mich in allen meinen Wünschen und Plänen unterstützt habt und mir in allen Phasen des Lebens beigestanden seid. Ich werde es euch nie vergessen.

- Anita Schröder: Vielen Dank für die Korrekturen an den deutschsprachigen Teilen der Arbeit, für dein Verständnis und dass du immer für mich da warst.

- Freie Universität Berlin: The Free University has been my home institution for the last eight years. I am very grateful for the guidance and advice I received during my time at the FU. Not only during my thesis time, but also before, when I was a student starting to figure out the mysteries of physics and of course also student life. I therefore want to thank all of my professors, tutors, advisers, and fellow students for leading/accompanying me on my path to this ultimate goal of finishing my PhD at my wonderful home institution. In fact the FU has been more than a home institution for me, it became somewhat of *home*, . . . at least if one considers, that I spent more time at the FU than any other place in the last eight years of my life.

- University of Cambridge: Thank you for hosting my two research stays during my diploma and PhD time at the Center for Advanced Photonics and Electronics (CAPE).

- European Research Council: The European Research Council gave me the funding and allowed me to follow my research ideas without worrying about money. I especially want to thank for the support of the ERC grant 210642 optnano.

I would further like to thank all contributors to the following software/program/tool packages, which have been extensively used to create this PhD thesis and the research performed within it:

- ATOM: Version 3.2.8 + 3.3.1 - see Reference [303]

- *Avogadro*: Version 1.0.3 - http://avogadro.openmolecules.net/wiki/Main_Page and Reference [57]

- Bader: Version 0.28a - http://theory.cm.utexas.edu/bader/ and References [271–273]

- CAGE: see Reference [265]

- gedit: Version 2.30.4 - http://www.gedit.org

- gnuplot: Version 4.6 - http://www.gnuplot.info/

- JabRef: Versions 2.5 to 2.8.1 - http://jabref.sourceforge.net/

- LaTeX: http://www.latex-project.org/

- libreoffice: Version 3.5.4.2 - http://www.libreoffice.org/about-us/credits/

- *Mathematica*: Version 7.0.1.0 - see Reference [287]

- SIESTA: various Versions - see http://icmab.cat/leem/siesta/ and Reference [216]

- wrapping: version 09/14/2004 by Shigeo Maruyama maruyama@photon.t.u-tokyo.ac.jp - http://reizei.t.u-tokyo.ac.jp/ maruyama/wrapping3/wrapping.zip

5.3 Selbstständigkeitserklärung

Hiermit versichere ich, dass ich die vorliegende Dissertation mit dem Titel:

"A Path to Monochiral Ensembles of Carbon Nanotubes and their Properties"

selbstständig und ausschließlich unter der Zuhilfenahme der angegebenen Hilfsmittel und Hilfen angefertigt habe. Ich versichere des Weiteren, dass die Arbeit in keinem früheren Promotionsverfahren angenommen oder als ungenügend beurteilt wurde. Diese Erklärung ist nach § 7 Absatz 4 der Promotionsordnung des Fachbereichs Physik der Freien Universität Berlin, veröffentlicht am 5. Februar 2010 im Amtsblatt der Freien Universität Berlin auf den Seiten 32 ff., Bestandteil der Dissertation.

Berlin, den 7. Januar 2013

Heiko Dumlich

"Yatta!" [Green Leaves, 2001]

The End